

# Magnetic Properties of Uranium Based Ferromagnetic Superconductors

The research described in this thesis was performed in the section Fundamental Aspects of Materials and Energy of the department Radiation, Radionuclides and Reactors, faculty of Applied Sciences, Delft University of Technology, Mekelweg 15, 2629 JB Delft, The Netherlands.

# Magnetic Properties of Uranium Based Ferromagnetic Superconductors

PROEFSCHRIFT

ter verkrijging van de graad van doctor  
aan de Technische Universiteit Delft,  
op gezag van de Rector Magnificus Prof. dr. ir. J.T. Fokkema,  
voorzitter van het College voor Promoties,  
in het openbaar te verdedigen op maandag 5 februari 2007 om 15:00 uur

door

Serdar SAKARYA

natuurkundig ingenieur  
geboren te 's-Gravenhage

Dit proefschrift is goedgekeurd door de promotor:

Prof. dr. I. M. de Schepper

Toegevoegd promotor: Dr. P. C. M. Gubbens

Samenstelling promotiecommissie:

Rector Magnificus	voorzitter
Prof. dr. I. M. de Schepper	Technische Universiteit Delft, promotor
Dr. P. C. M. Gubbens	Technische Universiteit Delft, toegevoegd promotor
Prof. dr. H. von Löhneysen	Universität Karlsruhe, Duitsland
Prof. dr. M. S. Golden	Universiteit van Amsterdam
Prof. dr. ir. T. M. Klapwijk	Technische Universiteit Delft
Dr. ir. N. H. van Dijk	Technische Universiteit Delft
Dr. P. Dalmas de Réotier	Commissariat à l'Energie Atomique, Frankrijk
Prof. dr. ir. T. H. J. J. van der Hagen	Technische Universiteit Delft, reservelid

Dr. ir. N. H. van Dijk heeft als begeleider in belangrijke mate aan de totstandkoming van dit proefschrift bijgedragen.

© 2006 S. Sakarya and IOS Press

All rights reserved. No part of this book may be reproduced, stored in a retrieval system, or transmitted, in any form or by any means, without prior permission from the publisher.

ISBN

Keywords: Ferromagnetism and superconductivity, muon spin relaxation, neutron depolarization, chemical substitution, URhGe, UGe<sub>2</sub>, UIr

*Published and distributed by IOS Press under the imprint Delft University Press*

*Publisher*

IOS Press

Nieuwe Hemweg 6b

1013 BG Amsterdam

The Netherlands

tel: +31-20-688 3355

fax: +31-20-687 0019

e-mail: [info@iospress.nl](mailto:info@iospress.nl)

[www.iospress.nl](http://www.iospress.nl)

[www.dupress.nl](http://www.dupress.nl)

LEGAL NOTICE

The publisher is not responsible for the use which might be made of the following information.

PRINTED IN THE NETHERLANDS

## **An die Musik**

Du holde Kunst, in wieviel grauen Stunden,  
Wo mich des Lebens wilder Kreis umstrickt,  
Hast du mein Herz zu warmer Lieb entzunden,  
Hast mich in eine bessre Welt entrückt!

Oft hat eine Seufzer, deiner Harf entflossen  
Ein süsßer, heiliger Akkord von dir  
Den Himmel bessrer Zeiten mir erschlossen,  
Du holde Kunst, ich danke dir dafür!

Franz von Schober  
(Musik: Franz Schubert)

*Aan mijn moeder*



---

# CONTENTS

<b>Contents</b>	<b>VII</b>
<b>1 Introduction</b>	<b>1</b>
1.1 General Introduction . . . . .	1
1.2 Outline of this thesis . . . . .	3
<b>2 Experimental Techniques</b>	<b>5</b>
2.1 Sample Preparation . . . . .	5
2.2 $\mu$ SR Spectroscopy . . . . .	6
2.2.1 Production, life, and decay of the muon . . . . .	6
2.2.2 Experimental Geometries . . . . .	9
2.2.3 $\mu$ SR Spectrometers: EMU, GPS, and GPD . . . . .	9
2.2.4 Depolarization and Relaxation Functions . . . . .	11
2.2.5 Magnetic Field at the Muon Site . . . . .	17
2.3 Three-Dimensional Neutron Depolarization . . . . .	20
2.4 Macroscopic techniques . . . . .	22
2.4.1 Magnetization . . . . .	22
2.4.2 Thermal Expansion and Magnetostriction . . . . .	23
2.4.3 Electrical Resistivity . . . . .	25
2.4.4 Specific Heat . . . . .	25
2.4.5 X-ray Powder Diffraction . . . . .	25
<b>3 Theory</b>	<b>27</b>
3.1 Heavy Fermions . . . . .	27
3.2 Quantum Phase Transitions . . . . .	33
3.3 Fermi liquid and non-Fermi liquid behavior . . . . .	36
3.3.1 Fermi gas . . . . .	37
3.3.2 Fermi liquid . . . . .	38

3.3.3	Non-Fermi liquid . . . . .	39
3.4	Grüneisen parameters . . . . .	41
3.5	Thermodynamic Considerations . . . . .	42
3.6	Ferromagnetic Superconductors . . . . .	43
<b>4</b>	<b>UGe<sub>2</sub></b>	<b>45</b>
4.1	Introduction . . . . .	45
4.2	Three-Dimensional Neutron Depolarization . . . . .	47
4.2.1	Introduction . . . . .	47
4.2.2	Experimental . . . . .	50
4.2.3	Three-dimensional neutron depolarization . . . . .	50
4.2.4	Results . . . . .	53
4.2.5	Discussion . . . . .	54
4.2.6	Conclusions . . . . .	59
4.3	Muon Spin Rotation and Relaxation . . . . .	59
4.3.1	Introduction . . . . .	59
4.3.2	Experimental . . . . .	60
4.3.3	Results . . . . .	62
4.3.4	Analysis . . . . .	78
4.3.5	Discussion . . . . .	88
4.3.6	Conclusions . . . . .	92
<b>5</b>	<b>URhGe</b>	<b>97</b>
5.1	Introduction . . . . .	97
5.2	Dilatometry . . . . .	99
5.2.1	Introduction . . . . .	99
5.2.2	Experimental . . . . .	99
5.2.3	Results . . . . .	99
5.2.4	Discussion . . . . .	100
5.2.5	Conclusions . . . . .	106
5.3	Muon Spin Rotation and Relaxation . . . . .	106
5.3.1	Introduction . . . . .	106
5.3.2	Experimental . . . . .	107
5.3.3	Results . . . . .	108
5.3.4	Analysis . . . . .	112
5.3.5	Discussion . . . . .	115
5.3.6	Conclusions . . . . .	119
<b>6</b>	<b>URh<sub>1-x</sub>Ru<sub>x</sub>Ge</b>	<b>121</b>
6.1	Introduction . . . . .	121
6.2	Experimental . . . . .	124
6.3	Results . . . . .	125
6.3.1	Magnetization at ambient pressure . . . . .	125
6.3.2	Electrical resistivity . . . . .	129



---

6.3.3	X-ray powder diffraction . . . . .	133
6.3.4	Specific heat . . . . .	134
6.3.5	Magnetization under pressure . . . . .	135
6.4	Analysis and Discussion . . . . .	137
6.5	Conclusions . . . . .	143
<b>7</b>	<b>UIr</b>	<b>145</b>
7.1	Introduction . . . . .	145
7.2	Magnetization in High Magnetic Fields . . . . .	148
7.2.1	Introduction . . . . .	148
7.2.2	Experimental . . . . .	149
7.2.3	Results . . . . .	149
7.2.4	Discussion . . . . .	150
7.2.5	Conclusions . . . . .	150
7.3	Specific Heat . . . . .	151
7.3.1	Introduction . . . . .	151
7.3.2	Experimental . . . . .	151
7.3.3	Results and Discussion . . . . .	151
7.4	Thermal Expansion and Magnetostriction . . . . .	153
7.4.1	Introduction . . . . .	153
7.4.2	Experimental . . . . .	153
7.4.3	Results . . . . .	154
7.4.4	Discussion and Conclusions . . . . .	158
	<b>Summary</b>	<b>163</b>
	<b>Samenvatting</b>	<b>167</b>
	<b>Bibliography</b>	<b>171</b>
	<b>Acknowledgements</b>	<b>181</b>
	<b>Curriculum Vitae</b>	<b>183</b>
	<b>List of publications</b>	<b>185</b>




---

# CHAPTER 1

---

## Introduction

### 1.1 General Introduction

 THE DISCOVERY OF SUPERCONDUCTIVITY within a limited pressure range (1.0-1.6 GPa) in UGe<sub>2</sub> [1] provided an unanticipated example of the coexistence of superconductivity and ferromagnetism, because these phenomena were long thought to be exclusive. One year later, a coexistence of these two phenomena was also found in URhGe [2]. The most striking difference with UGe<sub>2</sub> is that this coexistence occurs at ambient pressure and is therefore not a pressure induced effect. Just like in UGe<sub>2</sub>, a coexistence was later found in UIr [3], where it occurs within a limited pressure range (2.6-2.7 GPa), where ferromagnetic order is on the verge of its existence. With the coexistence of ferromagnetism and superconductivity, these three U compounds belong to a class of materials, which exhibit unconventional ground state properties in a strongly correlated ferromagnetic system. In this class of materials UIr holds a special place because it is a system in which the crystal structure lacks inversion symmetry.

In the late 1950s, Bardeen, Cooper and Schrieffer (BCS) showed that superconductivity involves the formation of bound pairs of electrons, named Cooper pairs [4]. They argued that the electron pairs were “glued together” by excitations. Although phonons were implicated in superconductivity many years before the BCS theory, it was not until the 1960s that it became possible to definitively identify them as the glue in conventional superconductivity. The model predicts that the attractive pairing interaction is reduced in a magnetic field and, as a consequence, is suppressed by ferromagnetic order. This prediction is consistent with experimental observations in a number of systems where ferromagnetic order sets in below the superconducting transition temperature and the superconducting pairing of the conduction electrons is either weakened or completely suppressed. This is nicely demonstrated by the

experiments on  $\text{ErRh}_4\text{B}_4$  [5, 6] and  $\text{HoMo}_6\text{S}_8$  [7], where the superconductivity is suppressed when ferromagnetic order sets in.

The 1970s and 1980s led to the discovery of superconductivity in two new, unconventional classes of materials, the heavy-fermion [8] and high-temperature [9] superconductors. Conventional superconductivity is suppressed by the tiniest concentration of magnetic atoms, but the unconventional superconductors contain a dense array of magnetic atoms, which appear to be actively involved in electron pairing. In the heavy-fermion systems, intermetallic compounds usually based on Ce or U, the  $4f$  or  $5f$  electrons play a crucial role leading to the formation of quasiparticles with a large effective mass. A better understanding of superconductivity in these type of materials has been sought ever since the pioneering discovery of heavy-fermion superconductivity in  $\text{CeCu}_2\text{Si}_2$  [8]. For these systems a new kind of magnetically mediated superconductivity was proposed in which the glue that causes electrons to form Cooper pairs is derived from magnetic fluctuations [10, 11].

However, until the discovery of the coexistence of ferromagnetic order and superconductivity, it was generally believed that these two phenomena were mutually exclusive. Superconductivity would be destroyed because of the paramagnetic effect (aligning of the opposite spins) and by the orbital effect (opposite Lorentz forces). With  $\text{UGe}_2$ ,  $\text{URhGe}$ , and  $\text{UIr}$ , a new class of materials has been shown to exhibit a stable phase in which superconductivity coexists within the ferromagnetic ordered state. This discovery has led to the study of intriguing new possibilities for unconventional mechanisms for magnetically mediated superconductivity.

Another fascinating feature of these three U-based ferromagnetic superconductors, is that this type of superconductivity was found to occur in the vicinity of a quantum critical point (QCP). A phase transition from a magnetically ordered phase to a disordered phase by tuning the pressure or by chemical substitution, is called a quantum phase transition since quantum fluctuations lead to a breakdown of the long-range order, in contrast to the classical phase transitions where thermal fluctuations play a crucial role. The critical pressure, or critical chemical composition, where the ordering temperature is tuned to  $T_C = 0$  K is referred to as a QCP. At this point the Fermi-liquid theory breaks down and new physics is observed.

Fermi-liquid theory has been successful in describing the low-temperature behavior of many metallic compounds. Within this theory the electron interactions are accounted for by an effective mass for the conduction electrons. Many Ce and U systems with very strong electronic correlations are well described in terms of Fermi-liquid theory. In recent years, several systems where the Fermi-liquid scenario does not apply, have been found. These systems, known as non-Fermi liquids, are mainly found in the vicinity of a quantum critical point.

The coexistence of ferromagnetism and superconductivity in the vicinity of a ferromagnetic quantum critical point, is the main motivation that the related compounds are investigated thoroughly. The fact that magnetic fluctuations are enhanced near a quantum critical point, just where superconductivity is found, strongly suggests that the attractive force between the electrons forming the Cooper pair,

originates from the magnetic fluctuations.

The magnetic fluctuations and the non-Fermi-liquid behavior observed near a ferromagnetic quantum critical point are not fully understood yet, neither how magnetic fluctuations cause an attractive force between electrons, nor how superconductivity and ferromagnetism can coexist. It is therefore of utmost importance to study the magnetic fluctuations, or more general, the magnetic properties, in  $\text{UGe}_2$ ,  $\text{URhGe}$ , and  $\text{UIr}$ , in combination with non-Fermi-liquid behavior. This thesis has the intention to contribute to the understanding of the role of ferromagnetism and ferromagnetic spin fluctuations in their coexistence with superconductivity.

## 1.2 Outline of this thesis

In Chapter 2 the details of several experimental techniques are discussed. First, the sample preparation is presented. After this, a description of the  $\mu\text{SR}$  technique follows, including the used experimental set-ups, the interpretation of muon depolarization data, and a discussion about the magnetic field at the muon site. The three-dimensional neutron depolarization technique is explained next. The Chapter ends with a basic description of the macroscopic techniques used in this thesis: magnetization, thermal expansion and magnetostriction, electrical resistivity, specific heat, and X-ray powder diffraction.

Chapter 3 deals with the relevant theory from solid state physics. A basic description is given about the main mechanism leading to the development of a strongly correlated state at low temperatures - the Kondo effect. A magnetic phase diagram results when the competition with the long-ranged RKKY interaction is taken into account. The concept of a quantum critical point is explained, as well as Fermi-liquid and non-Fermi-liquid behavior of the correlated electron system. After a review on the Grüneisen analysis, which enables the study of the volume dependence of thermodynamic energy scales, a few thermodynamic considerations on phase transition are presented. The Chapter ends with a review of the recent theories to explain the coexistence of superconductivity with ferromagnetism.

In Chapter 4 the ferromagnetic domain structure in  $\text{UGe}_2$  is studied by neutron depolarization. The question is whether the ferromagnetic domain size  $d$  is in the order of micrometers (*i.e.* much larger than the superconducting coherence length  $\xi_{\text{sc}}$ ) or in the order of nanometers (comparable to  $\xi_{\text{sc}}$ ). The implications of the size of  $d$  with respect to  $\xi_{\text{sc}}$  are discussed. Subsequently, muon spin rotation and relaxation measurements are presented. These measurements have been performed under pressures up to 1.0 GPa. An inner phase transition ( $T_X$ ), which occurs within the ferromagnetic phase, is monitored as a function of pressure. Subsequently, the critical dynamics close to  $T_C$  at a pressure of 0.95 GPa was studied. Conclusions are drawn about the nature of the magnetic fluctuations and their influence on the superconducting state.

In Chapter 5 experimental data on  $\text{URhGe}$  are presented. Thermal expansion measurements were performed in order to determine the uniaxial pressure depen-

dence of the Curie temperature  $T_C$ . The data are analyzed with the help of the Ehrenfest relation. The volume dependence of the energy scale for the spin fluctuations at low temperature is calculated. The magnetism in URhGe is further studied by muon experiments. The frequency scale and anisotropy of the magnetic fluctuations are measured by field scans in the vicinity of  $T_C$ .

In Chapter 6 a report is given on the attempts to tune URhGe to a quantum critical point ( $T_C = 0$ ) by appropriate chemical substitutions: Rh is substituted for Ru and for Co, and Ge for Si. The critical substitution concentration  $x_{cr}$  is obtained by measuring  $T_C$  as a function of concentration  $x$ , deduced from magnetization and electrical resistivity measurements. The URh<sub>1-x</sub>Ru<sub>x</sub>Ge samples are investigated further by means of X-ray powder diffraction, specific heat, and magnetization under pressure.


In Chapter 7 the magnetic properties of UIr are investigated by means of magnetization in a pulsed field up to 52 T, specific heat in fields up to 14 T, thermal expansion in zero field and 5 T, and magnetostriction up to 10 T. The high field measurements were performed to quantify the strength of the magnetic interactions in UIr.

---

## CHAPTER 2

---

# Experimental Techniques

 SEVERAL TECHNIQUES have been employed in the study of the magnetic properties of the ferromagnetic superconductors UGe<sub>2</sub>, URhGe, and UIr. They will be presented in this Chapter. After a brief discussion on sample preparation, the muon spin rotation and relaxation ( $\mu$ SR) technique is described in some detail, as well as the three-dimensional neutron depolarization technique. Subsequently, a simple description is given of a few techniques which probe macroscopic thermodynamic properties of the compounds under study: magnetization, electrical resistivity, specific heat, thermal expansion, and magnetostriction. The Chapter ends with a basic discussion on X-ray powder diffraction.

### 2.1 Sample Preparation

All the samples used and described in this thesis were prepared at the Van der Waals-Zeeman Institute (WZI) of the University of Amsterdam (UvA). Polycrystals were prepared in collaboration with N. T. Huy and single-crystalline samples were grown by Y. K. Huang and E. Brück. Only single crystals were used in the studies of UGe<sub>2</sub>, URhGe, and UIr, whereas measurements on U(Rh,Ru)Ge, U(Rh,Co)Ge, and URh(Ge,Si) were performed on polycrystals.

The polycrystalline samples were prepared by arc-melting the constituents in a stoichiometric ratio in an arc furnace with a water cooled copper crucible under an argon atmosphere (0.5 bar). The single-crystalline samples were grown from a polycrystalline ingot using the Czochralski technique in a tri-arc furnace. For details on the crystal growth of U intermetallic compounds, see *e.g.* Ref [12].

As far as the samples were annealed, they were wrapped in tantalum foil and put in a quartz tube together with a piece of uranium that served as a getter. After evacuating and sealing the tubes, the samples were annealed at high temperature.

The temperature and duration of annealing depended on the sample. Details are given in the experimental parts of the following Chapters.

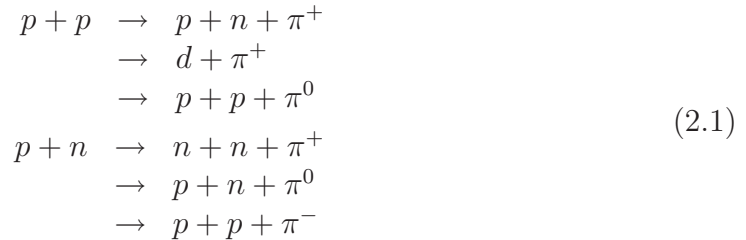
The single crystals were checked for their single-crystalline nature by means of the X-ray back-reflection Laue method [13] at Leiden University and at the University of Amsterdam (UvA). After orientation of the single crystals with the help of the computer program OrientExpress [14] the crystals were cut by spark-erosion in the appropriate shapes (platelets, bars, cubes, cylinders, and spheres).

## 2.2 $\mu$ SR Spectroscopy

The acronym  $\mu$ SR stands for Muon Spin Rotation, Relaxation, Resonance, or simply Research.  $\mu$ SR is a widespread technique used in solid state physics and is closely related to Nuclear Magnetic Resonance (NMR). The principle of the  $\mu$ SR technique is quite simple. Positive muons are produced and implanted in a sample where they localize at a particular site. The local magnetic field  $\mathbf{B}_{\text{loc}}$  at this interstitial site exerts a torque on the muon spin ( $\mathbf{S}_\mu = 1/2$ ), so that the spin precesses around the local magnetic field with a frequency of  $\omega = \gamma_\mu |\mathbf{B}_{\text{loc}}|$ . Here  $\gamma_\mu = 851.62 \text{ Mrad s}^{-1} \text{ T}^{-1}$  is the gyromagnetic ratio of the muon. After a certain time, the muon decays and a positron is emitted, preferentially in the direction of the muon spin, at the moment of decay. The positron is detected. After collecting several million positrons the time-evolution of the polarization of an ensemble of muons can be reconstructed. The polarization function  $P(t)$  reflects the spatial and temporal distribution of the magnetic field at the muon site. In this Section a few elements of the  $\mu$ SR technique will be elaborated on. A more detailed general description can be found in Refs. [15, 16, 17]. Experimental results on some exemplary materials can be found in Refs. [18, 19, 20]. Some physical properties of the muon are given in Table 2.1.

### 2.2.1 Production, life, and decay of the muon

The production of intense muon beams starts in large accelerators where protons ( $p$ ) gain energies up to  $\sim 600 \text{ MeV}$ . These highly energetic protons are aimed at a graphite or beryllium target. Several nuclear reactions take place between the protons and the protons and neutrons ( $n$ ) of the target, leading to the production of pions ( $\pi$ ):



where  $d$  stands for deuteron. The charged pions  $\pi^+$  and  $\pi^-$  have an average life time of 26 ns and decay into the muons  $\mu^+$  and  $\mu^-$  and the accompanying (anti-)neutrinos



**Table 2.1:** Several physical properties of the muon, compared to those of the electron ( $e$ ) and the proton ( $p$ ).

mass	$m_\mu$	206.763835 (11) $m_e$ 0.1126096 $m_p$
charge		$+e$ or $-e$
spin	$S_\mu$	1/2
magnetic moment	$\mu_\mu$	8.8905981 (13) $\mu_N$ 3.1833452 (20) $\mu_p$
gyromagnetic ratio	$\gamma_\mu$ $\gamma_\mu/2\pi$	851.62 Mrad s $^{-1}$ T $^{-1}$ 135.53879 (1) MHz T $^{-1}$
life time	$\tau_\mu$	2.19714 (7) $\mu$ s

( $\nu_\mu$  and  $\bar{\nu}_\mu$ ) according to:

$$\begin{aligned}\pi^+ &\rightarrow \mu^+ + \nu_\mu \\ \pi^- &\rightarrow \mu^- + \bar{\nu}_\mu\end{aligned}\tag{2.2}$$

The neutral pion  $\pi^0$  plays no role in the  $\mu$ SR technique, since it has a very short average life time of 0.089 fs before it decays into photons. In solid state physics almost all  $\mu$ SR research is carried out using positive muons  $\mu^+$ .

Pions possess zero spin and neutrinos have a spin  $S_\nu = 1/2$  polarized opposite to their momentum. Because angular momentum has to be conserved, the muon spin has to be antiparallel to its momentum in the rest frame of the pion. This allows the production of a highly spin polarized  $\mu^+$ -beam.

After production the muons are directed to the  $\mu$ SR instruments by electromagnetic guide fields using bending magnets and focussing quadrupole magnets. Along the path an electric and magnetic field separator is included to remove contaminant particles (mainly positrons) from the muon beam. (These are however absent in high-energy beamlines such as GPD, see Sec. 2.2.3.) After implantation in the sample the muon will thermalize. Along the first part of its track the muon thermalizes by energy exchange through ionizing host atoms and creating vacancies. This however does not influence the experimental results since the final area of localization will not be affected. Along the last part of its track the muon thermalizes by successive captures and dissociation of electrons from the host. The neutral bound state with an electron is known as muonium ( $\mu^+e^-$ ), an exotic light version of the hydrogen atom. In semi-conductors and insulators muonium can be stable, and it can even be incorporated in some organic materials. In metals, however, muonium finally dissociates, and the muon will localize at an interstitial site, where it will be surrounded by a charge screening cloud of conduction electrons of its host. The

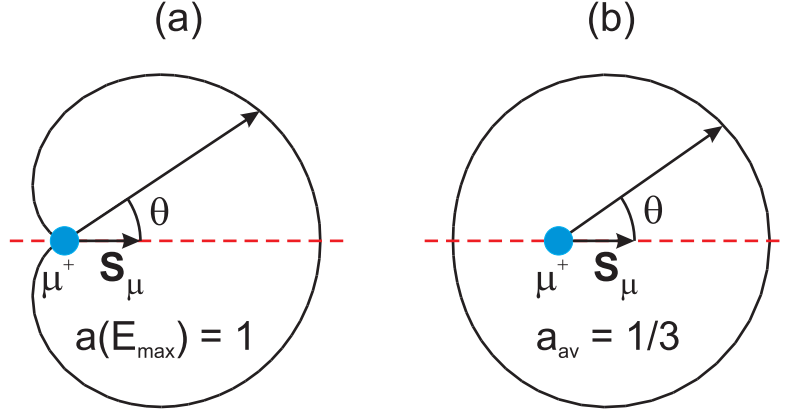


**Figure 2.1:** The angular distribution  $W_{e^+}(\theta)$  of the decay positrons for (a) the maximum positron energy of 52.83 MeV ( $a = 1$ ) and (b) integrated over all energies ( $a = 1/3$ ).

implantation and thermalization processes occur so rapidly ( $10^{-9}$  s) that depolarization is insignificant. At its localization site the muon magnetically interacts with the surrounding matter. The muon carries a relatively large magnetic moment, which even exceeds the proton's magnetic moment:  $\mu_\mu = 3.2 \mu_p$ . It therefore acts as a very sensitive local magnetic field probe. Due to the absence of a quadrupolar electric moment ( $S_\mu = 1/2$ ) the muon does not couple to electric field gradients.

The average muon life time is  $2.2 \mu\text{s}$  after which the muon decays into a positron  $e^+$  according to

$$\mu^+ \rightarrow e^+ + \nu_e + \bar{\nu}_\mu \quad (2.3)$$

where  $\nu_e$  and  $\bar{\nu}_\mu$  are the neutrinos and antineutrinos associated with the positron and the muon respectively. The decay positrons are emitted preferentially in the direction of the  $\mu^+$  spin which allows a determination of the time evolution of the polarization. The probability distribution of the positron emission is given by

$$W_{e^+}(\theta) \propto (1 + a(E) \cos \theta) \quad (2.4)$$

where  $\theta$  is the angle between the muon spin at the moment of decay and the direction in which the positron is emitted. In Fig. 2.1 two characteristic angular patterns  $W_{e^+}(\theta)$  are represented. The asymmetry parameter  $a$  depends on the energy of the positron.  $a$  increases monotonically with the positron energy and is 1 for the maximum positron energy  $E_{\max} = 52.83$  MeV. For  $E = 0$ ,  $a = -1/3$  and changes sign for  $E = \frac{1}{2}E_{\max}$ . However, very few positrons are emitted with low energies and those which are will usually not be detected. When integrated over all energies one obtains  $a = 1/3$  [21]. The positron detectors used around the world in  $\mu\text{SR}$  set-ups do not determine the incoming energy of the positrons and therefore one always measures the asymmetry parameter  $a$  averaged over all energies.

Because of their large kinetic energy ( $\approx 30$  MeV), the positrons are only weakly absorbed by the sample and cryostat walls. They are monitored and stored by

detection electronics in a counts versus time histogram. The time histogram of the collected intervals is of the form

$$N_{e^+}(t) = N_0 e^{-t/\tau_\mu} [1 + aP(t) \cos(\phi_{\text{det}})] + b \quad (2.5)$$

where  $b$  is a time independent background,  $N_0$  a normalization constant, and  $e^{-t/\tau_\mu}$  accounts for the  $\mu^+$  decay with the average decay time  $\tau_\mu$ .  $P(t)$  reflects the time dependence of the  $\mu^+$  polarization and is normalized to unity for  $t = 0$ . The value of the initial asymmetry  $a$  depends on the experimental set-up and is in practice smaller than the theoretical value of  $1/3$ . Due to the finite solid angle of the detectors, energy dependent efficiency of detection and possible reduced beam polarization,  $a$  is usually  $\simeq 0.23 - 0.25$ . The phase factor  $\phi_{\text{det}}$  accounts for the angle between the initial muon polarization and the positron detector.

### 2.2.2 Experimental Geometries

In  $\mu$ SR two types of experimental geometries are used. They are depicted in Fig. 2.2. Measurements in zero magnetic field and in longitudinal field are performed with the same geometry. The positron detectors are set parallel and antiparallel to the initial beam polarization  $\mathbf{S}_\mu(0)$ . They are called the “forward” and “backward” detector, respectively.

By definition the magnetic field  $\mathbf{B}_{\text{ext}}$  is applied along the  $\mathbf{Z}$  direction. In the longitudinal geometry the field is applied parallel to the beam polarization  $\mathbf{S}_\mu(0)$ . The measured polarization function is called  $P_Z(t)$ . In the transverse geometry  $\mathbf{B}_{\text{ext}}$  is perpendicular to  $\mathbf{S}_\mu(0)$ , which is then along  $\mathbf{X}$ . The positrons are detected in a direction perpendicular to  $\mathbf{B}_{\text{ext}}$ , from which  $P_X(t)$  is reconstructed.

It should be noted that for *e.g.* a ferromagnet in zero field, with  $\mathbf{S}_\mu(0)$  perpendicular to the local field,  $P_X(t)$  is measured and not  $P_Z(t)$ , although the measurements are performed in zero applied magnetic field. Physically for the muon spin there is no difference between a static externally applied magnetic field  $\mathbf{B}_{\text{ext}}$  or a constant field with its origin in the ferromagnetism of the compound under study.

The transverse geometry is in practice often different from the situation in Fig. 2.2. For practical reasons  $\mathbf{B}_{\text{ext}}$  is often directed along the beam direction and the muon spin is rotated in the vertical direction.

### 2.2.3 $\mu$ SR Spectrometers: EMU, GPS, and GPD

Muon beams are produced either as a continuous beam (PSI, Switzerland and TRIUMF, Canada) or as a pulsed one (ISIS, UK and KEK, Japan). For continuous beams every event is treated separately. A clock is started at the moment that a muon enters the sample. This clock is stopped when the corresponding decay positron is detected. The elapsed time is stored in a counts versus time histogram. For pulsed beams all muons come in at the same time  $t_0$ . This pulse has however a finite width distributed around  $t_0$ . Due to this uncertainty in  $t_0$  continuous beams

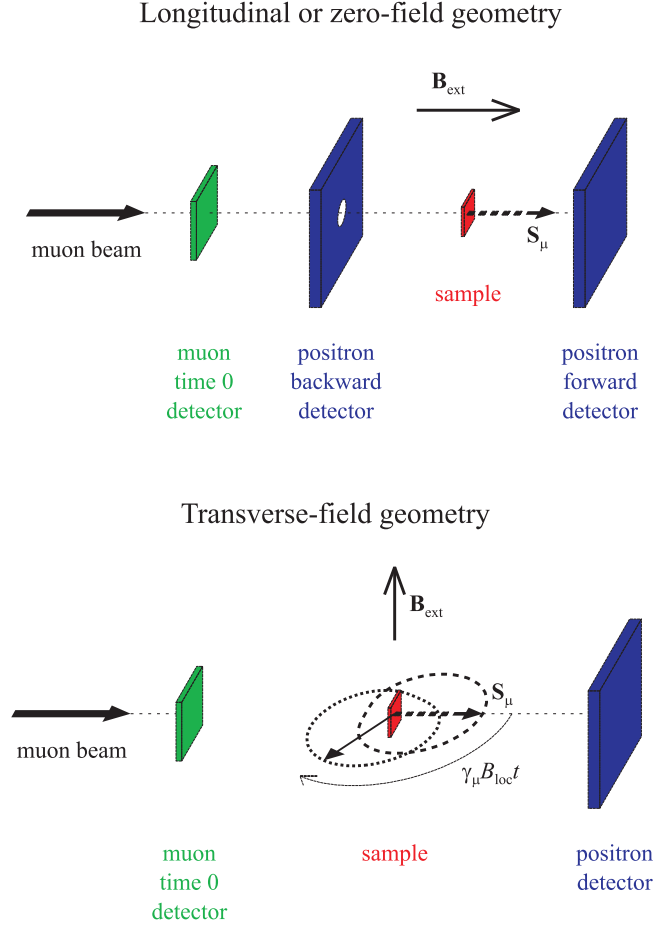


**Figure 2.2:** Two types of experimental geometry: the longitudinal and the transverse set-up. Although the muon spin is actually antiparallel to the muon’s momentum, here the muon spin is drawn parallel to the momentum for clarity. The arrows and cardioids in the transverse set-up represent the Larmor precession of the muon spin in the applied field and the accompanying angular positron distribution. This figure is taken from Ref. [18].

have a better time resolution than pulsed beams. The advantage of the pulsed beams is their lower background. The background  $b$  of Eq. 2.5 is reduced since after the pulse the beamline is shut and no other muons enter the sample. The lower background leads to a longer time window for the pulsed beam sources. Typically, the time window of a pulsed beam source is twice as long as for a conventional continuous source.

All the  $\mu\text{SR}$  measurements presented in this thesis have been carried out at PSI using the GPS and GPD spectrometers, and at ISIS on EMU.

GPS uses surface muons. They are called like this, since they are obtained from the pions decaying at rest near the surface of the production target. The surface beam is fully polarized and monochromatic, with a kinetic energy of 4.1 MeV. Due to this small energy, the beam has a stopping range  $L_{\text{eff}} = c/\rho$ , where  $c$  is around

160-200 mg/cm<sup>2</sup> and  $\rho$  the density of the compound in mg/cm<sup>3</sup>.

The GPD is a high-energy muon beam line. The pions that decay into muons leave the target at high energies. The polarization of the muon beam is limited to around 80 %. Muons are generated in bunches at a rate given by the frequency of the accelerator (50.63 MHz at PSI). Although the bunch structure is smeared out during the transport of the beam to the sample, it is still visible in the  $\mu$ SR spectra as an oscillating accidental background in the time dependence of the number of counts. In the analysis of the spectra additional oscillating terms are required, with frequencies equal to the accelerator frequency and higher harmonics, multiplied by  $e^{t/\tau_\mu}$ , to compensate for the muon decay in the fitting procedure. The penetration depth of the muons into the sample is larger for the high-energy beam than that of the surface beam and the former should therefore be used when studying samples within pressure cells, as discussed in Chapter 4.

EMU is a 32-detector  $\mu$ SR spectrometer which is optimized for zero field and longitudinal field measurements. The ISIS synchrotron produces a double pulse of protons with a repetition rate of 50 Hz. Each pulse has a width of about 70 ns and the two pulses are separated by 330 ns. Only one of these pulses is directed towards the EMU spectrometer. The repetition rate of 50 Hz makes ISIS unsuitable for measuring frequencies higher than 8 MHz and relaxation rates larger than 5  $\mu$ s<sup>-1</sup>. The advantage however is the very low background, *i.e.*  $b \approx 0$  in Eq. 2.5. The polarization is then simply calculated by

$$aP(t) = \frac{N_F(t) - \alpha N_B(t)}{N_F(t) + \alpha N_B(t)}. \quad (2.6)$$

Here  $N_F(t)$  ( $N_B(t)$ ) is the number of counts in the forward (backward) detector and  $\alpha$  is an experimental factor determined by detector efficiencies, exact experimental factors like distance between sample and detectors, cryostat, etc. It is measured by applying a transverse field (in the paramagnetic state) at exactly the same experimental conditions. With the correct  $\alpha$ ,  $P_X(t)$  should oscillate symmetrically around zero.

### 2.2.4 Depolarization and Relaxation Functions

In the previous Sections the basic ideas behind the  $\mu$ SR experiment have been discussed, as well as the spectrometers used in this thesis. The polarization function  $P_\alpha(t)$  ( $\alpha = \{X, Z\}$ ) extracted from the experiment contains the information on the magnetic distribution at the muon site and the time scale of the magnetic fluctuations. A few polarization functions will be discussed here, as far as they were used in this thesis. For a more extensive study, see *e.g.* Refs. [18, 19, 17].

#### Static Magnetic Fields

The starting point of all calculations is the consideration of a single muon spin in a static local magnetic field  $\mathbf{B}_{\text{loc}}$  oriented in an arbitrary direction. As explained

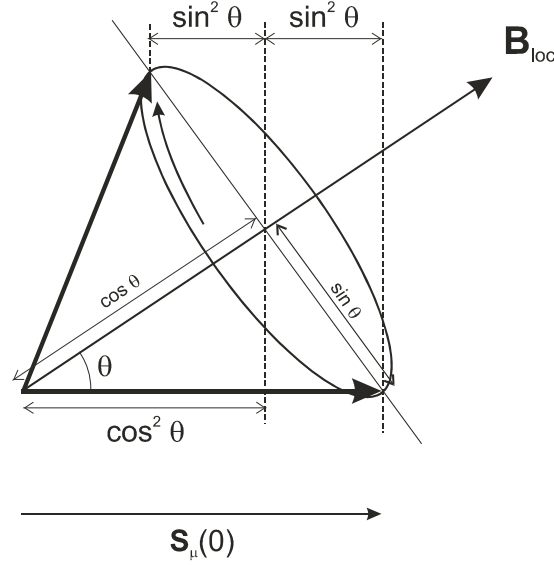


**Figure 2.3:** Muon spin precession describing a cone around a local magnetic field  $\mathbf{B}_{\text{loc}}$ . Here  $\theta$  denotes the angle between the initial muon spin polarization and the local field.

before, the polarization function  $\mathbf{P}(t)$  is measured either along the  $\mathbf{X}$  axis or along the  $\mathbf{Z}$  axis. Therefore  $P_\alpha(t)$ , with  $\alpha = \{X, Z\}$ , reflects the projection of  $\mathbf{S}_\mu(t)$  along the  $\mathbf{X}$  or  $\mathbf{Z}$  direction. The Larmor precession of a single muon spin and its projection along the  $\alpha$  direction (depending on whether  $\mathbf{S}_\mu(0) \parallel \mathbf{X}$  or  $\mathbf{S}_\mu(0) \parallel \mathbf{Z}$ ) are illustrated in Fig. 2.3. If all muon spins precess in the same static magnetic field, oriented at an angle  $\theta$  relative to the initial muon spin direction  $\mathbf{S}_\mu(0)$ , the Larmor equation yields

$$P_\alpha(t) = \cos^2 \theta + \sin^2 \theta \cos(\omega_\mu t). \quad (2.7)$$

where  $\omega_\mu = \gamma_\mu |\mathbf{B}_{\text{loc}}|$ . The polarization  $P_\alpha(t)$  describes a cone with the local field  $\mathbf{B}_{\text{loc}}$  as the axis of rotation. It is only the component of the muon spin perpendicular to  $\mathbf{B}_{\text{loc}}$  which oscillates. The parallel component is time-independent. Both these components are projected onto the  $\mathbf{X}$  or  $\mathbf{Z}$  direction, depending on the geometry. Eq. 2.7 is the basic equation in  $\mu\text{SR}$ .

Clearly, the assumption of a single magnetic field direction for all muons throughout the sample is a very simple model. Neglecting spin dynamics, the assumption is only encountered in single crystals of ferromagnets and antiferromagnets with a negligible volume fraction of domain walls. Helical structured magnets for example are excluded, since in different unit cells the local field at the muon site will have another direction. Obviously, the next step is to assume a field distribution at the muon site. It is easy to see that the polarization function  $P_\alpha(t)$  can then be described by

$$P_\alpha(t) = \int f(\mathbf{B}_{\text{loc}}) \left\{ \cos^2 \theta + \sin^2 \theta \cos(\gamma_\mu |\mathbf{B}_{\text{loc}}| t) \right\} d\mathbf{B}_{\text{loc}} \quad (2.8)$$

where  $f(\mathbf{B}_{\text{loc}})$  is the normalized magnetic field probability function. If only a single

value of  $\mathbf{B}_{\text{loc}}$  is present,  $f(\mathbf{B}_{\text{loc}})$  is a Dirac  $\delta$ -function and Eq. 2.7 is recovered. For a polycrystalline ferromagnet with no preferred direction for the grains (“texture”) one can write  $f(\mathbf{B}_{\text{loc}}) = 1/(4\pi B_0^2) \delta(|\mathbf{B}_{\text{loc}}| - B_0)$  to obtain

$$P_\alpha(t) = \frac{1}{3} + \frac{2}{3} \cos(\gamma_\mu B_0 t). \quad (2.9)$$

A static distribution of local magnetic fields at the muon site, as the one arising from randomly oriented static nuclear magnetic moments through their dipole fields, can be very well approximated by a Gaussian field distribution because of the statistical law of large numbers. This distribution is isotropic and has zero average field, so no net precession is observed. Including an external magnetic field  $\mathbf{B}_{\text{ext}}$  parallel to  $\mathbf{Z}$  leads to

$$f(\mathbf{B}_{\text{loc}}) = \left( \frac{\gamma_\mu}{\sqrt{2\pi}\Delta} \right)^3 \exp\left( -\frac{(\gamma_\mu B_{\text{loc}}^x)^2}{2\Delta^2} \right) \exp\left( -\frac{(\gamma_\mu B_{\text{loc}}^y)^2}{2\Delta^2} \right) \exp\left( -\frac{\gamma_\mu^2 (B_{\text{loc}}^z - B_{\text{ext}})^2}{2\Delta^2} \right) \quad (2.10)$$

where  $\Delta^2/\gamma_\mu^2 = \langle B_i^2 \rangle$  is the square of the width of the field distribution along the cartesian axis  $i = \{X, Y, Z\}$ . Introducing this function in Eq. 2.8 gives for the case of  $\mathbf{B}_{\text{ext}} = \mathbf{0}$  the well known Kubo-Toyabe function [22]

$$P_{\text{KT}}(\Delta, t) = \frac{1}{3} + \frac{2}{3} (1 - \Delta^2 t^2) \exp\left( -\frac{1}{2} \Delta^2 t^2 \right). \quad (2.11)$$

This function is illustrated in Fig. 2.4. It is seen that  $P_{\text{KT}}(\Delta, t)$  is a strongly damped oscillation. The function has a minimum at  $t = \sqrt{3}/\Delta$  and saturates at a value of  $1/3$ . Solving the integral in Eq. 2.8 for  $\mathbf{B}_{\text{ext}} \neq \mathbf{0}$  is less obvious. For a longitudinal external magnetic field ( $\mathbf{B}_{\text{ext}} \parallel \mathbf{S}_\mu(0)$ ) the solution is [23]

$$P_Z(\Delta, B_{\text{ext}}, t) = 1 - \frac{2\Delta^2}{\gamma_\mu^2 B_{\text{ext}}^2} \left\{ 1 - e^{-\frac{1}{2}\Delta^2 t^2} \cos(\gamma_\mu B_{\text{ext}} t) \right\} + \frac{2\Delta^3}{\gamma_\mu^3 B_{\text{ext}}^3} \int_0^{\Delta t} e^{-\frac{1}{2}\Delta^2 y^2} \cos\left( \frac{\gamma_\mu B_{\text{ext}}}{\Delta} y \right) dy. \quad (2.12)$$

This function is illustrated in Fig. 2.4 for several external field values, in units of  $\Delta/\gamma_\mu$ . The horizontal axis shows  $t$  in units of  $\Delta^{-1}$ . The application of a longitudinal field effectively aligns the random local field along the  $\mathbf{Z}$  axis. This will reduce the depolarization of the muon spin, as can be seen in Fig. 2.4. The general case for transverse external fields ( $\mathbf{B}_{\text{ext}} \perp \mathbf{S}_\mu(0)$ ) is beyond the scope of this thesis. For sufficiently large magnetic fields,  $P_X(t)$  is a Gaussian damped oscillation:

$$P_X(\Delta, B_{\text{ext}}, t) = e^{-\frac{1}{2}\Delta^2 t^2} \cos(\gamma_\mu B_{\text{ext}} t). \quad (2.13)$$

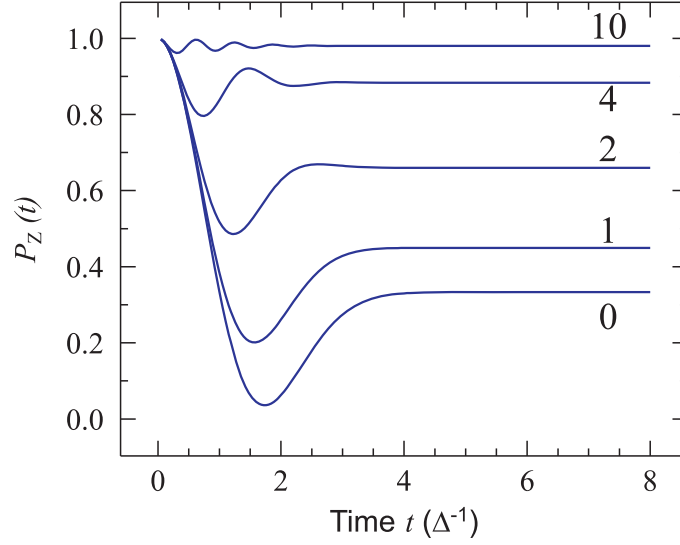


**Figure 2.4:** The external magnetic field  $\mathbf{B}_{\text{ext}}$  dependence of the longitudinal depolarization function  $P_Z(\Delta, B_{\text{ext}}, t)$  derived from a static Gaussian field distribution with width  $\Delta/\gamma_\mu$ . The values of the external magnetic field are given in units of  $\Delta/\gamma_\mu$ . The Kubo-Toyabe function corresponds to the curve labeled with 0.

The Kubo-Toyabe function is most often encountered in systems with nuclear magnetic moments. Since these moments are small, the magnetic interaction is weak and the fluctuation time is long. Therefore, the created magnetic field at the muon site can be regarded as static on the scale of the muon life time. In Chapter 4 a Cu-Be pressure cell is used in the study of  $\text{UGe}_2$ . In this material it is found that  $\Delta = 0.345 \mu\text{s}^{-1}$  or  $\sqrt{\langle B_i^2 \rangle} = 0.4 \text{ mT}$ , because of the nuclear moments of  $^{63}\text{Cu}$ ,  $^{65}\text{Cu}$ , and  $^9\text{Be}$ . In Chapter 5 this function is found as a background coming from the EMU spectrometer, with a typical value of  $0.300 \mu\text{s}^{-1}$  for  $\Delta$ .

For different types of magnetic systems, other field distributions at the muon site than the Gaussian distribution can be relevant. For example, dilute magnetic systems (spin glass) are often well described assuming a Lorentzian distribution. Other case with different field distributions include helical structured magnetism or the flux line lattice in a type-II superconductor [18].

### Fluctuating Magnetic Fields

In contrast to the assumption of a static magnetic field at the muon site - static compared to the life time of the muon - the magnetic fields are in reality more often fluctuating on the muon time scale. This can be because of paramagnetic fluctuations above the magnetic ordering temperature, or because of spin waves below this temperature. In Strongly Correlated Electrons Systems (SCES), or heavy-Fermion systems, a strong competition is present between the RKKY interaction and the Kondo effect, leading to small ordered magnetic moments and large fluctuations.



However, the local field at the muon site can also fluctuate because of the muon itself, *i.e.* because of its diffusion through the sample. This effect is however not of importance in this thesis and will not be discussed further.

A mathematical description of the polarization function  $P_\alpha(\nu, t)$  due to fluctuating magnetic fields can be obtained by applying the strong collision approximation. In this model, it is assumed that the local field  $\mathbf{B}_{\text{loc}}$  changes orientation and magnitude with a single fluctuation rate  $\nu$ . According to Poisson statistics, the probability of  $j$  jumps within a time  $t$  is  $\nu^j e^{-\nu t}$ , where the time  $t_i$  of the  $i$ th jump is arbitrary. The only restriction is that  $t_1 < \dots < t_i < \dots < t_j < t$ . After a “collision” the field is randomly chosen from the probability distribution  $f(\mathbf{B}_{\text{loc}})$  applicable to the compound under study and experimental conditions, without any correlation to the field before the collision. Before the first collision the polarization  $P_\alpha(t)$  should be described by Eq. 2.8. After the first collision the ensemble of muons will further depolarize according to the same function but with an initial time zero at the time of collision. This process for multiple collisions is given by

$$P_\alpha(\nu, t) = e^{-\nu t} \left[ P_\alpha(t) + \nu \int_0^t P_\alpha(t_1) P_\alpha(t - t_1) dt_1 + \nu^2 \int_0^t \int_0^{t_1} P_\alpha(t_1) P_\alpha(t_2 - t_1) P_\alpha(t - t_2) dt_1 dt_2 + \dots \right]. \quad (2.14)$$

In general, this expression can not be solved analytically and therefore one needs numerical computation. It is possible [24] to write this formula as

$$P_\alpha(\nu, t) = P_\alpha(t) e^{-\nu t} + \nu \int_0^t P_\alpha(\nu, t - t') P_\alpha(t') e^{-\nu t'} dt'. \quad (2.15)$$

This equation is much easier to solve numerically than Eq. 2.14, and is therefore used in the computations of  $P_\alpha(\nu, t)$ .

With  $P_\alpha(t)$  equal to the zero-field Kubo-Toyabe function  $P_{\text{KT}}(\Delta, t)$  of Eq. 2.11, the numerically calculated depolarization functions  $P_Z^{\text{KT}}(\nu, \Delta, t)$  are shown in Fig. 2.5 for several values of  $\nu$  in units of  $\Delta$ . It is seen that for increasing  $\nu$ , first the tail of the function collapses, followed by an increase of  $P_Z^{\text{KT}}(\nu, \Delta, t)$  at small  $t$ . For  $\nu/\Delta$  sufficiently large, the Laplace transform can be used to find a useful approximate analytical expression. The resultant formula [24] is given by

$$P_Z^{\text{KT}}(\nu, \Delta, t) = \exp \left\{ -\frac{2\Delta^2}{\nu^2} [\exp(-\nu t) - 1 + \nu t] \right\}. \quad (2.16)$$

In Fig. 2.5 this function is compared with the numerical calculation for  $\nu/\Delta = 3$  and  $\nu/\Delta = 10$ . It is seen that the agreement is reasonably good. For very fast fluctuations with respect to  $\Delta$ ,  $P_Z^{\text{KT}}(\nu, \Delta, t)$  reduces to

$$P_Z^{\text{KT}}(t) = \exp(-\lambda_Z t) \quad \text{with} \quad \lambda_Z = 2\Delta^2/\nu. \quad (2.17)$$

This is the so-called motional narrowing limit.

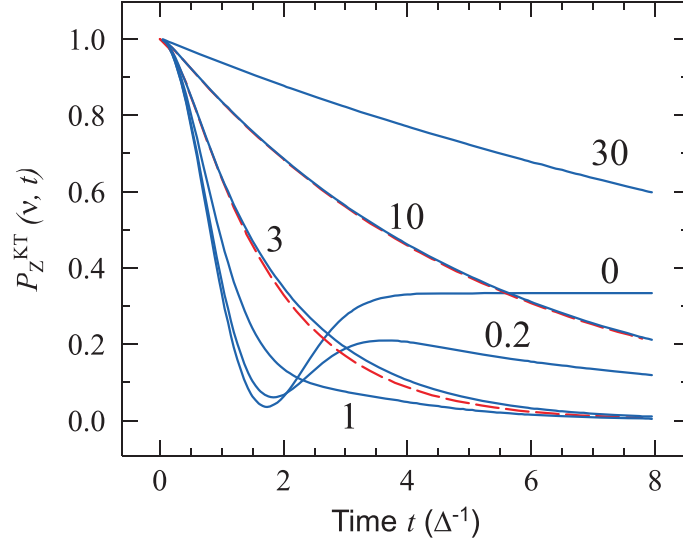


**Figure 2.5:** The dependence of the dynamical Kubo-Toyabe function on the fluctuation rate  $\nu$ , according to the strong collision approximation. The numbers indicate the fluctuating rate in units of  $\Delta$ . The static Kubo-Toyabe function corresponds to the curve labeled with 0. For  $\nu/\Delta = 3$  and  $\nu/\Delta = 10$ , a comparison is made between the numerical solution (full line) and the approximation for large  $\nu/\Delta$  in Eq. 2.16 (dashed line).

For applied magnetic fields  $\mathbf{B}_{\text{ext}}$  the integrals in Eq. 2.14 can also be evaluated. For a transverse field, the approximation

$$P_X^{\text{KT}}(\nu, \Delta, B_{\text{ext}}, t) = \exp \left\{ -\frac{\Delta^2}{\nu^2} [\exp(-\nu t) - 1 + \nu t] \right\} \cos(\gamma_\mu B_{\text{ext}} t) \quad (2.18)$$

is valid for large enough  $\nu/\Delta$ . This formula is found via the Laplace transform [24] and is known in NMR as the “Abragam formula”. It reduces to

$$P_X(\nu, \Delta, B_{\text{ext}}, t) = e^{-\lambda_X t} \cos(\gamma_\mu B_{\text{ext}} t) \quad \text{with} \quad \lambda_X = \Delta^2/\nu \quad (2.19)$$

in the motional narrowing limit ( $\nu/\Delta \gg 1$ ). For a longitudinal magnetic field, a second depolarization process should be considered. Up to now only a distribution in Larmor precession frequencies has been considered as an origin for depolarization. However, with a longitudinal field the muon energy is quantized into two energy levels. The muon spin can be flipped between the two states. The occupancies of these states are in theory governed by Boltzmann statistics at thermal equilibrium, although in practice calculations lead to a high degree of equipopulation of the two energy levels. The muon beam is however fully polarized at implantation and therefore the polarization will decrease towards the equilibrium. Note that transverse perturbations (relative to the applied field) with an energy equal to the Zeeman splitting are needed to flip the muon spin. In this way the spectral density function  $J(\gamma_\mu B_{\text{ext}})$  can be probed. A quantum-mechanical calculation [25, 26] shows that

$\lambda_Z$ , as appears in Eq. 2.17, is modified to

$$\lambda_Z(B_{\text{ext}}) = \frac{2\Delta^2\nu}{(\gamma_\mu B_{\text{ext}})^2 + \nu^2} = \frac{2\Delta^2\tau}{1 + \gamma_\mu^2 B_{\text{ext}}^2 \tau^2} \quad (2.20)$$

with  $\tau = 1/\nu$  the correlation time of the fluctuation. This equation is only valid in the limit of  $\nu/\Delta \gg 1$ . This formula is used in Chapters 4 and 5. Here it is found that a small applied longitudinal field of  $B_{\text{ext}} = 2$  mT is enough to reduce  $\lambda_Z$  to almost 0. From the value of  $\lambda_Z(0)$  one can then estimate  $\Delta$ .

### Comments

By applying longitudinal magnetic fields a discrimination between static and fluctuating fields can be made. An external field decouples the muon spin and internal fields when these are static. The field distribution does not affect the time evolution of the muon spin polarization. An example is shown in Fig. 2.4. For  $|\mathbf{B}_{\text{ext}}| > 10\Delta/\gamma_\mu$  the polarization can be considered constant at 1. Fluctuations, however, are time dependent perturbations and induce spin-flip transitions between the two Zeeman-levels of the muon spin. An exponential function in zero field will therefore still be exponential in non-zero field, although the value of  $\lambda_Z$  is reduced.

It often occurs that the muons stop at magnetically inequivalent sites. This can be due to a phase separation in the sample (*e.g.* magnetic domains with a different direction of the magnetization), but also the presence of more than one muon stopping site at crystallographic inequivalent sites with different magnetic environment belongs to the possibilities. In all these cases the polarization function  $P_\alpha(t)$  is the sum of the contributions from the inequivalent muon sites:  $aP_\alpha(t) = \sum_i a_i P_{\alpha,i}(t)$ . Here the relative values of  $a_i$  directly measure the volume or population fraction of the stopping site, if the muons are implanted uniformly into the sample.

In the previous Sections it was explained that either  $P_X(t)$  or  $P_Z(t)$  is measured, depending on the direction of the external field  $\mathbf{B}_{\text{ext}}$  relative to the initial muon spin  $\mathbf{S}_\mu(0)$ , see Fig. 2.2. However, even in zero field  $P_X(t)$  is measured, when  $\mathbf{S}_\mu(0)$  is perpendicular to the easy direction of *e.g.* a ferromagnet. The observed wiggles in  $P_X(t)$  are then referred to as “spontaneous precession”.

### 2.2.5 Magnetic Field at the Muon Site

The muon localizes at an interstitial site in the host crystal lattice. At this site a local magnetic induction  $\mathbf{B}_{\text{loc}}$  is present. The muon spin will precess with an angular frequency  $\omega = \gamma_\mu |\mathbf{B}_{\text{loc}}|$  (see Fig. 2.3). A detailed study of  $\mathbf{B}_{\text{loc}}$  is given in Ref. [19]. In a metal, the field at the muon site can be split into several terms:

$$\mathbf{B}_{\text{loc}} = \mathbf{B}_{\text{ext}} + \mathbf{B}_{\text{dem}} + \mathbf{B}'_{\text{dip}} + \mathbf{B}_{\text{L}} + \mathbf{B}_{\text{con}} + \mathbf{B}_{\text{P}} + \mathbf{B}_{\text{dia}}, \quad (2.21)$$

where  $\mathbf{B}_{\text{ext}}$  is the externally applied magnetic field and  $\mathbf{B}_{\text{dem}}$  the associated demagnetization field, which is given by  $\mathbf{B}_{\text{dem}} = -\mu_0 \mathcal{N} \mathbf{M}_{\text{bulk}}$ . Here  $\mathcal{N}$  is the demagnetization

factor tensor that depends only on the shape of the sample.  $\mathbf{M}_{\text{bulk}}$  is the macroscopic or bulk magnetization. For a zero-field-cooled ferromagnet,  $\mathbf{M}_{\text{bulk}} = \mathbf{0}$ , and therefore,  $\mathbf{B}_{\text{dem}} = \mathbf{0}$ .

A magnetic moment  $\mathbf{m}_i$ , localized at an atomic site, produces a dipolar field

$$\mathbf{B}_{\text{dip}}^i = \frac{\mu_0}{4\pi} \left\{ \frac{3(\mathbf{m}_i \cdot \mathbf{r}_i) \mathbf{r}_i}{r_i^5} - \frac{\mathbf{m}_i}{r_i^3} \right\}, \quad (2.22)$$

where  $\mathbf{r}_i$  is the distance between the muon and the magnetic moment  $\mathbf{m}_i$  on atom  $i$ . Since all magnetic atoms will contribute to  $\mathbf{B}_{\text{loc}}$ , a sum has to be taken extending over all magnetic atom positions in the sample. For this purpose a so-called Lorentz sphere with radius  $r_{\text{LS}}$  is defined with the muon at its center.

The magnetic moments outside the Lorentz sphere are regarded as a continuous and homogeneous magnetization density and will contribute to  $\mathbf{B}_{\text{L}}$ . The Lorentz sphere is a “non-magnetic cavity” in a magnetic environment. When the Lorentz sphere is assumed to be within one single magnetic domain, then the field  $\mathbf{B}_{\text{L}}$  is equal to  $\mathbf{B}_{\text{L}} = (\mu_0/3)\mathbf{M}$ , where  $\mathbf{M}$  is the saturation magnetization.

A discrete sum is taken over all the magnetic moments inside the Lorentz sphere:

$$\mathbf{B}'_{\text{dip}} = \sum_{r_i < r_{\text{LS}}} \mathbf{B}_{\text{dip}}^i \quad (2.23)$$

Together with the Lorentz field this results, for most ferromagnets and paramagnets (in applied field), in

$$\mathbf{B}'_{\text{dip}} + \mathbf{B}_{\text{L}} = \frac{\mu_0}{v} \mathbf{C}(\mathbf{q} = \mathbf{0}) \mathbf{m}. \quad (2.24)$$

Here it is assumed that all magnetic moments  $\mathbf{m}_i$  are equal ( $\mathbf{m}_i \equiv \mathbf{m}$ ,  $\forall i$ ). Therefore, the macroscopic magnetization  $\mathbf{M}$  is parallel to all  $\mathbf{m}_i$ .  $v$  is the volume per magnetic atom.  $\mathbf{C}(\mathbf{q})$  is the coupling tensor that generally depends on the wave vector transfer  $\mathbf{q}$  [27]. Because ferromagnets are considered in this thesis the wave vector  $\mathbf{q}$  is equal to  $\mathbf{0}$ . The dipolar interaction shows a strong angular dependence (Eq. 2.22), and therefore  $\mathbf{C}(\mathbf{q} = \mathbf{0})$  will be completely determined by the crystal structure together with the assumed muon site. If  $T > T_{\text{C}}$ , Eq. 2.24 can be written as

$$\mathbf{B}'_{\text{dip}} + \mathbf{B}_{\text{L}} = \mathbf{C}(\mathbf{q} = \mathbf{0}) \chi \mathbf{B}_{\text{ext}}, \quad (2.25)$$

where  $\chi$  is the atomic susceptibility tensor with  $\mu_0 \mathbf{M}_{\text{bulk}} = \chi \mathbf{B}_{\text{ext}}$ .

The next term in Eq. 2.21 is the Fermi contact hyperfine field  $\mathbf{B}_{\text{con}}$ . The origin of this field is the spin polarization of the conduction electrons at the  $\mu^+$  position, which in turn predominantly originates from the RKKY exchange interaction between the spins of the conduction electrons and the localized magnetic moments  $\mathbf{m}_i$  at the magnetic atoms.  $\mathbf{B}_{\text{con}}$  can be expressed by [27]:

$$\mathbf{B}_{\text{con}} = \mu_0 \left( \frac{r_{\mu} H}{4\pi} \right) \mathbf{M}_i \stackrel{T > T_{\text{C}}}{=} \left( \frac{r_{\mu} H}{4\pi} \right) \chi \mathbf{B}_{\text{ext}}. \quad (2.26)$$

The term in the brackets is the contact coupling constant, which is in general a tensor. However, as a first approximation it may be assumed to be isotropic (*i.e.* a scalar) and temperature independent. Here  $r_\mu$  is the number of nearest-neighbor magnetic ions to the muon localization site and  $H$  the hyperfine interaction tensor.

An additional small contribution  $\mathbf{B}_P$  is caused by the Pauli spin paramagnetism of the conduction electrons:  $\mathbf{B}_P = \mathcal{A}_P \chi_P \mathbf{B}_{\text{ext}}$ . Here  $\mathcal{A}_P$  is an isotropic and temperature-independent tensor (and may therefore be replaced by the scalar  $A_P$ ) and  $\chi_P$  the Pauli spin susceptibility tensor.

The last contribution in Eq. 2.21,  $\mathbf{B}_{\text{dia}}$ , is due to the diamagnetic response of the electron screening of the muon charge. The diamagnetic screening produces only a very small contribution to the local magnetic field. For materials with an enhanced effective electron mass  $m^*$ , the small diamagnetic contribution is reduced by a factor  $m_e/m^*$ , becoming negligible for heavy-fermion compounds. For superconductors, however, this term is important.

### Knight Shift - determination of the muon site

For the case of a paramagnet in an externally applied field  $\mathbf{B}_{\text{ext}}$  with  $\mathbf{S}_\mu(0) \perp \mathbf{B}_{\text{ext}}$ , a muon frequency shift is usually observed with respect to  $\omega = 2\pi\nu_\mu = \gamma_\mu |\mathbf{B}_{\text{ext}}|$ , *i.e.*  $\mathbf{B}_{\text{loc}} \neq \mathbf{B}_{\text{ext}}$  [19, 28]. In a general case  $\mathbf{B}_{\text{loc}}$  and  $\mathbf{B}_{\text{ext}}$  are not necessarily parallel to each other. As  $|\mathbf{B}_{\text{loc}} - \mathbf{B}_{\text{ext}}| \ll |\mathbf{B}_{\text{ext}}|$ , it is useful to define an experimental or apparent muon Knight shift  $K_\mu$  by the projection of  $(\mathbf{B}_{\text{loc}} - \mathbf{B}_{\text{ext}})$  onto  $\mathbf{B}_{\text{ext}}$ :

$$K_\mu = \frac{\mathbf{B}_{\text{ext}} \cdot (\mathbf{B}_{\text{loc}} - \mathbf{B}_{\text{ext}})}{|\mathbf{B}_{\text{ext}}|^2}. \quad (2.27)$$

This is, with respect to  $\omega = 2\pi\nu_\mu = \gamma_\mu |\mathbf{B}_{\text{ext}}|$ , the relative frequency shift experienced by the muon spin.

Assuming the paramagnetic susceptibility tensor  $\chi$  is diagonal with elements  $\chi_a$ ,  $\chi_b$ , and  $\chi_c$ , and writing  $\mu_0 \mathbf{M}_{\text{bulk}} = \chi \mathbf{B}_{\text{ext}}$ ,  $K_\mu$  can be written with the help of Eq. 2.21 as ( $\mathbf{B}_{\text{dia}}$  is neglected)

$$K^i = \left[ C^{ii}(\mathbf{q} = \mathbf{0}) - \mathcal{N}^{ii} + \left( \frac{r_\mu H}{4\pi} \right) \right] \chi_i + A_P \chi_P, \quad (2.28)$$

$$i = \{a, b, c\}, \quad \mathbf{B}_{\text{ext}} \parallel \mathbf{i}$$

which is independent of  $|\mathbf{B}_{\text{ext}}|$  and where  $a$ ,  $b$ , and  $c$  represent the crystal axes. Here  $\mathbf{C}(\mathbf{q} = \mathbf{0})$  is the tensor that couples the U magnetic moments  $\mathbf{m}$  to the magnetic field  $\mathbf{B}'_{\text{dip}} + \mathbf{B}_L$  (Eq. 2.24) at the muon site. For a spherically shaped sample ( $\mathcal{N}^{ii} = \frac{1}{3}$ ) the contribution of the demagnetization field  $\mathbf{B}_{\text{dem}}$  and the Lorentz field  $\mathbf{B}_L$  cancel exactly. Since  $K_\mu^i$  depends linearly on  $\chi_i$ ,  $K_\mu$  is presented as a function of  $\chi$  for a given direction of  $\mathbf{B}_{\text{ext}}$  with the temperature as an implicit parameter. From these so-called Clogston-Jaccarino plots, together with the fact that  $\text{Tr } \mathbf{C}(\mathbf{q} = \mathbf{0}) = 1$ , the values of  $C^{ii}(\mathbf{q} = \mathbf{0})$  and of  $r_\mu H/4\pi$  can be extracted. Comparing the measured values of  $C^{ii}(\mathbf{q} = \mathbf{0})$  with calculated ones, the muon site can be determined.

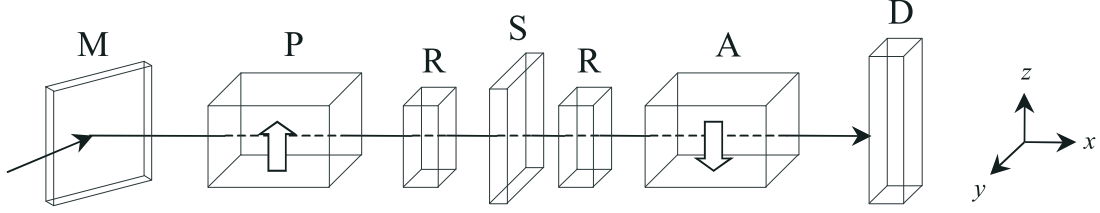


**Figure 2.6:** Schematic setup of the PANDA. Indicated are the monochromator M, the polarizer P, the rotators R, the sample S, the analyzer A, and the detector D. The direction of the neutron beam is denoted  $x$  and the vertical direction  $z$ . The applied magnetic field is along  $z$ .

### 2.3 Three-Dimensional Neutron Depolarization

In this Section a brief summary is given on the three-dimensional neutron depolarization (3DND) technique. In Fig. 2.6 a schematic picture of the set-up is given of the poly axis neutron depolarization analyzer (PANDA) at the Reactor Institute Delft (RID) of the Delft University of Technology.

The neutron depolarization (ND) technique is based on the loss of polarization of a polarized neutron beam after transmission through a (ferro)magnetic sample. Each neutron undergoes only a series of consecutive rotations on its passage through the (ferro)magnetic domains in the sample. It is important to note that the beam cross section covers a huge number of domains, which results in an averaging over the magnetic structure of the whole illuminated sample volume. This averaging causes a loss of polarization, which is related to the mean domain size and the mean direction cosines of the domains. The rotation of the polarization during transmission probes the average magnetization.

In a ND experiment, a  $3 \times 3$  depolarization matrix  $D$  expresses the relation between the polarization vector  $\mathbf{P}^0$  before and  $\mathbf{P}^1$  after transmission through the sample according to [29, 30, 31]

$$\mathbf{P}^1 = D \mathbf{P}^0. \quad (2.29)$$

The monochromator M selects a fixed neutron wave length of  $2.03 \text{ \AA}$  which corresponds to a velocity of  $1949 \text{ m/s}$ . The polarization of the monochromatic neutron beam is created and analyzed by magnetic multilayer polarization mirrors (P and A in Fig. 2.6). In order to obtain the complete matrix  $D$ , one polarization rotator (R) is placed before the sample and another one right after the sample. Each rotator provides the possibility to turn the polarization vector parallel or antiparallel to the coordinate axes  $x$ ,  $y$ , and  $z$ . The resultant neutron intensity is finally detected by a  $^3\text{He}$  detector D. The polarization rotators enable the measurement of any matrix element  $D_{ij}$  with the aid of the intensity of the unpolarized beam  $I_S$

$$I_S = \frac{I_{ij} + I_{-i,j}}{2}, \quad (2.30)$$

where  $I_{ij}$  is the intensity for  $\mathbf{P}^0$  along  $i$  and  $\mathbf{P}^1$  along  $j$ . The matrix element  $D_{ij}$  is then calculated according to

$$D_{ij} = \frac{1}{P_0} \frac{I_S - I_{ij}}{I_S}, \quad (2.31)$$

where  $P_0$  is the degree of polarization in the absence of a sample. In the present case,  $P_0 = 0.965$ , which is experimentally determined.

Now the correlation matrix  $\alpha_{ij}$  is introduced as [29, 30, 31]

$$\alpha_{ij} = \left\langle \int_0^L dx' \Delta B_i(x, y, z) \Delta B_j(x', y, z) \right\rangle, \quad (2.32)$$

where  $\Delta \mathbf{B}(\mathbf{r}) = \mathbf{B}(\mathbf{r}) - \langle \mathbf{B} \rangle$  is the variation of the magnetic induction and angular brackets denote the spatial average over the sample volume. The integral is taken over the neutron transmission length  $L$  through the sample. Assuming  $\alpha_{ij} \equiv 0$  for  $i \neq j$ , the correlation function  $\xi$  is defined as

$$\xi = \sum_i \alpha_{ii}. \quad (2.33)$$

With these quantities it can be shown that if there is no macroscopic magnetization ( $\langle \mathbf{B} \rangle = 0$ ) the depolarization matrix is diagonal and under the assumption that  $\alpha_{ij} \equiv 0$  for  $i \neq j$  given by [29, 30, 31]

$$D_{ii} = e^{-\frac{\gamma^2}{v^2} L \{\xi - \alpha_{ii}\}} \quad i = x, y, z, \quad (2.34)$$

where  $\gamma = 1.83 \times 10^8 \text{ s}^{-1} \text{T}^{-1}$  is the gyromagnetic ratio of the neutron and  $v = 1949 \text{ m/s}$  the neutron velocity.

The phenomenon that for magnetically isotropic media the depolarization depends on the orientation of the polarization vector with respect to the propagation direction of the neutron beam, is known as intrinsic anisotropy. The origin of this intrinsic anisotropy is that the line integral of the demagnetization fields around magnetized volumes in the sample along the neutron trajectory is not isotropic due to  $\nabla \cdot \mathbf{B} = 0$ . In the following it will be assumed that the demagnetization fields are negligible for needle-shaped magnetic domains.

When the sample shows a net magnetization, the polarization vector will rotate in a plane perpendicular to the magnetization direction. If the sample shape gives rise to macroscopic stray fields, the rotation angle  $\phi$  is related to the net magnetization  $\langle M \rangle$  by

$$\phi = \eta \frac{\gamma}{v} L \mu_0 \langle M \rangle = \eta \frac{\gamma}{v} L \mu_0 M_S \langle m \rangle, \quad (2.35)$$

where  $\eta$  is a geometrical factor given in Eq. 4.51 for a rectangular-shaped sample and  $\langle m \rangle = M/M_S$  the reduced sample magnetization in terms of the saturation magnetization  $M_S = M_S(T)$ . If the mean magnetic induction  $\langle \mathbf{B} \rangle$  in the sample is oriented along the  $z$  axis, the depolarization matrix is, for  $\phi \gg (\gamma/v)^2 |\alpha_{xx} - \alpha_{yy}| L/2$



(the weak damping limit), given by [29, 30, 31]

$$\begin{aligned}
D_{xx} &= D_{yy} = e^{-\frac{\gamma^2}{v^2} L \left\{ \xi - \frac{\alpha_{xx} + \alpha_{yy}}{2} \right\}} \cos \phi, \\
D_{xy} &= -D_{yx} = e^{-\frac{\gamma^2}{v^2} L \left\{ \xi - \frac{\alpha_{xx} + \alpha_{yy}}{2} \right\}} \sin \phi, \\
D_{zz} &= e^{-\frac{\gamma^2}{v^2} L \left\{ \xi - \alpha_{zz} \right\}}, \\
D_{xz} &= D_{zx} = D_{zy} = D_{yz} = 0.
\end{aligned} \tag{2.36}$$

With the net magnetization along the  $z$  axis, the rotation angle  $\phi$  of the beam polarization is obtained from the measurements by

$$\phi = \arctan \left( \frac{D_{xy} - D_{yx}}{D_{xx} + D_{yy}} \right) \tag{2.37}$$

and  $\xi$  is calculated with

$$\xi = -v^2 \ln \{ \det D \} / 2\gamma^2 L. \tag{2.38}$$

As mentioned earlier, ND provides information about the mean-square direction cosines of the magnetic induction vector in the (ferro)magnetic domains. These are directly given by the quantities  $\gamma_i = \alpha_{ii}/\xi$  ( $i = x, y, z$ ), and can be estimated from the measurements by

$$\gamma_i = 1 - 2 \ln \{ D_{ii} \} / \ln \{ \det D \}. \tag{2.39}$$

This equation is only valid for those directions that show no net rotation of the beam polarization.

## 2.4 Macroscopic techniques

### 2.4.1 Magnetization

The measurements of magnetization  $M$  and magnetic susceptibility  $\chi$  at ambient pressure were performed on a Quantum Design's magnetic property measurement system (MPMS). This instrument uses a Superconducting QUantum Interface Device (SQUID), which is the most sensitive device available for measuring magnetic fields. The principles of operation are nicely demonstrated in Ref. [32]. Magnetization measurements at fields up to 5.5 T were performed in the temperature range of 1.8 to 300 K at Leiden University and the University of Amsterdam (UvA).

Magnetization measurements at pressures up to 0.43 GPa were performed using an Oxford Instruments MagLab vibrating sample magnetometer (VSM) at the Physikalisches Institut of the Universität Karlsruhe (TH). Magnetic field scans were performed in fields up to 12 T at several temperatures. The pressure clamp cell was made of a CuBe alloy. The pressure was determined by measuring the superconducting transition temperature  $T_s$  of a piece of lead inside the pressure cell ( $T_s = 7.2$  K at ambient pressure). The pressure transmitting medium was a mixture of methanol and ethanol (1 : 4).



Magnetization at ambient pressure has also been measured in magnetic fields up to 52 T using the pulsed magnetic field facility of the Laboratoire National des Champs Magnétiques Pulsés (LNCMP) in Toulouse. The magnetization in pulsed magnetic fields is deduced from the voltage  $V(t)$  induced by a time varying magnetic induction  $\mathbf{B}(t)$  in a pickup coil. Maxwell's second law reads in differential form  $\nabla \times \mathbf{E} = -\partial \mathbf{B}(t)/\partial t$  and in integral form

$$\oint_C \mathbf{E} \cdot d\mathbf{l} = - \iint \frac{\partial \mathbf{B}(t)}{\partial t} \cdot d\mathbf{S} \quad (2.40)$$

where  $\mathbf{E}$  is the electric field and  $\mathbf{l}$  and  $\mathbf{S}$  are the length and the enclosed area of the contour  $C$ , respectively. For a coil with  $N$  windings and an inner area  $A$  it reduces to

$$V(t) = -NA \frac{\partial B(t)}{\partial t} \quad (2.41)$$

when  $\mathbf{B}$  is parallel to the coil axis. Note that  $B = \mu_0(H + M)$  where  $H$  is the applied magnetic field and  $M$  the magnetization of the sample (along the coil axis). To get  $M$ , the voltage induced by the external field has to be compensated by additional compensation coils. The induced voltages can then be written as

$$\begin{aligned} V_1(t) &= -\mu_0 NA \left( \frac{\partial H(t)}{\partial t} + \frac{\partial M(t)}{\partial t} \right), \\ V_2(t) &= -\mu_0 NA \frac{\partial H(t)}{\partial t}. \end{aligned} \quad (2.42)$$

These two signals can be subtracted from one another, or the two coils can be connected and wound in opposite direction. Apart from a calibration factor, the magnetization  $M(t)$  is obtained by numerical integration of  $V(t) = V_2(t) - V_1(t)$  over  $t$ . From the values of  $H(t)$ , deduced from  $V_2(t)$ , it is possible to reconstruct  $M(H)$ .

### 2.4.2 Thermal Expansion and Magnetostriction

High-precision measurements of the sample length as a function of temperature  $T$  or magnetic field  $B$  were performed on single-crystalline samples using the parallel-plate capacitance method. The sample is connected to one of the plates, whereas the other plate is fixed. Because the capacitance  $C$  is given by

$$C = \frac{\epsilon A}{d}, \quad (2.43)$$

where  $d$  is the distance between the plates,  $A$  the area of the plates, and  $\epsilon = \epsilon_r \epsilon_0$  the dielectric constant of the medium between the plates, the length of the sample is inversely proportional to the capacitance.  $\epsilon_0$  is the dielectric constant of the vacuum and  $\epsilon_r$  the dielectric constant of a medium, relative to  $\epsilon_0$ .

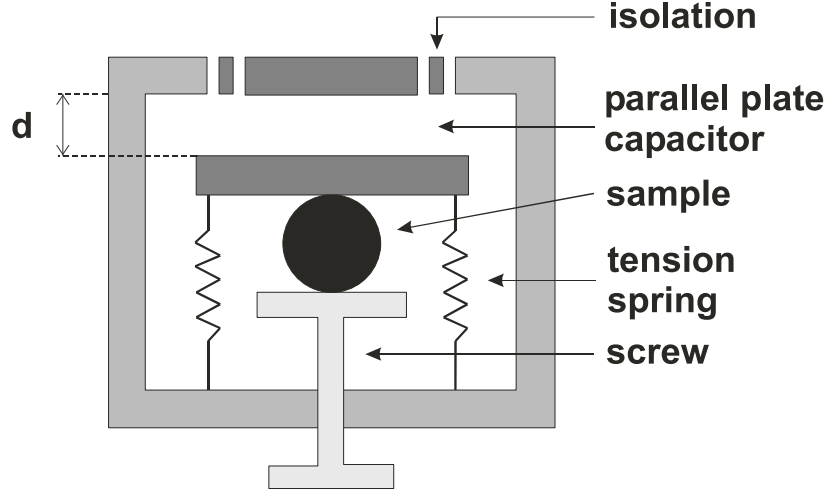


**Figure 2.7:** Schematic illustration of a parallel-plate capacitance cell to measure thermal expansion and magnetostriction. The two plates of the capacitor are electrically charged. The sample is pressed against the lower plate of the capacitor by turning the screw, on the bottom of the cell, tight. When the sample expands, it pushes the lower plate upwards, thereby enlarging the capacitance.

A schematic illustration of the parallel-plate capacitance method is shown in Fig. 2.7. In this thesis, measurements are presented which have been performed using home-built measuring cells at the Van der Waals-Zeeman Institute (WZI) of the University of Amsterdam (UvA) and at the Institut für Festkörperphysik (IFP) of the Forschungszentrum Karlsruhe (FZK). Details can be found in Refs. [33, 34] (Amsterdam) and Ref. [35] (Karlsruhe) or in Ref. [36] for a more general treatise on thermal expansion measurements with the parallel-plate capacitance method.

In Fig. 2.7 one can see that the upper capacitance plate is fixed while the lower is resting on the sample. The lower plate is positioned with springs, to ensure good contact with the sample. The bottom of the sample is placed on a plateau, fixed by a screw. The distance  $d$  between the two plates is chosen to be  $\sim 100\mu\text{m}$ .

The coefficient of thermal expansion  $\alpha$  is calculated by  $\alpha = (1/L)(dL/dT)$ . Here  $L$  is the length of the sample. In Amsterdam, the linear thermal expansion was determined with a discrete method, *i.e.* the temperature is varied stepwise. In Karlsruhe, the temperature was slowly raised at a reproducible rate of 20 mK/s over the whole temperature range. Averages are made every 0.1 K. The linear thermal expansion of the sample is calculated by

$$\alpha_{\text{sample}} = -\frac{1}{L} \left( \frac{\Delta d}{\Delta T} \right)_{\text{cell+sample}} + \frac{1}{L} \left( \frac{\Delta d}{\Delta T} \right)_{\text{cell+Cu}} + \alpha_{\text{Cu}}, \quad (2.44)$$

where the first term corresponds to the change in the distance between the plates when the sample is mounted in the cell. The second term accounts for the so-called cell effect, *i.e.* the signal observed when a copper sample of the same length as the

sample under investigation is mounted. This cell effect is found to reproduce very well. The last term is the linear thermal expansion of the copper of the cell.

Because the capacitance can be measured very accurately, total length changes down to  $0.05 \text{ \AA}$  are measurable. This means that for samples of just  $1 \text{ mm}$  length, a resolution of  $5 \cdot 10^{-8} \text{ K}^{-1}$  can be obtained in  $\alpha(T)$  for a temperature step of  $\Delta T = 0.1 \text{ K}$ .

The linear magnetostriction  $\lambda(B) = (L(B) - L(0))/L(0)$  was measured by monitoring the length change of the sample as a function of the applied magnetic field  $B$  at a constant temperature. The magnetostriction of the copper of the cell turns out to be negligible. The measurements were performed in Karlsruhe during field scans with a sweep rate of  $dB/dt = 0.25 \text{ T/min}$ . The constant temperature was controlled by a metal plate with low magnetoresistivity.

### 2.4.3 Electrical Resistivity

Electrical resistivity measurements were performed at the Van der Waals-Zeeman Institute (WZI) of the University of Amsterdam (UvA) using a standard four probe ac technique in zero field in the temperature range from 2 to 300 K. A MagLab system of Oxford Instruments was used.

### 2.4.4 Specific Heat

The specific heat  $C_p(T)$  measurements presented in Chapter 6 were performed at the Van der Waals-Zeeman Institute (WZI) of the University of Amsterdam (UvA) using the semi-adiabatic method in combination with a mechanical heat switch in a  $^3\text{He}$  cryostat. The set-up was home-built. The samples were 3 - 4 grams in mass.

The specific heat  $C_p(T)$  measurements presented in Chapter 7 were performed at the Institut für Festkörperphysik (IFP) of the Forschungszentrum Karlsruhe (FZK) using the commercially available Physical Property Measurement Systems (PPMS) of Quantum Design. The measurements were performed by the heat relaxation method in a temperature range between 3 and 300 K and in magnetic fields up to 14 T. Heat capacity was obtained by fitting a heat relaxation curve recorded after a heat pulse caused a temperature increase of approximately 2%. The heat capacity of the addenda (Apiezon N grease) had been measured in a separate run without the sample, and was subtracted from the data. For further details, see Ref. [37].

### 2.4.5 X-ray Powder Diffraction

X-ray diffraction measurements at room temperature were performed using a Bruker D3 Advance X-ray diffractometer with  $\text{Cu-K}\alpha$  radiation. Powders prepared from the polycrystalline samples were covered by Kapton foil to prevent contamination. Rietveld analysis of the diffraction data was performed using the GSAS program [38].

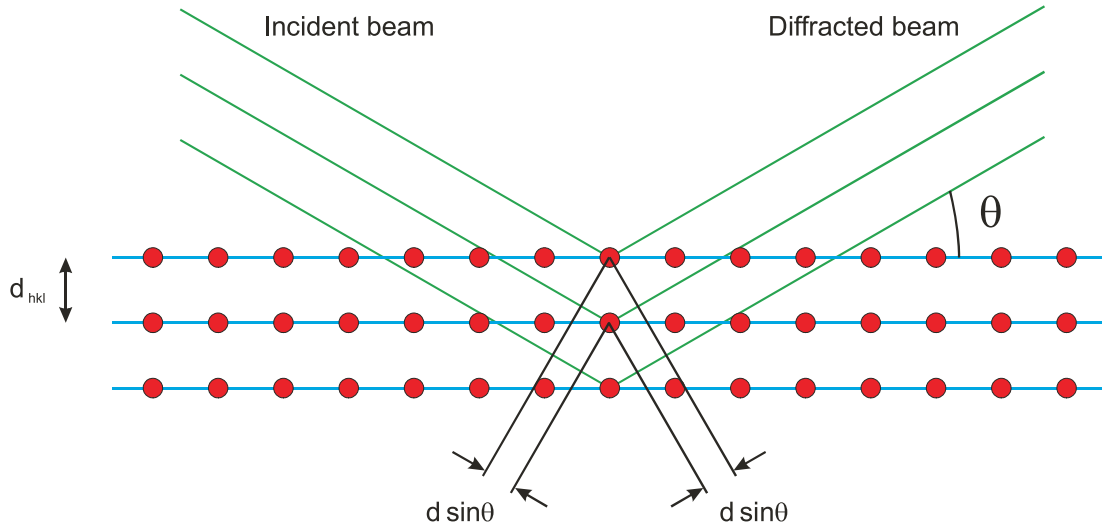


**Figure 2.8:** Illustration of how the angles  $\theta$  at which constructive interference of scattered waves occurs, can be found. Diffracted X-rays are in phase when the path length difference  $2d \sin \theta$  is equal to  $n\lambda$ , with  $n$  an integer, *i.e.* an integral number of wave length  $\lambda$ .

X-ray powder diffraction is a powerful technique used to identify crystal structures of compounds. The principle behind this technique is based on the constructive interference of X-rays, scattered from the illuminated sample. The measured intensity as a function of the scattering angle  $2\theta$  yields information on the spacing between planes of atoms in the crystal structure, as well as the sites of the atoms within the unit cell.

In Fig. 2.8 it is illustrated how the Bragg angles  $\theta$  at which constructive interference of scattered waves occurs, can be found. The diffracted rays will only be in phase if the difference in path length is equal to an integer times the wavelength  $\lambda$ . This is summarized by Bragg's law

$$n\lambda = 2d \sin \theta \quad (2.45)$$

where  $n$  is the order of diffraction and  $d$  the interplanar spacing.

The accuracy with which the lattice parameters of a compound can be determined, depends on the accuracy in the determination of  $2\theta$ . In this thesis (Chapter 6) the lattice parameters were measured with an uncertainty of 0.01 Å.

The relative intensity of the diffraction peaks is mainly controlled by the structure factor. The structure factor  $F_{hkl}$  is given by

$$F_{hkl} = \sum_{n=1}^N f_n \exp \left( 2\pi i (hu_n + kv_n + lw_n) \right) \quad (2.46)$$


where  $h$ ,  $k$ , and  $l$  are the Miller indices of the scattering plane and  $u$ ,  $v$ , and  $w$  are the reduced position indices of the  $N$  atoms in the unit cell. The atomic scattering factor  $f_n$  is a measure for the ability of an atom to scatter X-rays, relative to that of a single electron. The scattered intensity  $I$  is proportional to  $|F_{hkl}|^2$ .

---

# CHAPTER 3

---

## Theory

 HIS CHAPTER intends to introduce the basic concepts of the theories relevant to the work described in this thesis and is organized as follows. First, the nature of the electron correlations between the conduction electrons and the  $f$  electrons from the magnetic ions is described by introducing the relevant energy scales. Then the concept of a quantum critical point is discussed, followed by a description of Fermi liquid behavior and non-Fermi liquid behavior. After the introduction of Grüneisen parameters and a review on (magnetic) phase transitions, a few recent theories about ferromagnetic superconductors will be presented. This discussion is not aimed to be complete but gives a general overview.

### 3.1 Heavy Fermions

In the field of strongly correlated electrons systems (SCES), different classes of compounds are at the focus in present research. Among them, the intermetallic compounds known as heavy-fermion compounds have already been studied extensively. The known heavy-fermion compounds generally are Ce, Yb, and U based intermetallics, although Np and Pu compounds are also reported. For these systems the term “heavy” is connected to the large characteristic effective masses of the conduction electrons. Experimentally this is observed in a large electronic contribution to the specific heat at low temperatures. Direct proof of heavy quasiparticles can be obtained by the de Haas-van Alphen effect. Here one measures the cyclotron masses of the quasiparticles in magnetic resonance measurements of the magnetization.

Within the standard description of heavy-fermion physics, the large mass enhancement is thought to be generated by an exchange interaction between localized and conduction electrons. This is called the Kondo effect. Originally, the Kondo effect was established for a single magnetic impurity interacting with the conduction

electrons of a non-magnetic matrix [39]. In a lattice of magnetic ions that strongly interact with the conduction electrons, a so-called Kondo lattice is formed.

### Anderson Hamiltonian

In order to study the heavy-fermion state, it is useful to start with the single-impurity case. Anderson considered a single magnetic impurity (in this thesis an  $f$ -electron impurity will be assumed) within a non-magnetic metallic host lattice [40] and reached at the often used Anderson model to describe magnetic impurities in a host:

$$\begin{aligned}
 H_A = & \sum_{\mathbf{k}\sigma} \epsilon(\mathbf{k}) n_{\mathbf{k}\sigma} + \epsilon_f \sum_m n_{fm} + \frac{1}{2} U \sum_{m \neq m'} n_{fm} n_{fm'} \\
 & + \sum_{\mathbf{k}m} \left( V_{m\sigma}(\mathbf{k}) f_m^\dagger c_{\mathbf{k}\sigma} + V_{m\sigma}^*(\mathbf{k}) c_{\mathbf{k}\sigma}^\dagger f_m \right)
 \end{aligned} \tag{3.1}$$

The first term represents the energy of the conduction electrons. Here  $\epsilon(\mathbf{k})$  is the energy dispersion relation of the conduction-electron band and  $n_{\mathbf{k}\sigma}$  the number operator for wave vector  $\mathbf{k}$  and conduction electron spin  $\sigma$ . The second term accounts for the energy of the  $f$ -electrons localized at the magnetic impurity, where  $\epsilon_f$  is the energy of the degenerate  $f$ -orbital and  $n_{fm}$  is the number operator with  $m$  the spin index of the  $2j + 1$  impurity states. The third term describes the on-site Coulomb interaction between two localized  $f$ -states.  $U$  is the energy needed to add a second  $f$ -electron to the localized, partially filled,  $f$ -orbital. It causes an energy splitting of the valence states  $f^n$ . If  $U$  is high enough, double occupancy is not favorable and one state is pushed above the Fermi level. This leads to a polarized splitting and as a consequence to a magnetic impurity state. The last term in Eq. 3.1 corresponds to the hybridization between the  $f$ -states and the conduction electron states. Here  $V_{m\sigma}(\mathbf{k})$  is the hybridization integral that mixes the localized and extended states. The operators  $f^\dagger$  and  $c^\dagger$  ( $f$  and  $c$ ) are the creation (annihilation) operators of the localized and conduction-electron states, respectively.

### Kondo interaction

Due to the hybridization both  $f$ -states (spin “up” and spin “down”) are broadened. The energy width of the state is defined as  $\Gamma = \pi N(E_F) |V|^2$ , where the matrix elements  $V(\mathbf{k})$  have been averaged over the Fermi surface.  $N(E_F)$  denotes the density of states at the Fermi level  $E_F$ . For a weak hybridization and a large enough  $U$ , one impurity  $f$ -state is below the Fermi level and the other above, while neither of them is significantly broadened, *i.e.*  $|\Gamma/(\epsilon_f - E_F)| \ll 1$  and  $|\Gamma/(\epsilon_f + U - E_F)| \ll 1$ .

For a weak hybridization of the localized  $f$ -states and the conduction states the Anderson Hamiltonian can be transformed into the Kondo Hamiltonian [41]

$$H_K = -2J \mathbf{S} \cdot \boldsymbol{\sigma} \tag{3.2}$$

where  $\mathbf{S}$  is the localized impurity spin and  $\boldsymbol{\sigma}$  the conduction-electron spin.  $J$  is an effective exchange parameter which originates from the hybridization and can be expressed as

$$J = |V|^2 \frac{U}{(\epsilon_f - E_F)(\epsilon_f - E_F + U)} < 0. \quad (3.3)$$

Because of the negative value of  $J$  the coupling between the impurity spin and the conduction-electron spin has an antiferromagnetic nature. In the ground state the impurity spin is found to be completely screened (compensated) by the surrounding conduction electron spins. The ground state of the system is a non-magnetic singlet. This singlet state leads to the formation of a narrow peak in the density of states close to the Fermi level, which is known as the Abrikosov-Suhl or Kondo resonance.

Due to the formation of a singlet the energy of the system is lowered. The energy gain can be expressed by a characteristic temperature. This is the Kondo temperature  $T_K$  and can be written as

$$k_B T_K = D \exp \left( -\frac{1}{N(E_F)|J|} \right) \quad (3.4)$$

where  $D$  is the bandwidth of the Kondo resonance peak and is of the order of  $k_B T_K$ . The classical signature of the Kondo effect is a minimum in the temperature dependence of the electrical resistivity  $\rho(T)$  followed by a logarithmic increase with decreasing temperature. As a consequence of the enhanced density of states at the Fermi level  $N(E_F)$ , a large linear term  $\gamma$  in the electronic specific heat is observed at low temperatures. The scaling behavior corresponds to  $\gamma \propto N(E_F) \propto 1/T_K$ .

### From Kondo impurity to Kondo lattice

So far a single magnetic impurity in a non-magnetic matrix has been considered. However, intermetallic compounds without chemical substitution containing *e.g.* U or Ce atoms form a periodic array of magnetic impurities. One then speaks of a Kondo lattice.

The low-temperature properties of the Kondo lattice differ drastically from the single-impurity Kondo case. In the latter case, the resistivity shows a minimum around  $T = T_K$  and follows  $\rho \propto -\ln(T/T_K)$  at low temperatures. In the former case, however, this upturn changes again into a decrease in  $\rho(T)$  for decreasing temperatures, with a  $T^2$ -temperature dependence at the lowest temperatures.

This behavior can be understood by considering the electron-screening cloud around a localized moment. For  $T > T_K$  local magnetic moments are observed, (with Curie-Weiss behavior of the magnetic susceptibility) since thermal fluctuations break the hybridization between the local moment and the conduction electrons. Below  $T < T_K$  the conduction electrons tend to screen the magnetic moment. This electron-screening cloud has a certain correlation length which grows with decreasing temperature. Below a certain temperature  $T_{\text{coh}} < T_K$  this correlation length is so

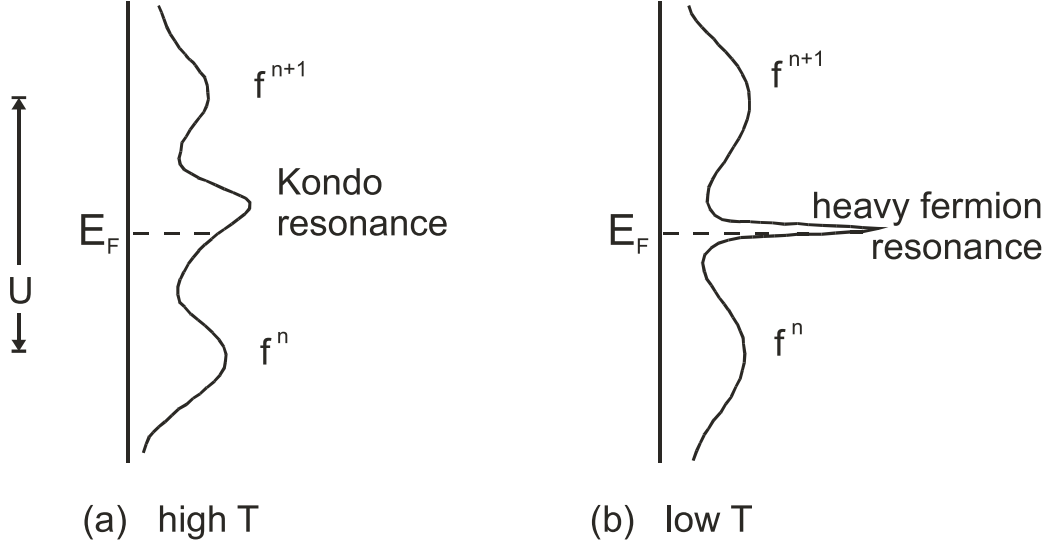


**Figure 3.1:** Schematic picture of the density of states in the Kondo lattice. For high temperatures ( $T_{\text{coh}} < T < T_K$ ), a Kondo resonance peak is present around  $E_F$ . For low temperatures ( $T < T_{\text{coh}}$ ) the coherent electronic state is characterized by a narrow many-body band just above  $E_F$ .

large that the screening clouds show a significant overlap and a coherent many-body band with Fermi-liquid characteristics is induced [42].

A schematic picture of the density of states in the Kondo lattice is presented in Fig. 3.1 [34, 43]. As the temperature is lowered from high temperatures to below  $T_K$ , a broad peak develops around the Fermi level  $E_F$ , originating from the Kondo resonance, as explained above. In addition there are two peaks from the broadened  $f$ -orbitals of the magnetic ions. These two peaks are separated by the Coulomb interaction  $U$ . At these temperatures the characteristics of the system are still governed by the broad  $f$ -peak below  $E_F$  (since the Kondo resonance, which is centered just above  $E_F$ , is not sharp enough to have much influence), resulting in a more localized picture. For lower temperatures, the Kondo resonance peak transforms into a very narrow many-body band just above  $E_F$  and electronic coherence sets in. This peak now accounts for the observed properties in heavy-fermion systems, resulting in the characteristic Fermi-liquid behavior with a high effective mass for the conducting quasiparticles.

A very nice example of this behavior is  $\text{CeCu}_6$  [44]. The resistivity data, presented in Fig. 3.2, clearly indicate the existence of the two energy scales. The high temperature energy scale is the Kondo temperature  $T_K \approx 200$  K. Below this temperature the scattering is enhanced and still incoherent, due to the single-ion Kondo effect. This results in a logarithmic increase below  $T_K$ . As the temperature is lowered, coherence sets in which manifests itself in a maximum in the resistivity at  $T_{\text{coh}} \approx 10$  K. At low temperatures the resistivity shows a  $T^2$  dependence.



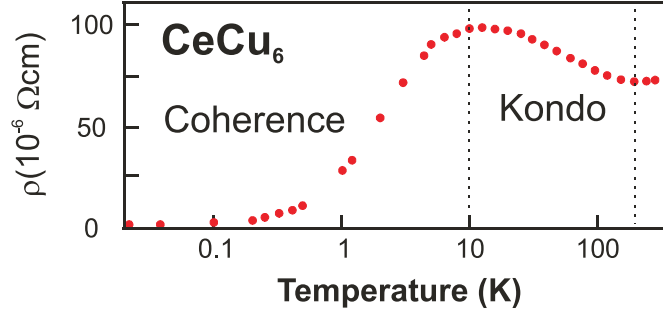


**Figure 3.2:** Temperature dependence of the electrical resistivity of  $\text{CeCu}_6$ . The logarithmic increase below 200 K is associated with the incoherent single-ion Kondo effect. As coherence sets in, a maximum is observed and the resistivity drops. At low temperatures the resistivity shows a  $T^2$  dependence.

### RKKY interaction

In a system of well separated, localized magnetic moments there is hardly any direct interaction between the moments. However, there does exist an indirect exchange through the polarization of the conduction electrons. This exchange causes an interaction between the localized moments, called the RKKY interaction (after Ruderman, Kittel, Kasuya, and Yosida [45, 46, 47]). It is based on the electrostatic interaction in conjunction with the Pauli exclusion principle. Near a localized spin  $\mathbf{S}_1$  the spins of the conduction electrons are polarized due to an interaction which can be described by a Hamiltonian identical to Eq. 3.2. The spin polarization is a damped, oscillatory function in space and extends over a long range. A second spin  $\mathbf{S}_2$  at distance  $\mathbf{r}$  is in turn polarized by the conduction-electron polarization. This interaction can lead to magnetic order. The strength is characterized by an energy equal to

$$k_B T_{\text{RKKY}} \propto N(E_F) J^2 \quad (3.5)$$

where  $J$  is the exchange parameter of the localized moment and the conduction-electron spin.

### Doniach phase diagram

The ground state of a Kondo-lattice system mainly depends on the balance of the two aforementioned effects, both depending on the same exchange parameter  $J$ . On the one hand the Kondo effect has the tendency to screen the localized moments and produce a non-magnetic ground state, on the other hand the RKKY interaction favors long-range magnetic order. The result of this competition is summarized in the Doniach phase diagram [42, 48] presented in Fig. 3.3. Within this simple model the compounds with stable  $f$  moments (characterized by  $T_{\text{RKKY}} > T_K$ ) have a small value for  $J$ . Long-range magnetic order is observed below the magnetic ordering temperature  $T_M$ , which is proportional to  $T_{\text{RKKY}}$ . For larger values of  $J$  the Kondo interaction gains in importance and  $T_M$  starts to decrease. The system shows a

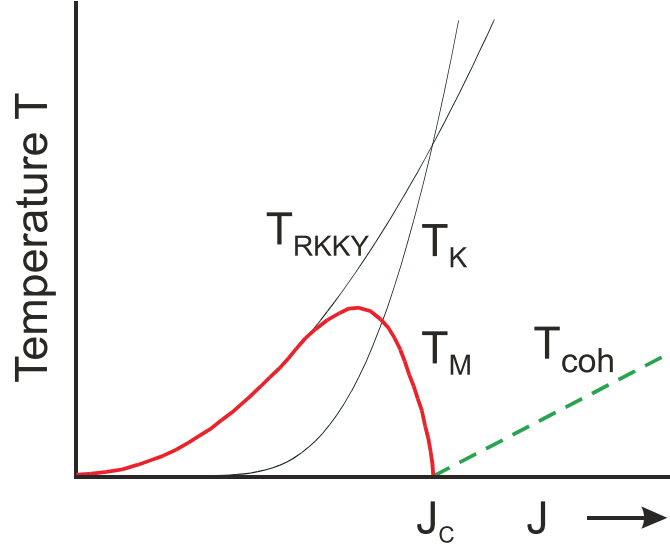


**Figure 3.3:** The Doniach phase diagram. The characteristic RKKY and Kondo temperatures are represented as functions of the exchange parameter  $J$ . Different types of ground states are also represented. The thick solid line indicates the temperature of the magnetic transition  $T_M$ .

magnetic instability at a critical value of  $J = J_c$ . At this point the Kondo and RKKY interaction strengths are equal. Because the magnetic fluctuations are not thermally driven but quantum mechanical in nature, this point is called a quantum critical point (QCP). For  $J > J_c$  the Kondo effect prevails ( $T_K > T_{RKKY}$ ) and a non-magnetic ground state is observed. Below  $T_{coh}$  a coherent ground state is found, as explained above.

### Hill's limit

As can be seen from the preceding discussion, the type of magnetic behavior depends strongly on the strength of the interaction between the localized magnetic states and the conduction electrons. When this interaction is mediated by the conduction electrons, one speaks about an indirect exchange interaction, of which the RKKY mechanism is an example. However, in the case of a  $5f$ -electron system with a small separation of the local moments, overlap between  $5f$ -wave functions can also cause a direct interaction.

Hill [49] has performed a systematic study of magnetic properties of intermetallic uranium compounds, known at that time (1970) as a function of the nearest neighbor distance  $d_{U-U}$ . It was shown that for  $d_{U-U} < 3.4 \text{ \AA}$  the uranium compounds had a paramagnetic ground state and were often superconducting at low temperatures. For  $d_{U-U} > 3.6 \text{ \AA}$  the compounds were generally magnetic. The interpretation for these observations is that the ground state is a consequence of the extent to which the  $5f$ -orbitals overlap. For small values of  $d_{U-U}$  uranium  $f$ -electron orbitals

in the lattice overlap directly with those of the neighboring U ions and produce itinerant  $f$ -electron behavior. The  $f$ -electrons are delocalized from the U ion to the conduction band and open the way to superconductivity. On the other hand, for large values of  $d_{U-U}$  long-ranged magnetic order sets in with the  $f$ -electrons localized at the uranium ion. At  $d_{U-U} \approx 3.5 \text{ \AA}$ , the uranium systems, being on the edge of becoming magnetic, exhibit strong spin fluctuations.

For more than one decade the Hill criterion was remarkably successful. However, when several compounds, among which the heavy-fermion systems, were found to violate this criterion, it was realized that the overlap of the  $5f$ -orbital with  $s$ ,  $p$ , or  $d$ -orbitals of non-uranium neighbors could considerably contribute to the delocalization of the U  $5f$ -electrons.

The degree of delocalization of the  $5f$ -orbitals due to  $f$ -ligand hybridization (where ligand stands for non- $5f$  atom) has been discussed by Koelling *et al.* [50]. It was shown that not the magnitude of the ligand orbital governs the  $f$ -ligand hybridization, but its spatial curvature. A consequence is that the hybridization is largest for the top of the ligand band *i.e.* the electron wave functions with the highest kinetic energy. From the systematic trends in Ce and U compounds it was concluded that in heavy-fermion systems it is the  $f$ -ligand hybridization, rather than the direct  $f$ - $f$  orbital overlap, which is the primary mechanism determining the magnetic properties of the system.

## 3.2 Quantum Phase Transitions

Phase transitions occur upon variation of an external control parameter. Their common characteristic is a qualitative change in the system properties. Well-known phase transitions, like paramagnetism to magnetic order or from a metallic state into a superconducting one, occur at finite temperature. Here macroscopic order is destroyed by thermal fluctuations for increasing temperatures. A different class of phase transitions shows a transition at zero temperature. It was pointed out by Hertz [51] that when a non-thermal control parameter such as pressure, magnetic field, or chemical composition is varied to access the transition point, long-range order is destroyed solely by quantum fluctuations. Hence, one speaks of a quantum phase transition. Experimental and theoretical developments in the last decades have made clear that the presence of such zero-temperature phase transitions plays an important role in the so-far unsolved puzzles in heavy-fermion compounds, see *e.g.* Refs. [52, 53]. The physical properties of the quantum fluctuations, which can destroy long-range order at absolute zero temperature, are quite distinct from those of the thermal fluctuations responsible for traditional, finite-temperature phase transitions [54, 55].

A transition is usually characterized by an order parameter. This is a thermodynamic quantity that is zero in the disordered phase and non-zero in the ordered phase. In the case of a ferromagnetic transition, the total magnetization is the order parameter. While the thermodynamic average of the order parameter is zero

in the disordered phase, its fluctuations are non-zero. When the critical point is approached, the spatial correlation of the order parameter fluctuations become long-range. Close to the critical point their typical length scale, the correlation length  $\xi$ , diverges as

$$\xi \propto |\tau|^{-\nu_{\text{cor}}} \quad (3.6)$$

where  $\nu_{\text{cor}}$  is the correlation length critical exponent and  $\tau = |T - T_C|/T_C$ . In addition to the long-range correlations in space there are analogous long-range correlations in time. The typical timescale for the decay of a fluctuation is the correlation time  $\tau_c$  which diverges as

$$\tau_c \propto \xi^z \propto |\tau|^{-\nu_{\text{cor}}z} \quad (3.7)$$

where  $z$  is the dynamic critical exponent. Close to the critical point there are no other characteristic length and time scale than  $\xi$  and  $\tau_c$ , respectively.

Since close to the critical point the correlation length  $\xi$  is the only relevant length scale, the physical properties must be unchanged if all lengths in the system (much smaller than  $\xi$ ) are rescaled by a common factor and at the same time the external parameters are adjusted in such a way that the correlation length retains its old value. In the case of a magnetic compound the external parameters are the reduced temperature  $\tau$  and the applied magnetic field  $B$ . This gives rise to the homogeneity relation for the free energy density in the classically critical regime [56, 57, 58]:

$$f(\tau, B) = b^{-d} f(\tau b^{1/\nu_{\text{cor}}}, B b^{y_B}), \quad (3.8)$$

where  $y_B$  is a critical exponent,  $b$  is an arbitrary positive number, and  $d$  the dimension of the system.

In order to address the question whether quantum mechanics influences the critical behavior, the characteristic energy of long-distance order parameter fluctuations,  $\hbar\omega_c$ , has to be compared to the thermal energy  $k_B T$ . Since  $\tau_c \propto |\tau|^{-\nu_{\text{cor}}z}$ , the typical energy scale  $\hbar\omega_c$  goes to zero as

$$\hbar\omega_c \propto |\tau|^{\nu_{\text{cor}}z}. \quad (3.9)$$

Quantum mechanics is unimportant as long as  $\hbar\omega_c \ll k_B T$ , which enables a purely classical description of the order parameter fluctuations. On the other hand, a quantum mechanical description of the fluctuations is inevitable when  $\hbar\omega_c > k_B T$ .

For all finite-temperature phase transitions with a transition temperature  $T_c$  a temperature range can be found where  $\hbar\omega_c \propto |\tau|^{\nu_{\text{cor}}z} < k_B T_c$ . In other words, the critical behavior asymptotically close to the transition is entirely classical. Although quantum mechanics can still be important on microscopic scales, the classical thermal fluctuations dominate on the macroscopic scale, which controls the critical behavior. If, however, the transition takes place at zero temperature as a function of a non-thermal parameter  $r$ , like pressure, magnetic field, or chemical substitution concentration, the behavior is always dominated by quantum fluctuations.

The interplay of classical and quantum fluctuations leads to an interesting phase diagram in the vicinity of a quantum critical point (see Fig. 3.4). A classical phase

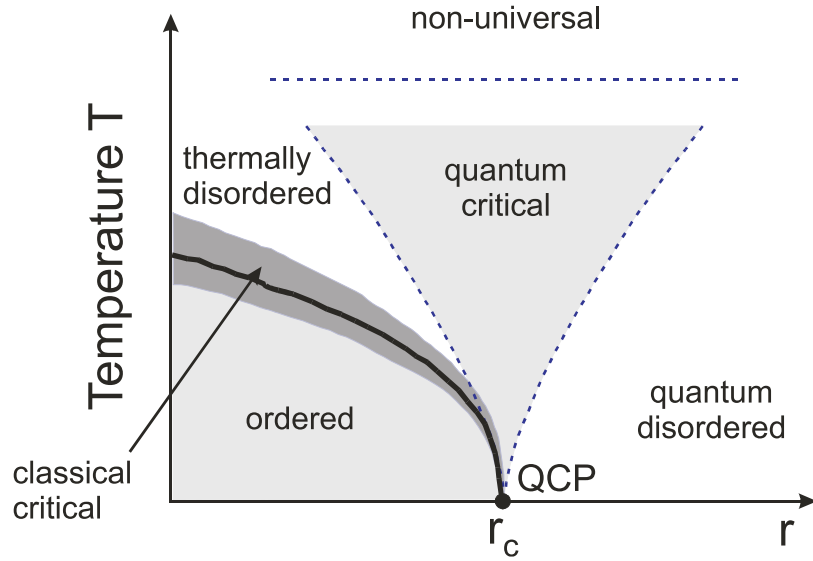


**Figure 3.4:** Schematic phase diagram in the vicinity of a quantum critical point. The horizontal axis represents the control parameter  $r$  used to tune the system through the quantum phase transition, and the vertical axis is the temperature  $T$ . The solid line marks the finite-temperature boundary between the ordered and thermally disordered phases. Close to this line, the critical behavior is classical. The dashed lines indicate the boundaries of the quantum critical region. These crossover lines are given by  $k_B T \propto |r - r_c|^{\nu_{\text{cor}z}}$ . Figure taken from Ref. [55].

transition is encountered upon variation of  $T$  at small  $r$ . The quantum critical point can be viewed as the endpoint of the line of finite-temperature transitions. Above this line, the system is thermally disordered. For  $r > r_c$  at low  $T$ , the physics is dominated by quantum fluctuations. An example is the Kondo effect, discussed in the previous Section. Between these two disordered phases a quantum critical region exists, where both types of fluctuations are important. It is located near the critical point at  $r = r_c$ . Its boundaries are determined by the condition  $k_B T > \hbar \omega_c \propto |r - r_c|^{\nu_{\text{cor}z}}$ . Physically this means that the system looks critical with respect to the tuning parameter  $r$ , but it is driven away from criticality by thermal fluctuations. The upper boundary is determined as the temperature at which  $k_B T$  exceeds the characteristic microscopic energy scale, *e.g.* the exchange energy  $J$  for magnetic materials. Since in the quantum critical region the physics is controlled by the thermal excitations of the quantum critical ground state, unusual finite-temperature properties, such as unconventional power laws and non-Fermi liquid behavior, are observed. In other words, non-Fermi liquid properties arise because close to  $r = r_c$  the low-temperature thermodynamics is determined by *collective* modes (excitations of the order parameter). This is in contrast to the *single*-fermion excitations (quasiparticles) from collective interactions in the Fermi-liquid regime.

Thermodynamic properties are derived from the partition function

$$Z = \text{Tr} e^{-H/k_B T} \quad (3.10)$$

where  $H = H_{\text{kin}} + H_{\text{pot}}$  is the Hamiltonian of the system. In a classical system the kinetic and potential part of  $H$  commute. Since in this case  $Z = Z_{\text{kin}} Z_{\text{pot}}$ , the dynamics and statics are decoupled. However, in a quantum mechanical approach  $H_{\text{kin}}$  and  $H_{\text{pot}}$  in general do not commute, and therefore dynamics and statics are coupled. According to Eq. 3.7, the correlation time scales as the  $z$ th power of a correlation length. For second-order phase transformations the classical homogeneity law (Eq. 3.8) for the free energy density can now, be written for the quantum mechanical case at zero temperature as [55]

$$f(\delta, B) = b^{-(d+z)} f(\delta b^{1/\nu_{\text{cor}}}, B b^{y_B}), \quad (3.11)$$

where  $\delta = |r - r_c|/r_c$ . This shows that a quantum phase transition in  $d$  dimensions is related to a classical transition in  $d_{\text{eff}} = d + z$  dimensions. With  $z = 3$  for ferromagnets, the effective dimension  $d_{\text{eff}} = 6$ . In this case the fluctuations may then be accounted for in a self-consistent mean field approximation [56].

The search for a second order quantum phase transition in itinerant-electron systems, which is believed to be responsible for exotic quantum phases like magnetically mediated superconductivity and non-Fermi liquid behavior, has become the subject of many researchers in recent years. The compounds  $\text{CePd}_2\text{Si}_2$  and  $\text{CeIn}_3$  [59] are good examples of superconductivity emerging around a quantum phase transition. However, also notable differences from standard second order behavior have been found.  $\text{MnSi}$  [60] and  $\text{ZrZn}_2$  [61] undergo a *first* order quantum phase transition.  $\text{UGe}_2$ , one of the ferromagnetic compounds studied in this thesis, shows a first order quantum phase transition at 1.6 GPa. Theoretical studies [62, 63] suggest that ferromagnetic transitions in clean three-dimensional itinerant ferromagnets are *always* first order at  $T = 0$  K. However, these compounds show the same behavior (superconductivity and a non-Fermi liquid phase) as expected for materials with a second order quantum phase transitions. The understanding of the physics of these first order quantum phase transitions is still a challenge for both theoretical and experimental studies [64].

### 3.3 Fermi liquid and non-Fermi liquid behavior

In the previous two Sections the terms Fermi liquid and non-Fermi liquid have been mentioned several times. In this Section these terms will be explained further. First, it is instructive to summarize a few properties of a gas of non-interacting electrons - the Fermi gas.

The specific heat of a system of electrons within a lattice of magnetic ions can be written as the sum of three components:  $c(T) = c_{\text{el}}(T) + c_{\text{phonon}}(T) + c_{\text{mag}}(T)$ . The phonon contribution (due to vibrations of the lattice) is often described in terms

of the Debye temperature  $\Theta_D$  and the Debye function [65]. At low temperatures ( $T \ll \Theta_D$ ) the phonon contribution can be approximated by  $c_{\text{phonon}} = \frac{12\pi^4}{5} n k_B \left( \frac{T^3}{\Theta_D^3} \right)$ , where  $n$  is the number of atoms per mole of formula units. The magnetic contribution (due to the atomic moments) depends strongly on the system under investigation. For a ferromagnet with a gapless magnon dispersion curve [65] one obtains at low temperatures  $c_{\text{mag}}(T) \propto T^{3/2}$ , but  $c_{\text{mag}}(T) \propto T^{-1/2} e^{-\Delta/k_B T}$  if a gap  $\Delta$  is present in the dispersion curve [66].

### 3.3.1 Fermi gas

An electron gas consists of non-interacting, independent electrons. Note that independent means that there are no interactions with the lattice of magnetic ions and no interactions between the electrons other than the Pauli exclusion principle for Fermions. The electrons gas itself has a specific heat of

$$c_{\text{el}}(T) = \frac{\pi^2}{3} N(E_F) k_B^2 T. \quad (3.12)$$

This is usually written as  $c_{\text{el}}(T) = \gamma T$  and  $\gamma$  is called the Sommerfeld coefficient. Note that the density of states amounts to  $N(E_F) = (m_e k_F)/(\pi^2 \hbar^2)$ , with  $k_F$  the Fermi wave vector, is proportional to the electron mass  $m_e$ . Systems for which the independent-electron model holds (Fermi gas), typically have values of  $\gamma \approx 1 \text{ mJ/mol K}^2$ .

The electrical resistivity is a measure for the scattering probabilities of electrons when traveling through a sample. In a model of non-interacting electrons, the Fermi gas itself has no resistivity. The electrons only scatter from lattice irregularities and magnetic waves. The electrical resistivity can therefore be written as  $\rho(T) = \rho_0 + \rho_{\text{phonon}}(T) + \rho_{\text{mag}}(T)$ . Interaction of conduction electrons with lattice imperfections (dislocations, stacking faults, vacancies, interstitials) causes a temperature independent term  $\rho_0$ . Thermally excited lattice vibrations yield pronounced temperature dependencies. In the Debye model [67] it can be calculated that the resistivity follows  $\rho_{\text{phonon}}(T) \propto T^5$  at low temperatures ( $T \ll \Theta_D$ ). The magnetic contribution again depends on the system. For a magnet above its ordering temperature there is a temperature independent contribution due to scattering by the magnetic atomic moments. As the magnetic moments start to show order below the ordering temperature, the magnetic contribution decreases for decreasing temperatures. For a ferromagnet at low temperatures it can be written as  $\rho(T) \propto T^2$ .

When a magnetic field is applied to a gas of independent electrons the energy of the electron is raised or lowered depending on its spin. As a consequence, the corresponding energy bands shift with respect to each other, resulting in a higher population of the up-band than the down-band. The so-called Pauli susceptibility is essentially temperature independent and can be written as [67]

$$\chi_P = \mu_0 \mu_B^2 N(E_F). \quad (3.13)$$



This susceptibility is usually small compared to the paramagnetic Curie-Weiss behavior of magnetic ions in the crystal. The Pauli susceptibility can therefore only be observed in unordered compounds.

### 3.3.2 Fermi liquid

Up to now a gas of electrons was considered, *i.e.* independent electrons with no interactions with each other or with the lattice (except for Fermi-Dirac statistics). Although this model works for a limited amount of compounds, it is clear that this picture does not apply in general. For example, in Sec. 3.1 the Kondo effect was discussed, which is based on the interaction between a localized moment and the conduction electrons (hybridization). Taking the Fermi-gas model as a starting point, one can imagine gradually turning on the interactions. Then the step is made to a Fermi liquid, which is a Fermi gas plus interactions.

The arguments leading to a Fermi liquid are very subtle. In the Fermi gas model the electrons are independent. Then, quasiparticles are introduced that behave as independent conduction electrons, with a parabolic energy dispersion. These quasiparticles are also called dressed electrons as their properties are modified by the interaction with the lattice. Analysis of electron-electron and electron-lattice interactions lead to a substantially modified energy versus wave vector relation for one-electron levels. It is, however, far from clear that there is still any validity in treating the electrons as independent. Nevertheless, Landau has shown [68, 69, 70] that this picture does in fact hold, at least for levels within  $k_B T$  of the Fermi energy. Since many of the most interesting electronic properties of a metal are almost completely determined by electrons within  $k_B T$  of the Fermi energy, the way is open to a relatively simple description of the electronic states.

However, when interactions are strong, it is not likely that the independent electron approximation is appropriate. Landau solved this problem by considering an independent quasiparticle approximation. He showed that by gradually turning on the interactions, the electron states evolve in a continuous way and therefore have a one-to-one correspondence with the states of the noninteracting system. An extensive description of the Fermi-liquid theory can be found in Refs. [71, 72].

A consequence of describing heavy-Fermion systems within the framework of the Fermi-liquid theory, is the introduction of effective masses  $m^*$  of the quasiparticles exceeding the free-electron mass by a factor up to several hundred for heavy-fermion systems, and correspondingly large values of the Sommerfeld coefficient  $\gamma$  and the Pauli spin susceptibility  $\chi_P$ .

With the correspondence of the quasiparticles of an interacting-electron system with a free-electron gas, it can be derived [71, 72] that the low-temperature properties of the Fermi liquid obey the same laws as the Fermi gas, with a renormalized effective mass  $m^*$  and a few additional parameters taking into account the residual interactions among the quasiparticles.



The electronic part of the specific heat is given by

$$c_{\text{el}}(T) = \gamma T \equiv (m^*/m_0)\gamma_0 T \quad (3.14)$$

where  $\gamma_0 = \frac{1}{3}\pi^2 N(E_F)k_B^2$  is the Sommerfeld constant of the free-electron gas given in Eq. 3.12 and  $m_0$  the free-electron mass. Therefore, the specific-heat coefficient at low temperatures gives direct information on the effective mass  $m^*$ . The Pauli susceptibility of the Fermi liquid is given by

$$\chi_P = \frac{m^*}{m_0} \frac{\chi_0}{1 + F_0^a} \quad (3.15)$$

where  $\chi_0$  is the Pauli susceptibility of the free-electron gas (Eq. 3.13) and  $F_0^a$  an antisymmetric Landau parameter [71, 72]. The electrical resistivity  $\rho(T)$  at low temperatures is the sum of the residual resistivity  $\rho_0$  and an additional quadratic term that describes the electron-electron interaction:

$$\rho(T) = \rho_0 + AT^2. \quad (3.16)$$

The coefficient  $A$  is related to  $\gamma$  by the empirical Kadowaki-Woods relation  $A/\gamma^2 \approx 10 \mu\Omega \text{ cm K}^2 \text{ mol}^2 \text{ J}^{-2}$  [73]. As  $\gamma \propto m^*$  the coefficient  $A$  scales as  $A \propto (m^*)^2$ . It should be noted that for a ferromagnet below  $T_C$  the spin waves also give rise to a  $\rho(T) = a_{\text{fsw}} T^2$  dependence at low temperatures, see Sec. 3.3.1. However, because of the coherent Fermi-liquid state,  $A \gg a_{\text{fsw}}$ .

### 3.3.3 Non-Fermi liquid

The Fermi-liquid theory has been successful in describing the low-temperature behavior of many compounds. Even many actinide systems with very strong electronic correlations are well described in terms of Fermi-liquid theory. In recent years, the cases where the Fermi-liquid scenario does not apply have attracted much attention.

The main macroscopic properties of the systems that have been identified as non-Fermi liquids are a diverging specific heat divided by temperature,  $c/T$ , a diverging magnetic susceptibility  $\chi$  and a non-quadratic electric resistivity  $\rho \propto T^\alpha$  with  $\alpha < 2$ . At present there is no theoretical model that yields a universal description of non-Fermi liquid behavior. Several models have been put forward in order to describe the microscopic mechanisms that lead to non-Fermi liquid behavior. The most important models will be discussed below. By comparing the measured temperature dependencies of  $c/T$ ,  $\chi$  and  $\rho$ , it might be possible to determine which model describes the system best.

#### Multichannel Kondo effect

In this model,  $M$  degenerate conduction-electron bands couple with identical exchange integrals to an impurity with spin  $S_I$  [74, 75, 76]. When  $M > 2S_I$ , the

impurity spin is overscreened by the spins of the conduction electrons. As a consequence, a non-trivial non-Fermi-liquid critical point governs the low-temperature properties of the system. The most likely observable version of this model is the case of  $M = 2$ ,  $S_I = 1/2$  for rare-earth and actinide systems. This model is primarily relevant for diluted heavy-fermion alloys, *e.g.*  $\text{Y}_{1-x}\text{U}_x\text{Pd}_3$  [77],  $\text{Th}_{1-x}\text{U}_x\text{Ru}_2\text{Si}_2$  [78], and  $\text{La}_{1-x}\text{Ce}_x\text{Cu}_{2.2}\text{Si}_2$  [79]. The characteristics are summarized as

$$\begin{aligned}\frac{c(T)}{T} &\propto -a \ln T + b \\ \chi(T) &\propto -\ln T \\ \rho(T) &\propto 1 - cT^{\frac{1}{2}}\end{aligned}\tag{3.17}$$

### Kondo disorder model

The central idea of the Kondo disorder model is that a moderate disorder in a lattice model of localized moments is magnified due to the strong local correlations between the moments and the conduction electrons. In particular, a broad distribution of local energy scales (Kondo temperatures) is generated [80]. A few local sites with very small Kondo temperatures are unquenched at low temperatures and dominate the thermodynamic and transport properties, forming a dilute gas of low-lying excitations above the disordered metallic ground state. The presence of these unquenched moments leads to the formation of a non-Fermi-liquid phase. As in the case of the multichannel Kondo effect, this model is applicable to substitutional system, but only when the disorder is moderate. The properties of the compound  $\text{UCu}_{5-x}\text{Pd}_x$  with  $x = 1$  and  $1.5$ , are reported to be described by this model [81]. The predictions are

$$\begin{aligned}\frac{c(T)}{T} &\propto -\ln T + a \\ \chi(T) &\propto -\ln T + b \\ \rho(T) &\propto 1 - cT\end{aligned}\tag{3.18}$$

### Proximity to a quantum critical point

As discussed in Sec. 3.2, a quantum critical point occurs when a critical point, *e.g.* a ferromagnetic phase transition at some temperature  $T_{\text{cr}}$ , is tuned to 0 K by an external parameter  $r$ . This can be pressure, magnetic field, or chemical substitution. At the quantum critical point, the low-temperature thermodynamics is characterized by *collective* modes corresponding to fluctuations of the order parameter, rather than by *single*-fermion excitations as in a Fermi liquid. Therefore, non-Fermi-liquid properties arise. The temperature dependencies depend strongly on the dimensionality  $d$  of the system and on the nature of the magnetic interactions. For a ferromagnet  $z = 3$  in Eq. 3.7, for an antiferromagnet  $z = 2$ . The dependencies are summarized in Table 3.1.

**Table 3.1:** Predicted scaling behavior of the Millis-Moriya spin-fluctuation model for the temperature dependence of the linear specific heat coefficient  $c/T$  and the electrical resistivity  $\rho$  at the QCP at low temperatures [82, 83, 84].

	$d = 3$		$d = 2$	
	$z = 3$	$z = 2$	$z = 3$	$z = 2$
$c/T$	$-\ln(T/T_0)$	$\gamma_0 - \beta\sqrt{T}$	$T^{-1/3}$	$-\ln(T/T_0)$
$\rho$	$T^{5/3}$	$T^{3/2}$	$T^{4/3}$	$T$

### Griffiths phase model

The Griffiths phase model takes into account the effect of disorder near a quantum critical point [85]. The presence of disorder is considered to lead to the coexistence of a metallic paramagnetic phase and a granular magnetic phase. In the former, the magnetic moments are quenched by the Kondo interaction, giving rise to Fermi-liquid behavior, while the latter is dominated by the RKKY interaction giving rise to ordered regions.

There is an analogy with a lattice of magnetic atoms diluted with a concentration  $x$  of non-magnetic atoms. Long-range order is lost at a certain concentration  $x_{\text{cr}}$  when infinite clusters of magnetic moments can no longer be formed.

For small values of  $x$ , the RKKY interaction dominates and the system orders magnetically. With increasing chemical substitution, the quantum fluctuations grow due to the Kondo effect and the critical temperature, *e.g.*  $T_C$  for a ferromagnet, decreases until it vanishes at the critical value  $x_{\text{cr}}$ . For larger values of  $x$ , *i.e.* in the paramagnetic phase, only finite clusters of magnetic atoms can be found. Among these clusters, there are some rare ones that are large and strongly coupled, in which the spins behave coherently as a magnetic grain. In this phase, the thermodynamic functions show essential singularities with strong effects at low temperatures. The specific heat coefficient and the static susceptibility diverge as

$$c/T \propto T^{-1+\lambda} \quad (3.19)$$

$$\chi \propto T^{-1+\lambda} \quad (3.20)$$

with  $\lambda < 1$ . The Fermi liquid is recovered for  $\lambda = 1$ . In general, non-Fermi-liquid behavior can be observed over an extended region in the paramagnetic phase next to a quantum critical point.

## 3.4 Grüneisen parameters

It is found experimentally that intermetallic compounds with unstable  $4f$  or  $5f$  shells, like the heavy-fermion systems, show an anomalously large volume depen-

dence for variations in temperature, magnetic field, and pressure. The electronic properties of the heavy-fermion state are described by a certain characteristic temperature  $T^*$ . A measure of the volume dependence of this temperature can be determined by a phenomenological Grüneisen parameter, that represents the coupling between the relevant energy scale for the heavy fermions and the lattice. The origin of this coupling lies in the single-ion Kondo or Kondo-lattice effect and the presence of (paramagnetic) spin fluctuations.

For the volume dependence of the characteristic temperature  $T^*$  the Grüneisen parameter is defined as [86, 87]

$$\Gamma_T = -\frac{d \ln T^*}{d \ln V} \quad (3.21)$$

which can be written as

$$\Gamma_T = \frac{V \alpha}{\kappa c_V}. \quad (3.22)$$

Here  $\alpha = V^{-1}(\partial V/\partial T)$  is the linear volume thermal expansion coefficient,  $\kappa = -V^{-1}(\partial V/\partial P)$  the compressibility, and  $c_V$  the specific heat. Since several processes contribute to the measured  $\alpha(T)$  and  $c_V(T)$ , one experimentally measures the *effective* Grüneisen parameter  $\Gamma_{\text{eff}}(T)$ . If in a certain temperature range a certain energy scale is dominant,  $\Gamma_{\text{eff}}(T)$  will be equal to the Grüneisen parameter of this process. For example, at high temperatures the phonon contribution is the largest factor in the volume dependence and  $\Gamma_{\text{eff}}(T) \approx 2$  is found. As the temperature is lowered towards a magnetic transition temperature  $T_C$ , the magnetic fluctuations will determine the value of  $\Gamma_{\text{eff}}(T)$ . At the lowest temperatures, the physics is dominated by the heavy-fermion state, characterized by a spin-fluctuation temperature  $T_{\text{sf}}$  and therefore  $\Gamma_{\text{eff}}(T) = d \ln \gamma / d \ln V$ , since  $T_{\text{sf}} \propto N^{-1}(E_F) \propto \gamma^{-1}$ .

### 3.5 Thermodynamic Considerations

For a magnetic sample in an external magnetic field the thermodynamic quantities can be derived from the Gibbs free energy

$$dG = -SdT + VdP - MdB \quad (3.23)$$

where  $S$  is the entropy,  $T$  the temperature,  $V$  the volume,  $P$  the pressure,  $M$  the magnetization, and  $B$  the magnetic field. The equilibrium of the system is determined by the variables  $T$ ,  $P$ , and  $B$ . The first derivatives of the Gibbs free energy,  $S$ ,  $V$ , and  $M$ , are found by differentiating  $G$  with respect to  $T$ ,  $P$ , and  $B$ , respectively, while keeping the other variables constant.

At a phase transition, the Gibbs free energy is continuous, *i.e.*  $dG = 0$ . However, its first or second derivatives do not need to be continuous. When the first derivatives are discontinuous, one speaks of a first-order phase transition. The thermodynamical

properties at the phase-transition temperature  $T_C$  are related by [88]

$$\frac{\partial x_i}{\partial x_j} = -\frac{\Delta y_j}{\Delta y_i} \quad (3.24)$$

with  $\{x_1, x_2, x_3\} = \{T, P, B\}$  and  $\{y_1, y_2, y_3\} = \{-S, V, -M\}$ . Here  $\Delta y_i$  denotes the step in  $y_i$  at  $T_C$ , *i.e.* the difference between  $y_i(T \downarrow T_C)$  and  $y_i(T \uparrow T_C)$ . This equation is known as the Clausius-Clapeyron relation.

In many systems the first derivatives of  $G$  are continuous, but the second derivatives are not. Hence the name second-order phase transition. Since at  $T_C$  there are no steps in  $S$ ,  $V$ , and  $M$ , the above equation does not apply. By expanding  $dS$  in terms of  $T$  and  $P$  one obtains

$$dS = \left( \frac{\partial S}{\partial T} \right)_P dT + \left( \frac{\partial S}{\partial P} \right)_T dP. \quad (3.25)$$

Noting that the entropy just above and below  $T_C$  are equal ( $dS^+ = dS^-$ ), one obtains, together with the specific heat  $c_P = V_m T (\partial S / \partial T)$  and the Maxwell relation  $(\partial S / \partial P)_T = (\partial V / \partial T)_P$ , the Ehrenfest relation

$$\frac{dT_C}{dP} = \frac{\Delta \alpha V_m}{\Delta (c_P / T)}. \quad (3.26)$$

Here  $\alpha = V^{-1}(\partial V / \partial T)_P$  is the linear thermal expansion coefficient and  $V_m$  is the molar volume.

## 3.6 Ferromagnetic Superconductors

Since the discovery of superconductivity well within the ferromagnetic phase of  $\text{UGe}_2$  [1] and  $\text{URhGe}$  [2], numerous theoretical studies have tried to answer the question what the attractive forces are between the electrons leading to the formation of the Cooper pairs [89, 90, 91, 92, 93, 94, 95, 96, 97, 98, 99]. The general features of the proposed models are:

1. The superconducting pairing of the conduction electrons is mediated by spin fluctuations rather than by phonons, as is the case in conventional superconductors.
2. In the superconducting state the quasiparticles form Cooper pairs in which the spins are parallel ( $S = 1$ ) in contrast to conventional superconductors with opposite spin ( $S = 0$ ).
3. The ferromagnetism is itinerant and therefore carried by the conduction electrons. This arises from a splitting of the spin-up and spin-down band. A consequence is that the ferromagnetism and the superconductivity is carried by the same electrons.

With these assumptions, it was possible to show [93] that for the quasiparticles with a spin parallel to the ferromagnetic order a gap in the momentum distribution is present, leading to superconductivity, whereas for quasiparticles with antiparallel spins this gap is not present, leading to normal, non-superconducting behavior. Moreover, a comparison [94, 95] between the superconducting pairing by ferromagnetic spin fluctuations in the ferromagnetically ordered phase and the pairing in the paramagnetic phase, indicate that the superconducting transition temperatures in the ferromagnetically ordered phase are generally significantly higher than those found in the paramagnetic phase. This is because the magnetic fluctuations are stronger on the ferromagnetic side of the magnetic phase boundary, which substantially enhances the pairing interaction of the conduction electrons. The maximum transition temperatures are found just below the quantum critical point, in qualitative agreement with the temperature-pressure phase diagram of  $\text{UGe}_2$ .

Other studies [100, 101], however, have shown that spin-singlet superconductivity is still feasible under the constraint that conducting electrons involved in the superconductivity and localized electrons involved in the ferromagnetic order belong to different subsets of  $5f$  electrons. The pairing mechanism is then based on the interaction of electron spins via localized magnetic moments. A  $^{73}\text{Ge}$ -NQR study under pressure [102, 103] clearly showed the existence of unconventional superconductivity with a line node gap, which would normally exclude the possibility of  $s$ -wave (spin-singlet) superconductivity.

---

# CHAPTER 4

---

## UGe<sub>2</sub>

### 4.1 Introduction

**C**OEEXISTENCE OF SUPERCONDUCTIVITY AND FERROMAGNETISM, at low temperatures, was found in the binary compound UGe<sub>2</sub> [1]. It crystallizes in the orthorhombic ZrGa<sub>2</sub>-type structure (space group *Cmmm*) [104, 105]. The unit cell, with dimensions  $a = 4.036$  Å,  $b = 14.928$  Å, and  $c = 4.116$  Å, contains four formula units. The structure is shown in Fig. 4.1. The U atoms all occupy the  $4j$  positions  $(0, y, \frac{1}{2})$ , whereas the Ge atoms are at the  $4i$  positions  $(0, y, 0)$ , the  $2a$  positions  $(0, 0, 0)$ , and at the  $2c$  positions  $(\frac{1}{2}, 0, \frac{1}{2})$ . The U atoms are arranged in zig-zag chains of nearest neighbors in the  $a$  direction. The nearest neighbor distance  $d_{U-U}$  is equal to  $d_{U-U} \approx 3.82$  Å at zero pressure, but is possibly reduced to about 3.5 Å at 1.3 GPa, due to a slight flattening of the chains [106]. This would compare well with the Hill limit of 3.5 Å. See Ref. [49] and Sec. 3.1.

In UGe<sub>2</sub> ferromagnetic order at ambient pressure is found below the Curie temperature  $T_C = 52$  K. The magnetic moment is directed along the  $a$  axis, with a saturation value of  $1.4 \mu_B/\text{U}$  at ambient pressure [107]. Magnetic measurements indicate a very strong magnetocrystalline anisotropy [108].  $T_C$  is suppressed for increasing pressures and finally vanishes at a pressure of  $P_C = 1.5 - 1.6$  GPa. Within the ferromagnetic phase, a second transition occurs. At ambient pressure, this transition takes place at  $T_X \approx 30$  K, but is not pronounced. As the pressure is enhanced,  $T_X$  goes to 0 K, but the transition itself gets better observable. At a pressure of  $P \approx 1.2$  GPa,  $T_X = 0$ . Below  $T_X$  the magnetic moment is enhanced and therefore the temperature region between  $T_C$  and  $T_X$  was named the weakly polarized phase, whereas the lower temperature region  $T < T_X$  was called the strongly polarized phase [109]. The origin of this transition is still not understood. Superconductivity is found only in a limited pressure range between 1.0 and 1.5 GPa with a maximum

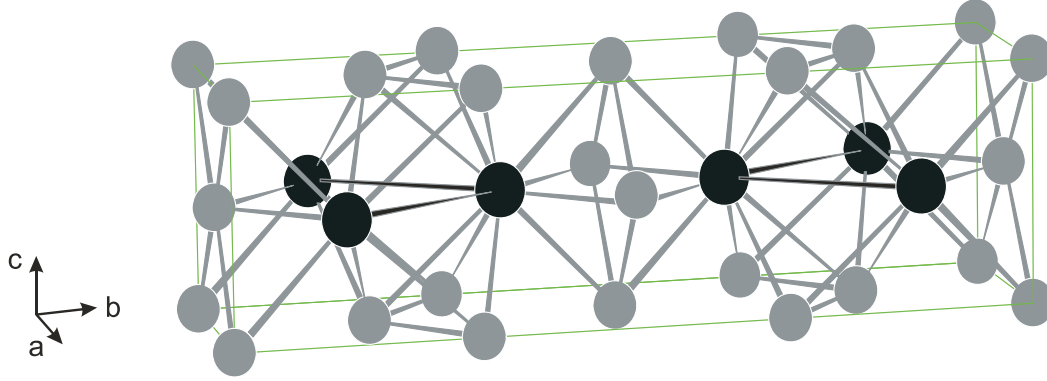


**Figure 4.1:** The orthorhombic crystallographic structure of UGe<sub>2</sub>. The uranium atoms are indicated in black and germanium atoms in gray. The figure shows the unit cell of UGe<sub>2</sub> containing four formula units.

transition temperature of  $T_s \approx 0.7$  K. In this pressure range, the magnetic moment is still appreciable ( $1 \mu_B/U$ ).

The pressure dependence of the ferromagnetic transition temperature  $T_C$ , the transition temperature within the ferromagnetic state  $T_X$ , and the superconducting transition temperature  $T_s$ , is shown in Fig. 4.2. The data points were obtained from measurements with various techniques [1, 110, 111, 112, 113, 114].

In a very small pressure region below  $P_X$ , the pressure at which  $T_X = 0$ , the transition at  $T_X$  is reported to be first order [102], in contrast to second order at lower pressure. However, Tateiwa *et al.* [115] found on the basis of specific heat measurements that the transition is only weakly first order or even second order. The PM-WP phase transition at  $T_C$  unambiguously changes from second to first order around 1.2 GPa [114, 116].

In this Chapter two techniques are used, namely three-dimensional neutron depolarization and muon spin relaxation ( $\mu$ SR), to study the ferromagnetic order in UGe<sub>2</sub>. It is generally accepted that antiferromagnetic order and superconductivity can coexist, since the superconducting coherence length  $\xi_{sc}$  is much larger than the periodicity of the static magnetic order. In contrast to antiferromagnets, for ferromagnets the reverse is the case.  $\xi_{sc}$  is much smaller than the periodicity of the magnetic order (*i.e.* the domain size). However, based on jumps in the magnetization at low temperature and at regular intervals of applied magnetic field, it was suggested that the ferromagnetic domain size in UGe<sub>2</sub> is so small, that it is even smaller than  $\xi_{sc}$  [117, 118]. This would enable the coexistence of ferromagnetism and superconductivity. In this thesis, however, it is shown with the three-dimensional neutron depolarization technique that the ferromagnetic domain size is much larger than  $\xi_{sc}$ , in contrast to Refs. [117, 118].

When superconductivity sets in at low temperatures and high pressures, conduction electrons condense into Cooper pairs. It is of utmost importance to investigate the magnetic properties of UGe<sub>2</sub>, and specifically the conduction electrons, in detail.



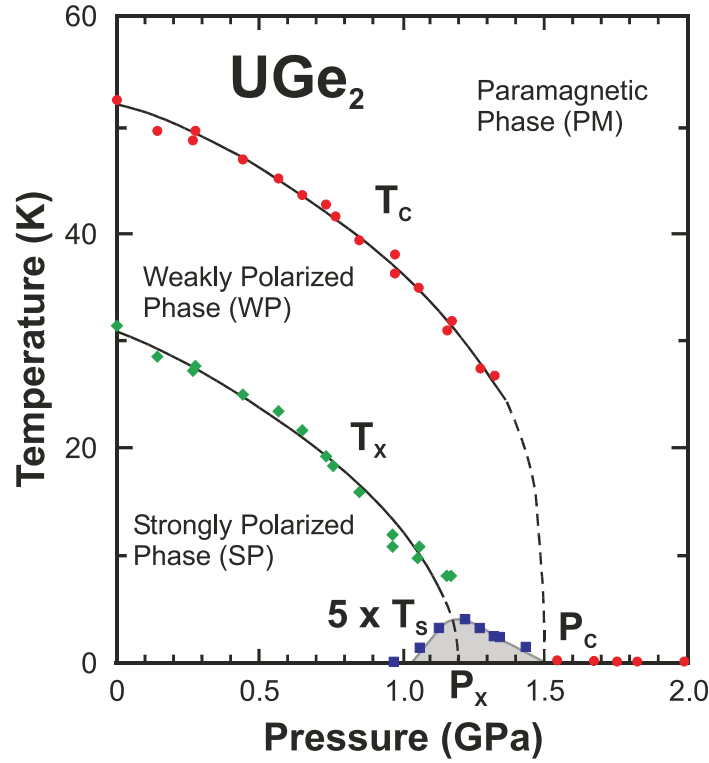


**Figure 4.2:** The temperature  $T$  versus pressure  $P$  magnetic phase diagram of  $\text{UGe}_2$ . Below the Curie temperature  $T_c$ , there are two ferromagnetic phases, a weakly polarized phase (WP), and a strongly polarized phase (SP). The transition temperature between these two phases is denoted  $T_x$ . Above the critical pressure  $P_c$ , the system remains paramagnetic (PM) down to the lowest temperature. Around 1.2 GPa the PM-WP phase transitions changes from second order (low  $P$ ) to first order (high  $P$ ). The change in order for the WP-SP transition is still under discussion (see main text). For clarity the superconducting region between 1.0 and 1.6 GPa (shaded area) is exaggerated. The lines are guides to the eye. Figure taken from Ref. [102].

Muons are very sensitive magnetic probes and are sensitive to a time frame which is complementary to neutron techniques. The  $\mu\text{SR}$  technique thus has the potentiality to yield information on the question whether the magnetism found in  $\text{UGe}_2$  is of a localized or an itinerant nature.

## 4.2 Three-Dimensional Neutron Depolarization<sup>\*</sup>

### 4.2.1 Introduction

Until the discovery of coexistence of superconductivity and ferromagnetism in  $\text{UGe}_2$  [1], only superconducting compounds exhibiting *antiferromagnetic* order had been

<sup>\*</sup>Parts of this Section have been published in Physical Review B **71** (2005) 174417.

known such as DyMo<sub>6</sub>S<sub>8</sub>, GdMo<sub>6</sub>S<sub>8</sub>, and TbMo<sub>6</sub>S<sub>8</sub> [119, 120, 121]. Later on, coexistence of antiferromagnetism and superconductivity was also found in heavy fermion compounds, of which CeIn<sub>3</sub>, CePd<sub>2</sub>Si<sub>2</sub>, and UPd<sub>2</sub>Al<sub>3</sub> [122, 123, 124] form several examples. In these cases, superconductivity and antiferromagnetism appear simultaneously because the Cooper pairs are insensitive to the internal fields arising from the antiferromagnetic ordering, since the superconducting coherence length  $\xi_{sc}$  is much larger than the periodicity of the static antiferromagnetic-ordered structure. However, in a ferromagnetic structure it is expected that the internal fields do not cancel out on the scale of  $\xi_{sc}$  and therefore influence the Cooper pairs. That ferromagnetic order excludes superconductivity is nicely demonstrated in ErRh<sub>4</sub>B<sub>4</sub> [5, 6] and HoMo<sub>6</sub>S<sub>8</sub> [7], where standard BCS singlet-type superconductivity is suppressed when ferromagnetic order sets in. Alternatively, if one would consider unconventional spin-triplet superconductivity mediated by ferromagnetic spin fluctuations, the pairing is relatively insensitive to a local magnetic field and can, therefore, coexist with ferromagnetic order. When the ferromagnetic domain size  $d$  is much smaller than the superconducting coherence length  $\xi_{sc}$ , one effectively also has no internal magnetic field acting on the Cooper pairs.

The superconducting coherence length  $\xi_{sc}$  for UGe<sub>2</sub> is estimated [1, 125] to be 130 – 200 Å. Interestingly, Nishioka *et al.* [117, 118] predicted the domain size  $d$  to be of the order of 40 Å. The model leading to this prediction will be discussed briefly. The starting point was the observation of jumps in the (macroscopic) magnetization at regular intervals of applied magnetic field  $H$  (parallel to the easy axis **a**) and temperatures below 1 K, instead of a continuous  $M - H$  curve. The discrete nature of the magnetization occurring only at low temperatures, led the authors to the idea of a quantum-mechanical effect.

The anisotropy and Zeeman energies for a single domain can be written as [126]

$$E = (K_1 + K_2 \sin^2 \phi) \sin^2 \theta - M_0 H (1 - \cos \theta), \quad (4.1)$$

where  $K_1$  and  $K_2$  are anisotropy constants per unit volume,  $\theta$  and  $\phi$  denote angles for the direction of **M** and  $M_0$  indicates the magnitude of **M**. Equation 4.1 is illustrated in Fig. 4.3 for different values of  $H$ . The potential barrier has a height  $U$ . The corresponding Hamiltonian per domain with volume  $V$  is [126]

$$\mathcal{H} = -d_1 J_{\parallel}^2 + d_2 J_{\perp}^2 + g_{\text{eff}} \mu_B J_{\parallel} H. \quad (4.2)$$

Here  $g_{\text{eff}}$  is an effective  $g$  factor and  $J_{\parallel}$  ( $J_{\perp}$ ) is the component of the total angular momentum of the domain parallel (perpendicular) to the **a** axis. Although the  $d_2$  term plays a crucial role in generating quantum transitions between two energy minima, it can be neglected when calculating the energy eigenvalues because the anisotropy within the plane perpendicular to the **a** axis is very small. The energy levels are displayed in Fig. 4.3. Furthermore,  $K_1 = d_1 J(J+1)/V$  and  $\mathbf{J} = N\mathbf{j}$ , where  $N$  is the number of spins contained in the domain with volume  $V$  and  $\mathbf{j}$  is the single ion total angular momentum.  $K_1$  can be approximated by  $K_1 \approx d_1 J^2/V = d_1 (N^2 j^2)/(Nv) = d_1 N j^2/v$  where  $v = 60 \text{ Å}^3/\text{U}$  is the volume per U atom.

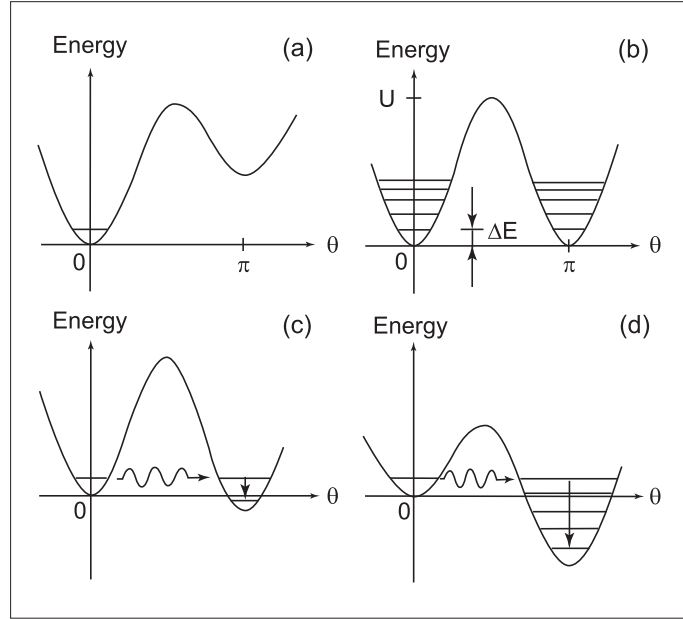


**Figure 4.3:** Illustration of the model describing field-tuned resonant tunneling between quantum spin states. The horizontal axis is  $\theta$ , the angle of the magnetization from the easy axis. (a) At a magnetic field high enough to obtain magnetic saturation, every domain is assumed to be in the ground state of the left-hand minimum at  $\theta = 0$  (parallel to the field). (b) When  $H = 0$ , the two energy minima at  $\theta = 0$  and  $\pi$  are degenerate. (c) As the magnetic field is increased, in direction opposite to (a), a tunneling of several magnetic domains from the metastable state in the left to the first excited state in the right occurs at a well-defined value of magnetic field. (d) After  $\sim 5$  times, most of the domains have tunneled from the left to the right and thus there will be no more jump in the magnetization. Figure taken from Nishioka *et al.*, Ref. [117].

The energy level of the ground state on the left coincides with the  $n$ th excited level on the right when the condition  $H = n(d_1/g_{\text{eff}}\mu_B)$  is satisfied. When at these particular fields a resonance occurs and the tunneling probability is, as a result, strongly enhanced, sharp and large jumps will be observed in the magnetization at equidistant values of  $H$ . With an estimate for the anisotropy constant  $K_1 = 100 \text{ T} \times 1.4 \mu_B/60 \text{ \AA}^3$  (a field in excess of 100 T is needed to align the magnetic moments of  $1.4 \mu_B$  [108, 117]), with the  $U 5f^2$  configuration ( $g_{\text{eff}} = 4/5$  and  $j = 4$ ), and with steps occurring about every 0.03 T (depending on pressure), it is found that  $N \approx 1000$ . This leads to an estimated ferromagnetic domain size  $d$  of the order of 40  $\text{\AA}$ . The derived values of  $U \approx 10^4 \text{ K}$  and  $\Delta E \approx 10 \text{ K}$  seem to be consistent with the starting point of the model: discrete quantum effects only observed at low temperatures, where  $\Delta E \gg k_B T$ . The authors indicate that for conventional domain sizes of the order of  $10^4 \text{ \AA}$ , the tunneling probability would be too small for macroscopic quantum resonances to occur, since the energy barrier  $U$  is proportional to  $N^2$ :  $U \simeq d_1 J^2 = d_1 j^2 N^2$ .

Since  $d$  would be several times smaller than  $\xi_{\text{sc}}$ , it was proposed that the ferromagnetism can be canceled out on the scale of the coherence length of the Cooper pairs. A boundary such as a ferromagnetic domain wall may in general distort the Cooper pair wave function. With a small domain size, one has a relatively large number of domain walls, resulting in spatially inhomogeneous superconductivity.

In this Section, three-dimensional neutron depolarization (3DND) measurements are reported. They are performed on single-crystalline UGe<sub>2</sub> at ambient pressure between 2 and 80 K. The principal aim was to determine the ferromagnetic domain size  $d$  in UGe<sub>2</sub> and compare the value to the ferromagnetic domain size of 40 Å estimated by Nishioka *et al.* [117] as explained above. Since the neutron is a very sensitive probe to local magnetic fields, neutron depolarization is an excellent technique to measure the average domain size and the domain-wall width.

### 4.2.2 Experimental

The measurements were performed on the poly axis neutron depolarization analyzer (PANDA) at the Interfaculty Reactor Institute (IRI) of the Delft University of Technology. A description of the instrument and the 3DND technique can be found in Sec. 2.3. The neutron wave length used was 2.03 Å which corresponds to a velocity of 1949 m/s.

The neutron depolarization measurements on UGe<sub>2</sub> were performed on a single-crystalline sample with dimensions  $4.0 \times 0.440 \times 3.0$  mm<sup>3</sup> along the  $a$ ,  $b$ , and  $c$  axes respectively. The  $b$  axis was oriented along the transmitted neutron beam ( $x$ ) with a transmission length  $L$  and the easy axis for magnetization  $a$  along the vertical axis ( $z$ ) within the plate of the sample. The crystal has been grown from a polycrystalline ingot using a Czochralski tri-arc technique. No subsequent heat treatment was given to the crystal. The illuminated area was a rectangle with dimensions  $y \times z = 1 \times 2$  mm<sup>2</sup> centered at the middle of the sample.

The measurements in zero field were performed during a temperature sweep from 2 K up to 80 K and down to 2 K with a low sweep rate of 10 K/hr. The measurements in nonzero field (4 and 8 mT) were done during a similar temperature sweep with a sweep rate of 25 K/hr. The sample was first zero-field cooled, whereafter the field was switched on at the start of the measurements. The subsequent measurements were performed during heating and cooling in a constant field.

### 4.2.3 Three-dimensional neutron depolarization

The neutron depolarization (ND) technique is based on the loss of polarization of a polarized neutron beam after transmission through a (ferro)magnetic sample. Each neutron undergoes only a series of consecutive rotations on its passage through the (ferro)magnetic domains in the sample. It is important to note that the beam cross section covers a huge number of domains, which results in an averaging over the magnetic structure of the whole illuminated sample volume. This averaging causes a

loss of polarization, which is related to the mean domain size and the mean direction cosines of the domains. The rotation of the polarization during transmission probes the average magnetization.

In a ND experiment, a  $3 \times 3$  depolarization matrix  $D$  expresses the relation between the polarization vector  $\mathbf{P}^0$  before and  $\mathbf{P}^1$  after transmission through the sample according to [29, 30, 31]

$$\mathbf{P}^1 = D \mathbf{P}^0. \quad (4.3)$$

A monochromator M selects a fixed neutron wave length of  $2.03 \text{ \AA}$  which corresponds to a velocity of  $1949 \text{ m/s}$ . The polarization of the monochromatic neutron beam is created and analyzed by magnetic multilayer polarization mirrors. In order to obtain the complete matrix  $D$ , one polarization rotator is placed before the sample and another one right after the sample. Each rotator provides the possibility to turn the polarization vector parallel or antiparallel to the coordinate axes  $x$ ,  $y$ , and  $z$ . The resultant neutron intensity is finally detected by a  $^3\text{He}$  detector. The polarization rotators enable the measurement of any matrix element  $D_{ij}$  with the aid of the intensity of the unpolarized beam  $I_S$

$$I_S = \frac{I_{ij} + I_{-i,j}}{2}, \quad (4.4)$$

where  $I_{ij}$  is the intensity for  $\mathbf{P}^0$  along  $i$  and  $\mathbf{P}^1$  along  $j$ . The matrix element  $D_{ij}$  is then calculated according to

$$D_{ij} = \frac{1}{P_0} \frac{I_S - I_{ij}}{I_S}, \quad (4.5)$$

where  $P_0$  is the degree of polarization in the absence of a sample. In the present case,  $P_0 = 0.965$ , which is experimentally determined.

Now the correlation matrix  $\alpha_{ij}$  is introduced as [29, 30, 31]

$$\alpha_{ij} = \left\langle \int_0^L dx' \Delta B_i(x, y, z) \Delta B_j(x', y, z) \right\rangle, \quad (4.6)$$

where  $\Delta \mathbf{B}(\mathbf{r}) = \mathbf{B}(\mathbf{r}) - \langle \mathbf{B} \rangle$  is the variation of the magnetic induction and angular brackets denote the spatial average over the sample volume. The integral is taken over the neutron transmission length  $L$  through the sample. Assuming  $\alpha_{ij} \equiv 0$  for  $i \neq j$ , the correlation function  $\xi$  is defined as

$$\xi = \sum_i \alpha_{ii}. \quad (4.7)$$

With these quantities it can be shown that if there is no macroscopic magnetization ( $\langle \mathbf{B} \rangle = 0$ ) the depolarization matrix is diagonal and under the assumption that  $\alpha_{ij} \equiv 0$  for  $i \neq j$  given by [29, 30, 31]

$$D_{ii} = e^{-\frac{\gamma^2}{v^2} L \{\xi - \alpha_{ii}\}} \quad i = x, y, z, \quad (4.8)$$

where  $\gamma = 1.83 \times 10^8 \text{ s}^{-1}\text{T}^{-1}$  is the gyromagnetic ratio of the neutron and  $v = 1949 \text{ m/s}$  the neutron velocity.

The phenomenon that for magnetically isotropic media the depolarization depends on the orientation of the polarization vector with respect to the propagation direction of the neutron beam, is known as intrinsic anisotropy. The origin of this intrinsic anisotropy is that the line integral of the demagnetization fields around magnetized volumes in the sample along the neutron trajectory is not isotropic due to  $\nabla \cdot \mathbf{B} = 0$ . In the following it will be assumed that the demagnetization fields are negligible for needle-shaped magnetic domains.

When the sample shows a net magnetization, the polarization vector will rotate in a plane perpendicular to the magnetization direction. If the sample shape gives rise to macroscopic stray fields, the rotation angle  $\phi$  is related to the net magnetization  $\langle M \rangle$  by

$$\phi = \eta \frac{\gamma}{v} L \mu_0 \langle M \rangle = \eta \frac{\gamma}{v} L \mu_0 M_S \langle m \rangle, \quad (4.9)$$

where  $\eta$  is a geometrical factor given in Eq. 4.51 in the Appendix for a rectangular-shaped sample and  $\langle m \rangle = M/M_S$  the reduced sample magnetization in terms of the saturation magnetization  $M_S = M_S(T)$ . If the mean magnetic induction  $\langle \mathbf{B} \rangle$  in the sample is oriented along the  $z$  axis, the depolarization matrix is, for  $\phi \gg (\gamma/v)^2 |\alpha_{xx} - \alpha_{yy}| L/2$  (the weak damping limit), given by [29, 30, 31]

$$\begin{aligned} D_{xx} &= D_{yy} = e^{-\frac{\gamma^2}{v^2} L \left\{ \xi - \frac{\alpha_{xx} + \alpha_{yy}}{2} \right\}} \cos \phi, \\ D_{xy} &= -D_{yx} = e^{-\frac{\gamma^2}{v^2} L \left\{ \xi - \frac{\alpha_{xx} + \alpha_{yy}}{2} \right\}} \sin \phi, \\ D_{zz} &= e^{-\frac{\gamma^2}{v^2} L \left\{ \xi - \alpha_{zz} \right\}}, \\ D_{xz} &= D_{zx} = D_{zy} = D_{yz} = 0. \end{aligned} \quad (4.10)$$

With the net magnetization along the  $z$  axis, the rotation angle  $\phi$  of the beam polarization is obtained from the measurements by

$$\phi = \arctan \left( \frac{D_{xy} - D_{yx}}{D_{xx} + D_{yy}} \right) \quad (4.11)$$

and  $\xi$  is calculated with

$$\xi = -v^2 \ln \{ \det D \} / 2\gamma^2 L. \quad (4.12)$$

As mentioned earlier, ND provides information about the mean-square direction cosines of the magnetic induction vector in the (ferro)magnetic domains. These are directly given by the quantities  $\gamma_i = \alpha_{ii}/\xi$  ( $i = x, y, z$ ), and can be estimated from the measurements by

$$\gamma_i = 1 - 2 \ln \{ D_{ii} \} / \ln \{ \det D \}. \quad (4.13)$$

This equation is only valid for those directions that show no net rotation of the beam polarization.

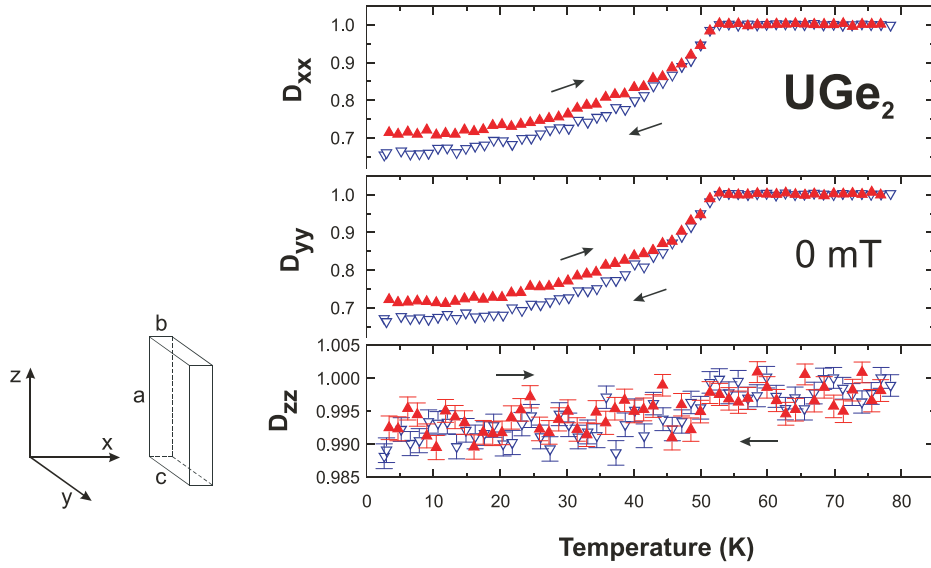


**Figure 4.4:** The diagonal elements of the measured depolarization matrix  $D$  for increasing and decreasing temperature for  $\text{UGe}_2$ . All other elements of the depolarization matrix are zero within the experimental uncertainty. For  $D_{xx}$  and  $D_{yy}$  the experimental uncertainty is within the symbol size.

## 4.2.4 Results

### Measurements in zero field

In Fig. 4.4 the diagonal elements of the depolarization matrix are shown for  $\text{UGe}_2$  measured in zero magnetic field. All off-diagonal elements are zero within the experimental uncertainty in the studied temperature range. The measurements for increasing temperature are qualitatively the same as those for decreasing temperature, as expected.

The Curie temperature of  $T_C = 52$  K is clearly indicated in Fig. 4.4 by the kink in  $D_{xx}$  and  $D_{yy}$ . Note that  $D_{xx} \equiv D_{yy}$  below  $T_C$  indicates that there is no intrinsic anisotropy and hence that the magnetic domains produce virtually no stray fields. Furthermore,  $D_{zz} \approx 1$  indicates that all moments are oriented along the  $a$  axis.

### Measurements in small field

In Fig. 4.5 the determinant of the depolarization matrix  $\det D$  and the rotation angle  $\phi$  are shown after passage through the sample for measurements in fields of, respectively, 4 and 8 mT (after zero-field cooling). The data of  $\phi$  have been corrected by subtracting the mean value above  $T_C$ , since this rotation is merely due to the applied field.

At low temperatures the magnetic fields (applied after zero-field cooling) are too small to fully align the magnetic domains. Therefore, the measurements for increasing and decreasing temperature do not yield the same results. Whereas for

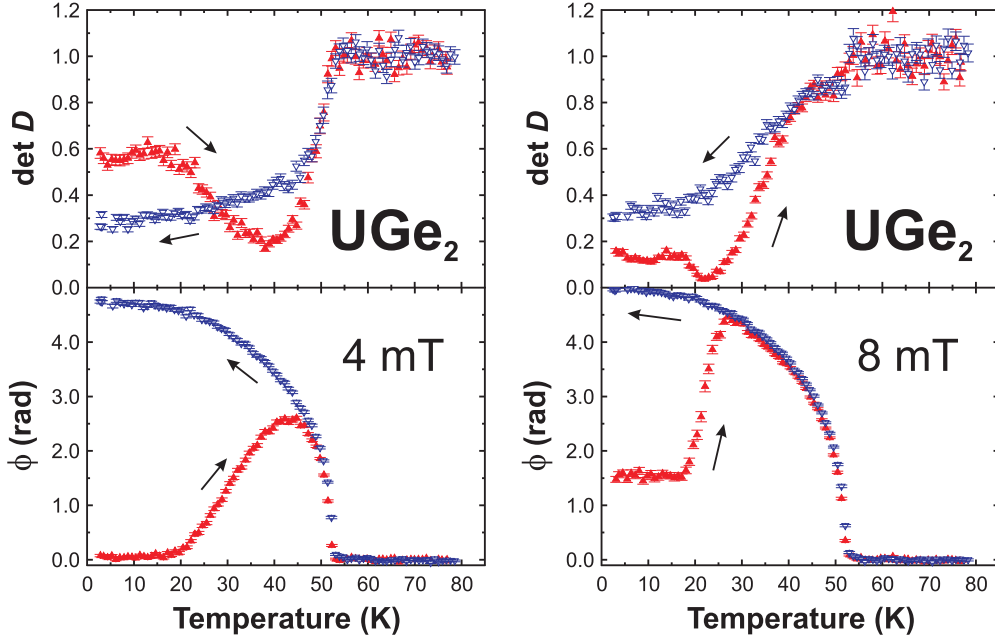


**Figure 4.5:** The determinant of the measured depolarization matrix  $\det D$  and the rotation angle  $\phi$  of the beam polarization after passage through the sample of UGe<sub>2</sub> in 4 and 8 mT for increasing and decreasing temperature.

increasing temperature the rotation shows an increase, for decreasing temperature the data represent a monotonous magnetization curve, as expected for a field-cooled ferromagnet. Close to  $T_C$  there is no difference between field cooling or field warming.

Figure 4.5 shows that, below  $T_X$ , the depolarization for 4 mT is at the same level as for 0 mT. Above  $T_X$ , however, extra depolarization occurs. This means the system gets more inhomogeneous, *i.e.*, the domains grow and the magnetic correlation length increases ( $\xi$  in Eq. 4.10), leading to extra depolarization. Close to  $T_C$  the depolarization disappears because the magnetic moment decreases sharply. For decreasing temperature the determinant has the same shape as in the case of 0 mT. At 8 mT the determinant is already reduced below  $T_X$ , indicating larger domains.

Again, the Curie temperature of  $T_C = 52$  K is clearly indicated by the kink in  $\det D$  and  $\phi$ . Also note the abrupt increase in  $\phi$  around  $T_X \approx 20$  K. Evidently the system passes, with increasing temperature, from a strongly polarized phase to a weakly polarized phase, as reported earlier [109].

## 4.2.5 Discussion

### Model

The measurements confirm that UGe<sub>2</sub> is a highly anisotropic uniaxial ferromagnet. Furthermore, the magnetic domains are long compared to their (average) width,



because  $D_{xx} \equiv D_{yy}$  indicates relatively weak stray fields produced by the magnetic domains. This allows the assumption  $\mathbf{B}(\mathbf{r}) = \mu_0 \mathbf{M}(\mathbf{r})$  inside the domains. In order to analyze the data a model is considered where the sample is split into  $N$  long needles along the  $a$  axis with a fixed width  $\Delta$  and a magnetic induction  $B_S = \mu_0 M_S$  along the  $a$  axis. With  $N_\uparrow$  ( $N_\downarrow$ ) the number of domains with a magnetic induction pointing upward (downward), the reduced macroscopic magnetization of the sample, pointing along the  $z$  direction, can be defined as

$$\langle m_z \rangle = \frac{N_\uparrow - N_\downarrow}{N_\uparrow + N_\downarrow} = \frac{\langle B_z \rangle}{B_S}. \quad (4.14)$$

Each needle will have magnetic induction  $\uparrow$  or  $\downarrow$  with probability  $p_\uparrow = (1 + \langle m_z \rangle)/2$  and  $p_\downarrow = (1 - \langle m_z \rangle)/2$ , respectively. The polarized neutron beam traversing the sample will therefore see a binomial distribution of  $\uparrow$  and  $\downarrow$ , which results in a depolarization matrix  $D$  with elements

$$\begin{aligned} D_{xx} = D_{yy} &= e^{-\frac{\gamma^2}{v^2} \frac{B_S^2 L}{2} \Delta (1 - \langle m_z \rangle^2)} \cos \left( \frac{\gamma B_S L}{v} \langle m_z \rangle \right), \\ D_{xy} = -D_{yx} &= e^{-\frac{\gamma^2}{v^2} \frac{B_S^2 L}{2} \Delta (1 - \langle m_z \rangle^2)} \sin \left( \frac{\gamma B_S L}{v} \langle m_z \rangle \right), \\ D_{zz} &= 1, \end{aligned} \quad (4.15)$$

and all other elements equal to 0. (Note that, since the macroscopic stray fields have not been taken into account, the angle  $\phi = \gamma B_S L \langle m_z \rangle / v$  should be corrected by the factor of  $\eta$  (Eq. 4.9 and Eq. 4.51 in the Appendix) before calculating  $\langle m_z \rangle$  in Eq. 4.15.)

Within this binomial distribution model it is easy to show that for the case  $\langle m_z \rangle = 0$  the average ferromagnetic domain size  $d$  is equal to  $2\Delta$ . Given a domain wall (*i.e.*, two adjacent needles with an opposite magnetic induction), the probability of forming a domain of  $n$  needles is  $(\frac{1}{2})^n$  and the average is calculated by  $\sum_{n=1}^{\infty} n (\frac{1}{2})^n = 2$ . When a field is applied, one has to distinguish between a domain (with size  $d_\uparrow$ ) in which the magnetic induction is parallel to the field and a domain (with size  $d_\downarrow$ ) with opposite induction. The probability of forming a domain of size  $n$  is  $p_\uparrow^{n-1} p_\downarrow = p_\uparrow^{n-1} (1 - p_\uparrow)$ , which leads to  $d_\uparrow / \Delta = 1 / (1 - p_\uparrow) = 2 / (1 - \langle m_z \rangle)$ . Similarly,  $d_\downarrow / \Delta = 2 / (1 + \langle m_z \rangle)$ .

In order to estimate the domain-wall thickness  $\delta$  it is assumed that  $m_z$  changes sinusoidally from  $+1$  to  $-1$  over a distance  $\delta$  in the form of a Bloch wall. The consequence is that  $D_{zz}$  is slightly less than 1 in the ordered state. For such a domain wall it is straightforward to show that the domain-wall thickness  $\delta$  can be estimated by the mean square direction cosine along  $z$

$$\gamma_z = \langle m_z^2 \rangle = 1 - \frac{1}{2} \left( \frac{\delta}{\Delta} \right), \quad (4.16)$$

which can be determined experimentally by Eq. 4.13.

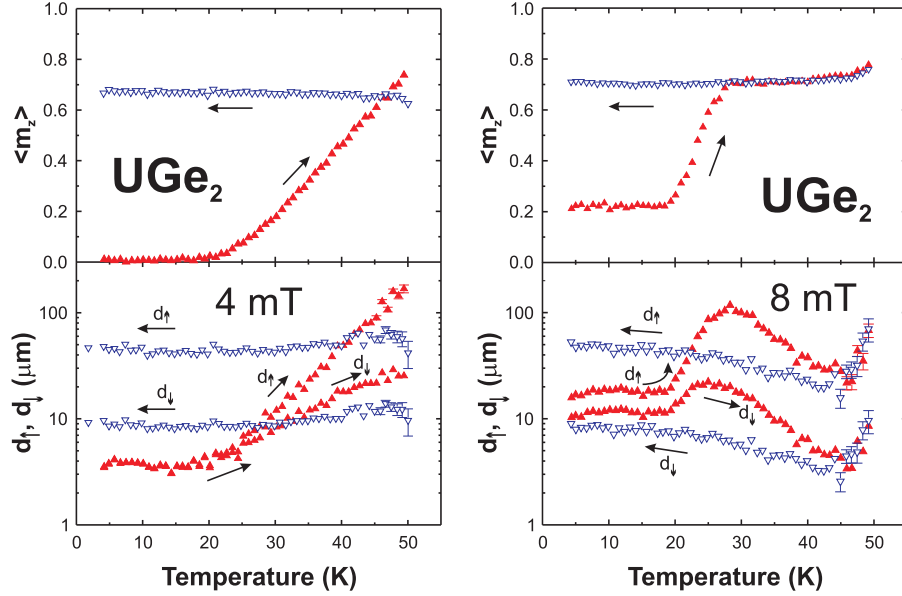


**Figure 4.6:** Calculated values of the reduced macroscopic magnetization  $\langle m_z \rangle$  and the average ferromagnetic domain sizes with magnetic induction parallel ( $d_{\uparrow}$ ) or antiparallel ( $d_{\downarrow}$ ) to the applied magnetic field of 4 and 8 mT in UGe<sub>2</sub> for increasing and decreasing temperature, respectively.

For the values of  $B_S$  needed in Eq. 4.15, the experimental magnetic moment of Ref. [114] is used, which is converted to magnetic induction, remembering there are four formula units per unit cell. For the value of  $\eta$  in Eq. 4.9,  $\eta = 0.6$  is used.

From Fig. 4.4 it is clear that the data for increasing and decreasing temperature give slightly different results for the ferromagnetic domain size  $d$  in zero magnetic field. The values found for  $d = 2\Delta$  are  $5.1(2) \mu\text{m}$  when cooling down slowly and  $4.4(1) \mu\text{m}$  when heating up after fast cooling. Both values are independent of temperature. These values indicate the domain size perpendicular to the  $a$  axis (along the  $b$  axis). Along the  $a$  axis it is assumed that the domain size is much larger.

The magnetic domain-wall thickness  $\delta$  divided by the magnetic domain size  $d = 2\Delta$  is calculated with Eq. 4.16 from the experimental data in Fig. 4.4 and amounts to  $\delta/d = 0.047(23)$ , independent of temperature. This gives  $\delta = 0.22 \mu\text{m}$ . The size of the domain-wall thickness is thus found to be only a minor fraction of the domain size.

Analysis of the data in a small magnetic field (Fig. 4.5) with Eq. 4.15 gives the results shown in Fig. 4.6 and Table 4.1. For 4 mT and increasing temperature (after zero field cooling), the reduced magnetization  $\langle m_z \rangle$  remains equal to 0 up to  $T_X \approx 20$  K. As a consequence  $d_{\downarrow}$  is equal to  $d_{\uparrow}$  and of the same order of the zero-field values. Above  $T_X$ , however, the system gets magnetically soft and  $\langle m_z \rangle$  starts to increase linearly toward 0.7. Domain walls are expelled above  $T_X$ , since  $d_{\uparrow}$  increases much faster than  $d_{\downarrow}$ . (Note the logarithmic vertical scale.) Although  $d_{\uparrow}$  gets of the order of  $100 \mu\text{m}$ ,  $d_{\downarrow}$  only reaches  $25 \mu\text{m}$ . When the domains grow

**Table 4.1:** Ferromagnetic domain sizes in UGe<sub>2</sub> for increasing temperature after zero-field cooling (ZFC) and decreasing temperature in field (FC). The sizes of the domains with magnetization parallel to the applied magnetic field is denoted by  $d_{\uparrow}$  and the domains with antiparallel magnetization by  $d_{\downarrow}$ . Below  $T_X$  the domain sizes are temperature independent. Above  $T_X$  the domains grow. The values shown are at a few Kelvin below  $T_C$ .

$\mu_0 H$ (mT)	Temperature incr./decr.	$d_{\uparrow}$ ( $\mu\text{m}$ ) $T < T_X$	$d_{\downarrow}$ ( $\mu\text{m}$ ) $T < T_X$	$d_{\uparrow}$ ( $\mu\text{m}$ ) $T \approx T_C$	$d_{\downarrow}$ ( $\mu\text{m}$ ) $T \approx T_C$
0	ZFC, incr.	4.4(1)	4.4(1)	4.4(1)	4.4(1)
0	FC, decr.	5.1(2)	5.1(2)	5.1(2)	5.1(2)
4	ZFC, incr.	3.9(1)	3.8(1)	100(20)	25(5)
4	FC, decr.	46.4(8)	9.5(2)	55(10)	13(2)
8	ZFC, incr.	17.9(2)	11.4(1)	85(20)	13(2)
8	FC, decr.	45(5)	8.2(1)	55(10)	15(5)

in width, at a certain moment it is no longer allowed to assume  $\mathbf{B}(\mathbf{r}) = \mu_0 \mathbf{M}(\mathbf{r})$  because stray fields produced by the domains have to be taken into account. The model, therefore, is no longer appropriate close to  $T_C$ .

For field cooling in 4 mT, the system has  $\langle m_z \rangle = 0.668(1)$  for the whole temperature range below  $T_C$ . The values of the domain size are shown in table 4.1.

When after zero-field cooling a field of 8 mT is turned on, the sample does get a macroscopic magnetization, in contrast to the case of 4 mT. Up to  $T_X \approx 20$  K the reduced magnetization  $\langle m_z \rangle = 0.221(2)$  is independent of temperature. Then  $\langle m_z \rangle$  starts to increase up to 0.718(3) around 30 K and is constant afterwards up to  $T_C$ . When cooling down in 8 mT,  $\langle m_z \rangle = 0.708(1)$  over the whole temperature range below  $T_C$ .

For field warming after zero-field cooling, the calculation of the domain sizes yields unexpected temperature dependencies of the domain sizes above  $T_X$ . As can be seen in Fig. 4.6, according to the model the domain sizes grow above  $T_X$  to decrease in size again at higher temperature. Clearly there is another source of depolarization, not accounted for by the model. Since the field is strong enough to overcome the pinning energy (at least partly) of the magnetic domains to crystals defects, additional depolarization arises from an inhomogeneous magnetic domain structure.

If the domain width becomes relatively large compared to its length, stray fields become important and the simple model assuming  $\mathbf{B}(\mathbf{r}) = \mu_0 \mathbf{M}(\mathbf{r})$  is no longer valid. Calculation of the mean-square direction cosine  $\gamma_z$  along the  $z$  direction with Eq. 4.13, indeed shows a decrease from unity above  $T_X$ , indicating that the magnetic induction  $\mathbf{B}$  is not along the  $a$  axis throughout the sample. The model can of course be improved if no longer a length/width ratio of infinity (no stray fields) is assumed for the domains. The simple model together with the present measurements, however, do show that the magnetic domain sizes in zero field are a few micrometers and

that by applying small fields the domains grow. The measurements in this Section therefore indicate that the domain sizes in UGe<sub>2</sub> at ambient pressure and down to 2 K are certainly larger than the 40 Å predicted by Nishioka *et al.* [117, 118].

In Fig. 4.4 it is shown that  $D_{zz}$  is less than unity below  $T_C$ . This can be caused by the domain walls, but can also be accounted for by a misalignment. A simple calculation shows that a misalignment of 8° would fully account for the values of  $D_{zz}$  below  $T_C$ . The stated value of  $\delta = 0.22 \mu\text{m}$  [or  $\delta/d = 0.047(23)$ ] should therefore be regarded as an upper limit.

From the above considerations it is concluded that the domain structure of UGe<sub>2</sub> behaves like in a conventional ferromagnet. The magnetic domain size largely exceeds the superconducting coherence  $\xi_{sc}$  length of the Cooper pair. The magnetic domain boundaries can therefore only give secondary effects on the superconducting order.

### Comparison with Theoretical Predictions

Several interesting predictions have been made about the magnetic domain structure within the superconducting phase of superconducting ferromagnets. According to Sonin [127] there is no equilibrium domain structure when the sample is in its Meissner state ( $H < H_{c1}$ ) and in the spontaneous vortex phase ( $H_{c1} < H < H_{c2}$ ) the period of the domain structure would exceed the period found in the case that the sample were non-superconducting under the same experimental conditions. However, calculations by Fauré and Buzdin [128] lead to contradicting conclusions. They demonstrated that a domain structure is fully compatible with the Meissner state. It was also shown that the domain structure in the superconducting phase is always more dense than in the normal state, the density depending on the domain size  $d$ , the domain wall thickness  $\delta$ , and the London penetration depth  $\lambda(0)$  at  $T = 0$  K. Moreover, it was shown that the evolution of the domain size with temperature is non-monotonous for triplet pairing superconductivity, in contrast to the monotonous shrinkage of the domain size for singlet pairing superconductivity. Further discussions can be found in Refs. [129, 130].

For the present study, the main question is whether a shrinking or growing of the ferromagnetic domains in the superconducting phase of UGe<sub>2</sub> (and URhGe and UIr) can be observed experimentally. The equilibrium domain size is inversely proportional to the saturation magnetization  $B_S$ :  $d \approx \sqrt{l}/B_S(T)$ , where  $l$  is the length of the sample along the domains [131]. Despite of the temperature dependence of  $B_S(T)$ , the data presented in this Section strongly indicate a temperature independent magnetic domain structure. This observation can be attributed to the pinning of domain walls to impurities, dislocations, and other crystal imperfections. If this pinning is strong enough, it could prevent the domains to shrink or grow when the material is cooled. One could, however, try to use a simple trick to reach equilibrium magnetic state in a sample. By applying a damped, slowly oscillating external magnetic field along the easy axis, the equilibrium state could to be approached.

The PANDA, the instrument on which the 3DND measurements were performed (see Sec. 2.3) is not designed for measurements at dilution temperatures or at high pressures. However, it would be interesting enough to perform similar measurements on URhGe (superconducting at ambient pressure) at a neutron instrument which does have the needed features (polarizer/analyzer and dilution cryostat). If successful, the measurements have the possibility to distinguish between singlet and triplet pairing superconductivity [128].

### 4.2.6 Conclusions

The ferromagnetic domain sizes of UGe<sub>2</sub> were studied by means of three-dimensional neutron depolarization at ambient pressure. It is concluded that the existence of field-tuned resonant tunneling between spin quantum states [117, 118] is highly unlikely. The requirement of this model is a ferromagnetic domain size of 40 Å, whereas the measurements presented in this Section indicate a size a factor of 1000 larger. The observed jumps in the magnetization should be attributed to a Barkhausen effect as discussed by Lhotel *et al.* [132, 133]. The superconductivity, therefore, exists within a single ferromagnetic domain. The domain walls are not expected to strongly affect the bulk Cooper pair wave function, as suggested by Nishioka *et al.* [117, 118], since the domain-wall size is less than a few percent of the average domain size.

## 4.3 Muon Spin Rotation and Relaxation

### 4.3.1 Introduction

When superconductivity sets in at low temperature, conduction electrons condense into Cooper pairs. In the reported ferromagnetic superconductors, the electronic pairing mechanism needed for superconductivity is believed to be magnetic in origin. It is therefore important to investigate the magnetic properties of UGe<sub>2</sub> and specifically of its conduction electrons.

Several theoretical studies have been performed to explain the coexistence of superconductivity and ferromagnetism. Most studies use the itinerant nature of the ferromagnetism as a starting point. These have indeed shown the possibility of (spin-triplet) superconductivity in a ferromagnetic material [89, 90, 91, 92]. In these studies the electrons forming the Cooper pairs are also responsible for the strong ferromagnetism, which can be explained by the spin-triplet nature of the superconductivity. Other studies [100, 101], however, have shown that spin-singlet superconductivity is still feasible under the constraint that conducting electrons involved in the superconductivity and localized electrons involved in the ferromagnetic order belong to different subsets of  $5f$  electrons. The pairing mechanism is then based on the interaction of electron spins via localized magnetic moments.

In order to determine which pairing mechanism is most probable, it is important to quantify the magnetic properties of the conduction electrons. As muons localize in interstitial sites and are very sensitive to magnetic fields whatever their origin (localized or itinerant magnetic moments), the muon spin rotation or relaxation technique ( $\mu$ SR) yields information on the itinerant electrons and associated magnetism.

### 4.3.2 Experimental

Two different samples were used in the  $\mu$ SR study of UGe<sub>2</sub>. A new single-crystalline sample of UGe<sub>2</sub> has been grown from a polycrystalline ingot using a Czochralski tri-arc technique. Afterwards it was annealed at 800 °C for one week. For the high pressure measurements a cylinder with a diameter of 5 mm and a length of 18 mm was cut from the single crystal. The crystal was oriented in such a way, that the initial muon polarization  $\mathbf{S}_\mu(0)$  was perpendicular to the easy magnetic axis, the **a** axis. For measurements at ambient pressure a sphere with a diameter of 4.5 mm was cut from the cylinder. This sphere was used to measure the muon Knight shift. The applied field  $B_{\text{ext}} = 0.6000$  T was perpendicular to the initial muon polarization  $\mathbf{S}_\mu(0)$ . For the two angular scans the sphere was rotated around the **b** or **c** axis at 65 K. For the three temperature scans in the range 65 K to room temperature,  $\mathbf{B}_{\text{ext}}$  was parallel to the **a**, **b**, and **c**, respectively. Further, the sphere was used to measure the critical dynamics of UGe<sub>2</sub> at ambient pressure on the GPS spectrometer in PSI. This first sample will be referred to as “sample A” in the rest of this Chapter.

The second sample is identical to the one used in the previous Section on three-dimensional neutron depolarization and in Ref. [134]. Here the critical dynamics of UGe<sub>2</sub> were studied at ambient pressure on the EMU spectrometer at ISIS. The crystal has been grown from a polycrystalline ingot using a Czochralski tri-arc technique. No subsequent heat treatment was given to the crystal. This second sample will be referred to as “sample B” in the rest of this Chapter.

For the measurements under pressure a pressure cell was used, made of non-magnetic copper-beryllium (Cu-Be 25 1/2HT). In Fig. 4.7 an overview of the pressure cell is shown. Since teflon gives a quite large  $\mu$ SR signal [135], the sample could not simply be put in a teflon cup. Therefore a different design was made by D. Andreica [135]. The teflon cup is still used (in combination with a gasket) in order to prevent leakage of the pressure liquid, but it is kept away from the sample space. In this way, the number of materials giving a background signal is reduced to one, namely the Cu-Be pressure cell. The muons stopped in the cell give a background signal which is well described by the Kubo-Toyabe function

$$P_{\text{KT}}(\Delta_G, t) = \frac{1}{3} + \frac{2}{3} (1 - \Delta_G^2 t^2) \exp\left(-\frac{1}{2} \Delta_G^2 t^2\right). \quad (4.17)$$

This function has its origin in static magnetic fields with a Gaussian field distribution with a width of  $\Delta_G/\gamma_\mu$ . The static magnetic field comes from the nuclear magnetic



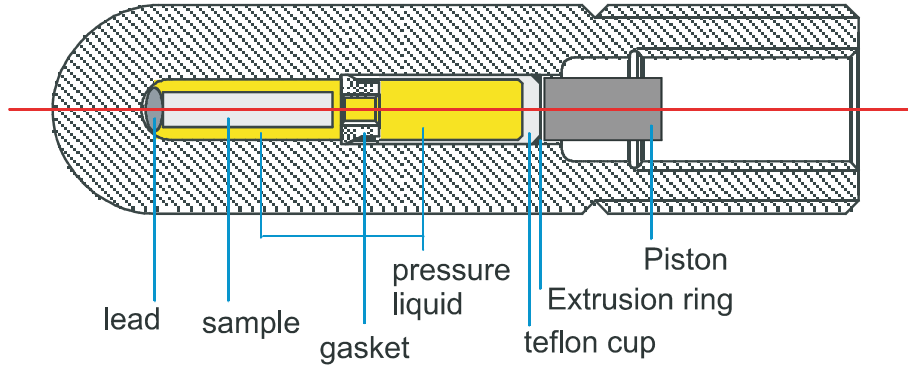


**Figure 4.7:** Overview of the pressure cell used for the muon experiments under pressure. Different parts of the cell are indicated in the figure. For details, see the main text and Ref. [135].

moments of  $^{63}\text{Cu}$ ,  $^{65}\text{Cu}$ , and  $^9\text{Be}$ . Below 40 K,  $\Delta_G$  is temperature independent and equal to  $0.345(2) \mu\text{s}^{-1}$ . Above 40 K there is a decrease to  $0.333(3) \mu\text{s}^{-1}$  at 100 K due to muon diffusion, while above 100 K a fit with Eq. 4.17 is no longer correct. The pressure was applied with the help of a manual hydraulic press. The pressure transmitting medium was a 1:1 mixture of n-pentane and isoamyl alcohol. For further details on the pressure cell, see Ref. [135].

The pressure is determined by measuring the a.c. susceptibility  $\chi_{ac}$  as a function of temperature of a piece of lead which is at the bottom of the pressure cell.  $\chi_{ac}$  shows a sharp drop as soon as the lead gets superconducting. Here the superconducting transition temperature  $T_s$ , which determines the pressure  $P$  by the formula  $T_s = 7.2 - 0.364 \times P$  [136] with  $P$  in GPa, is defined as the midpoint of this drop. An example is shown in Fig. 4.8. Here it is estimated that  $P = 0.92$  GPa. Measurements of critical dynamics have been performed at this pressure.

The  $\mu\text{SR}$  measurements described in this Section have been performed on the General Purpose Surface-Muon (GPS) and General Purpose Decay-Channel (GPD) spectrometers at the Paul Scherrer Institute (PSI) in Villigen, Switzerland. GPS uses surface muons, obtained from pions decaying at rest near the surface of the production target. The beam is fully polarized and monochromatic, with a kinetic energy of 4.1 MeV. Due to this small energy, the beam has a stopping range of around  $160 - 200 \text{ mg/cm}^2$ . The GPD is a high-energy muon beam line. Muons are generated in bunches at a rate given by the frequency of the accelerator (50.64 MHz at PSI). Although the bunch structure is smeared out during the transport of the beam to the sample, it is still visible in the  $\mu\text{SR}$  spectra as an oscillating accidental background. In the analysis of the spectra additional oscillating terms are required, with frequencies equal to the accelerator frequency and higher harmonics. The penetration depth of this type of beam is larger than that of the surface beam and should therefore be used when studying samples within pressure cells.

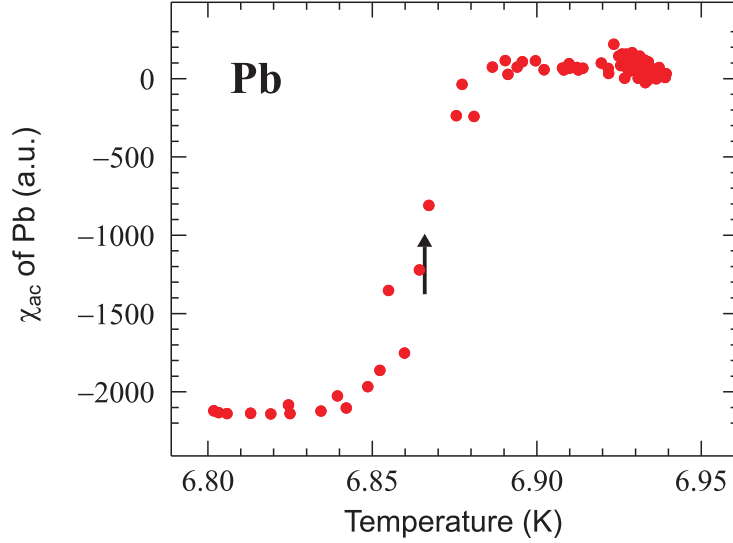


**Figure 4.8:** The pressure inside the pressure cell is determined by measuring the a.c. susceptibility of a piece of lead at the bottom of the pressure cell, just below the sample. See the main text for details. From this measurement  $P \approx 0.92$  GPa is found.

### 4.3.3 Results

#### Ambient pressure: Knight shift measurements on GPS

The muon frequencies  $\nu_\mu$  induced by an external magnetic field  $B_{\text{ext}} = 0.6000$  T were measured above the Curie temperature ( $T_C \approx 52$  K) as a function of the temperature  $T$  and the sample rotation angle  $\phi$  on the GPS spectrometer. The measured frequencies differ from  $\nu_{\text{BG}} = (\gamma_\mu/2\pi)B_{\text{ext}} = 81.32$  MHz where  $\gamma_\mu = 851.62$  Mrad s<sup>-1</sup>T<sup>-1</sup> is the gyromagnetic ratio of the muon. The muon Knight shift  $K$

$$K = \frac{\nu_\mu - \nu_{\text{BG}}}{\nu_{\text{BG}}} \quad (4.18)$$

follows from  $K_\mu$  in Eq. 2.27 by assuming that  $\mathbf{B}_{\text{ext}} \parallel \mathbf{B}_{\text{loc}}$ , with  $\mathbf{B}_{\text{loc}}$  the local magnetic field at the muon site. The principles of muon Knight shift measurements are discussed in Sec. 2.2.5. The initial muon polarization  $\mathbf{S}_\mu(0)$  is rotated perpendicular to the longitudinal magnetic field  $\mathbf{B}_{\text{ext}}$  (see Fig. 2.2).

Two angular scans have been performed along the **b** or **c** axis. For the choice of the temperature  $T > T_C$  a compromise had to be made between maximization of the Knight shift (closer to  $T_C$ ) and minimization of the depolarization rate  $\lambda_X$  of the induced muon frequencies  $\nu_\mu$  (away from  $T_C$ ). A temperature of  $T = 55$  K turned out to yield spectra with the best quality. A few Fourier transforms of the spectra recorded during the angular scan around the **c** axis are shown in Fig. 4.9 as an example. Three frequencies are observed in the Fourier transforms. The background signal at  $\nu_{\text{BG}}$  is indicated by the vertical dashed line. The two other signals come from muons stopped in the UGe<sub>2</sub> sample and show a strong angular



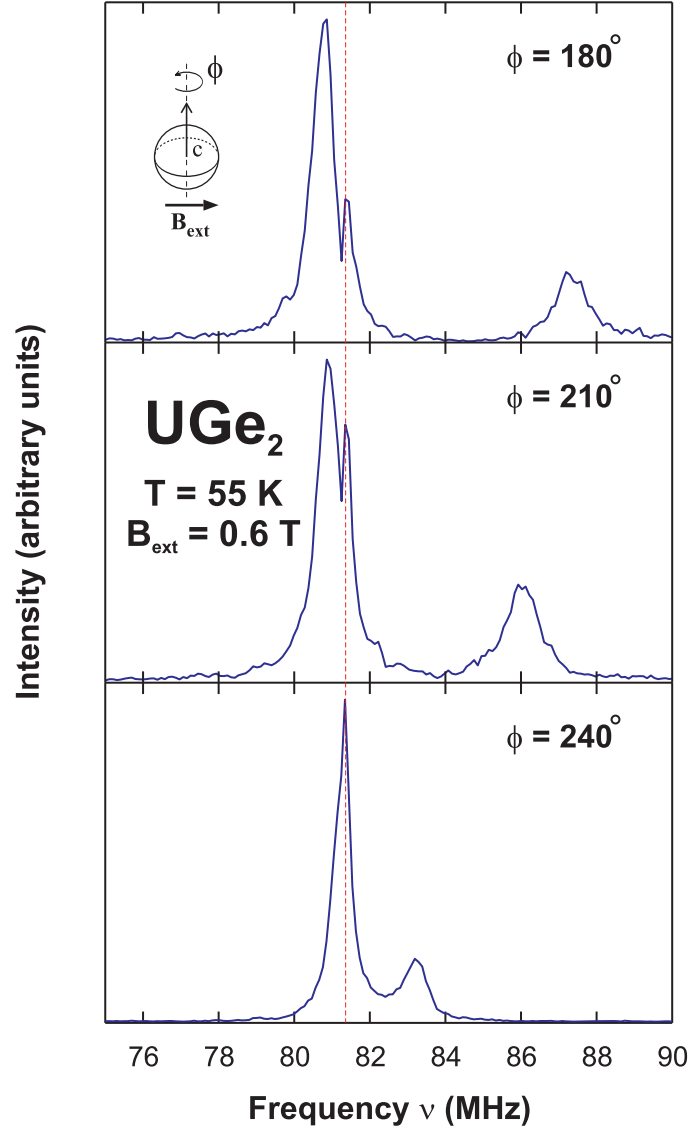


**Figure 4.9:** Examples of Fourier transforms of recorded  $\mu\text{SR}$  spectra. The angular dependence of the muon frequencies was measured at 55 K by rotating a sphere of single-crystalline  $\text{UGe}_2$  around the  $c$  axis in a field of  $B_{\text{ext}} = 0.6 \text{ T}$  perpendicular to the rotation axis. In turn, the initial muon spin polarization  $\mathbf{S}_\mu(0)$  was perpendicular to both the magnetic field and the rotation axis. Three frequencies are observed in the Fourier transforms. The background signal at  $\nu_{\text{BG}} = 81.39 \text{ MHz}$  is indicated by a dashed line. The other two signals come from muons stopped in the sample and show a strong angular dependence. For  $\phi = 240^\circ$ , the signal of the lower component is mixed with the background signal.

**Table 4.2:** Fitted values for  $\nu_{0,i}$  and  $\Delta\nu_i$  in Eq. 4.20.

	rotation around b axis		rotation around c axis	
	$i = 1$	$i = 2$	$i = 1$	$i = 2$
$\nu_{0,i}$ (MHz)	81.36 (2)	81.51 (4)	81.24 (3)	81.57 (4)
$\Delta\nu_i$ (MHz)	-0.58 (4)	5.77 (6)	-0.44 (5)	5.72 (6)

dependence. This points to two muon stopping sites in UGe<sub>2</sub>, as confirmed by the measurements of spontaneous muon frequencies below  $T_C$  in zero magnetic field.

Since three frequencies are observed for all the spectra, the asymmetry  $a_0 P_Z^{\text{exp}}(t)$  as a function of time  $t$  could be analyzed as a sum of three components:

$$a_0 P_X^{\text{exp}}(t) = \sum_{i=1}^3 a_i \exp(-\lambda_{X,i} t) \cos(2\pi\nu_i t - \phi). \quad (4.19)$$

The ratio of the asymmetries  $a_i$  is equal to the ratio of the number of muons stopped at site  $i$ .  $\lambda_{X,i}$  is the depolarization rate of frequency  $\nu_i$  and  $\phi$  accounts for the angle between  $\mathbf{S}_\mu(0)$  and the detector. One frequency accounts for the background, due to muons stopped *e.g.* in the sample holder, and is close to  $\nu_{\text{BG}} = \gamma/2\pi B_{\text{ext}} = 81.32$  MHz. The stray fields of the magnetized sample as well as a different value for  $B_{\text{ext}}$  can slightly shift this background. In the experiments  $\nu_{\text{BG}} = 81.39$  MHz was found, which corresponds to a field of 0.6005 T at the muon site. The two other frequencies are signals coming from muons stopped in the sample.

In Fig. 4.10 the measured muon frequencies are shown as a function of the rotation angle  $\phi$  around the **b** or **c** axis. The background signal shows no angular dependence. The two other signals are 180° out of phase. The first signal shows a relatively small and negative frequency shift, whereas the second one is large and positive. As demonstrated by the full curves in Fig. 4.10, the angular dependence of these two signals can be described very well by the function

$$\nu_i = \nu_{0,i} + \Delta\nu_i \cos^2(\phi - \phi_0) \quad (4.20)$$

where  $\phi_0$  depends on the orientation of the spherically shaped sample when inserted into the cryostat. The values for the parameters  $\nu_{0,i}$  and  $\Delta\nu_i$  can be found in Table 4.2. It should be mentioned that, for both angular scans, the values for the asymmetry  $a_1$  is always somewhat larger than those for  $a_2$  (0.12 vs. 0.10).

In addition to the angular scans, temperature scans have been performed with  $\mathbf{B}_{\text{ext}}$  parallel to the **a**, **b**, and **c** axes. In the upper figure of Fig. 4.11 the Knight shift  $K = (\nu_\mu - \nu_{\text{BG}})/\nu_{\text{BG}}$ , measured with  $\mathbf{B}_{\text{ext}} \parallel \mathbf{a}$ , is presented as a function of

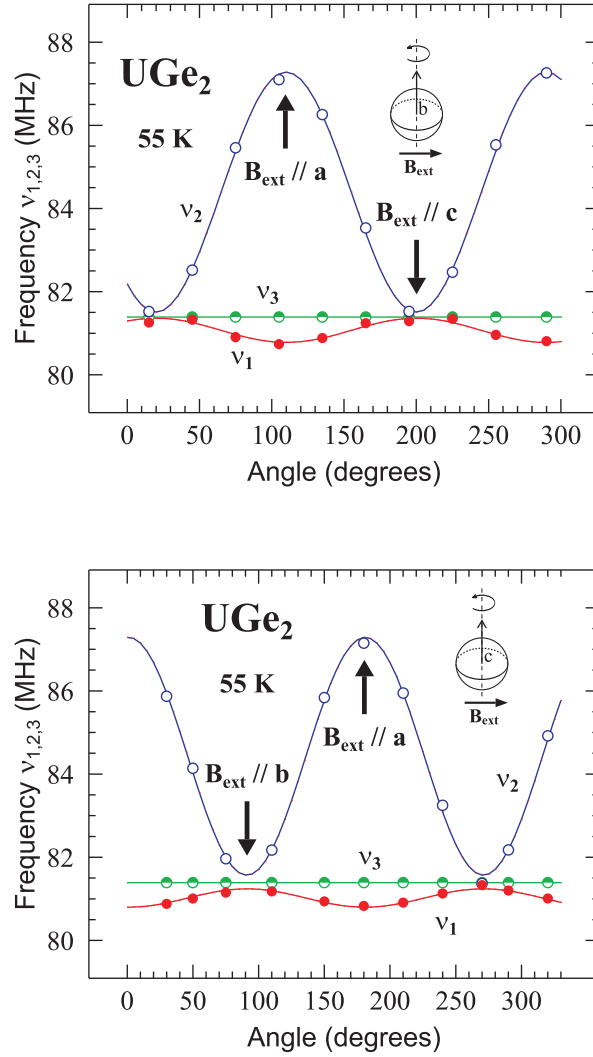


**Figure 4.10:** Angular dependence of the muon frequencies at 55 K. A sphere of single-crystalline  $\text{UGe}_2$  was rotated around the **b** and **c** axis (upper and lower picture, respectively) in a field of  $B_{\text{ext}} = 0.6$  T perpendicular to the rotation axis. In turn, the initial muon spin polarization  $\mathbf{S}_\mu(\mathbf{0})$  was perpendicular to both the magnetic field and the rotation axis. The full lines are fits to Eq. 4.20. The error bars of the frequencies are within the symbol size. The background signal at  $\nu_{\text{BG}} = 81.39$  MHz is shown as well and fit to a straight line.

the bulk susceptibility  $\chi_a$  (a Clogston-Jaccarino plot) for reasons explained below Eq. 2.28. Here the temperature  $T$  is an implicit parameter. The susceptibility has been measured on the same spherically shaped sample as the Knight shift measurements have been performed on, at the same temperatures and in an applied field of 0.6 T parallel to the **a** axis. The data have been corrected for the demagnetization field. As in the case of the angular scans, the asymmetry  $a_1$  for the negative Knight shift is slightly larger than  $a_2$  for the positive Knight shift, which indicates a larger muon population (55 %) for the first muon site than for the second one (45 %).

The full lines represent linear fits to the data. It is seen that for both signals the data are very well described by this linear relation, as predicted by Eq. 2.28. The first signal is described by  $K_1^a = -0.062(1) \chi_a - 0.00080(3)$  and the second one by  $K_2^a = 0.591(4) \chi_a + 0.0010(2)$ .

In the lower two figures of Fig. 4.11 the Knight shifts, measured with  $\mathbf{B}_{\text{ext}} \parallel \mathbf{b}$  or  $\mathbf{B}_{\text{ext}} \parallel \mathbf{c}$ , are presented as a function of the bulk susceptibilities  $\chi_b$  and  $\chi_c$ , respectively, for varying temperature. The susceptibility has been measured on the same spherically shaped sample as the Knight shift measurements have been performed on, at the same temperatures and in an applied field of 0.6 T parallel to the **b** axis or **c** axis. The data have been corrected for the demagnetization field. Comparing the asymmetries of the two signals per direction of  $\mathbf{B}_{\text{ext}}$ , it is possible to identify which curves stem from one muon site and which from the other. As in all previous cases the asymmetry  $a_1$  for the negative Knight shift is slightly larger than  $a_2$  for the positive Knight shift, indicating a larger fraction of the muons coming to rest at the first muon site than at the second.

Comparing the horizontal ( $\chi_i$ ) and vertical (Knight shift) scales in Fig. 4.11, it is clearly seen that there is a two orders of magnitude difference between the values for  $\mathbf{B}_{\text{ext}} \parallel \mathbf{b}$  and  $\mathbf{B}_{\text{ext}} \parallel \mathbf{c}$  on the one hand and  $\mathbf{B}_{\text{ext}} \parallel \mathbf{a}$  on the other hand. The small values for  $\mathbf{B}_{\text{ext}} \parallel \mathbf{b}$  and  $\mathbf{B}_{\text{ext}} \parallel \mathbf{c}$  make it difficult to obtain an accurate determination of the Knight shift.

The sharp drop of the Knight shift for  $\mathbf{B}_{\text{ext}} \parallel \mathbf{b}$  for low values of  $\chi_b$  probably indicates the start of muon diffusion. This happens at temperatures  $T > 66$  K. For  $\mathbf{B}_{\text{ext}} \parallel \mathbf{c}$  it is less clear at which temperature the muon starts to diffuse. It is assumed that for both directions of  $\mathbf{B}_{\text{ext}}$  the muon starts to diffuse through the sample at the same temperature. Therefore, the data points for  $T > 66$  K should not be taken into account when fitting the data. In Fig. 4.11 the linear fits are shown. For  $\mathbf{B}_{\text{ext}} \parallel \mathbf{b}$  it is found that  $K_1^b = 0.074(21) \chi_b - 0.00066(7)$  and  $K_2^b = 0.081(17) \chi_b + 0.00061(2)$ . For  $\mathbf{B}_{\text{ext}} \parallel \mathbf{c}$ ,  $K_1^c = -0.080(37) \chi_c - 0.00207(1)$  and  $K_2^c = -0.040(25) \chi_c + 0.00174(4)$  is obtained. The larger error bars for  $K_i^c$  than for  $K_i^b$  is caused by the difference in the amount of data points that could be used in the fit.

Since the muon is assumed to start diffusing for  $T > 66$  K, it would be expected to observe a deviation from the linear relation between the Knight shift  $K$  and the susceptibility  $\chi$  for  $\mathbf{B} \parallel \mathbf{a}$ , as for the cases  $\mathbf{B} \parallel \mathbf{b}$  and  $\mathbf{B} \parallel \mathbf{c}$ . In the upper panel of Fig. 4.11, the three data points per curve with the smallest  $\chi_a$  were measured at a temperature  $T > 66$  K. In contrast to  $\mathbf{B} \parallel \mathbf{b}, \mathbf{c}$ , no deviation is observed from a

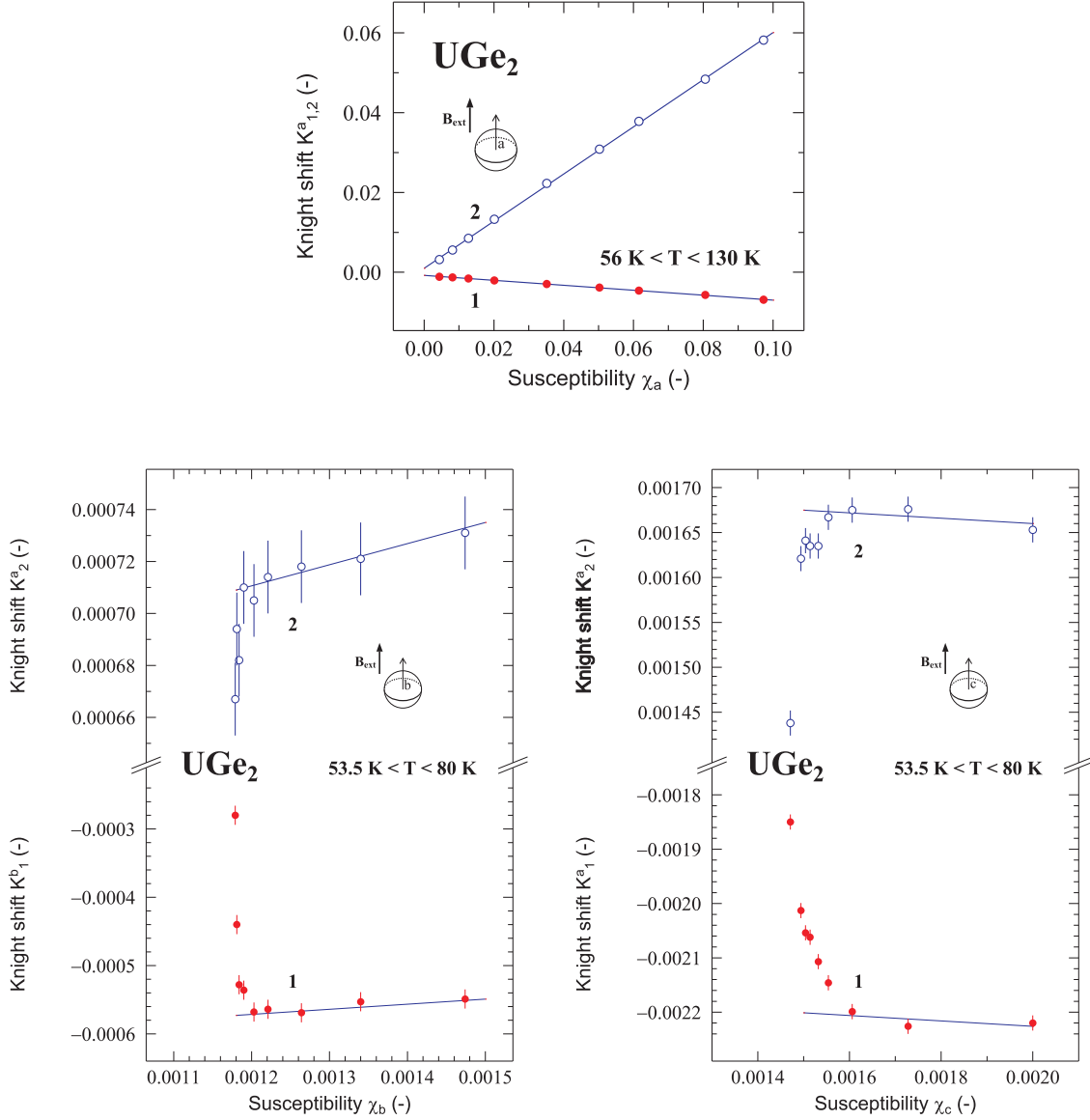


**Figure 4.11:** Clogston-Jaccarino plot of the muon Knight shift for  $\mathbf{B}_{\text{ext}} \parallel \mathbf{i}$  (where  $\mathbf{i} = \mathbf{a}, \mathbf{b}, \mathbf{c}$ ) as a function of the magnetic susceptibility  $\chi$ . The muon Knight shift  $K^i$  is plotted versus the bulk susceptibility  $\chi_i$  with the temperature  $T$  as an implicit parameter. Both quantities were measured in a magnetic field of  $B_{\text{ext}} = 0.6 \text{ T}$  and on the same spherically shaped sample and for each direction of  $\mathbf{B}_{\text{ext}}$  at the same temperatures.

linear relation. Including or excluding these data points in the fits does not change the linear equations found above.

### High pressure: spontaneous frequencies $\nu_\mu$ and depolarization rates $\lambda_X$

The spontaneous frequencies  $\nu_\mu$  below  $T_C$  and the associated depolarization rates  $\lambda_X$  were measured in zero magnetic field as a function of temperature  $T$  at several pressures  $P$ . The sample was oriented in such a way, that the initial muon polarization  $\mathbf{S}_\mu(0)$  was perpendicular to the  $\mathbf{a}$  axis. As explained in Sec. 4.3.2 for measurements that are performed on the GPD spectrometer, two oscillating background signals were present in  $N(t)$ , the number of detected positrons at time  $t$ .  $N(t)$  can therefore be written as (see also Eq. 2.5)

$$N(t) = N_0 \left\{ e^{-t/\tau_\mu} \left[ 1 + a_0 P_X^{\text{exp}}(t) \right] + f_{\text{bg}} \left[ 1 + \sum_{i=1}^2 f_i \cos(2\pi\nu_{\text{bg},i}t - \phi) \right] \right\} + b \quad (4.21)$$

where  $\tau_\mu$  is the muon life time (Table 2.1),  $\nu_{\text{bg},1} = 50.64$  MHz,  $\nu_{\text{bg},2} = 101.28$  MHz (higher harmonic), and  $b$  is a time independent background. Besides the two instrumental background signals  $\nu_{\text{bg},1}$  and  $\nu_{\text{bg},2}$ , a Kubo-Toyabe function  $P_{\text{KT}}(\Delta_G, t)$  (Eq. 4.17) accounting for the signal from the pressure cell was observed. The UGe<sub>2</sub> sample itself gave two spontaneous frequencies  $\nu_1$  and  $\nu_2$  with associated depolarization rates  $\lambda_{X,1}$  and  $\lambda_{X,2}$ , in accordance with the Knight shift measurements. Therefore,  $a_0 P_X^{\text{exp}}(t)$  could be written and analyzed as a sum of three components:

$$a_0 P_X^{\text{exp}}(t) = \sum_{i=1}^2 a_i \exp(-\lambda_{X,i}t) \cos(2\pi\nu_i t - \phi) + a_3 P_{\text{KT}}(\Delta_G, t). \quad (4.22)$$

The ratio of the asymmetries  $a_i$ ,  $i = 1 \dots 3$ , is equal to the ratio of the number of muons responsible for signal  $i$ .  $a_3$  is roughly 3/4 of  $a_0$ .  $a_1$  and  $a_2$  are roughly equal, although it should be mentioned that  $a_1$  is slightly but significantly larger than  $a_2$  (55 % vs. 45 %), for all measured temperatures and pressures. This indicates that the first muon site is more populated by muons than the second site. This was also the case for the Knight shift measurements. Therefore, different signals can be associated with either of the two muon sites.

In Fig. 4.12 the two measured muon frequencies  $\nu_i$  and associated depolarization rates  $\lambda_{X,i}$  are shown as a function of temperature for several pressures up to 1 GPa. The frequency curves resemble magnetization data under pressure [114]. In this Section the Curie temperature  $T_C(P)$  is defined as the temperature at which the spontaneous frequencies disappear. Below  $T_C$ ,  $\nu_1$  and  $\nu_2$  increase monotonously, to reach a saturation level at low temperatures. At higher pressures it is seen that there is a kink in the curve. The temperature at which this kink occurs, is named  $T_X$ . The values of  $T_C$  and  $T_X$  are in good agreement with the values known from literature [114]. At low temperatures, the saturation level of  $\nu_2$  is strongly dependent on pressure, whereas  $\nu_1$  remarkably shows no significant pressure dependence.

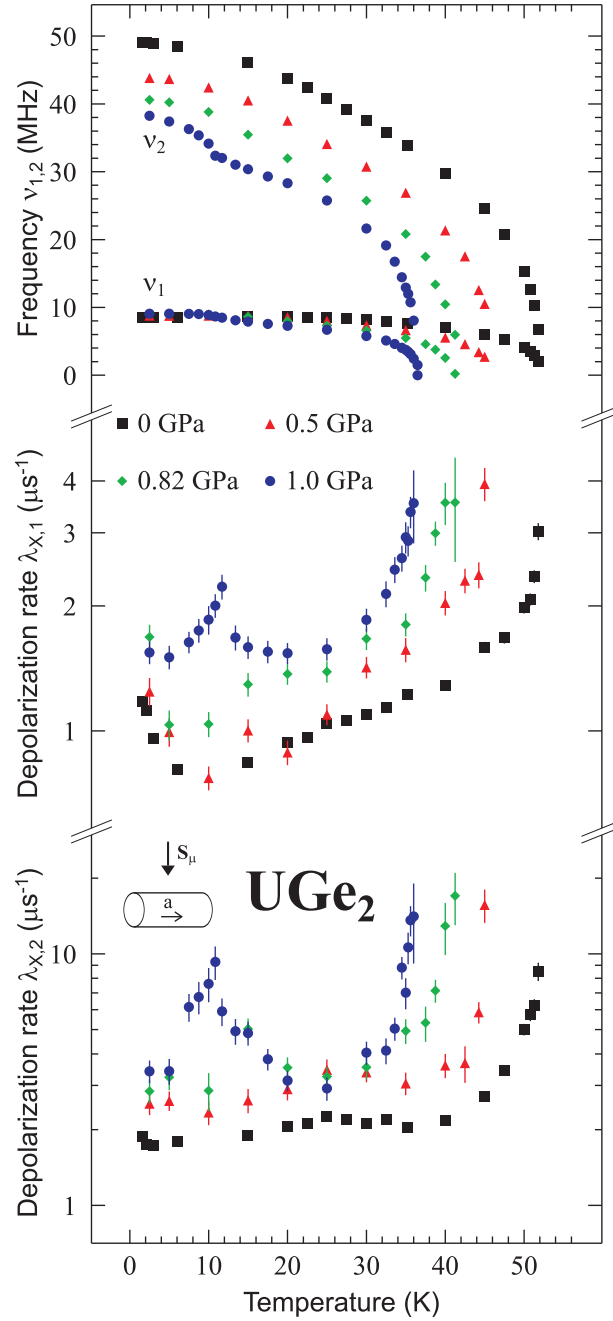


**Figure 4.12:** The two spontaneous frequencies  $\nu_1$  and  $\nu_2$  and associated depolarization rates  $\lambda_{X,1}$  and  $\lambda_{X,2}$  as a function of temperature and different pressures in UGe<sub>2</sub>. The asymmetry for the first signal ( $a_1$ ) is slightly larger than for the second ( $a_2$ ), for all temperatures and pressures. The frequency  $\nu_2$  shows a much larger pressure dependence than  $\nu_1$ . At higher pressures a peak in  $\lambda_X$  occurs below  $T_C$ .

The depolarization rates  $\lambda_{X,1}$  and  $\lambda_{X,2}$  show for all pressures a large increase as  $T_C$  is approached. Note the logarithmic vertical scales. The curves for 0 GPa look rather conventional:  $\lambda_{X,i}$  decreases with decreasing temperature. However, as the pressure is increased, a peak starts to develop at the temperature  $T_X$  at which a kink in the frequency curve occurs. This development of a peak is particularly clear in  $\lambda_{X,2}$ , but less clear in  $\lambda_{X,1}$ . For 1.0 GPa, however, the peak is evident for both depolarization rates. It should also be noticed that the curves of  $\lambda_{X,1}$  and  $\lambda_{X,2}$  shift to higher values as pressure increases. In Sec. 4.3.5 the origin of the peak will be discussed further.

### Ambient and high pressure: critical fluctuations

In this Section the data obtained in the critical regime, close to  $T_C$ , are discussed. Remember two samples were used in the study of the critical dynamics (see Sec. 4.3.2). Data at ambient pressure, recorded at the EMU spectrometer of the ISIS facility on sample B, were already published elsewhere by Yaouanc *et al.* [134]. The data measured in the pressure cell at ambient pressure on the GPD spectrometer at PSI on sample A and presented in this thesis, yielded qualitatively very similar results, although there were some quantitative differences. Therefore, sample A was remeasured on GPS at ambient pressure. This was done to check whether the quantitative difference stems from the fact that measurements were performed on different instruments (EMU  $\leftrightarrow$  GPD) with different, probably not perfectly described backgrounds, or from the fact that sample B used in Ref. [134] was not the same as sample A, the sample newly grown for the  $\mu$ SR measurements described in this thesis. It is important to understand what the origin is for this quantitative difference, in order to reliably compare the ambient and high pressure data obtained in the pressure cell at GPD. For completeness all results, including those published in Ref. [134], will be discussed here.

#### Measurements on EMU

The EMU data [134] at ambient pressure are discussed first. All the recorded spectra of the asymmetry  $a_0 P_Z^{\text{exp}}(t)$  as a function of time  $t$  could be analyzed as a sum of two components:

$$a_0 P_Z^{\text{exp}}(t) = a_s P_Z(t) + a_{\text{bg}}. \quad (4.23)$$

$P_Z(t)$  and  $P_Z^{\text{exp}}(t)$  are functions normalized to unity for  $t = 0$ . The first component describes the  $\mu$ SR signal from the sample and the second accounts for the muons contributing to the background, that were stopped in *e.g.* the sample holder. At the time of the measurements, the fly-past mode was not yet available, leading to relatively high backgrounds. This second component is time independent. In zero field and for the two orientations of  $\mathbf{S}_\mu(0)$  relative to the easy magnetic axis  $\mathbf{a}$ ,  $P_Z(t)$  is well described by an exponential function  $P_Z(t) = \exp(-\lambda_Z t)$ , where  $\lambda_Z$  measures



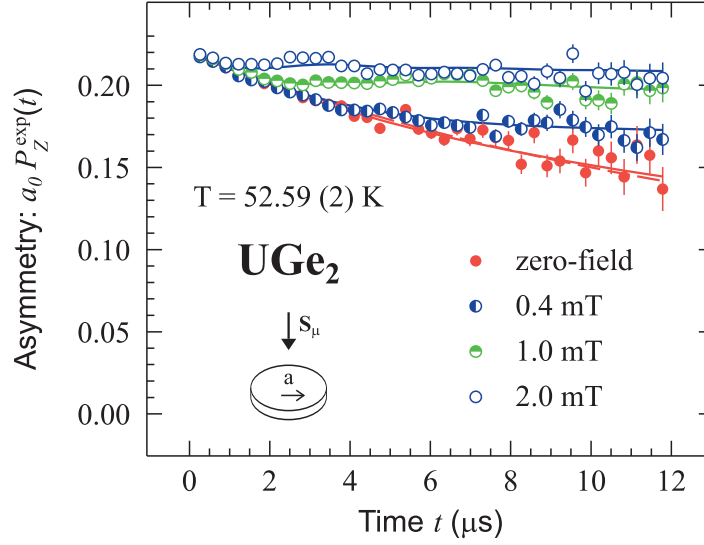


**Figure 4.13:** Examples of  $\mu$ SR spectra recorded in zero field and in longitudinal magnetic fields at  $T = 52.59 (2) \text{ K}$  (above  $T_C = 52.49 (2) \text{ K}$ ) for  $\mathbf{S}_\mu(0) \perp \mathbf{a}$ . The solid lines are fits to Eq. 4.23. Note the field dependence of  $P_Z(t)$  for small fields. The figure is taken from Ref. [134].

the spin-lattice relaxation rate at the muon site. In non-zero field,  $P_Z(t)$  can be best described by  $P_Z(t) = P_Z(\Delta_{\text{Lor}}, \nu_f, t)$ . Here it is assumed that the distribution of  $\mathbf{B}_{\text{loc}}$  is squared Lorentzian [137].  $\Delta_{\text{Lor}}$  characterizes the width of the field distribution and  $\nu_f$  denotes the fluctuation rate of the magnetic field. Examples of the spectra in zero and non-zero field are presented in Fig. 4.13.

The temperature dependence of  $\lambda_Z(T)$  in zero field is shown in Fig. 4.14. For both geometries,  $\lambda_Z(T)$  shows a maximum at  $T_C$ , which is due to the critical slowing down of the spin dynamics. The Curie temperature  $T_C$  was defined as the temperature at which the spontaneous frequencies disappear. This gave  $T_C = 52.49 (2) \text{ K}$ . The anisotropy between the  $\mu$ SR signal for the two orientations is very weak, unlike the strong anisotropy of the bulk magnetization in  $\text{UGe}_2$ . The solid and dashed lines in the inserts are fits to the dipolar Heisenberg model in Eq. 4.32 to be discussed in Sec. 4.3.4. Note that for magnetic fields as small as 2 mT the depolarization almost completely vanishes (see Fig 4.13). For large magnetic moments of  $1.4 \mu_B$  in the case of  $\text{UGe}_2$ , this is totally unexpected. For such large moments it is expected that the fluctuation energy is much larger than the magnetic energy corresponding to an applied field of 2 mT.

#### *Measurements on GPD*

The measurements of the critical paramagnetic spin dynamics at high pressure were performed on the GPD spectrometer at  $P = 0.95 (2) \text{ GPa}$ . The pressure was chosen

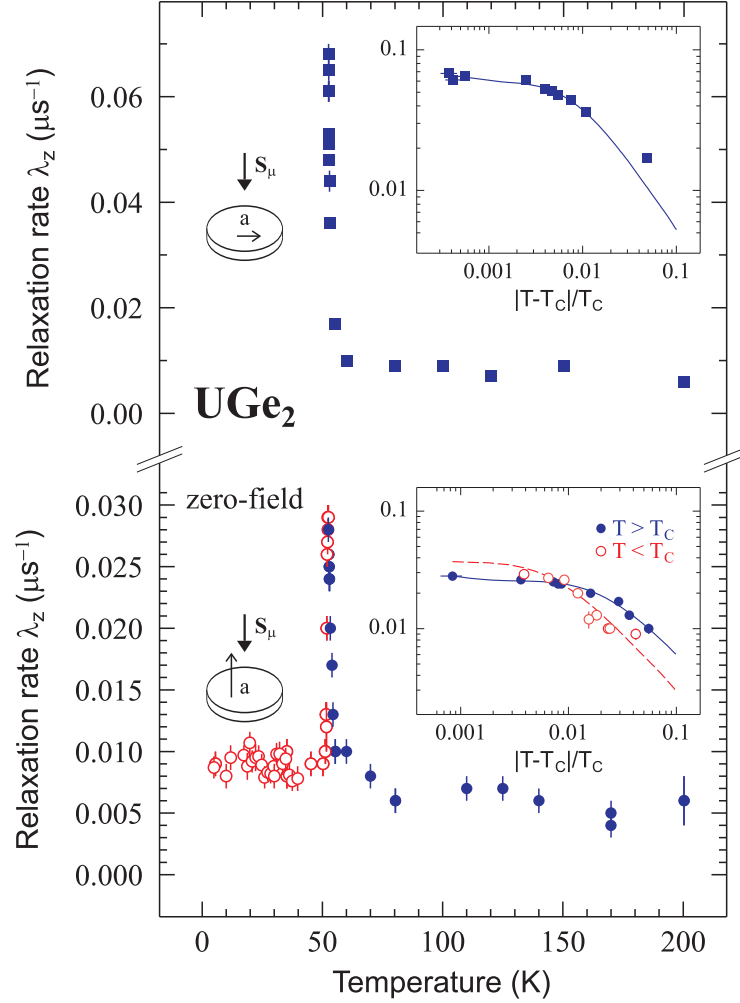


**Figure 4.14:** The spin lattice relaxation rate  $\lambda_Z$  versus temperature  $T$  for  $\mathbf{S}_\mu(0) \perp \mathbf{a}$  and  $\mathbf{S}_\mu(0) \parallel \mathbf{a}$  at ambient pressure in zero magnetic field. The measurements were performed on the EMU spectrometer at the ISIS facility. A very sharp strong increase in  $\lambda_Z$  is observed at  $T_C = 52.49$  (2) K. The inserts display  $\lambda_Z$  versus reduced temperature  $\tau = (T - T_C)/T_C$ . The solid and dashed lines are the results of fits to the model discussed in Sec. 4.3.4. Figure taken from Ref. [134].

to be below 1.2 GPa because the paramagnetic to ferromagnetic phase transition in UGe<sub>2</sub> changes around this pressure from second to first order [116]. Since the theory used in Sec. 4.3.4 to analyze the critical data is only valid for second order phase transitions, it was required to be certain to stay below the transition point where the order changes. Unfortunately, only the  $\mathbf{S}_\mu(0) \perp \mathbf{a}$  orientation could be measured in the pressure cell. This prevented a determination of the anisotropy in  $\lambda_Z(T)$  at high pressures.

In Fig. 4.15 experimental data are shown at 0.95 (2) GPa for different temperatures. All the recorded spectra of the asymmetry  $a_0 P_Z^{\text{exp}}(t)$  as a function of time  $t$ ,

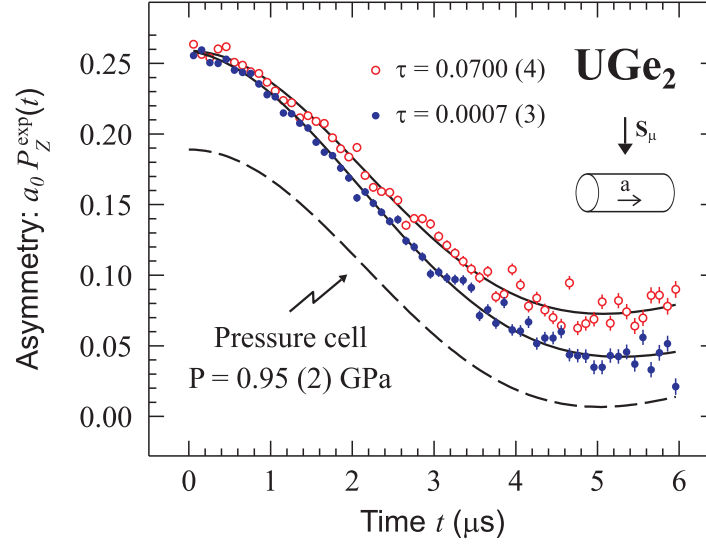


**Figure 4.15:** Examples of  $\mu$ SR spectra for  $\mathbf{S}_\mu(0) \perp \mathbf{a}$  at 0.95 (2) GPa in zero field for  $T = 39.03$  (1) K and  $T = 36.511$  (6) K. With  $T_C = 36.48$  (1) K these temperatures correspond to reduced temperatures of  $\tau = (T - T_C)/T_C = 0.0700$  (4) (open symbols) and 0.0007 (3) (solid symbols), respectively. The solid lines are fits to Eq. 4.24. The dashed line shows the background arising from the pressure cell.

recorded under a pressure of 0.95 (2) GPa above  $T_C$ , could be analyzed as a sum of two components:

$$a_0 P_Z^{\text{exp}}(t) = a_1 \exp(-\lambda_Z t) + a_2 P_{\text{KT}}(\Delta_G, t). \quad (4.24)$$

Here  $P_{\text{KT}}(\Delta_G, t)$  is the Kubo-Toyabe function given by Eq. 4.17 and accounts for the background arising from the pressure cell. The second term stems from the  $\text{UGe}_2$  sample, where  $\lambda_Z$  measures the spin-lattice relaxation rate at the muon site. For the fit  $\lambda_Z$  was free and the other parameters fixed to  $a_1 = -0.073$ ,  $a_2 = -0.183$ ,  $\Delta_G = 0.345 \mu\text{s}^{-1}$  for the first detector (not shown) and  $a_1 = 0.070$ ,  $a_2 = 0.189$ ,  $\Delta_G = 0.345 \mu\text{s}^{-1}$  for the second detector (shown). The ratio of  $a_1$  and  $a_2$  is equal to the ratio of the number of muons stopped in the sample and in the pressure cell. The upper solid line in Fig. 4.15 is a fit the data measured at a temperature far above  $T_C$  with  $\tau = (T - T_C)/T_C = 0.0700$  (4) and the lower solid line is a fit to data recorded close to  $T_C$  with  $\tau = 0.0007$  (3). The dashed line shows the temperature independent background  $a_2 P_{\text{KT}}(\Delta_G, t)$ .

In Fig. 4.16 the temperature dependence of  $\lambda_Z(T)$  is displayed.  $\lambda_Z(T)$  is measured at ambient pressure (in the pressure cell) and at 0.95 (2) GPa, both in zero field. For both pressures,  $\lambda_Z(T)$  exhibits a maximum at  $T_C$ . This is due to the critical slowing down of the spin dynamics. As before,  $T_C$  was defined as the temperature at which the spontaneous frequencies, which appear below  $T_C$ , disappear. At ambient pressure  $T_C = 52.16$  (1) K is obtained and  $T_C = 36.48$  (1) K at 0.95 (2) GPa. The solid lines in the lower plot of Fig. 4.16 are again fits to the dipolar Heisenberg

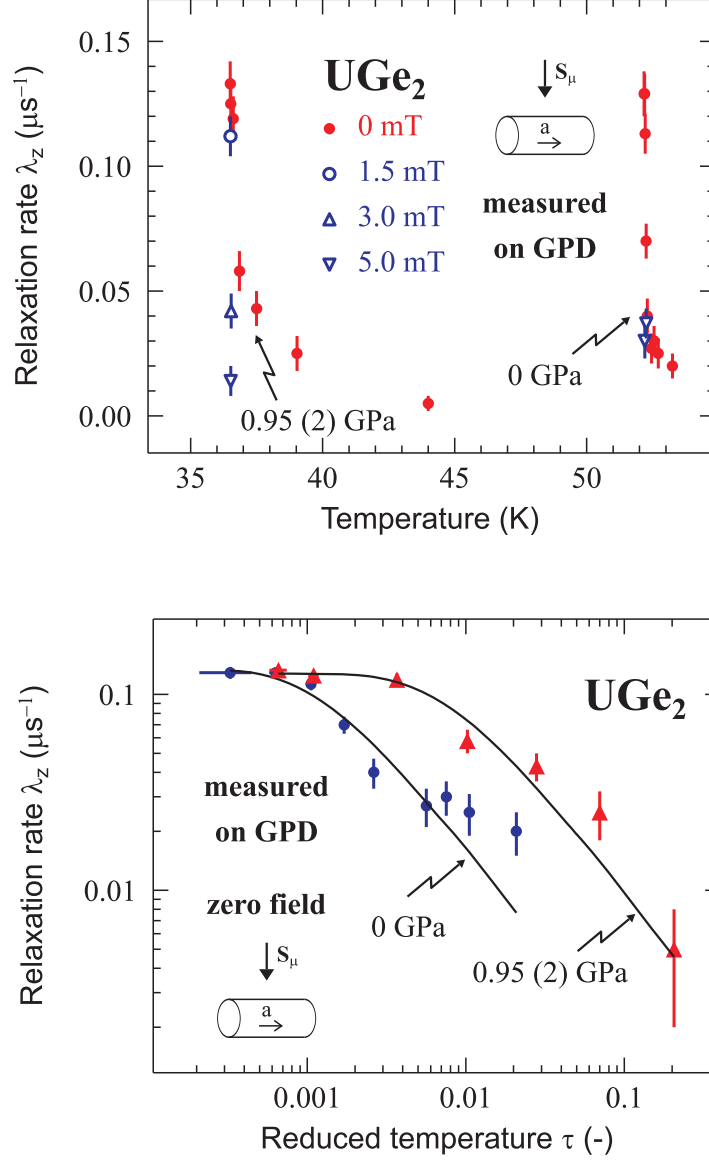


**Figure 4.16:** (Upper frame) The spin lattice relaxation rate  $\lambda_z$  versus temperature for ambient pressure and a pressure of 0.95 (2) GPa in zero magnetic field and small fields. In zero field there is a strong increase in relaxation rate just above  $T_C = 52.16(1)$  K at ambient pressure and just above  $T_C = 36.48(1)$  K at 0.95 (2) GPa. It is also shown that for a field as small as 5 mT the relaxation rate drops remarkably for both pressures. (Lower frame) The spin lattice relaxation rate  $\lambda_z$  as a function of the reduced temperature  $\tau = (T - T_C)/T_C$  for ambient pressure and a pressure of 0.95 (2) GPa in zero magnetic field. The solid lines are fits to the model discussed in Sec. 4.3.4.

model in Eq. 4.32 (see Sec. 4.3.4). The observed plateau for 0.95 (2) GPa is broader than for 0 GPa.

The GPD spectra in small magnetic fields could be satisfactorily described by the same model as for zero field (Eq. 4.24), *i.e.* the sum of a Kubo-Toyabe function accounting for the muons stopped in the pressure cell and an exponential function accounting for the muons stopped in the UGe<sub>2</sub> sample. The qualitative result is that the relaxation rate is already quenched for very small magnetic fields. This is shown for both pressures in the upper plot of Fig. 4.16. A mere 5 mT is enough to suppress the relaxation rate.

Note the similarity between the insets of Fig. 4.14 and the lower plot of Fig. 4.16. Both figures show clearly a saturation of  $\lambda_Z$  close to  $T_C$ .

### *Measurements on GPS*

The cylindrical sample A (used for the high pressure measurements of the spontaneous frequencies on GPD) was reshaped into a sphere of 4.5 mm diameter for the Knight shift measurements as well as for the measurements on GPS of the critical dynamics. For both sample A and B, the recorded spectra of the asymmetry  $a_0 P_Z^{\text{exp}}(t)$  as a function of time  $t$  could be analyzed as a sum of two components, as indicated in Eq. 4.23. The signal from the UGe<sub>2</sub> sample could be described by an exponential function.

The temperature dependence of  $\lambda_Z(T)$  in zero field, in the case of  $\mathbf{S}_\mu(0) \parallel \mathbf{a}$ , is shown in Fig. 4.17 for both sample A and B. For both samples  $\lambda_Z(T)$  shows a maximum at  $T_C$ , which is due to the critical slowing down of the spin dynamics. The Curie temperature  $T_C$  was defined as the temperature at which  $\lambda_Z(T)$  is maximum. This gave  $T_C = 52.20(1)$  for sample A and  $T_C = 52.27(1)$  for sample B. It is clearly seen that sample A shows a sharper transition than sample B. This may indicate a higher sample quality, although it is surprising that  $T_C$  is slightly lower, which suggests the opposite.

The lower figure in Fig. 4.17 shows a plot of  $\lambda_Z(T)$  versus the reduced temperature  $\tau = (T - T_C)/T_C$ . The solid lines are fits to the dipolar Heisenberg model of Eq. 4.32 (see Sec. 4.3.4). The transition for sample B is indeed broader than for sample A, as noted earlier. Since both samples are measured on the same instrument, the difference cannot originate from a wrongly modeled background or from a difference in thermometry. Although the critical dynamics is qualitatively reproducible, quantitatively there is a sample dependence.

The temperature dependence of  $\lambda_Z(T)$  in zero field is shown in Fig. 4.18 for  $\mathbf{S}_\mu(0) \perp \mathbf{a}$ . Sample A was measured at GPD and at GPS. In the upper plot of the figure it is seen that these results do not coincide perfectly. Since it is the same sample, this effect should be considered instrument related. At GPD the background was large (about 50 % of the total asymmetry) because of the pressure cell. At GPS the background is much lower.

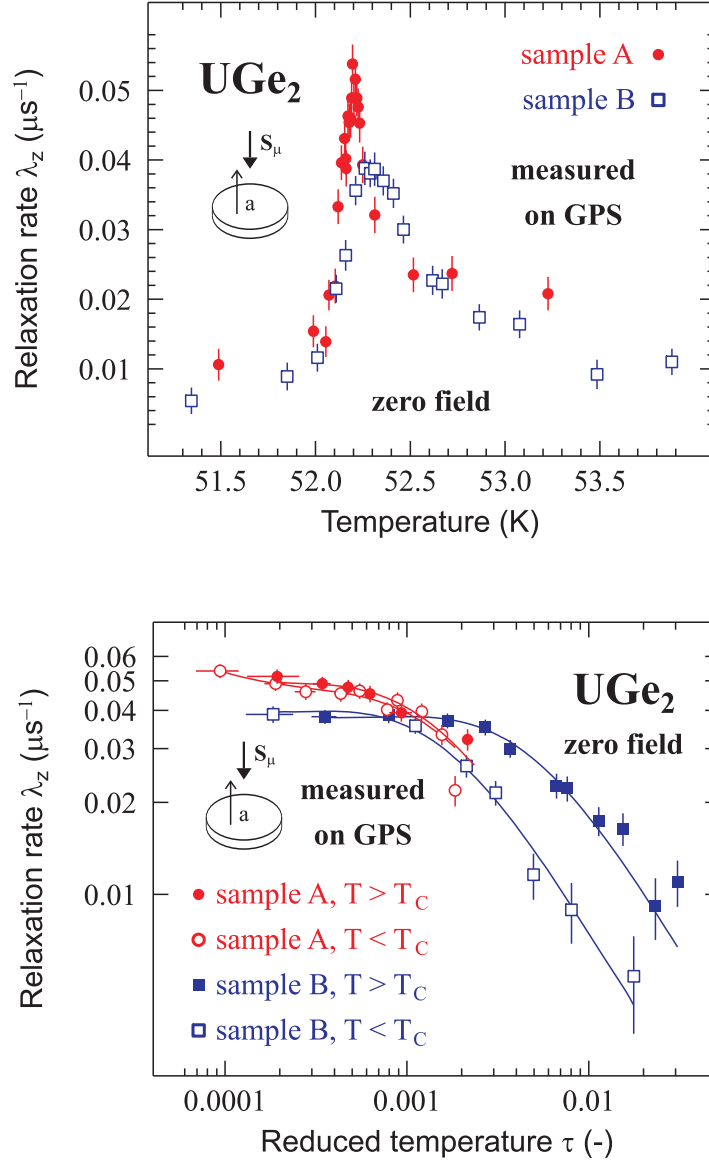


**Figure 4.17:** (Upper frame) The spin lattice relaxation rate  $\lambda_z$  as a function of temperature for sample A and sample B in zero magnetic field. There is a strong increase in relaxation rate when  $T_C$  is approached. Sample A shows a sharper transition than sample B. (Lower frame) The spin lattice relaxation rate  $\lambda_z$  versus reduced temperature  $\tau = (T - T_C)/T_C$  for sample A and sample B, in zero magnetic field. The solid lines are fits to the model discussed in Sec. 4.3.4.

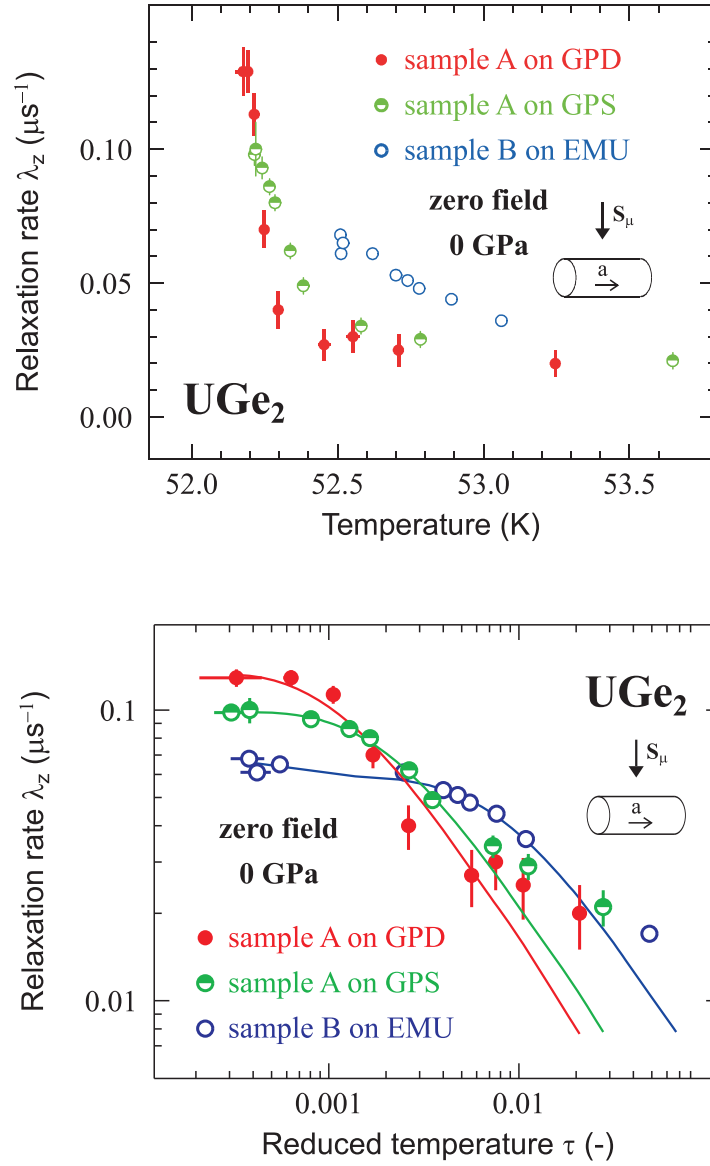


**Figure 4.18:** (Upper frame) The spin lattice relaxation rate  $\lambda_z$  versus temperature for sample A, measured on GPD and GPS, and sample B, measured on EMU, in zero magnetic field. There is a strong increase in relaxation rate when  $T_C$  is approached. Sample A shows a sharper transition than sample B. Measuring sample A on GPD or GPS yields slightly different results. (Lower frame) The spin lattice relaxation rate  $\lambda_z$  versus reduced temperature  $\tau = (T - T_C)/T_C$  for samples A and B, in zero magnetic field. The solid lines are the results of fits to the model discussed in Sec. 4.3.4.

In the lower plot of Fig. 4.18  $\lambda_Z(T)$  is shown as a function of the reduced temperature  $\tau$ . Here it is seen that the transition for sample B is indeed broader than for sample A. The solid lines are again fits to the dipolar Heisenberg model in Eq. 4.32.

In summary, it has been shown for both directions of  $\mathbf{S}_\mu(0)$  that at ambient pressure there is a large qualitative similarity between the temperature dependencies of  $\lambda_Z(T)$  for sample A used in this thesis and sample B used in Ref. [134]. Measuring the same sample A at different instruments yields slightly different results. In the next Section the influence of the sample and instrument dependencies on the data analysis will be investigated. In spite of the sample and instrument dependencies of the results on the critical dynamics in UGe<sub>2</sub>, the comparison between ambient pressure and a pressure of 0.95 (2) GPa should be considered reliable, since here it concerns a single experiment on the same sample at the same instrument for different pressures.

#### 4.3.4 Analysis

##### Ambient pressure: Knight shift

According to Eq. 2.28 the relation between the muon Knight shift  $K^i$  and the atomic susceptibility  $\chi_i$ , with  $i = \{\mathbf{a}, \mathbf{b}, \mathbf{c}\}$ , is given by

$$K^i = \left[ C^{ii}(\mathbf{q} = \mathbf{0}) - \mathcal{N}^{ii} + \left( \frac{r_\mu H}{4\pi} \right) \right] \chi_i + A_P \chi_P. \quad (4.25)$$

Here  $\mathbf{C}(\mathbf{q} = \mathbf{0})$  is the tensor that couples the U magnetic moments  $\mathbf{m}$  to the magnetic field  $\mathbf{B}'_{\text{dip}} + \mathbf{B}_L$  (Eq. 2.24) at the muon site.  $\mathcal{N}^{ii}$  is the demagnetization factor which depends on the shape of the sample and the orientation of the external field  $\mathbf{B}_{\text{ext}}$  with respect to the sample. Because a spherically shaped sample of UGe<sub>2</sub> was used during the experiments,  $\mathcal{N}^{ii} = 1/3$  for all measurements. The experimental values found in Sec. 4.3.3 for  $dK^i/d\chi_i$  for both muon sites are summarized in Table 4.3. The last term in Eq. 4.25, the Pauli contribution, plays no role in the analysis. The first signal has a slightly larger asymmetry than the second one.

The coupling tensor  $\mathbf{C}(\mathbf{q} = \mathbf{0})$  has the special property that it has a trace equal to unity. Assuming the contact term  $r_\mu H/(4\pi)$  to be isotropic the following relation holds:

$$\sum_i \frac{dK^i}{d\chi_i} = 3 \frac{r_\mu H}{4\pi}. \quad (4.26)$$

With this equation, the contact coupling term ( $r_\mu H/4\pi$ ) is calculated and the diagonal elements of the coupling tensor  $\mathbf{C}(\mathbf{q} = \mathbf{0})$  can be determined. They are presented in Table 4.3 for both signals. ( $r_\mu H/4\pi$ ) is negative for the first signal, but positive for the second. A positive contact term is unusual. In *e.g.* DyNi<sub>5</sub> [138] and in Fe and Ni [27] it is negative. The values of  $\mathbf{C}(\mathbf{q} = \mathbf{0})$  should be compared to the calculated ones in order to be able to determine the muon sites.



**Table 4.3:** Experimental coupling parameters for the two muon sites in UGe<sub>2</sub>. The contact term  $r_\mu H/(4\pi)$  is assumed to be isotropic.

	$i$	<b>a</b>	<b>b</b>	$c$
signal 1	$dK^i/d\chi_i$	-0.062 (1)	0.074 (21)	-0.080 (37)
	$\frac{r_\mu H}{4\pi}$	-0.023 (14)	-0.023 (14)	-0.023 (14)
	$C^{ii}$	0.294 (14)	0.430 (25)	0.276 (40)
signal 2	$dK^i/d\chi_i$	0.591 (4)	0.081 (17)	-0.040 (25)
	$\frac{r_\mu H}{4\pi}$	0.211 (10)	0.211 (10)	0.211 (10)
	$C^{ii}$	0.713 (11)	0.203 (20)	0.082 (27)

In UGe<sub>2</sub> several interstitial positions with a high symmetry are available. These are the best candidates for muon stopping sites. Table 4.4 contains the coupling tensors  $\mathbf{C}(\mathbf{q} = \mathbf{0})$  for several candidate muon sites, calculated with Eq. 2.22. The dipolar interaction is very anisotropic and therefore the coupling tensor has a very strong muon-site dependence. It is clearly seen, that the experimental coupling tensor for the first signal show good agreement with the calculated tensor for the site 2b.

Even better agreement could possibly be accomplished by assuming a slightly non-isotropic contact term. This possibility has been addressed in Ref. [139] for several compounds, as well as the temperature dependence of  $(r_\mu H/4\pi)$ . The temperature dependence of the contact term in UGe<sub>2</sub> below  $T_C$  will be discussed shortly. Other possibilities will not be discussed any further in this thesis.

Unfortunately, the second signal is not in agreement with any of the high-symmetric interstitial positions. In order to find the second muon site, a systematic scan through the UGe<sub>2</sub> unit cell is required. The corresponding coupling tensor should be diagonal as well, which can be seen from the angular scans. The full angular dependence of  $K^i$  for the rotation of the external field  $\mathbf{B}_{\text{ext}}$  in the **a** – **c** plane can be written, with  $\mathcal{N}^{ii} = 1/3$ , as [140]

$$\begin{aligned}
K^i(\phi) = & \left\{ \left( C^{aa} - \frac{1}{3} + \frac{r_\mu H}{4\pi} \right) \chi_a - \left( C^{cc} - \frac{1}{3} + \frac{r_\mu H}{4\pi} \right) \chi_c \right\} \cos^2 \phi \\
& + \left( C^{cc} - \frac{1}{3} + \frac{r_\mu H}{4\pi} \right) \chi_c + \frac{1}{2} (\chi_a + \chi_c) C^{ac} \sin 2\phi
\end{aligned} \tag{4.27}$$

where  $\phi$  is the angle between  $\mathbf{B}_{\text{ext}}$  and the **a**-axis. For the rotation of  $\mathbf{B}_{\text{ext}}$  in the

**Table 4.4:** Calculated dipolar coupling tensors  $\mathbf{C}(\mathbf{q} = \mathbf{0})$  at several candidate stopping sites for the muon in UGe<sub>2</sub>. The basis for the tensor is equal to the basis of the crystallographic unit cell.

Site		Coupling tensor $\mathbf{C}(\mathbf{q} = \mathbf{0})$
2b	$(0, \frac{1}{2}, 0)$	$\begin{pmatrix} 0.251 & 0 & 0 \\ 0 & 0.453 & 0 \\ 0 & 0 & 0.296 \end{pmatrix}$
2d	$(\frac{1}{2}, 0, \frac{1}{2})$	$\begin{pmatrix} -0.635 & 0 & 0 \\ 0 & 2.308 & 0 \\ 0 & 0 & -0.672 \end{pmatrix}$
4e	$(\frac{1}{4}, \frac{1}{4}, 0)$ $(\frac{3}{4}, \frac{1}{4}, 0)$	$\begin{pmatrix} 0.020 & \pm 0.320 & 0 \\ \pm 0.320 & 0.194 & 0 \\ 0 & 0 & 0.785 \end{pmatrix}$
4f	$(\frac{1}{4}, \frac{1}{4}, \frac{1}{2})$ $(\frac{3}{4}, \frac{1}{4}, \frac{1}{2})$	$\begin{pmatrix} 0.285 & \pm 1.570 & 0 \\ \pm 1.570 & 1.758 & 0 \\ 0 & 0 & -1.043 \end{pmatrix}$
4i	$(0, 0.1539, 0)$	$\begin{pmatrix} -0.677 & 0 & 0 \\ 0 & -0.712 & 0 \\ 0 & 0 & 2.390 \end{pmatrix}$
4j	$(\frac{1}{2}, 0.1922, \frac{1}{2})$	$\begin{pmatrix} 1.615 & 0 & 0 \\ 0 & 0.197 & 0 \\ 0 & 0 & -0.813 \end{pmatrix}$

$\mathbf{a} - \mathbf{b}$  plane it is written as

$$\begin{aligned}
K^i(\phi) = & \left\{ \left( C^{aa} - \frac{1}{3} + \frac{r_\mu H}{4\pi} \right) \chi_a - \left( C^{bb} - \frac{1}{3} + \frac{r_\mu H}{4\pi} \right) \chi_b \right\} \cos^2 \phi \\
& + \left( C^{bb} - \frac{1}{3} + \frac{r_\mu H}{4\pi} \right) \chi_b + \frac{1}{2} (\chi_a + \chi_b) C^{ab} \sin 2\phi
\end{aligned} \tag{4.28}$$

The maximum frequency shift was observed when  $\mathbf{B}_{\text{ext}}$  was parallel to the  $\mathbf{a}$ -axis (see also Fig. 4.10). Comparison with the above equations leads to the conclusion that  $C^{ab}$  and  $C^{ac}$  should be zero, or at least quite small. This is supported by the fact that the spontaneous frequencies below  $T_C$  show a full asymmetry for  $\mathbf{S}_\mu(0) \perp \mathbf{a}$ , whereas no oscillations are observed for  $\mathbf{S}_\mu(0) \parallel \mathbf{a}$ .

### Spontaneous frequencies $\nu_\mu$

The experimentally observed values for  $r_\mu H/4\pi$  and  $\mathbf{C}(\mathbf{q} = \mathbf{0})$  can be used to calculate the expected spontaneous frequencies at low temperatures. For a ferromagnet in zero external field, the magnetic field at the muon site (Eq. 2.21) is generally

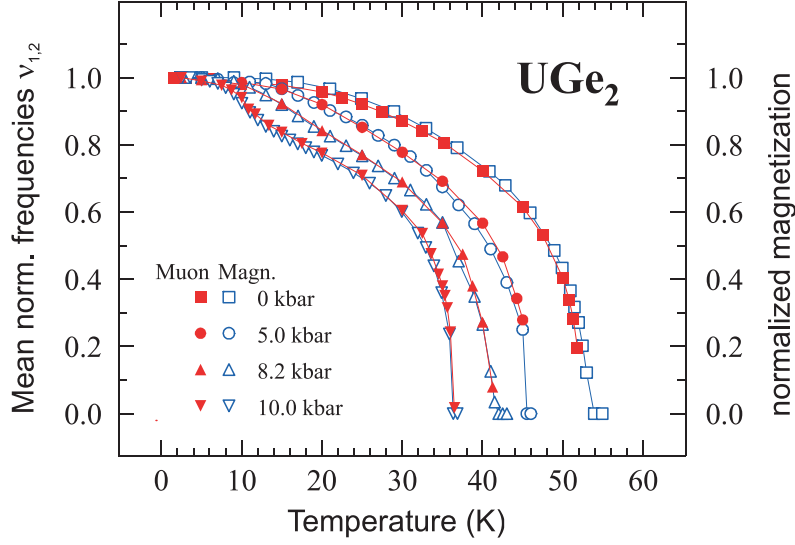


**Figure 4.19:** Normalized muon frequencies (see Fig. 4.12) averaged over the two observed muon sites (filled symbols) and normalized magnetization (open symbols, taken from Ref. [114]) versus temperature. The data have been normalized to the lowest temperature measured. The figure illustrates the empirical relation in Eq. 4.31. The lines simply link the symbols.

calculated by

$$B_{\text{loc}}^{\alpha} = \frac{\mu_0}{v} \sum_{\beta} \left[ C^{\alpha\beta}(\mathbf{q} = \mathbf{0}) + \left( \frac{r_{\mu} H}{4\pi} \right) \delta^{\alpha\beta} \right] m^{\beta} \quad (4.29)$$

where  $\delta^{\alpha\beta}$  is the Kronecker delta and  $\mathbf{m}$  the moment on the magnetic ions. Since for  $\text{UGe}_2$  the U magnetic moments [107] as well as the local field at the two muon sites (see above) are along the  $\mathbf{a}$  axis this equation reduces to

$$B_{\text{loc}}^a = \frac{\mu_0}{v} \left[ C^{aa}(\mathbf{q} = \mathbf{0}) + \left( \frac{r_{\mu} H}{4\pi} \right) \right] m^a. \quad (4.30)$$

Inserting the values for  $dK^a/d\chi_a = C^{aa} - \frac{1}{3} + (r_{\mu} H/4\pi)$  from Table 4.3 and thus assuming that the contact term  $r_{\mu} H/4\pi$  remains constant below  $T_C$ , yields  $\nu_1 = 9.68(4)$  MHz and  $\nu_2 = 32.97(14)$  MHz for  $m = 1.4 \mu_B/\text{U}$ . A comparison with the measured values,  $\nu_1 = 8.526(5)$  MHz and  $\nu_2 = 49.036(10)$  MHz (see Fig. 4.12), shows that there is some discrepancy. This problem can be solved by assuming a temperature dependent contact term. The other term,  $C^{aa}(\mathbf{q} = \mathbf{0})$  is independent of temperature. It turns out that both signals need, in absolute value, a larger contact term at lower temperatures than at higher temperatures.

In Fig. 4.19 a remarkable scaling of the muon frequencies presented in Fig. 4.12 is shown. The frequencies have been normalized with respect to the lowest temperature measured and compared to the normalized magnetization [114]. For this scaling the

empirical relation

$$\frac{M(T)}{M(0)} = \frac{1}{a_1 + a_2} \left( a_1 \cdot \frac{\nu_1(T)}{\nu_1(T=0)} + a_2 \cdot \frac{\nu_2(T)}{\nu_2(T=0)} \right) \quad (4.31)$$

holds for pressures up to 1.0 GPa. Here  $a_1$  and  $a_2$  are the asymmetries of the respective frequencies. The population distribution between the two muon sites is about 55 %-45 %.

According to Eq. 4.30, together with  $\nu_\mu = (\gamma_\mu/2\pi)B_{\text{loc}}^a$ , the normalized muon frequencies  $\nu_i$  should coincide with the normalized magnetization if and only if the contact term  $r_\mu H/(4\pi)$  is temperature independent (assuming  $C^{aa}(\mathbf{q} = \mathbf{0})$  is temperature independent). The experiments show they do not coincide. This can be seen from the fact that the frequencies  $\nu_1$  and  $\nu_2$  (Fig. 4.12) are not proportional to each other. However, Fig. 4.19 and Eq. 4.31 show that the average of the normalized frequencies does coincide with the normalized magnetization. Inserting Eq. 4.30 into Eq. 4.31, it is clear that the contact terms for both muon sites are intimately related. To quantify this relation, it can be assumed that, for  $T < T_C$ ,  $\left(\frac{r_\mu H}{4\pi}\right)$  is described by the sum of a constant term and a temperature dependent term  $\Delta_i(T)$ , *i.e.*  $\left(\frac{r_\mu H}{4\pi}\right)_i(T) = \text{const.} + \Delta_i(T)$ . Here the value of const. is taken from Table 4.3 for  $T > T_C$  and therefore, as an approximation,  $\Delta_i(T) \approx 0$  for  $T > T_C$ . No further assumptions are made about the exact temperature dependence of  $\Delta_i(T)$ . Using Eq. 4.30 and Table 4.3 for the values of  $C^{aa}(\mathbf{q} = \mathbf{0})$ , it follows from Eq. 4.31 and  $\nu_\mu = (\gamma_\mu/2\pi)B_{\text{loc}}^a$  that  $\Delta_2(T)/\Delta_1(T) = -5.8$ , which is independent of temperature. This is consistent with  $\left(\frac{r_\mu H}{4\pi}\right)_2 / \left(\frac{r_\mu H}{4\pi}\right)_1 = -9.2(5.9)$  (see Table 4.3).

From Eq. 4.30 it is clear why the first signal in Fig. 4.12 shows a much smaller pressure dependence than the second signal at low temperatures. From magnetization data [114] it is known that the saturation magnetic moment hardly changes with pressure up to 1.2 GPa. Therefore, any pressure dependence of the muon frequencies at low temperatures should come from  $\frac{1}{v} \left( C^{aa}(\mathbf{q} = \mathbf{0}) + \left(\frac{r_\mu H}{4\pi}\right) \right)$ . Remember that  $C^{aa}(\mathbf{q} = \mathbf{0})$  has two contributions, see Eq. 2.24. The first contribution is the Lorentz field  $\mathbf{B}_L$  which originates from the uranium magnetic moments outside the Lorentz sphere. These magnetic moments are treated as a continuous magnetization with the Lorentz sphere as a non-magnetic cavity. The second contribution is the dipolar field  $\mathbf{B}'_{\text{dip}}$  which is a sum of dipolar fields from the uranium magnetic moments within the Lorentz sphere. The volume  $v$  can be assumed constant in pressure. With an estimated value for the compressibility  $\kappa = 0.01 \text{ GPa}^{-1}$ , the volume change is about 1% up to 1 GPa. For the first signal,  $C^{aa}(\mathbf{q} = \mathbf{0}) + \left(\frac{r_\mu H}{4\pi}\right) = 0.271(1)$  is close to  $\frac{1}{3}$  (the contribution of the Lorentz field) for the first signal. However, for the second signal,  $C^{aa}(\mathbf{q} = \mathbf{0}) + \left(\frac{r_\mu H}{4\pi}\right) = 0.924(4)$  is much larger than  $\frac{1}{3}$ . This means that the contribution  $\mathbf{B}'_{\text{dip}}$  to  $C^{aa}(\mathbf{q} = \mathbf{0})$  and the contact term  $\left(\frac{r_\mu H}{4\pi}\right)$  is small for the first signal and large for the second. This implies that any pressure dependence

in  $\mathbf{B}'_{\text{dip}}$  or in  $\left(\frac{r_{\mu}H}{4\pi}\right)$  will have a much larger influence on the muon frequency  $\nu_2$  than on  $\nu_1$ . It should be noted that the pressure dependence of  $\mathbf{B}'_{\text{dip}}$  is probably caused by a relative displacement of the atoms under pressure [110].

### Critical fluctuations at ambient pressure and at 0.95 (2) GPa

The theory of critical phenomena used to explain the data presented in Figs. 4.14, 4.16, 4.17, and 4.18 has been developed by Yaouanc *et al.* [27] and applies to  $\mu\text{SR}$  measurements of the spin-lattice relaxation rate  $\lambda_Z(T)$  in the vicinity of  $T_C$ . In the next two paragraphs a few features of this theory will be discussed.

The theory concerns continuous phase transitions, *i.e.* second order transitions. As the critical temperature is approached, the fluctuations tend to slow down. This slowing down process is expected to manifest itself in  $\lambda_Z(T)$ , which probes the dynamics, by a maximum at the ordering temperature. Although dipolar interactions between magnetic ions are usually very weak relative to the Heisenberg interaction, they gain importance near  $T_C$ . This can easily be seen when one considers that dipolar interactions are long-range in nature. In the critical regime only long wavelength interactions (small  $\mathbf{q}$ ) are of importance. The Hamiltonian of the system is a sum of the Heisenberg and dipole interactions. The temperature dependence of  $\lambda_Z(T)$  in the critical regime has been derived by static and dynamic scaling laws from the mode coupling theory [27, 141, 142]. The model predicts

$$\lambda_Z = \mathcal{W} [a_L I^L(\phi) + a_T I^T(\phi)] . \quad (4.32)$$

Here  $L$  and  $T$  refer to the orientation (longitudinal or transversal) of the fluctuation mode relative to its wave vector  $\mathbf{q}$ .  $\mathcal{W}$  is a non-universal constant.  $I^{L,T}$  are scaling functions (shown in Fig. 4.20), which in turn depend on the wave vector dependent susceptibilities  $\chi^{L,T}(\mathbf{q})$  and fluctuation rates  $\Gamma^{L,T}(\mathbf{q})$ . They account for the longitudinal and transversal fluctuations. The temperature dependence follows through  $\phi = \tan^{-1}(q_D \xi)$ . Here  $\xi = \xi_0 (|T - T_C|/T_C)^{-\nu}$  is the correlation length and  $q_D$  the dipolar wave vector, which determines the relative strength of the dipolar and exchange interactions. For three-dimensional Heisenberg interactions the critical exponent amounts to  $\nu \simeq 0.69$ . The weighting factors  $a_L$  and  $a_T$  depend only on the characteristics of the dipole and hyperfine fields at the muon site and in fact determine the sensitivity to longitudinal or transversal fluctuation modes. It should be stressed that when the measurements show a saturation in  $\lambda_Z(T)$ , mostly longitudinal fluctuations play a dominant role in  $\lambda_Z$  [142]. In that case mainly modes with  $q \approx q_D$  are probed.

It is now shown how the dipolar wave vector  $q_D$ , the magnetic moment  $\mu$ , and the magnetic correlation length  $\xi_0 = \xi(T = 2T_C)$  can be determined from the experiment. For a given muon site, the experimental value of  $\mathcal{W}$  is known. The theoretical value of  $\mathcal{W}$  is obtained from mode coupling theory [27]:

$$\mathcal{W} = \frac{4\pi}{3P} \gamma_{\mu}^2 \hbar \sqrt{\mu_0 k_B T_C} \frac{q_D^{3/2}}{2\mu} \quad (4.33)$$

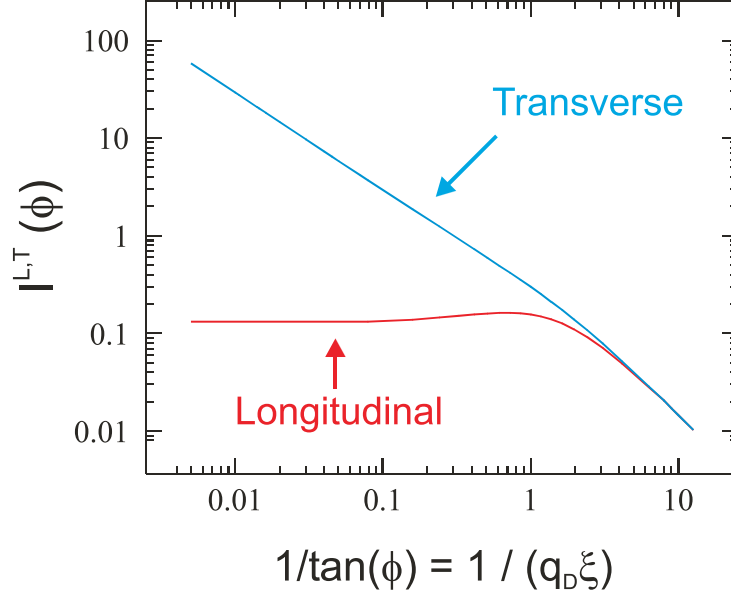


**Figure 4.20:** The two functions  $I^{L,T}(\phi)$  versus  $1/\tan(\phi) = 1/(q_D \xi)$ . The functions  $I^L(\phi)$  and  $I^T(\phi)$  account for the contributions of the fluctuations, longitudinal and transverse to the wave vector  $\mathbf{q}$ , respectively, to the muon spin-lattice relaxation.  $q_D$  is the dipolar wave vector and  $\xi$  the correlation length. Only  $\xi$  depends on temperature. Figure taken from Ref. [143].

where  $P = 5.1326$ ,  $k_B$  the Boltzmann constant, and  $\mu$  is the magnetic moment. From the same theory the fluctuation rate is predicted to be  $\hbar\Gamma(q) = \Omega q^{5/2}$  where  $\Omega$  is given in Ref. [27]. In the case mainly longitudinal fluctuations are probed in the experiment, the observed dynamics is largely driven by fluctuations around  $q_D$  [142]. Then the fluctuation rate  $\nu_f$  can be written as:

$$\nu_f \simeq \Gamma(q_D) = \frac{P}{2\pi^2 \hbar} \sqrt{\mu_0 k_B T_C} (2\mu) q_D^{3/2}. \quad (4.34)$$

Now  $q_D$  and  $\mu$  are calculated by

$$q_D = \left( \frac{3\pi}{2\gamma_\mu^2 \mu_0 k_B T_C} \cdot \mathcal{W} \nu_f \right)^{1/3} \quad \text{and} \quad \mu = \left( \frac{8\pi^3 \hbar^2 \gamma_\mu^2}{12P^2} \cdot \frac{\nu_f}{\mathcal{W}} \right)^{1/2} \quad (4.35)$$

From the calculated value of  $q_D$  and the measured value of  $q_D \xi_0$ , which determines the width of the plateau for the longitudinal fluctuations,  $\xi_0$  is determined. For the value of  $\xi_0$  in the case of  $T > T_C$ , the symbol  $\xi_0^+$  will be used, and  $\xi_0^-$  for  $T < T_C$ .

The data of the relaxation rate  $\lambda_Z$  as a function of reduced temperature  $\tau$  in Figs. 4.14, 4.16, 4.17, and 4.18 have been fitted to Eq. 4.32. These fits are shown in the figures as well. The extracted experimental parameters, the products  $q_D \xi_0^+$ ,  $q_D \xi_0^-$ ,  $\mathcal{W} a_L$ , and  $\mathcal{W} a_T$ , are summarized in Table 4.5. The reason for measuring both samples A and B also on GPS, was to explain the difference in fitting values

at ambient pressure for  $\mathbf{S}_\mu(0) \perp \mathbf{a}$  ( $q_D\xi_0^+ = 0.021(2)$  versus  $q_D\xi_0^+ = 0.0052(7)$ ). Several conclusions can be drawn from Table 4.5. First of all there is a dependence on instrument. This follows from the fact that for sample B ( $\mathbf{S}_\mu(0) \parallel \mathbf{a}$ ) the values of  $q_D\xi_0^+$  and  $q_D\xi_0^-$  are about three times smaller on GPS than on EMU. Also sample A shows slightly different results on GPD and on GPS. Second of all, there is a sample dependence. Looking at the measurements on GPS ( $\mathbf{S}_\mu(0) \parallel \mathbf{a}$ ) sample B has a larger  $q_D\xi_0^+$  than sample A.

Similar conclusions can be drawn for the weighting factor  $\mathcal{W}a_L$  and  $\mathcal{W}a_T$ . For the  $\mathbf{S}_\mu(0) \parallel \mathbf{a}$  orientation, the values for  $\mathcal{W}a_L$  seem to be in agreement with each other. For  $\mathbf{S}_\mu(0) \perp \mathbf{a}$  the difference is larger. Measuring the sample A at GPD (in the pressure cell) yields larger values for  $\mathcal{W}a_L$  than at GPS. Sample B on EMU has an even lower value. Unfortunately, this sample B was not measured at GPS. In general, however,  $\mathcal{W}a_T$  is much smaller than  $\mathcal{W}a_L$ . Because of the small values for  $\mathcal{W}a_T$  and the limited number of data points, it was difficult to get precise values.

In addition to the zero-field measurements, small longitudinal fields have been applied at fixed temperature, *i.e.* parallel to  $\mathbf{S}_\mu(0)$ . The relaxation rate  $\lambda_Z$  for sample B, measured on EMU, was almost completely suppressed for fields as small 2 mT [134]. For sample A, measured at GPD, the relaxation rate was suppressed for 5 mT at both ambient pressure and at 0.95(2) GPa (see Fig. 4.16). According to Eq. 2.20 the relaxation rate  $\lambda_Z$  in an external longitudinal magnetic field  $B_{\text{ext}}$  is described by

$$\lambda_Z(B_{\text{ext}}) = \frac{2\Delta^2\nu_f}{(\gamma_\mu B_{\text{ext}})^2 + \nu_f^2} = \frac{2\Delta^2\tau_c}{1 + \gamma_\mu^2 B_{\text{ext}}^2 \tau_c^2} \quad (4.36)$$

Here  $\Delta$  is the width of the field distribution at the muon site,  $\nu_f = 1/\tau_c$  the fluctuation rate of the fluctuating magnetic field with a correlation time  $\tau_c$ , and  $\gamma_\mu = 851.62 \text{ Mrad s}^{-1}\text{T}^{-1}$  the gyromagnetic ratio of the muon. For zero field this expression reduces to  $\lambda_Z(0) = 2\Delta^2\tau_c$ . With Eq. 4.36 and the field dependence of  $\lambda_Z(0)$ , as shown in Fig. 4.16, an estimate of the fluctuation rate  $\nu_f$  can be made. In Table 4.5 the field dependencies have been assumed independent of instrument.

Now before analyzing the data further, first the main features of the data in the vicinity of  $T_C$  will be summarized.

1.  $\text{UGe}_2$  is known to be a very anisotropic magnetic compound [108]. This is also seen from both the angular scans and the temperature scans in the Knight shift measurements. A magnetic field parallel to the  $\mathbf{a}$  axis induces a large Knight shift, whereas a field perpendicular to  $\mathbf{a}$  induces a very small Knight shift. This is illustrated in the Clogston-Jaccarino plots for the magnetic susceptibilities  $\chi_i$ . However, the dependence of the relaxation rate  $\lambda_Z(T)$  in the critical regime shows very weak anisotropy for the orientation of  $\mathbf{S}_\mu(0)$  with respect to  $\mathbf{a}$ . For both orientations, the values of  $\mathcal{W}a_L$  differ only by a factor of 2. This is shown for sample B on EMU and sample A on GPS.  $\mu\text{SR}$  is generally very sensitive to the anisotropy of magnetic fluctuations, as was nicely demonstrated in  $\text{NdRh}_2\text{Si}_2$  [144].







2. The measurements in applied magnetic field show that the relaxation rate  $\lambda_Z(B)$  in the critical regime is suppressed by a magnetic field in the order of 2 - 5 mT. Susceptibility data shows that a magnetic field of 5 mT induces a magnetic moment of less than  $0.01 \mu_B/U$ . Therefore it is hard to imagine that the fluctuations of the full U moments, which have a saturation magnetization of  $1.4 \mu_B/U$  at low temperatures, are suppressed by a field of 5 mT. Moreover, a suppression in a field of 5 mT yields a correlation time of  $\tau_c \approx 0.4 \mu s^{-1}$ . This can be considered to be quasi-static and does not reflect the expected rate for the large magnetic moments on the U atoms.
3. Since according to Eq. 4.36 the value of  $\lambda_Z$  in zero field is given by  $\lambda_Z = 2\Delta^2/\nu_f$ , it follows that  $\Delta \approx 0.3$  mT at the muon site. This indicates a very small distribution in local magnetic fields at the muon site.

Based on these observations it is proposed that in these experiments the muon spin is relaxed by the polarization of the conduction electrons. It is expected that this polarization is much less anisotropic than localized magnetic moments. Because of the strong electronic correlations in  $UGe_2$  (reflected by the large value of the Sommerfeld coefficient  $\gamma$  in the specific heat) these magnetic fluctuations are slow. Moreover, this assumption could account for the small value of  $\Delta$  observed.

So far only values for the products  $\mathcal{W}a_L$  and  $\mathcal{W}a_T$  were presented. In order to estimate a value for  $\mathcal{W}$  appearing in Eq. 4.35, estimates for  $a_L$  and  $a_T$  should be made. Theoretically, they are given by [27]

$$a_L = \frac{1}{2} [(1 - p_x)^2 + (1 - p_y)^2] \quad a_T = p_x^2 + p_y^2 \quad \mathbf{S}_\mu(0) \parallel \mathbf{z} \quad (4.37)$$

with  $p_\alpha = C^{\alpha\alpha}(\mathbf{q} = \mathbf{0}) + r_\mu H/(4\pi)$ . For the two muon sites (Table 4.3) with different orientations of  $\mathbf{S}_\mu(0)$  this would give values of the ratio  $a_L/a_T$  in the range of 0.2 to 4.0. However, experimentally only  $a_L \gg a_T$  is observed for all orientations of  $\mathbf{S}_\mu(0)$  (see Table 4.5).

In the expression for  $p_\alpha$  the term  $C^{\alpha\alpha}(\mathbf{q} = \mathbf{0})$  accounts for the fluctuations due to the localized magnetic moments [27]. However, when the muon only probes the itinerant part of the fluctuating magnetization, this term should be omitted and only the contact term  $r_\mu H/(4\pi)$  remains. With the data in Table 4.3  $a_L = 1.05$  and  $a_T = 0.001$  is obtained for the first muon site, and  $a_L = 0.62$  and  $a_T = 0.089$  for the second muon site. Since both muon sites have nearly equal population, the first site being slightly more populated than the second, the weighted average is  $a_L = 0.85$  and  $a_T = 0.04$ , with a ratio of  $a_L/a_T = 21$ , which is close to the ratio obtained by the data in Table 4.5 considering the uncertainty in the determination of  $a_T$ .

Now, using Eq. 4.35, the values for the magnetic moment  $\mu$ , which depolarizes the muon spin, the dipolar wave vector  $q_D$  and the correlation lengths  $\xi_0^+$  and  $\xi_0^-$  of the fluctuations can be calculated. They are shown in Table 4.5. Clearly, despite of all the sample and instrument dependencies, the overall picture is that the magnitude of the fluctuating polarization, that depolarizes the muon spin, is  $\mu = 0.02(1) \mu_B$ .

The correlation lengths  $\xi_0^+$  and  $\xi_0^-$  of the magnetic fluctuations is of the order of a lattice spacing for sample A, but several times larger for sample B. However, here also instrument dependence plays a role. The dipolar wave vector is about  $q_D = 0.0010 \text{ \AA}^{-1}$  for sample B, but about  $q_D = 0.0022 \text{ \AA}^{-1}$  for sample A.

The main results are given by the pressure experiments on sample A. These results at ambient pressure and at 0.95 (2) GPa are not sample or instrument dependent because they were measured under identical conditions. The values for  $\mu$  show that the polarization may be slightly reduced. The same applies for the dipolar wave vector  $q_D$ . The main difference, leading to different critical dynamics (see Fig. 4.16) is the enhancement of the correlation length  $\xi_0^+$  of the magnetic fluctuations.

### 4.3.5 Discussion

#### High pressure: spontaneous frequencies $\nu_\mu$ and depolarization rates $\lambda_X$

By consideration of classical Larmor precession, as in Chapter 2, it can be understood that the muon spin is not sensitive to parallel magnetic field fluctuations and therefore only magnetic excitations are probed which are perpendicular to the muon spin. For  $\mathbf{S}_\mu(0) \parallel \mathbf{B}_{\text{loc}}$ , where  $\mathbf{B}_{\text{loc}}$  is the local magnetic field at the muon site and  $\mathbf{B}_{\text{loc}} \parallel \mathbf{a}$  (with  $\mathbf{a}$  the easy magnetic axis) in the case of UGe<sub>2</sub>, only excitations along the  $\mathbf{b}$  and  $\mathbf{c}$  axis are probed. This includes spin waves and magnetic fluctuations. This depolarization is called the spin-lattice relaxation  $\lambda_Z$ . For  $\mathbf{S}_\mu(0) \perp \mathbf{a}$ , the depolarization is due to magnetic excitations along  $\mathbf{a} \times \mathbf{S}_\mu(0)$  and the  $\mathbf{a}$  axis, and in addition due to the loss of Larmor phase coherence because of static magnetic inhomogeneity (crystal defects, domain structures, etc.). This is called the transverse depolarization  $\lambda_X$ . Unfortunately, because of the orientation of the  $\mathbf{a}$  axis with respect to the cylindrical shape of the sample, it was only possible to measure  $\lambda_X$ .

The measurements in Fig. 4.12 show the development of a peak in  $\lambda_{X,i}$  around  $T_X$  which can in principle be attributed to three different cases. First, some extra inhomogeneity like a small spin reorientation or a charge and spin density wave [145, 146] can cause the muon spin polarization to decrease. Second, a change in the spin wave spectrum, facilitating the excitation of spin waves, can be responsible. Finally, a slowing down of the fluctuations, similar to a paramagnetic-to-ferromagnetic-state transition is possible.

Extra inhomogeneity can be ruled out on the basis of neutron scattering experiments. Extensive neutron studies [147] have shown no sign of static order due to a charge and spin density wave. It has also been shown [116] that reorientation of the magnetic moments when crossing the transition at  $T_X$  at 1.2 GPa, is unlikely. Measurements of the phonon spectrum [148] indicate no special feature around  $T_X$ . Moreover, the  $\mu$ SR spectra can all be fitted by the exponentially damped oscillations of Eq. 4.22. If static inhomogeneities would be present, then the damping would rather be Gaussian in nature. These findings point in the direction of extra depolarization by magnetic fluctuations or spin waves.

A change in the spin wave spectrum at  $T_X$  that facilitates the excitations could lead to an increase in  $\lambda_X$ , but should be considered highly improbable. Although perhaps theoretically possible, no experimental report has suggested this exotic possibility up to date. It has been shown that the anomaly shows the usual features of a phase transition [115]. The strong resemblance of the peak in  $\lambda_X$  at  $T_X$  with the peak at  $T_C$  (*e.g.* Fig. 4.17) also points in this direction. From here on it will be considered a phase transition. It should however be stressed that only measurements of  $\lambda_Z$  (*i.e.*  $\mathbf{S}_\mu(0) \parallel \mathbf{a}$ ) can unambiguously demonstrate that at high pressures extra spin dynamics develop that are normally associated with a phase transition, since  $\lambda_Z$  is not sensitive to inhomogeneity of the magnetic moments.

When  $T_C$  is approached from high temperatures, the paramagnetic fluctuations tend to slow down. In  $\mu$ SR, the relaxation rate  $\lambda_Z$  can be described by  $\lambda_Z = 2\Delta^2\tau_c$ , where  $\Delta$  is the width of the field distribution at the muon site and  $\tau_c$  is the correlation time of the fluctuations. Therefore,  $\lambda_Z$  increases for  $T \downarrow T_C$ . For  $\text{UGe}_2$  this is demonstrated in Fig. 4.16 at ambient pressure and at  $P = 0.95(2)$  GPa. Below  $T_C$ ,  $\lambda_X$  is measured for the orientation of  $\mathbf{S}_\mu(0)$  perpendicular to  $\mathbf{a}$ .  $\lambda_X$  decreases at temperatures below  $T_C$  because less fluctuations (*i.e.* spin waves) are excited at low temperatures.

The slowing down of the magnetic moments as  $T \downarrow T_C$  has also been shown by inelastic neutron scattering [149]. In this study  $\Gamma_{\mathbf{q}}$  was measured for several  $\mathbf{q}$  values around  $T_C$ . For each (fixed value of)  $\mathbf{q}$  there was a minimum in  $\Gamma_{\mathbf{q}}(T)$  as a function of temperature at  $T = T_C$ . Because  $\tau_c^{-1}(\mathbf{q}) \propto \Gamma_{\mathbf{q}}$ , the link between  $\mu$ SR and inelastic neutron scattering is roughly indicated by the relation  $\lambda_Z(T) \propto \Gamma^{-1}(T)$  with  $\Gamma$  some average of  $\Gamma_{\mathbf{q}}$  over  $\mathbf{q}$ . A minimum in  $\Gamma(T)$  therefore corresponds to a maximum in  $\lambda_Z(T)$ . Unfortunately, no neutron study around  $T_X$  could be found in literature for high pressures.

The present  $\mu$ SR data were in fact performed around  $T_X$  and at high pressure. As  $T_X$  is approached from high temperatures,  $\lambda_X \approx \Gamma^{-1}(T)$  increases, indicating a slowing down of the spin dynamics, as discussed above. (At the moment, however, this remains somewhat speculative since only  $\lambda_Z$  can prove this slowing down unambiguously.) If so, this means that a minimum in  $\Gamma(T)$  at  $T = T_X$  would be found, just like at ambient pressure around  $T_C$ . As suggested in Ref. [149], and theoretically supported by numerical calculations [150], a decrease of  $\Gamma$  ( $\propto \lambda_X^{-1}$ ) enhances the superconducting transition temperature  $T_{\text{sc}}$ . The transition at  $T_X$  vanishes at the same pressure as where  $T_{\text{sc}}$  is maximum and therefore it seems likely that the observed slowing down of the magnetic fluctuations could play a role in the formation of Cooper pairs.

### High pressure: critical fluctuations

All the data in the critical regime of  $\text{UGe}_2$  unambiguously show that the spin-lattice relaxation rate  $\lambda_Z(T)$  increases as  $T_C$  is approached from above, but does not diverge. This is explained by taking into account the dipolar interactions between

the magnetic moments and by assuming that the muon spin is only relaxed by fluctuations that are longitudinal to their wave vector  $\mathbf{q}$  [27]. The reason why hardly any transversely polarized fluctuations are detected by the muon, is given in the paragraph below Eq. 4.37. The assumption that the muon only probes the itinerant part of the magnetic fluctuations, automatically leads to  $a_L \gg a_T$ . A consequence of the high sensitivity to especially longitudinal fluctuations is that the muon spin is for the greater part relaxed by fluctuation modes with  $q \approx q_D$  [142], where  $q_D$  is the dipolar wave vector and determines the relative strength of the dipolar and exchange interactions in the system. From the measurements it follows that  $q_D \approx 0.002 \text{ \AA}^{-1}$ . The  $\mu$ SR technique probes fluctuations with very small  $q$  values, that are largely inaccessible to (neutron) scattering techniques.

A fully consistent analysis of the experimental critical dynamics is obtained by assuming an itinerant nature of the magnetism that relaxes the muon spin. It explains the low anisotropy in the data for different directions of  $\mathbf{S}_\mu(0)$ . From the calculations a small effective moment of  $\mu \approx 0.02(1) \mu_B$  follows, which is consistent with the quasi-static nature as observed from measurements in magnetic field. Finally, it explains why at ambient as well as at high pressures  $\lambda_Z$  can be described satisfactorily by the Heisenberg model with dipolar interactions, whereas UGe<sub>2</sub> is an Ising system.

The anisotropy of  $\lambda_Z$  for different directions of  $\mathbf{S}_\mu(0)$  can be explained by a possible anisotropy of the contact coupling term  $r_\mu H/(4\pi)$ . See Sec. 4.3.4 for a discussion. Recently it has been acknowledged for several compounds that the contact term is indeed anisotropic [139].

The  $\mu$ SR result that the polarization of the conduction electrons in UGe<sub>2</sub> is as small as  $\mu \sim 0.02(1) \mu_B$  at ambient pressure as well as at high pressure, is supported by polarized neutron experiments. Since this is a diffraction technique, the polarization of the delocalized electrons can not be determined directly. Delocalized states possess a form factor that falls rapidly to zero by about  $0.1 \text{ \AA}^{-1}$  in  $(\sin \theta)/\lambda$  and thus are hard to observe in a neutron experiment. The polarization of these states can, however, be determined by the difference between the uranium moment deduced from bulk measurements and the moment derived from the form factor measurements (localized states). For UGe<sub>2</sub>, at ambient pressure [107] an inverse Fourier technique shows that the magnetization distribution is concentrated at the U sites. Also, the diffuse magnetic contribution is estimated to be  $\approx 0.05(3) \mu_B/\text{U}$ , which is small compared to the ordered magnetic moment of  $\approx 1.4 \mu_B/\text{U}$ . This means that the polarization of the conduction electrons in UGe<sub>2</sub> should be small. For UPd<sub>2</sub>Al<sub>3</sub> [151] it was found that  $0.140(4) \mu_B$  is localized at each U atom with a diffuse part of  $0.020(4) \mu_B$ . This implies that 12 % of the total magnetization is delocalized. In U<sub>2</sub>Co<sub>2</sub>Sn [152] a localized magnetic moment of  $0.118(3) \mu_B$  was obtained and a delocalized part of  $0.021(4) \mu_B$ . Thus 15 % is diffuse. With a diffuse part of about only 1 %, UGe<sub>2</sub> contrasts these two compounds, but is comparable to *e.g.* USb<sub>0.8</sub>Te<sub>0.2</sub> [153] and in agreement with previous  $\mu$ SR results [134].

The data therefore suggest that UGe<sub>2</sub> is a dual system where itinerant magnetism

coexists with localized  $5f$  magnetism. Within this model the weakly anisotropic magnetic fluctuations probed by  $\mu$ SR arise from the small polarization of the conduction electrons. The large anisotropy of the bulk magnetization arises from the localized  $5f$  states. No depolarization due to these states is detected in the present  $\mu$ SR experiments. This can be understood from a simple estimation of fluctuation rate  $\nu_f \approx k_B T_C / \hbar$ , which leads to a fluctuation rate of the order of THz instead of the observed MHz. The relaxation rate  $\lambda_Z$  corresponding to such a large fluctuation rate is too small to be observed because of strong motional narrowing. In contrast, URhGe, with a Curie temperature 4 to 5 times smaller than UGe<sub>2</sub> (depending on pressure) is a compound in which a relaxation of both localized and delocalized states is observed. A thorough discussion of URhGe follows in Chapter 5.

Returning to the polarized neutron experiments, at high pressures and low temperatures (1.2 GPa [116] and 1.4 GPa [154]) it is found that both  $C_2$  (the ratio between the orbital and total uranium magnetic moment) and  $R_L$  (the ratio between the orbital and spin moment) are almost the same as at ambient pressure. Although the measured  $R_L$  is reduced compared to the value for free U<sup>3+</sup> or U<sup>4+</sup> ions, indicating a certain degree of delocalization of the  $5f$  electrons, it should be concluded that also at higher pressures the magnetic moments are mainly localized, with a small itinerant polarization.

The idea of a system of two more or less separated magnetic subsets has been presented in literature before. Several techniques, among which  $\mu$ SR, have shown anomalous behavior in UPd<sub>2</sub>Al<sub>3</sub> [124, 155, 156, 157, 158], UCu<sub>5</sub> [159], and USb [160], which was attributed to two different types of magnetism.

If in UGe<sub>2</sub> indeed localized magnetism coexists together with itinerant  $5f$  states with small polarization, as strongly suggested by the  $\mu$ SR data presented in this Chapter and supported by polarized neutron scattering, this has implications for the nature of the Cooper pairs in the superconducting state. Assuming an itinerant nature of the ferromagnetism, theoretical studies have shown the possibility of spin-triplet superconductivity [89, 90, 91, 92]. In this case the electrons forming the Cooper pairs are also responsible for the strong ferromagnetism. Other studies [100, 101], however, have shown that spin-singlet superconductivity is still feasible under the constraint that conducting electrons involved in the superconductivity and localized electrons involved in the ferromagnetic order belong to different subsets of  $5f$  electrons. The pairing mechanism is then based on the interaction of electron spins via localized magnetic moments. *The  $\mu$ SR data presented in this Chapter suggest the latter case of Cooper pairs of itinerant electrons with small polarization in a frame of magnetic U ions.* Whether the Abrikosov-Suhl mechanism is indeed the true pairing mechanism or not, can not be concluded from the present data. However, the other theoretical models [89, 90, 91, 92] seem to contradict the present results.

### 4.3.6 Conclusions

The results from the data in the critical regime, presented in this Chapter, suggest a coexistence of two subsystems with localized  $5f$  states responsible for the magnetic ordering and delocalized states responsible for the superconducting properties. It is likely that electrons do not participate in both phenomena simultaneously, but are separated either in real space and/or in reciprocal space, *i.e.* different parts of the Fermi surface.

The depolarization of the spontaneous frequencies exhibit a peak at temperature  $T_X$ . It is shown that the peak could possibly develop because of the slowing down of magnetic fluctuations. As the transition at  $T_X$  vanishes at the same pressure as where  $T_{sc}$  is maximum, it is likely that the observed slowing down of the magnetic fluctuations plays an important role in the formation of Cooper pairs. The  $\mu$ SR data show that it seems likely that the observed slowing down of the magnetic fluctuations could play a role in the formation of Cooper pairs.

## Appendix: Effect of stray fields induced by a homogeneously magnetized sample on 3D neutron depolarization measurements

In this appendix the magnetic induction  $\mathbf{B}$ , generated by a uniformly magnetized sample with length  $l$ , width  $w$ , and thickness  $t$  (see Fig. 4.21), will be calculated. Moreover, analytical expressions will be given for the line integrals of  $\mathbf{B}$  along the path of a neutron. The center of the sample is taken as the origin of the reference frame.

The starting point of the calculations is the Biot-Savart law

$$\mathbf{B}(x, y, z) = \frac{\mu_0}{4\pi} \int_S \frac{(\mathbf{M} \times \mathbf{n}) \times \mathbf{r}}{r^3} dS + \frac{\mu_0}{4\pi} \int_\tau \frac{(\nabla \times \mathbf{M}) \times \mathbf{r}}{r^3} d\tau, \quad (4.38)$$

where  $\mu_0 = 4\pi \times 10^{-7}$  H/m,  $\mathbf{M}$  is the magnetization,  $\mathbf{n}$  the unit vector perpendicular to the surface  $S$  of the sample,  $\mathbf{r}$  the vector pointing from the surface  $S$  to the point  $(x, y, z)$ , and  $\tau$  the volume of the sample. Since the sample has a homogeneous

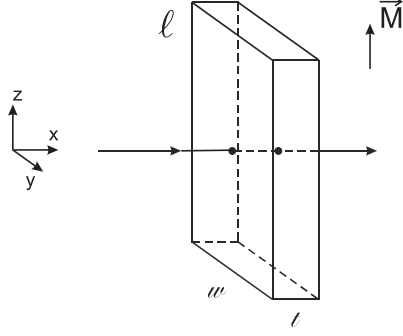


**Figure 4.21:** Schematic layout of a homogeneously magnetized rectangular sample.

magnetization, the second term vanishes and, with  $\mathbf{m} = \mathbf{M}/M$ ,

$$\mathbf{B} = \frac{\mu_0 M}{4\pi} \int_S \frac{(\mathbf{m} \times \mathbf{n}) \times \mathbf{r}}{r^3} dS. \quad (4.39)$$

is obtained.

A straightforward but tedious calculation shows that

$$\begin{aligned} B_x &= -\frac{\mu_0 M}{4\pi} \sum_{\epsilon_1, \epsilon_2, \epsilon_3 = \pm 1} \epsilon_1 \epsilon_2 \epsilon_3 \ln [\mathcal{S} - (2y + \epsilon_2 w)] \\ B_y &= -\frac{\mu_0 M}{4\pi} \sum_{\epsilon_1, \epsilon_2, \epsilon_3 = \pm 1} \epsilon_1 \epsilon_2 \epsilon_3 \ln [\mathcal{S} - (2x + \epsilon_1 t)] \\ B_z &= \frac{\mu_0 M}{4\pi} \sum_{\epsilon_1, \epsilon_2, \epsilon_3 = \pm 1} \epsilon_1 \epsilon_2 \epsilon_3 \arctan \left( \frac{2z + \epsilon_3 l}{(2x + \epsilon_1 t)(2y + \epsilon_2 w)} \mathcal{S} \right), \end{aligned} \quad (4.40)$$

where

$$\mathcal{S} = \sqrt{(2x + \epsilon_1 t)^2 + (2y + \epsilon_2 w)^2 + (2z + \epsilon_3 l)^2}. \quad (4.41)$$

The rotation of the polarization of a neutron beam depends on the line integral of the magnetic field along the neutron path. From the Larmor equation  $\frac{d}{dt} \mathbf{P}(t) = \gamma \mathbf{P}(t) \times \mathbf{B}(t)$ , or equivalently  $\frac{d}{dx} \mathbf{P}(x) = (\gamma/v) \mathbf{P}(x) \times \mathbf{B}(x)$  where  $\gamma = 1.83 \times 10^8 \text{ s}^{-1} \text{ T}^{-1}$  the gyromagnetic ratio of the neutron and  $v$  its velocity, the general solution

$$\mathbf{P}(x, y, z) = \left\{ \exp \left( \frac{\gamma}{v} \int_{-\infty}^x \overline{\overline{\mathbf{B}}}(x', y, z) dx' \right) \right\} \mathbf{P}(-\infty, y, z) \quad (4.42)$$

is obtained, where the magnetic-field tensor  $\overline{\overline{\mathbf{B}}}$  is defined as

$$\overline{\overline{\mathbf{B}}}(x, y, z) = \begin{pmatrix} 0 & B_z & -B_y \\ -B_z & 0 & B_x \\ B_y & -B_x & 0 \end{pmatrix} (x, y, z). \quad (4.43)$$



Thus, in order to calculate the rotation of the neutron-beam polarization because of a homogeneously magnetized sample, the following line integrals are required

$$\begin{aligned}
X(y, z) &= \int_{-\infty}^{\infty} B_x(x', y, z) dx' = 0 \\
Y(y, z) &= \int_{-\infty}^{\infty} B_y(x', y, z) dx' = \\
&\quad -\frac{t\mu_0 M}{4\pi} \sum_{\epsilon_2, \epsilon_3} \epsilon_2 \epsilon_3 \ln((2y + \epsilon_2 w)^2 + (2z + \epsilon_3 l)^2) \\
Z(y, z) &= \int_{-\infty}^{\infty} B_z(x', y, z) dx' = \\
&\quad \frac{t\mu_0 M}{2\pi} \sum_{\epsilon_2, \epsilon_3} \epsilon_2 \epsilon_3 \arctan\left(\frac{2z + \epsilon_3 l}{2y + \epsilon_2 w}\right)
\end{aligned} \tag{4.44}$$

For completeness the line integrals in the case that the neutron beam is along the  $z$  direction are given:

$$\begin{aligned}
X'(x, y) &= \int_{-\infty}^{\infty} B_x(x, y, z') dz' = 0 \\
Y'(x, y) &= \int_{-\infty}^{\infty} B_y(x, y, z') dz' = 0 \\
Z'(x, y) &= \int_{-\infty}^{\infty} B_z(x, y, z') dz' = \mu_0 M l.
\end{aligned} \tag{4.45}$$

From Eq. 4.42 and the above line integrals it is obtained for the final polarization that  $\mathbf{P}(\infty, y, z) = \bar{\bar{D}}(y, z) \times \mathbf{P}(-\infty, y, z)$  with

$$\bar{\bar{D}}(y, z) = \frac{1}{\Sigma} \begin{pmatrix} \Sigma \cos a\sqrt{\Sigma} & Z\sqrt{\Sigma} \sin a\sqrt{\Sigma} & -Y\sqrt{\Sigma} \sin a\sqrt{\Sigma} \\ -Z\sqrt{\Sigma} \sin a\sqrt{\Sigma} & Z^2 \cos a\sqrt{\Sigma} + Y^2 & YZ(1 - \cos a\sqrt{\Sigma}) \\ Y\sqrt{\Sigma} \sin a\sqrt{\Sigma} & YZ(1 - \cos a\sqrt{\Sigma}) & Y^2 \cos a\sqrt{\Sigma} + Z^2 \end{pmatrix}, \tag{4.46}$$

where  $\Sigma(y, z) = Y^2(y, z) + Z^2(y, z)$  and  $a = \gamma/v$ .

Now Eq. 4.46 relates the initial polarization to the final polarization for a beam passing through the sample at  $(y, z)$ . For a neutron beam with finite cross section, the matrix  $\bar{\bar{D}}$  should be integrated over the beam cross section. If the integration is symmetric relative to the origin, then one can make use of the fact that

$$B_y(\epsilon_1 x, \epsilon_2 y, \epsilon_3 z) = \epsilon_2 \epsilon_3 B_y(x, y, z), \tag{4.47}$$

where  $\epsilon_1, \epsilon_2, \epsilon_3 = \pm 1$ . This means that  $B_y(x, y, z)$  and, therefore,  $Y(y, z)$  are antisymmetric with respect to  $y$  and  $z$ . Therefore, from Eq. 4.46, one only has to



integrate the matrix

$$\frac{1}{\Sigma} \begin{pmatrix} \Sigma \cos a\sqrt{\Sigma} & Z\sqrt{\Sigma} \sin a\sqrt{\Sigma} & 0 \\ -Z\sqrt{\Sigma} \sin a\sqrt{\Sigma} & Z^2 \cos a\sqrt{\Sigma} + Y^2 & 0 \\ 0 & 0 & Y^2 \cos a\sqrt{\Sigma} + Z^2 \end{pmatrix} \quad (4.48)$$

over the cross section of the neutron beam.

An infinitely narrow neutron beam passing exactly through the middle of the sample will only have its polarization rotated by  $B_z(x, 0, 0)$  since  $B_x(x, 0, 0)$  and  $B_y(x, 0, 0)$  vanish. As long as  $Y^2(y, z)$  is small compared to  $Z^2(y, z)$ , which is valid if  $(y, z)$  is sufficiently far from the edges, Eq. 4.48 is a pure rotation matrix.

It is now possible to calculate the magnetization of the sample from the measured rotation angle (Eq. 4.11). If no stray fields were present, the rotation angle would be given by  $t\mu_0 M\gamma/v$ . However, the stray fields reduce the rotation angle to  $\gamma/vZ(y, z)$  with  $Z(y, z)$  given in Eq. 4.44. Therefore the geometrical factor  $\eta$  can be defined as

$$\phi = \eta\mu_0 M t \gamma / v, \quad (4.49)$$

where  $\eta(y, z)$  is given by

$$\eta(y, z) = \frac{1}{2\pi} \sum_{\epsilon_2, \epsilon_3} \epsilon_2 \epsilon_3 \arctan \left( \frac{2z + \epsilon_3 l}{2y + \epsilon_2 w} \right). \quad (4.50)$$

Since  $\eta(0, 0)$  is a saddle point ( $\eta(0, z)$  has a local maximum and  $\eta(y, 0)$  a local minimum), an average over the cross section of the neutron beam, centered around the middle of the sample, will yield a result very close to the value of  $\eta(0, 0)$ , which is given by

$$\eta = \frac{2}{\pi} \arctan \left( \frac{l}{w} \right). \quad (4.51)$$



---

# CHAPTER 5

---

## URhGe

### 5.1 Introduction

THE SECOND URANIUM BASED COMPOUND discovered to show superconductivity within its ferromagnetic state is the ternary intermetallic URhGe [2]. It crystallizes in the orthorhombic TiNiSi-type structure with space group  $P_{nma}$  [161, 162]. The unit cell, with dimensions  $a = 6.87 \text{ \AA}$ ,  $b = 4.33 \text{ \AA}$ , and  $c = 7.51 \text{ \AA}$ , contains four formula units. The structure is shown in Fig. 5.1. The U, Rh, and Ge atoms each occupy  $4c$  positions  $(x, \frac{1}{4}, z)$ , with distinct parameters  $x$  and  $z$ . The U atoms are arranged in zig-zag chains of nearest neighbors in the  $a$  direction. The nearest neighbor distance of the uranium atoms is equal to  $d_{U-U} \approx 3.44 \text{ \AA}$  [163], which compares well with the Hill limit of  $3.5 \text{ \AA}$  [49]. However, the shortest U-Rh and U-Ge distance  $d_{U-Rh} \approx 2.99 \text{ \AA}$  and  $d_{U-Ge} \approx 2.94 \text{ \AA}$  suggest that the hybridization between the uranium atom and the ligands plays an important role in the delocalization of U  $5f$  states. Theoretical work [164, 165] has supported this hypothesis.

Neutron diffraction experiments on single-crystalline URhGe [2, 163, 166] revealed a collinear ferromagnetic order below  $T_C = 9.6 \text{ K}$  with ordered U moments of  $0.35 - 0.42 \mu_B$  along the  $c$  axis. No component of the ordered moment was observed along the  $a$  axis, which acts as the hard magnetic direction for the magnetization. In addition to the neutron-diffraction experiments, the ferromagnetic order in single-crystalline URhGe was studied by specific-heat, magnetization, and electrical resistivity [163, 167], which showed a sizeable influence of applied magnetic fields on the ferromagnetic order and on the ferromagnetic spin fluctuations in the  $b-c$  plane. In the low-temperature limit, the specific heat is characterized by the electronic contribution of the ferromagnetic spin fluctuations with a moderately enhanced linear term of  $\gamma = 164 \text{ mJ/mol K}^2$ . The magnetic properties of single-crystalline URhGe are in good agreement with the results from earlier measurements on polycrystalline

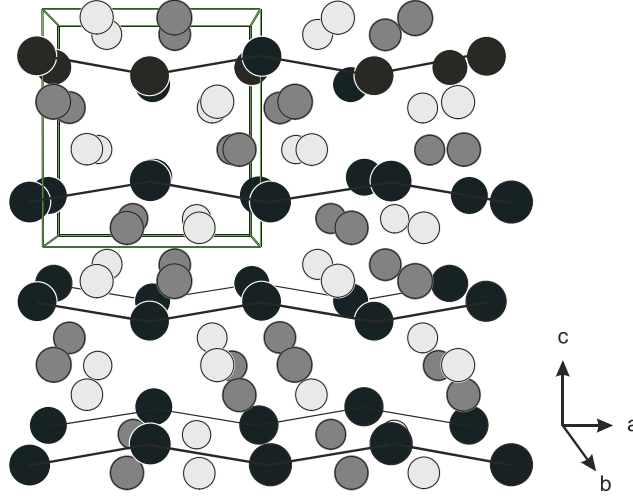


**Figure 5.1:** The orthorhombic crystallographic structure of URhGe. Uranium atoms are black, rhodium atoms light gray, and germanium atoms dark gray. The uranium nearest neighbors are connected. The unit cell, containing four formula units, is indicated as well.

and powder samples [168, 162, 169, 170, 171, 172], which have been reviewed by Sechovský and Havela [161]. Recently, band-structure calculations were performed by Diviš and co-workers [164] and Shick [165] to study the origin of the magnetic order in URhGe. These calculations suggest a substantial hybridization between the U-5*f* and Rh-4*d* states and a relatively small uranium magnetic moment of  $0.3 \mu_B$  originating from a partial cancelation of the spin and orbital components. The calculated moments are in good agreement with the measured values.

URhGe has attracted much attention because of the unusual coexistence of superconductivity ( $T_c = 0.25$  K) and ferromagnetism ( $T_C = 9.5$  K) [2]. From the beginning it was believed that ferromagnetic spin fluctuations, which are strongly enhanced near a quantum critical point, are the “glue” between the electrons forming a Cooper pair. Indeed, field induced superconductivity was found [173] at the magnetic field at which a spin reorientation takes place (12 T), inducing new fluctuations.

In this Chapter two techniques are used, namely dilatometry and muon spin relaxation ( $\mu$ SR), to study the ferromagnetic order in URhGe. Pressure-dependent experiments on UGe<sub>2</sub> and UIr suggest that in these systems superconductivity emerges near a ferromagnetic quantum critical point. One may therefore expect that ferromagnetic order in URhGe is also very sensitive to pressure. The volume dependence of several electronic quantities can be determined by thermal expansion measurements at ambient pressure. When superconductivity sets in at low temperature, conduction electrons condense into Cooper pairs. It is therefore of interest to investigate the magnetic properties of URhGe and specifically of the conduction electrons in detail. Muons are very sensitive magnetic probes and thus have the potentiality to yield information on the question whether the magnetism found in URhGe is of a localized or an itinerant nature.

## 5.2 Dilatometry<sup>\*</sup>

### 5.2.1 Introduction

In this Section thermal expansion measurements of single-crystalline URhGe in the temperature range from  $T = 2$  to 200 K are reported. The principal aim was to determine the pressure dependence of the ferromagnetic transition temperature  $T_C$ . For a second-order phase transition, the uniaxial pressure dependence of  $T_C$  (at ambient pressure) can be determined with the Ehrenfest relation from the anomalies in the specific heat and the linear coefficient of thermal expansion. The initial pressure dependence may give an estimate of the critical pressure needed to suppress the ferromagnetic order and reach the quantum critical point at  $T_C = 0$  K. In addition, the electronic Grüneisen parameter, which characterizes the volume dependence of the ferromagnetic spin fluctuations at low temperatures, has been determined.

### 5.2.2 Experimental

The dilatometry experiments were performed on a single-crystalline URhGe sample with dimensions  $a \times b \times c = 2.4 \times 5.0 \times 2.4$  mm<sup>3</sup>. The sample was cut from the material used in earlier specific-heat measurements performed by Hagmusa and co-workers [167]. The crystal has been grown from a stoichiometric melt of at least 99.95 % pure materials by means of the Czochralski technique in a tri-arc furnace with a continuous gettered Ar atmosphere. No subsequent heat treatment was given to the crystal. Due to the relatively high residual resistivity at low temperatures no superconductivity was observed in this particular crystal [163]. The coefficient of linear thermal expansion  $\alpha(T) = (1/L)(dL/dT)$  was measured using a sensitive parallel-plate capacitance dilatometer [34] along the orthorhombic  $a$ ,  $b$ , and  $c$  axes. From these measurements the volume expansion  $\alpha_v = \alpha_a + \alpha_b + \alpha_c$  was determined.

### 5.2.3 Results

In Fig. 5.2 the coefficient of linear thermal expansion  $\alpha$  along the  $a$ ,  $b$ , and  $c$  axis of single-crystalline URhGe is shown as a function of temperature in the range from  $T = 2$  to 200 K. The temperature dependence of the volume expansion  $\alpha_v = \alpha_a + \alpha_b + \alpha_c$  is shown for comparison (notice the figure shows  $\alpha_v/3$ ). At high temperatures the thermal expansion is governed by the phonon contribution for all three orientations. Around a temperature of 25 K a remarkable crossing of the curves for the thermal expansion along the  $a$ ,  $b$ , and  $c$  axis is observed. This crossing is a clear sign for the development of an additional contribution from ferromagnetic spin fluctuations at low temperatures. It is interesting to note that this additional contribution from ferromagnetic spin fluctuations mainly affects the anisotropy of the thermal expansion in the  $b - c$  plane, which acts as the easy plane for the

---

<sup>\*</sup>Parts of this Section have been published in Physical Review B **67** (2003) 144407.

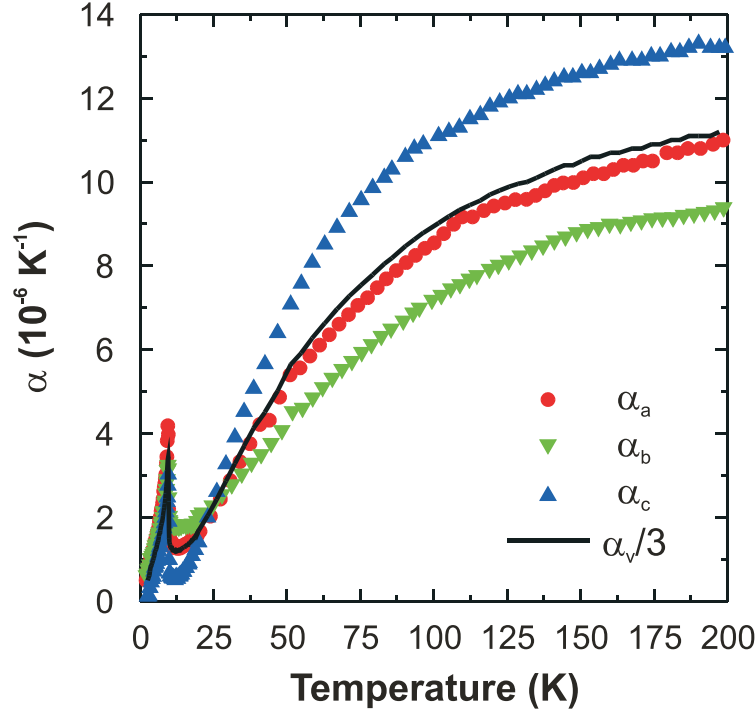


**Figure 5.2:** The coefficients of linear thermal expansion  $\alpha$  of URhGe as a function of temperature  $T$  along the orthorhombic  $a$ ,  $b$ , and  $c$  axis. For comparison the volume expansion divided by a factor 3 ( $\alpha_v/3$ ) is also shown. The high-temperature behavior is governed by the phonon contribution, while the anomaly at  $T_C = 9.7$  K reflects the onset of ferromagnetic order.

magnetization. At  $T_C = 9.7$  K the ferromagnetic order sets in and a peak in the coefficient of linear thermal expansion is observed for all three directions.

The low-temperature behavior of the coefficients of linear thermal expansion along the  $a$ ,  $b$ , and  $c$  axis is shown in more detail in Fig. 5.3. The observed steps in the coefficients of linear thermal expansion have the same sign but different sizes for the three orthorhombic axes of single-crystalline URhGe. The values of the steps are listed in Table 5.1. In Fig. 5.4 the low-temperature volume expansion divided by temperature ( $\alpha_v/T$ ) is shown as a function of temperature and compared with the specific heat divided by temperature ( $c/T$ ) measured on a sample prepared from the same single-crystalline batch [167].

#### 5.2.4 Discussion

The temperature dependence of the thermal expansion at high temperatures is governed by the phonon contribution and closely resembles a Debye curve. The estimated Debye temperature of  $\theta_D \approx 200$  K is in good agreement with the specific heat data [163, 167]. At low temperatures the Debye curve for the phonon contribution is expected to show a  $T^3$  temperature dependence. Below  $T = 30$  K the thermal

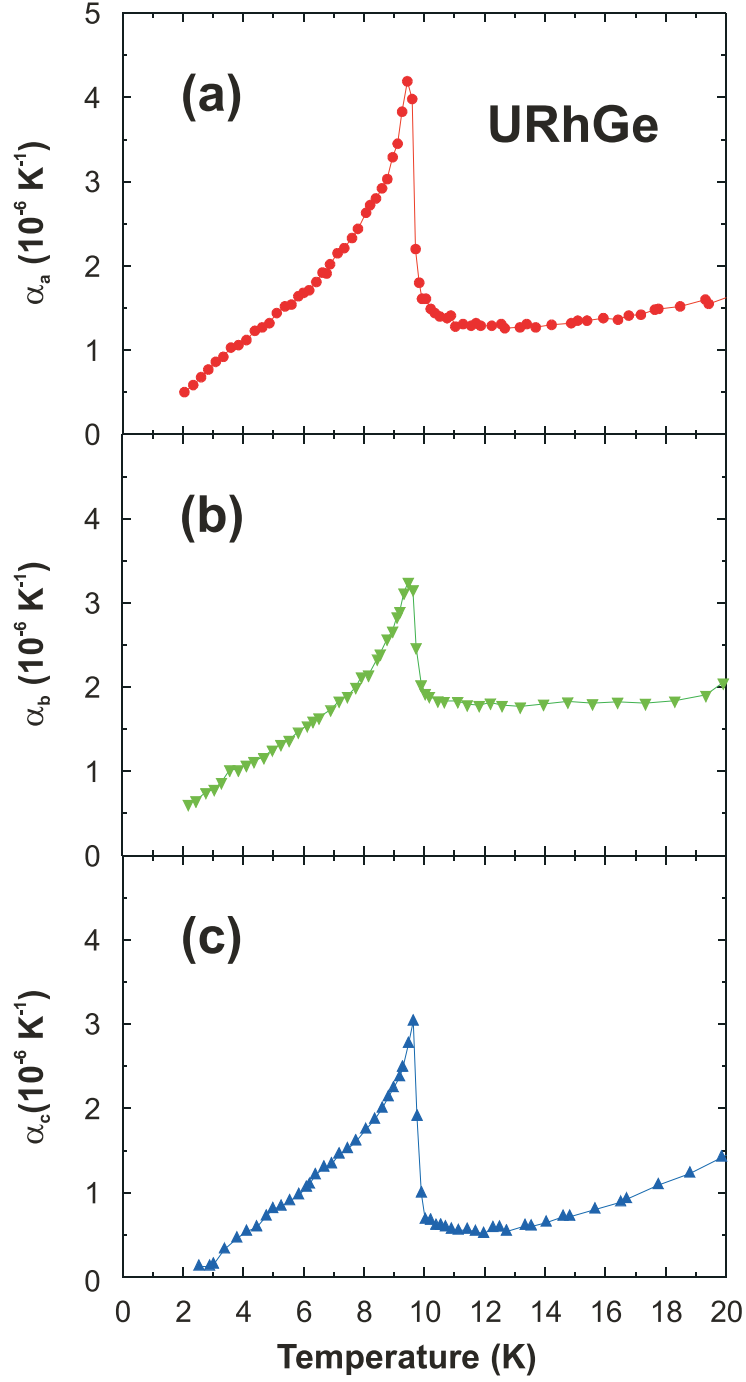


**Figure 5.3:** The coefficients of linear thermal expansion  $\alpha$  of URhGe as a function of temperature  $T$  along the orthorhombic  $a$ ,  $b$ , and  $c$  axis at low temperatures. The anomaly at  $T_C = 9.7 \text{ K}$  reflects the onset of ferromagnetic order. The large linear term at low temperatures is due to spin fluctuations.

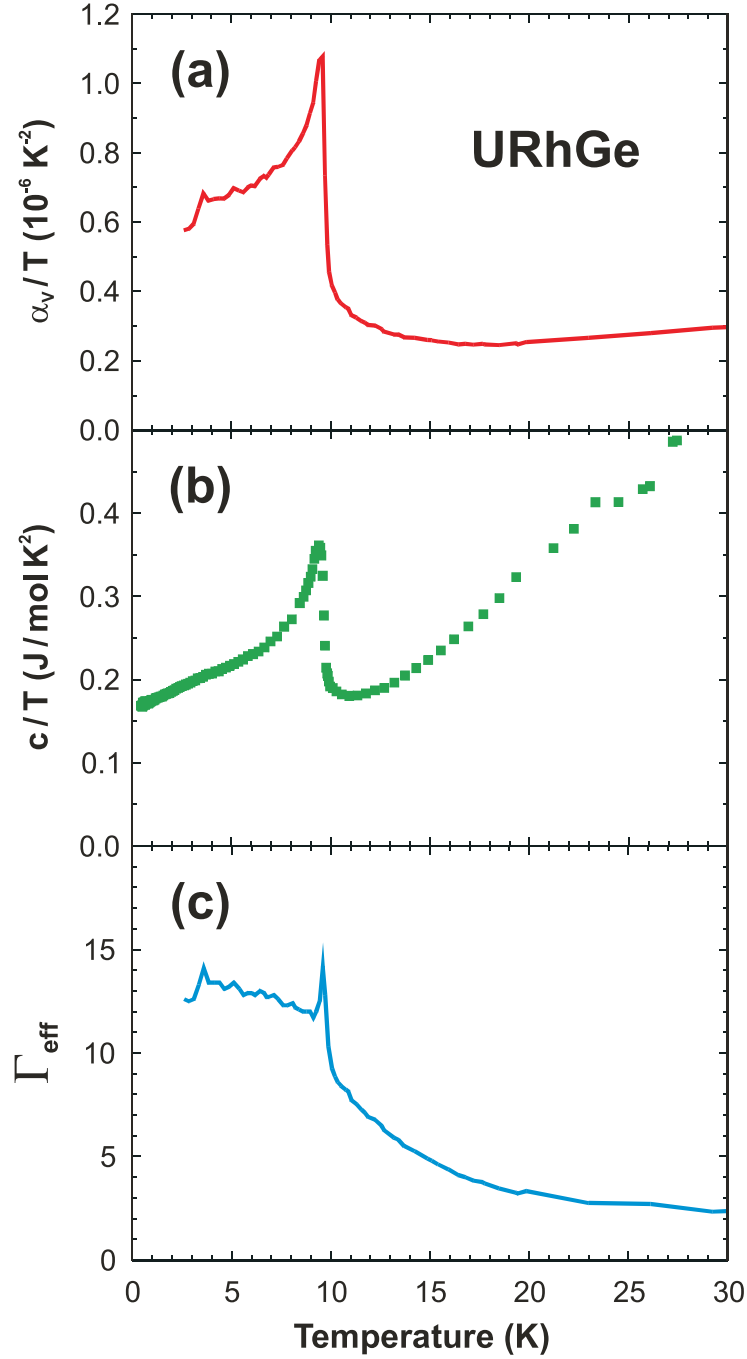


**Figure 5.4:** The volume expansion divided by temperature ( $\alpha_v/T$ ) of URhGe as a function of temperature  $T$  at low temperatures. For comparison the specific heat divided by temperature ( $c/T$ ) of a sample prepared from the same single-crystalline batch is shown [167]. The bottom frame shows the effective Grüneisen parameter  $\Gamma_{\text{eff}}$ , determined from the experimental data of the volume expansion and the specific heat (see main text).



**Table 5.1:** Step anomalies in the coefficients of linear thermal expansion of single-crystalline URhGe along the orthorhombic  $a$ ,  $b$ , and  $c$  axis. The corresponding pressure dependence of the Curie temperature,  $dT_C/dp$ , was deduced from the Ehrenfest relation (see text).

	$\Delta\alpha$ ( $10^{-6} \text{ K}^{-1}$ )	$dT_C/dp$ (K/kbar)
$a$ axis	3.4(1)	0.052(3)
$b$ axis	1.7(1)	0.026(2)
$c$ axis	2.7(1)	0.041(2)
volume	7.8(2)	0.119(6)

expansion along the  $a$  axis shows a clear deviation of this behavior, which is even more pronounced along the  $b$  axis. This deviation indicates the development of an additional contribution due to ferromagnetic spin fluctuations. This additional contribution was also observed in the specific heat measurements and described in terms of an enhanced electronic contribution [163]. In the ferromagnetically ordered state below  $T_C = 9.7 \text{ K}$ , the temperature dependence of the volume expansion closely resembles that of the specific heat, as shown in Fig. 5.4. In line with the analysis of the specific heat measurements [163], three different contributions to the thermal expansion can be identified in the ferromagnetically ordered state, namely, contributions due to phonons, ferromagnetic spin waves, and ferromagnetic spin fluctuations. As discussed, the phonon contribution shows a  $T^3$  power-law behavior at low temperatures. The ferromagnetic spin-wave contribution is expected to obey a  $T^{3/2}$  power-law behavior, while the ferromagnetic spin fluctuations lead to an enhanced linear term at low temperatures. Both the phonon and spin-wave contributions to the volume expansion divided by temperature ( $\alpha_v/T$ ) [and the specific heat divided by temperature ( $c/T$ )] vanish at low temperatures and, as a consequence, the extrapolated value of  $\alpha_v/T = 5.8(2) \times 10^{-7} \text{ K}^{-2}$  at  $T = 0 \text{ K}$  is solely due to the contribution of the ferromagnetic spin fluctuations.

In order to determine the uniaxial and hydrostatic pressure dependence of the ferromagnetic transition temperature, the Ehrenfest relation can be applied. For a second-order phase transition, the uniaxial pressure dependence of the transition temperature is directly related to the step anomalies in the coefficient of linear thermal expansion and the specific heat by the Ehrenfest relation

$$\frac{dT_C}{dp_i} = \frac{V_m \Delta\alpha_i}{\Delta(c/T)}, \quad (5.1)$$

where the index  $i$  refers to the orthorhombic axis,  $V_m = 3.36 \times 10^{-5} \text{ m}^3/\text{mol}$  is the molar volume, and  $\Delta(c/T) = 0.22(1) \text{ J/mol K}^2$  is the anomaly in the specific heat divided by temperature [163]. By applying this relation to the experimental step anomalies in the coefficients of linear thermal expansion, the uniaxial pressure

dependence of  $T_C$  along the  $a$ ,  $b$ , and  $c$  axis is obtained. The calculated values are listed in Table 5.1. The hydrostatic pressure dependence of  $T_C$  can be obtained by inserting the volume expansion for the coefficient of linear expansion in Eq. 5.1, or by summing the three contributions of the uniaxial pressure dependence. The different pressure dependencies of  $T_C$  as listed in Table 5.1 are all positive. This strongly suggests that the ferromagnetic order cannot be suppressed by moderate mechanical hydrostatic or uniaxial pressures, like in the case of  $\text{UGe}_2$  and  $\text{UIr}$ . Instead a *negative* uniaxial pressure is needed to suppress  $T_C$  for all crystallographic directions. Using a simple linear extrapolation of the initial pressure dependence calculated from the Ehrenfest relation, a negative critical hydrostatic pressure of  $p_{cr} \approx -8.0$  GPa is obtained. It is important to note that this value should be regarded as an upper bound for the negative critical pressure as the pressure dependence of  $T_C$  is expected to show significant non-linear corrections to the initial pressure dependence at ambient pressure. A negative critical pressure of the order of  $p_{cr} \approx -8.0$  GPa might be achieved by suitable chemical substitutions. A detailed study on which substitution is appropriate in tuning  $T_C$  to 0 K, is presented in Chapter 6.

In order to characterize the volume dependence of the electron correlations, the effective Grüneisen parameter of URhGe has been calculated. The thermal Grüneisen parameter  $\Gamma_T$  is defined as

$$\Gamma_T = -\frac{d \ln T^*}{d \ln V} \quad (5.2)$$

where  $T^*$  is a characteristic temperature that reflects the dominant energy scale of the system. The effective thermal Grüneisen parameter  $\Gamma_{\text{eff}}$  can be calculated from the measured temperature-dependent volume expansion  $\alpha_v(T)$  and specific heat  $c(T)$  by [86]

$$\Gamma_{\text{eff}}(T) = \frac{V_m \alpha_v(T)}{\kappa c(T)}, \quad (5.3)$$

where  $\kappa = -(1/V)(dV/dp)$  is the isothermal compressibility. As the compressibility of URhGe is unknown an estimated value  $\kappa = 0.8 \text{ Mbar}^{-1}$  is used. Experimental values for the compressibility of other UTX compounds vary from  $\kappa = 0.6$  to  $1.0 \text{ Mbar}^{-1}$  [174]. In Fig. 5.4 the effective Grüneisen parameter  $\Gamma_{\text{eff}}$ , calculated from the experimental volume expansion and the reported specific heat [167], is shown as a function of temperature. At high temperatures the effective Grüneisen parameter shows a small constant value of  $\Gamma_{\text{ph}} = 2$  and describes the volume dependence of the characteristic energy scale for the phonons. Below 30 K the effective Grüneisen parameter rapidly increases and reaches a value of  $\Gamma_{\text{eff}} \approx 14$  just above  $T_C$ . Below  $T_C$  a slow increase of the effective Grüneisen parameter is observed for decreasing temperatures. In the low-temperature limit  $\Gamma_{\text{eff}}$  corresponds to the enhanced electronic Grüneisen parameter  $\Gamma_{\text{sf}} = d \ln \gamma / d \ln V \approx 14$  of the ferromagnetic spin fluctuations. The corresponding relative pressure dependence of the electronic specific heat amounts to  $d \ln \gamma / dp = -\kappa \Gamma_{\text{sf}} \approx -11 \text{ Mbar}^{-1}$ .

The relation between the magnetic order and the spin fluctuations can be studied by comparing the volume dependence of the energy scales for the ferromagnetic order

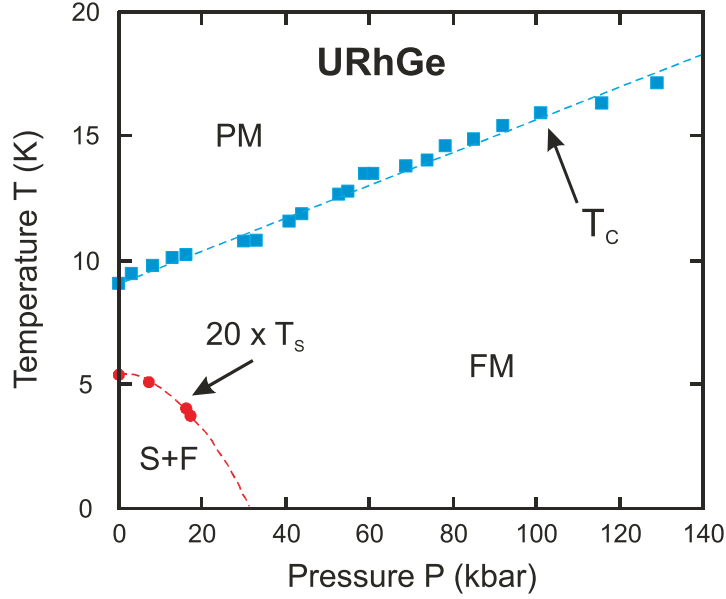


**Figure 5.5:** Temperature versus pressure phase diagram of URhGe. The lines are guides to the eyes. The Curie temperature  $T_C$  increases monotonically up to 14.0 GPa and the superconducting transition temperature  $T_s$  decreases continuously and vanishes around 3.0 GPa. (Figure taken from Ref. [176].)

( $T_C$ ) and the ferromagnetic spin fluctuations ( $T_{sf}$ ). It turns out that the Grüneisen parameter for the ferromagnetic order  $\Gamma_F = -d \ln T_C / d \ln V = (1/\kappa T_C)(dT_C/dp) \approx 16$  is of the same order of magnitude and has the same sign as the Grüneisen parameter for the ferromagnetic spin fluctuations  $\Gamma_{sf} = -d \ln T_{sf} / d \ln V = d \ln \gamma / d \ln V \approx 14$ . This last equation holds because  $\gamma \propto N(E_F) \propto T_{sf}^{-1}$ . The situation here is in strong contrast to pressure-induced antiferromagnetic superconductors such as CePd<sub>2</sub>Si<sub>2</sub> [175], where the antiferromagnetic order competes with the spin fluctuations with an opposite scaling behavior with volume. It can therefore be expected that the spin-mediated superconductivity of URhGe exists over a wide pressure range. This in contrast to the situation in the ferromagnetic superconductor UGe<sub>2</sub> [1] and UIr [3], where superconductivity is only observed in a small pressure region close to the critical pressure where the ferromagnetic order is suppressed.

### Comparison with other measurements

F. Hardy *et al.* have succeeded in growing a single crystal of URhGe which is superconducting at low temperatures [176, 177]. The temperature versus pressure phase diagram is shown in Fig. 5.5. The observed Curie temperature  $T_C$  increases linearly up to 14.0 GPa with an estimated slope of  $dT_C/dp \approx 0.065 \text{ K kbar}^{-1}$ . This is roughly comparable to the value of  $0.119 \text{ K kbar}^{-1}$  estimated from the dilatometry measurements presented in this Section. The difference can originate from errors in the determination of the values of  $\Delta\alpha$  and  $\Delta c/T$ . Another possibility is that this

value only represents the slope of  $T_C$  versus  $p$  for  $p = 0$  GPa. It might be possible that at low pressures  $T_C$  is not perfectly linear with  $p$ .

In Fig. 5.5 the superconducting transition temperature  $T_s$  is shown as well. It is seen that  $T_s$  vanishes at an estimated pressure of  $p = 3.0$  GPa. In comparison with  $\text{UGe}_2$ , in which compound the superconductivity is only found between 1.0 and 1.6 GPa, or with  $\text{UIr}$ , with 2.6-2.7 GPa as superconducting pressure region, this is a very broad pressure range, especially because the diagram is expected to extend below  $p = 0$  to negative pressures. This is consistent with the fact that  $\Gamma_F$  and  $\Gamma_{sf}$  are equal in sign and have the same order of magnitude.

Further comparison can be made between the dilatometry data and the measurement of Hardy [176, 177]. The coefficient  $A$  in the electrical resistivity  $\rho(T) = \rho_0 + AT^2$  was measured as well as a function of pressure [178]. Since  $A \propto m^{*2}$  and  $\gamma \propto m^*$ , where  $m^*$  is the enhanced effective mass of the heavy quasiparticles, an estimation can be made for  $d \ln \gamma / dp$ . The reduction of  $A$  with pressure results in  $\Delta m^* / m^* = -0.23$  for  $\Delta p = 2.0$  GPa. This gives  $d \ln \gamma / dp = -13 \text{ Mbar}^{-1}$  which compares well with a value of  $-11 \text{ Mbar}^{-1}$  as estimated from our thermal expansion measurements.

### 5.2.5 Conclusions

Thermal expansion measurements on a single-crystalline sample of the itinerant ferromagnet URhGe have been performed. Below the ferromagnetic ordering temperature of  $T_C = 9.7$  K an increase in the coefficient of linear thermal expansion was observed along all three orthorhombic axes. The uniaxial pressure dependence of the ferromagnetic transition temperature was determined by the Ehrenfest relation from the anomalies in the coefficients of linear thermal expansion and the specific heat. Positive values of  $dT_C/dp$  are found for all principal axes. Consequently, the hydrostatic pressure dependence is also positive and amounts to  $dT_C/dp = 0.119 \text{ K/kbar}$ . This positive pressure dependence contrasts the behavior reported for  $\text{UGe}_2$  and  $\text{UIr}$ . In addition, the effective Grüneisen parameter was determined. The resulting low-temperature behavior points to an enhanced volume dependence of the ferromagnetic spin fluctuations at low temperatures and an equal volume scaling of the energy scales for the ferromagnetic order and the ferromagnetic spin fluctuations.

## 5.3 Muon Spin Rotation and Relaxation

### 5.3.1 Introduction

When superconductivity sets in at low temperature, the conduction electrons condense into Cooper pairs. In ferromagnetic superconductors, the pairing mechanism of the conduction electrons needed for superconductivity is believed to be magnetic in origin. It is therefore of utmost importance to investigate the magnetic properties of URhGe and specifically of its conduction electrons.

Several theoretical studies have been performed to explain the coexistence of superconductivity and ferromagnetism. Most studies consider an itinerant nature of the ferromagnetism as a starting point and indeed have shown the possibility of superconductivity in a ferromagnetic material. See *e.g.* Refs. [89, 90, 91, 92]. In these cases the electrons forming the Cooper pairs are also responsible for the ferromagnetism, which can be explained by the spin-triplet nature of the superconductivity. Other studies [100, 101], however, have shown that spin-singlet superconductivity is still feasible under the constraint that conducting electrons involved in the superconductivity and localized electrons involved in the ferromagnetic order belong to different subsets of  $5f$  electrons. The pairing mechanism is then based on the interaction of electron spins via localized magnetic moments.

In order to determine which type of pairing is most probable, it is important to quantify the magnetic properties of the conduction electrons. These are difficult to be measured directly by diffraction techniques, since the magnetic scattering due to the polarization of delocalized electrons will only be significant at small  $Q$ . However, as muons localize at interstitial sites and are very sensitive to magnetic fields whatever their origin (localized or itinerant magnetic moments), the muon spin rotation or relaxation technique ( $\mu$ SR) does have the possibility to yield information on the itinerant electrons and associated magnetism.

### 5.3.2 Experimental

A single-crystalline sample of URhGe with a diameter of 5 mm and a length of 2.5 cm has been grown from a polycrystalline ingot using a Czochralski tri-arc technique. The ingot was prepared by arc melting the constituents U, Rh, (all 3N purity) and Ge (5N) under a high-purity argon atmosphere. No subsequent heat treatment was given to the single crystal. The single-crystalline nature was checked by X-ray Laue diffraction. The single-phase nature of the crystal was checked by electron probe micro-analysis (EPMA) which showed no sign of impurity phases within the resolution, except for a small amount of uranium oxide (less than 1 volume %).

For the experiments two samples with a different orientation were cut from the single crystal. The first sample consisted out of platelets with the  $a$  axis perpendicular to the platelet. In the second sample the  $c$  axis was perpendicular to the platelet. The initial muon polarization  $\mathbf{S}_\mu(0)$  was directed perpendicular to the platelets of the samples. A total surface area with a diameter of about 2 cm of sample was realized by wrapping several platelets next to one another in an aluminium foil. The thickness of the platelets was 0.3 mm.

The experiments were performed at the EMU spectrometer of the ISIS facility at the Rutherford Appleton Laboratory in the United Kingdom. The fly-past mode [179] was used to reduce background. In this mode, the muons which do not hit the sample, fly past and do not contribute to the signal. However, some muons are stopped in the walls of the cryostat and these cause a small, but observable, well-defined background. A blue Oxford Instruments cryostat was used for tem-

peratures above 2 K, whereas at lower temperatures a  $^3\text{He}$  cryostat was used. The measurements were performed in the temperature range from 0.5 to 300 K and in magnetic fields up to 0.45 T, oriented parallel to  $\mathbf{S}_\mu(0)$ .

### 5.3.3 Results

The first step in the study of the critical spin dynamics of compounds is an accurate determination of the Curie temperature  $T_C$ . In the sample for which the initial muon polarization  $\mathbf{S}_\mu(0)$  was parallel to the hard magnetic axis ( $\mathbf{a}$ ) and perpendicular to the easy magnetic axis ( $\mathbf{c}$ ), the full asymmetry for the wiggles in the signal was found, resulting from a spontaneous muon spin precession. Defining  $T_C$  as the temperature at which the wiggles disappear,  $T_C = 9.51(6)$  K is obtained. This value is consistent with the maximum of the relaxation rate for the second sample, in which  $\mathbf{S}_\mu(0) \parallel \mathbf{c}$ . Since the spontaneous muon precession has the full asymmetry for  $\mathbf{S}_\mu(0) \parallel \mathbf{a}$ , whereas no precession is observed for  $\mathbf{S}_\mu(0) \parallel \mathbf{c}$ , it can be concluded that the local field  $\mathbf{B}_{\text{loc}}$  at the muon site is parallel to the easy magnetic axis  $\mathbf{c}$ : *i.e.*  $\mathbf{B}_{\text{loc}} \parallel \mathbf{c}$ .

Examples of the measured spectra during a field scan in the paramagnetic state of URhGe are given in the upper panel of Fig. 5.6. All the spectra of the asymmetry  $a_0 P_Z^{\text{exp}}(t)$  as a function of time  $t$ , taken in the paramagnetic state (and for  $\mathbf{S}_\mu(0) \parallel \mathbf{c}$  also in the ferromagnetic state), could be analyzed as a sum of two components:

$$a_0 P_Z^{\text{exp}}(t) = a_1 \exp(-\lambda_Z t) + a_2 P_Z^{\text{KT}}(t, \Delta_{\text{KT}}, B_{\text{ext}}). \quad (5.4)$$

Here  $P_Z^{\text{exp}}(t)$  and  $P_Z^{\text{KT}}(t, \Delta_{\text{KT}}, B_{\text{ext}})$  are functions which are normalized to unity for  $t = 0$ . The first component in Eq. 5.4 describes the  $\mu\text{SR}$  signal from the sample where  $\lambda_Z$  measures the spin-lattice relaxation rate at the muon site. The second term accounts for the muons stopped in the background, *e.g.*, the cryostat walls. It can be modeled by a time and field dependent static Kubo-Toyabe function  $P_Z^{\text{KT}}(t, \Delta_{\text{KT}}, B_{\text{ext}})$  where  $\Delta_{\text{KT}}$  is the width of the static magnetic field distribution at the muon site and  $B_{\text{ext}}$  the external magnetic field. For each sample, the asymmetry  $a_2$  and  $\Delta_{\text{KT}}$  were fixed to appropriate and temperature independent values. These values were obtained by iteratively searching for those values of  $a_2$  and  $\Delta_{\text{KT}}$  which gave on average the best fits for all temperatures. Since the fly-past mode was used, low background asymmetries with maximum of  $a_2 = 0.01$  were found.

In the lower panel of Fig. 5.6 a decomposition into the two components of Eq. 5.4 is given for the fit to the data measured in 0 mT. The Kubo-Toyabe function is small compared to the exponential function. For  $t > 5 \mu\text{s}$  the exponential function is almost indistinguishable from the total fit function.

In Fig. 5.7 the temperature dependence of the spin-lattice relaxation rate  $\lambda_Z$  in the paramagnetic state of URhGe is displayed. It is measured in zero field with  $\mathbf{S}_\mu(0)$  parallel to the hard magnetic axis  $\mathbf{a}$ . Above  $T \sim 100$  K the relaxation is temperature independent. The decrease at temperatures above 200 K can be attributed to muon diffusion. Below  $T \sim 100$  K the relaxation  $\lambda_Z(T)$  starts to increase. Two

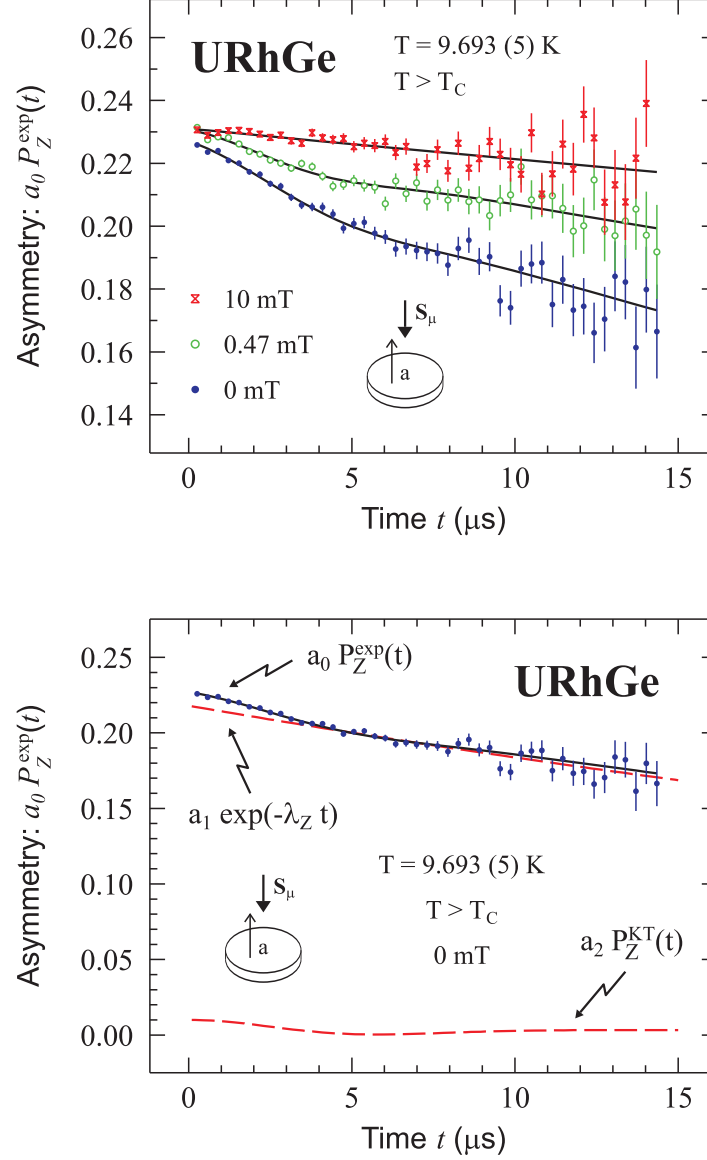


**Figure 5.6:** (Upper panel) Examples of  $\mu\text{SR}$  spectra  $a_0 P_Z^{\text{exp}}(t)$  as a function of time  $t$  recorded at ISIS. The figure shows spectra taken at different values of the applied magnetic field in the paramagnetic state of URhGe ( $T_C = 9.51(6) \text{ K}$ ). The initial muon polarization  $\mathbf{S}_\mu(0)$  as well as the external magnetic field  $\mathbf{B}_{\text{ext}}$  were oriented parallel to the  $\mathbf{a}$  axis. The solid lines are fits to Eq. 5.4. For 0, 0.47, and 10 mT it is found that  $\lambda_Z = 0.0171(5)$ ,  $0.0094(5)$ , and  $0.0045(5) \mu\text{s}^{-1}$ , respectively. The background Kubo-Toyabe function was assumed constant with parameters  $a_2 = 0.0100$  and  $\Delta_{\text{KT}} = 0.300 \mu\text{s}^{-1}$ . The effect of  $\mathbf{B}_{\text{ext}}$  on the Kubo-Toyabe function was taken into account. For the sake of clarity, the curve for 0.47 mT is shifted upwards by of 0.01. (Lower panel) Decomposition of the fit to the 0 mT data into the two components of Eq. 5.4.



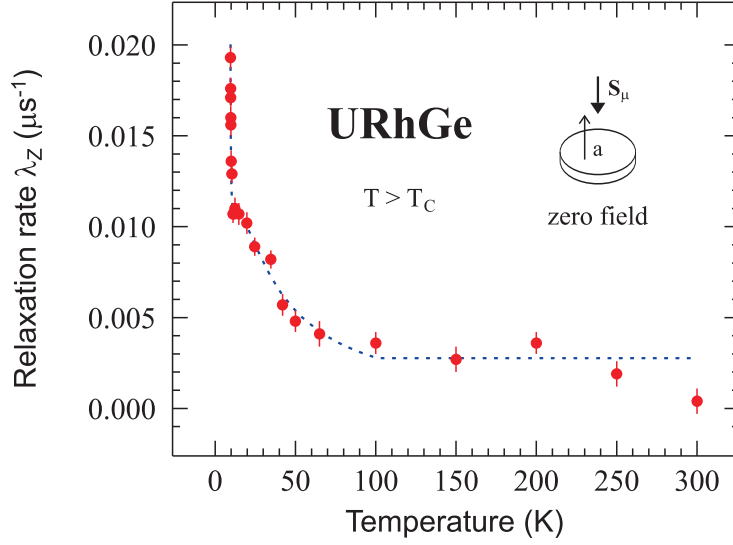


**Figure 5.7:** Temperature dependence of the muon relaxation rate  $\lambda_Z$  in the paramagnetic state of URhGe ( $T_C = 9.51$  K). The initial muon polarization  $\mathbf{S}_\mu(0)$  was oriented parallel to the  $\mathbf{a}$  axis. Above  $T \sim 100$  K  $\lambda_Z$  is constant. The decrease above 200 K is attributed to muon diffusion. Below  $T \sim 100$  K the depolarization increases in two steps. Between 100 K and 11.5 K  $\lambda_Z$  increases relatively slowly with decreasing temperature. Between 11.5 K and  $T_C = 9.51$  K a very sharp increase is observed. The dashed line below  $T = 100$  K is a guide to the eye. Above  $T = 100$  K, the line has a constant value.

temperature regions can be distinguished. Between 100 and 11.5 K  $\lambda_Z(T)$  increases relatively slowly with decreasing temperature, followed by a very sharp increase between 11.5 and  $T_C = 9.51$  (6) K. A zoom of  $\lambda_Z(T)$  below 100 K is shown in Fig. 5.8 as a function of the reduced temperature  $\tau = (T - T_C)/T_C$ . Note the logarithmic scales. Here it is seen that below  $T = 11.5$  K ( $\tau = 0.2$ ) a second term in  $\lambda_Z(T)$  develops. The dashed line is a guide to the eye.

In order to study the anisotropy in URhGe, it is necessary to measure the temperature dependence of  $\lambda_Z$  in zero field for  $\mathbf{S}_\mu(0)$  parallel to the easy axis for magnetization,  $\mathbf{S}_\mu(0) \parallel \mathbf{c}$ , as well. In Fig. 5.9  $\lambda_Z(T)$  is displayed for the temperature range from 0.4 to 300 K. Note the logarithmic temperature scale. Above  $T \sim 15$  K the relaxation rate is temperature independent. As in the previous paragraph, the decrease at higher temperatures ( $T > 200$  K) can be attributed to muon diffusion. Below  $T \sim 15$  K the relaxation increases and shows a maximum at  $T_C = 9.51$  (6) K. This maximum is a factor 2 lower than the maximum for  $\mathbf{S}_\mu(0) \parallel \mathbf{a}$ . For  $\mathbf{S}_\mu(0) \parallel \mathbf{a}$  two temperature regions of increasing  $\lambda_Z$  could clearly be distinguished. Here, however, the situation is less clear. Below  $T_C$  the relaxation shows a monotonous decrease with decreasing temperature down to 0.6 K. At the lowest temperatures, however,  $\lambda_Z(T)$  seems to increase below  $T = 0.5$  K.

Also shown in Fig. 5.9 is the specific heat divided by temperature,  $C/T$ , of a piece of the  $\mu$ SR sample, measured in zero field between 3 and 20 K. A transition temper-



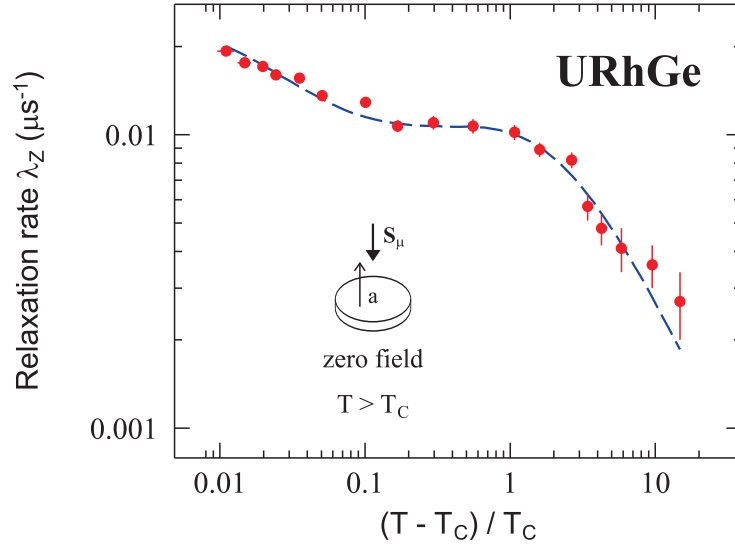


**Figure 5.8:** The dependence of the muon relaxation rate  $\lambda_Z$  on the reduced temperature  $\tau = (T - T_C)/T_C$  in the paramagnetic state of URhGe ( $T_C = 9.51(6)$  K). The initial muon polarization  $\mathbf{S}_\mu(0)$  was oriented parallel to the  $\mathbf{a}$  axis. The dashed line is a guide to the eye.

ature of  $T_C = 9.52$  K is observed. Linear extrapolation of  $C/T$  to zero temperature yields an enhanced linear electronic specific heat term of  $\gamma = 160$  mJ/mol·K<sup>2</sup>. These results are in good agreement with previously published data [163, 167], confirming the quality of the sample.

In order to further characterize the spin-lattice relaxation, longitudinal field measurements were performed at a fixed temperature close to  $T_C$  for the two orientations of  $\mathbf{S}_\mu(0)$  relative to easy magnetic axis  $\mathbf{c}$ . These measurements give information on the frequency scale and magnitude of the fluctuations.

In Fig. 5.10 the field dependence of the relaxation rate  $\lambda_Z$  in the paramagnetic state of URhGe is shown for the case that the initial muon polarization  $\mathbf{S}_\mu(0)$  as well as the external magnetic field  $\mathbf{B}_{\text{ext}}$  were parallel to the  $\mathbf{a}$  axis. The temperature was equal to  $T = 9.693(5)$  K. The relaxation rate  $\lambda_Z(B_{\text{ext}})$  is field dependent at extremely small external fields  $B_{\text{ext}}$ . Within 1 mT  $\lambda_Z(B_{\text{ext}})$  has reduced to about 1/3 of its value in zero field. In the insert in Fig. 5.10 a zoom is given for small fields. Once  $\lambda_Z(B_{\text{ext}})$  has dropped sharply, it is very weakly dependent on the field.

Figure 5.11 shows the dependence of the relaxation rate  $\lambda_Z(B_{\text{ext}})$  on the external longitudinal magnetic field  $\mathbf{B}_{\text{ext}}$  parallel to the  $\mathbf{c}$  axis in the paramagnetic state of URhGe. The temperature was equal to  $T = 10.46(1)$  K. Just like in the previous case  $\lambda_Z(B_{\text{ext}})$  shows a sharp decrease to about 1/3 of its initial value for very small fields. For higher fields  $\lambda_Z(B_{\text{ext}})$  continues to decrease, but at a lower rate. For fields of 10 mT and above the relaxation is  $\lambda_Z(B_{\text{ext}}) = 0 \mu\text{s}^{-1}$  within the uncertainty. The insert shows that for the whole field range up to 450 mT,  $\lambda_Z(B_{\text{ext}}) = 0 \mu\text{s}^{-1}$  is obtained within the uncertainty. This is in contrast to the case for  $\mathbf{S}_\mu(0) \parallel \mathbf{a}$

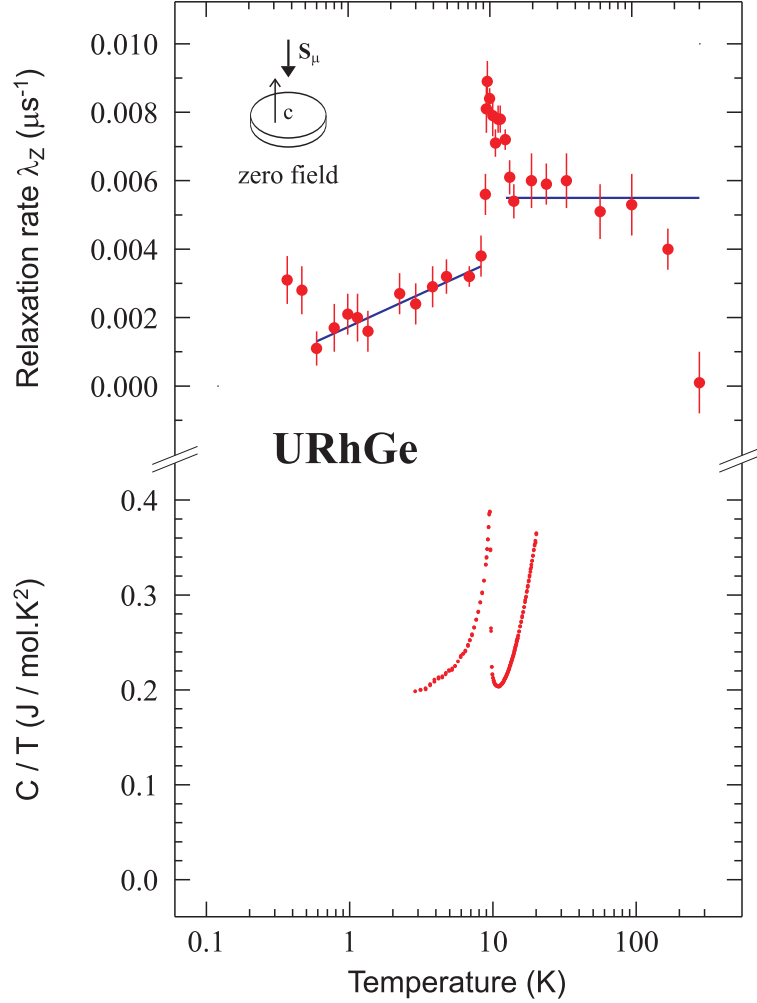


**Figure 5.9:** (Above) Muon relaxation rate  $\lambda_Z$  versus temperature  $T$ . The initial muon polarization  $\mathbf{S}_\mu(0)$  was oriented parallel to the  $\mathbf{c}$  axis. Note the logarithmic scale. Above  $T \sim 15$  K the relaxation rate is constant. The decrease at higher temperatures ( $T > 200$  K) can be attributed to muon diffusion. Below  $T \sim 15$  K the relaxation increases and shows a maximum at  $T_C = 9.51(6)$  K. The solid line below  $T_C$  is a fit to Eq. 5.6. (Below) Specific heat measured on the same sample. A sharp peak occurs at the same transition temperature as in the  $\mu$ SR data.

(Fig. 5.10) where a non-zero relaxation is measured up to 450 mT.

### 5.3.4 Analysis

#### Magnetic Field Scans

In order to analyze the data in longitudinal field of Figs. 5.10 and 5.11, a comparison with Nuclear Magnetic Resonance (NMR) is made. For this technique it can be shown that the  $1/T_1$  relaxation rate (equal to  $\lambda_Z$  in  $\mu$ SR) is proportional to the

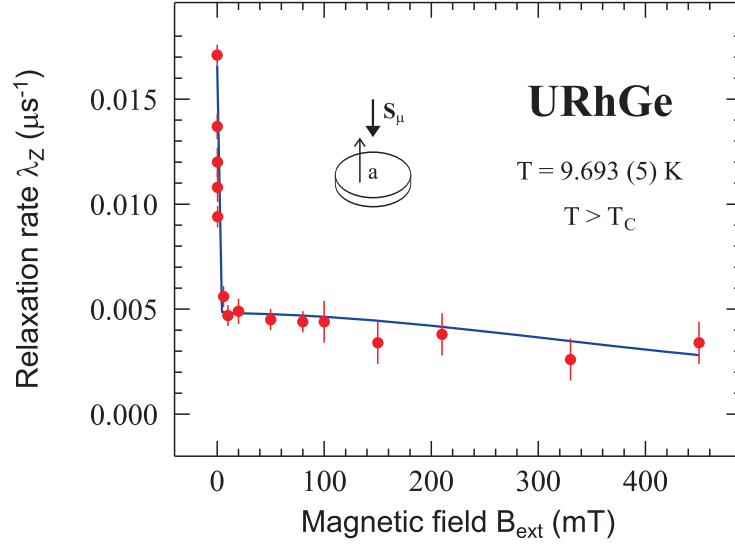


**Figure 5.10:** Field dependence of the muon relaxation rate  $\lambda_Z$  in the paramagnetic state of URhGe ( $T_C = 9.51 \text{ K}$ ). The initial muon polarization  $\mathbf{S}_\mu(0)$  as well as the external magnetic field  $\mathbf{B}_{\text{ext}}$  were parallel to the hard magnetic  $\mathbf{a}$  axis. The solid line is a fit to the sum of two Lorentzian functions (Eq. 5.5). See the main text for the extracted parameters. The insert shows a zoom at low fields.

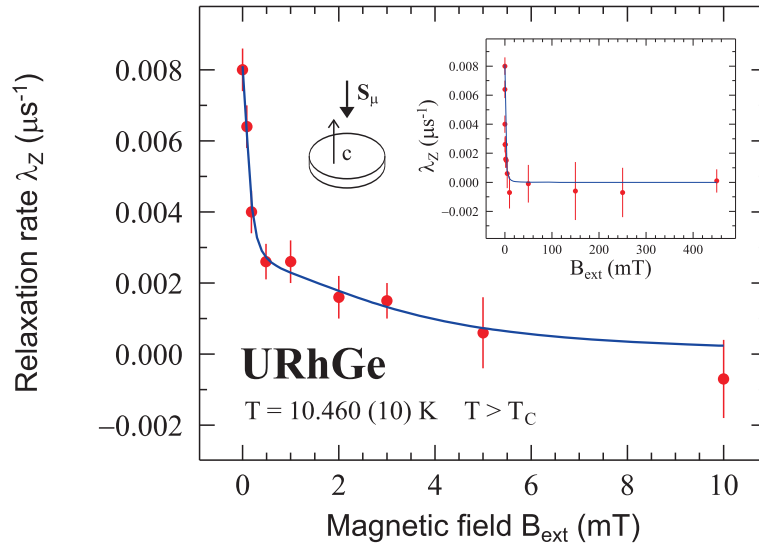


**Figure 5.11:** Field dependence of the muon relaxation rate  $\lambda_Z$  in the paramagnetic state of URhGe ( $T_C = 9.51 \text{ K}$ ). The initial muon polarization  $\mathbf{S}_\mu(0)$  as well as the external magnetic field  $\mathbf{B}_{\text{ext}}$  were parallel to the easy magnetic  $\mathbf{c}$  axis. The solid line is a fit to the sum of two Lorentzian functions (Eq. 5.5). See the main text for the extracted parameters. The insert shows the whole field range. For fields of 10 mT and above  $\lambda_Z = 0 \mu\text{s}^{-1}$  is obtained within the uncertainty.

**Table 5.2:** Fit parameters, as extracted from a fit of the muon data to Eq. 5.5. Listed are the field width  $\Delta$  and the relaxation time  $\tau$  of the fluctuating field at the muon site in the paramagnetic state of URhGe, close to  $T_C = 9.51(6)$  K, for the two different directions of the initial muon polarization  $\mathbf{S}_\mu(0)$ . The parameters of the first Lorentzian differ by a factor 2.5 for the two directions, whereas the second Lorentzian is much more anisotropic.

	$\mathbf{S}_\mu(0) \parallel \mathbf{a}$		$\mathbf{S}_\mu(0) \parallel \mathbf{c}$	
	$\Delta$ (mT)	$\tau$ ( $\mu\text{s}$ )	$\Delta$ (mT)	$\tau$ ( $\mu\text{s}$ )
1 <sup>st</sup> Lor.	0.048 (3)	3.5 (3)	0.021 (2)	9.0 (1.4)
2 <sup>nd</sup> Lor.	1.2 (2)	0.0022 (6)	0.068 (13)	0.36 (10)

time average of the square of the local field multiplied by the spectral density of the field fluctuations at a certain frequency  $\omega$ . The spectral density has the form of  $J(\omega, \tau_c) = \frac{\tau_c}{1 + \omega^2 \tau_c^2}$  where  $\tau_c$  is the correlation time of the fluctuations [180, 181].

In fact this model is a special case of the more general formula in Eq. 5.7 (to be discussed in the next Section) without imposing  $\omega_\mu = 0$ . With the assumption that the spectral density is Lorentzian, the  $\mathbf{q}$  integration can be decoupled from the  $\omega_\mu = \gamma_\mu B_{\text{ext}}$  dependence and the same result as for NMR (explained above) is obtained.

The data in Figs. 5.10 and 5.11 suggest there are two independent relaxation channels. The first contribution can be suppressed in longitudinal fields smaller than 1 mT for both directions of  $\mathbf{S}_\mu(0)$  with respect to the easy magnetic axis  $\mathbf{c}$ , whereas the second contribution can be suppressed in fields which are significantly higher. Further, the second contribution strongly depends on the orientation of the field. Therefore, a fit is made to a model of two independent relaxation processes. Each is due to magnetic field fluctuations with a correlation time  $\tau_i$  and a time averaged square of the local magnetic field  $\Delta_i^2$ . The formula for this model is

$$\lambda_Z(B_{\text{ext}}) = \sum_{i=1}^2 \frac{2 \gamma_\mu^2 \Delta_i^2 \tau_i}{1 + (\gamma_\mu B_{\text{ext}})^2 \tau_i^2} \quad (5.5)$$

where  $\gamma_\mu = 851.6 \text{ Mrads}^{-1} \text{ T}^{-1}$  is the gyromagnetic ratio of the muon.

The extracted values for the field distribution width  $\Delta_i$  at the muon site and the relaxation time  $\tau_i$  of the fluctuating field are shown in Table 5.2 for the two different directions of  $\mathbf{S}_\mu(0)$  in the paramagnetic state of URhGe. When the parameters of the first Lorentzian are compared for the two geometries, it is seen that  $\Delta$  and  $\tau$  differ by a factor 2.5. The second Lorentzian however is much more anisotropic. While  $\Delta_2^a$  and  $\Delta_2^c$  differ by a factor of 18, the ratio between  $\tau_2^c$  and  $\tau_2^a$  amounts to 160.

Comparing the two Lorentzian functions per geometry, it is seen that the correlation time for the first component is much larger than for the second one. For

$\mathbf{S}_\mu(0) \parallel \mathbf{a}$ ,  $\tau_1^a$  is of the order of  $\mu\text{s}$ , whereas  $\tau_2^a$  is in the ns regime. For  $\mathbf{S}_\mu(0) \parallel \mathbf{c}$  the difference is smaller but still amounts to a factor 25. Looking at the field distribution width  $\Delta$ , it is seen that  $\Delta_2^a$  is 25 times larger than  $\Delta_1^a$  and that  $\Delta_2^c$  is about 3 times larger than  $\Delta_1^c$ .

### Spin-lattice relaxation in the ferromagnetically ordered state

The spin-lattice relaxation  $\lambda_Z(T)$  below  $T_C$  for  $\mathbf{S}_\mu(0) \parallel \mathbf{c}$  (Fig. 5.9) can be fitted in the temperature region 0.6 to 8 K to the empirical logarithmic function

$$\lambda_Z = a + b \ln \left( \frac{T}{T_C} \right). \quad (5.6)$$

The fit yields  $a = 0.00357(22) \mu\text{s}^{-1}$  and  $b = 0.00082(8) \mu\text{s}^{-1}$  for  $T_C = 9.51(6) \text{ K}$  and is shown in Fig 5.9. In the next Section the spin-lattice relaxation  $\lambda_Z(T)$  below  $T_C$  will be discussed in more detail.

### 5.3.5 Discussion

In the previous Section two different types of magnetic field fluctuations at the muon site have been identified, through the signature of their relaxation processes. One type is nearly isotropic, has long relaxation times, and causes small fluctuations in the local magnetic field at the muon site, whereas the other type is highly anisotropic, has short relaxation times, and causes much larger magnetic field fluctuations.

Measurements of the magnetic susceptibility and specific heat in field [163] indicate that the magnetic order in URhGe is almost of an easy-plane type, *i.e.*, the anisotropy between the **b-c** plane and the **a** axis is large, whereas the anisotropy between the **b** and **c** axes is small. It should however be noted that the spontaneous magnetic moment below  $T_C$  is along the **c** axis. Also, for URhGe the local magnetic field  $\mathbf{B}_{\text{loc}}$  at the muon site is parallel to the **c** axis. With  $\mathbf{S}_\mu(0) \parallel \mathbf{B}_{\text{loc}} \parallel \mathbf{c}$ , the magnetic excitations along the **a** and **b** axes are probed and for  $\mathbf{S}_\mu(0) \parallel \mathbf{a}$  the magnetic excitations along the **b** and **c** axes are measured. This can be understood by the consideration of classical Larmor precession, as in Chapter 2: the muon spin is not sensitive to parallel magnetic field fluctuations. It is therefore expected that  $\lambda_Z(B_{\text{ext}})$  also shows the anisotropy between the **a** and **c** axis. That  $\mu\text{SR}$  is capable of measuring the anisotropy of critical magnetic fluctuations, if present, is nicely shown in the rare-earth compound NdRh<sub>2</sub>Si<sub>2</sub> [144], a uniaxial antiferromagnet. The values of  $\lambda_Z(T)$  for  $\mathbf{S}_\mu(0)$  parallel and perpendicular to the easy axis, differ by a factor 100 in the critical regime above  $T_C$ . In Table 5.2 the anisotropy of URhGe is found for the second Lorentzian. For the system it is much more difficult to excite a fluctuation along **a** than along **c**, giving rise to longer correlation times  $\tau$  and smaller field distribution widths  $\Delta$  for  $\mathbf{S}_\mu(0) \parallel \mathbf{c}$ . Although some anisotropy is also observed for by the first Lorentzian in Table 5.2, it is far too small to account for the macroscopically observed anisotropic behavior. The two components are therefore expected to have a different origin.

The present results can be compared to the proposed models, described in the Introduction. It can be assumed that the ferromagnetism is itinerant in nature [89, 90, 91, 92], or localized [100, 101]. Here it is shown that the latter model is able to explain the  $\mu$ SR data presented in this Chapter. The existence of two subsets of U  $5f$  magnetism is assumed. The first subset is composed of an itinerant electron density with a small, quasi-static, and slowly fluctuating polarization. The second subset consists of an electron density localized at the U atoms, resulting in large, anisotropic, and fast fluctuating magnetic moments.

A justification of this model is given by the relaxation times in Table 5.2. There are several indications that itinerant magnetic moments fluctuate slower than localized ones. The fluctuation rate for itinerant moments with ferromagnetic correlations is given, in lowest order, by  $\Gamma(\mathbf{q}) \propto q$  [182], or by  $\Gamma(\mathbf{q}) \propto q^{5/2}$  [27] when dipolar interactions are taken into account close to  $T_C$ . When mainly longitudinal fluctuations are probed by the muon,  $\Gamma(\mathbf{q})$  is essentially probed at  $q_D$  [142]. (Comparing Fig. 5.8 with Fig. 4.20 shows that this is in fact the case for URhGe.) Since the dipolar interactions in itinerant systems is smaller than in localized systems [142],  $q_D$  is smaller for itinerant systems than for localized systems.  $\Gamma(\mathbf{q})$  is a growing function of  $q$  which leads to a smaller value of  $\Gamma(\mathbf{q})$  for itinerant systems than for localized systems. That  $\Gamma(\mathbf{q})$  is a growing function of  $q$ , is nicely demonstrated by quasi-elastic neutron scattering for UGe<sub>2</sub> [149]. These measurements show unambiguously a growing  $\Gamma(\mathbf{q})$  with increasing  $q$ . With  $\tau \propto \Gamma^{-1}(\mathbf{q})$  it follows that the longer the relaxation time, the more itinerant the magnetism behaves. A heuristic argument for URhGe, in which large electronic correlations are present as indicated by the large linear electronic term  $\gamma$  in the specific heat, is that correlations tend to slow down the spin dynamics at low temperatures. The large differences in the width  $\Delta$  of the fluctuating field at the muon site (Table 5.2) indicate a large difference in polarization of the two components. Furthermore, the large anisotropy is expected for localized moments due to the strongly anisotropic hybridization, whereas band structures are usually less anisotropic.

Zwicky *et al.* [183, 184] have developed a theory for the electronic excitations in UPt<sub>3</sub>, assuming the localization of two of the  $5f$  electrons and the delocalization of the remaining  $5f$  electrons. With this dual ansatz the authors could reproduce the de Haas-van Alphen data on UPt<sub>3</sub> and UPd<sub>2</sub>Al<sub>3</sub>. Furthermore, LDA calculations show that the hopping matrix elements for different  $5f$  orbitals vary, leading to a difference in behavior for the  $5f$  electrons in the system. For UPd<sub>2</sub>Al<sub>3</sub> various techniques, including photoemission, inelastic neutron scattering, and  $\mu$ SR, indicate the same dual nature of  $5f$  electrons [156, 157, 158, 185]. Of course, the dual model should allow for a rather natural description of heavy-fermion superconductivity coexisting with  $5f$  magnetism. This has indeed been shown to be the case for UPt<sub>3</sub> [183]. The mass enhancements of the quasiparticles are shown to follow from the local exchange interaction of the delocalized  $5f$  electrons with localized  $5f^2$  configurations. The data on URhGe, presented in this Chapter, fit well into this picture.

The present results can be compared to the magnetic form factor of URhGe. These measurements were performed by Prokeš *et al.* using polarized neutron scattering at 2 K in a field of 6 T [186]. The recorded flipping ratios could be fitted to the ordered moment  $\mu$  multiplied by the magnetic form factor  $f(Q) = [\langle j_0 \rangle + C_2 \langle j_2 \rangle]$  where  $C_2$  is related to the ratio of the spin and orbital contribution to the magnetic moment, and  $\langle j_n \rangle$  are averages of the spherical Bessel functions  $j_n(Qr)$  over the squared radial wave-functions for the unpaired electrons in the atom. Within the dipolar approximation the magnetic form factor agrees well with the theoretical  $5f$  form factors for free  $U^{3+}$  and  $U^{4+}$  ions. Because of the strong similarity between the form factor of both ions it was not possible to distinguish them within error bars. Moreover, a magnetic moment of  $0.41(1) \mu_B/U$  was found. This value is fully consistent with magnetic bulk measurements. In summary, polarized neutron measurements indicate that the magnetic moments are localized on the U sites and that a complementary itinerant magnetic moment falls within the uncertainty of the determination of  $\mu$ .

If indeed localized magnetism coexists together with itinerant  $5f$  states with a small polarization, as strongly suggested by the  $\mu$ SR data presented in this Chapter and supported by polarized neutron scattering, this has implications for the nature of the Cooper pairs in the superconducting state. Assuming an itinerant nature of the ferromagnetism, theoretical studies have shown the possibility of spin-triplet superconductivity [89, 90, 91, 92]. In this case the electrons forming the Cooper pairs are also responsible for the strong ferromagnetism. Other studies by Abrikosov and Suhl [100, 101], however, have shown that spin-singlet superconductivity is still feasible under the constraint that conducting electrons involved in the superconductivity and localized electrons involved in the ferromagnetic order belong to different subsets of  $5f$  electrons. The pairing mechanism is then based on the interaction of electron spins via localized magnetic moments. *The  $\mu$ SR data presented in this Chapter suggest the latter case of Cooper pairs formed by itinerant electrons coupled by the spin fluctuations of the magnetic U ions.*

Measurements of the upper critical field for magnetic fields along the three crystallographic axes for a superconducting single crystal of URhGe [177] suggest the existence of odd-parity, spin triplet superconductivity. This observation would rule out the mechanism of Abrikosov and Suhl [100, 101]. However, the  $\mu$ SR measurements presented in this Section show that it is improbable that the ferromagnetism below  $T_C$  is carried by the same electrons as those forming the Cooper pairs. Further theoretical studies are needed to clarify this apparent discrepancy.

A similar  $\mu$ SR study on UGe<sub>2</sub> at ambient pressure [134] and at 0.95 GPa (Chapter 4) shows the same picture as for URhGe. The relaxation rate  $\lambda_Z$  just above  $T_C$  is suppressed in very small magnetic fields. However, the localized component is not observed, probably because the fluctuations are too fast (motional narrowing limit). Again, polarized neutron scattering indicates that almost all the magnetism is localized at the U atoms. As mentioned earlier, also UPt<sub>3</sub> and UPd<sub>2</sub>Al<sub>3</sub> are thought to show a coexistence of localized magnetism and itinerant  $5f$  states. The conclusion



drawn in this Chapter might therefore be more general than for URhGe alone.

### Spin-lattice relaxation at high temperatures

For a paramagnetic system the static wave vector dependent susceptibility  $\chi_{\mathbf{Q}_0}(\mathbf{q})$ , where  $\mathbf{Q}_0$  is the wave vector of the magnetic structure, is a key quantity. Note that for a ferromagnet  $\mathbf{Q}_0 \equiv \mathbf{0}$ . For temperatures much higher than  $T_C$ ,  $\chi_{\mathbf{Q}_0}(\mathbf{q})$  becomes wave vector independent (*i.e.* the pair-correlations are negligible) and shows Curie-Weiss behavior ( $\chi \propto (T - \theta_{CW})^{-1}$ ). In the same limit the linewidth  $\Gamma(\mathbf{q})$  of the paramagnetic fluctuations becomes temperature independent [187] for ferromagnets. Since [143]

$$\lambda_Z \propto \int \sum_{\beta, \gamma} \mathcal{A}^{\beta\gamma}(\mathbf{q}) \Lambda^{\beta\gamma}(\mathbf{q}, \omega_\mu = 0) \frac{d^3\mathbf{q}}{(2\pi)^3}, \quad (5.7)$$

where  $\mathcal{A}^{\beta\gamma}$  are constants accounting for the coupling between the muon spin and the spins of the sample and since  $\Lambda^{\beta\gamma}$  corresponds to:

$$\Lambda^{\alpha\alpha}(\mathbf{q}, \omega_\mu = 0) \propto k_B T \frac{\chi^{\alpha\alpha}(\mathbf{q})}{\Gamma^\alpha(\mathbf{q})}, \quad (5.8)$$

it is easily seen that  $\lambda_Z$  becomes temperature independent for  $T \gg \theta_{CW}$  for localized as well as for itinerant systems. Note that antiferromagnets maintain the temperature dependence of  $\Gamma(\mathbf{q})$  and that  $\lambda_Z \propto T^{1/2}$  for  $T \gg T_N$  [143, 188].

If the exchange interaction would play an important role at higher temperatures,  $\lambda_Z(T)$  would not be temperature independent [143]. For instance, when mainly antiferromagnetic fluctuations drive the relaxation,  $\lambda_Z(T)$  would increase at high temperatures. If crystal electric field (CEF) effects play a role (*i.e.* higher CEF energy levels start to get involved in the excitations relaxing the muon spin),  $\lambda_Z$  would show a significant drop at higher temperatures [189]. (For experimental examples on muon relaxation rates in systems with CEFs, see Ref. [190].) Therefore, the constant  $\lambda_Z$  at temperatures up to 200 K indicates that for  $T \gg T_C$  the spin-correlations are negligible and that the higher CEF levels are above 200 K. It is most likely that the drop in  $\lambda_Z$  at 200 K is due to muon diffusion, because the decrease occurs at the same temperatures for both directions of  $\mathbf{S}_\mu(0)$ .

### Spin-lattice relaxation in the ferromagnetically ordered state

In Section 5.3.4 it has been shown that  $\lambda_Z(T)$  can be fitted to a logarithmic function below  $T_C$ . A priori, two possible sources of relaxation contribute to  $\lambda_Z$ : magnons (spin wave excitations of the ordered part of the magnetic moment) and magnetic fluctuations (unordered part of the magnetic moments). For magnons with a simple ferromagnetic dispersion relation  $\hbar\omega_{\mathbf{q}} = D_m q^2 + \Delta$ , where  $D_m$  is the magnon stiffness constant and  $\Delta$  the anisotropy energy, it can be shown that [191]

$$\lambda_Z \propto T^2 \ln \left( \frac{k_B T}{\Delta} \right). \quad (5.9)$$



This equation is only valid for ferromagnets with small anisotropy, *i.e.*  $\Delta \ll k_B T$ . The  $T^2 \ln T$  behavior is nicely demonstrated for the rare-earth compound GdNi<sub>5</sub> [18]. Clearly, for URhGe  $\lambda_Z(T)$  does not show this  $T^2 \ln(T)$  behavior. The contribution of the magnetic fluctuations should be further investigated in order to explain the empirical  $\lambda_Z(T) = a + b \ln(T/T_C)$  behavior, *e.g.* by magnetic field scan in the ferromagnetic state. At this stage, a mathematical derivation of this behavior and the contribution of magnetic spin fluctuations to  $\lambda_Z(T)$  is unknown.

Extrapolation of the fit to Eq. 5.6 in Fig. 5.9 to  $\lambda_Z = 0$  yields a temperature of  $T = 0.12$  K. This would implicate that temperatures lower than 0.12 K correspond to energies too small to excite magnetic fluctuations. This may indicate the existence of a gap in the fluctuation spectrum

### Spin-lattice relaxation at the lowest temperature

In Fig. 5.9 it is seen that below 0.6 K the relaxation  $\lambda_Z(T)$  increases with decreasing temperature. The limited number of data points showing this trend prohibits drawing strong conclusions. Clearly, more research is needed to provide a starting point of understanding the spin dynamics in URhGe at the lowest temperatures.

Assuming the increase is not an artefact, *e.g.*, a change in background due to the <sup>3</sup>He cryostat, the result could be very interesting. Below  $T_s \sim 0.3$  K superconductivity sets in [2]. The glue between the electrons forming Cooper pairs, is thought to be ferromagnetic fluctuations. It is therefore necessary that  $\lambda_Z \neq 0$ , which is shown by the data. Possibly, the increase of  $\lambda_Z(T)$  with decreasing temperature could even enhance the attractive forces that bind electrons into a pair, since the fluctuations get larger. This conjecture and the confirmation of the upturn of  $\lambda(T)$  can be verified by additional experiments at temperatures below 0.3 K.

### 5.3.6 Conclusions

In this Section  $\mu$ SR data on URhGe have been presented. Field scans in the paramagnetic state clearly show two different magnetic contributions, which can be identified as localized and itinerant magnetism. This fact strongly suggests that the 5*f* electrons responsible for both magnetic order and superconductivity do not participate in both phenomena simultaneously but are separated either in real space and/or in reciprocal space, *i.e.* different parts of the Fermi surface.



---

# CHAPTER 6

---

## URh<sub>1-x</sub>Ru<sub>x</sub>Ge

### 6.1 Introduction



RECENTLY, URhGe has attracted significant attention because ferromagnetism (Curie temperature  $T_C = 9.5$  K) and superconductivity ( $T_s = 0.25$  K) were found to coexist at ambient pressure [2]. The superconducting state is believed to have its origin in the proximity to a ferromagnetic instability: near the quantum critical point (QCP) enhanced ferromagnetic spin fluctuations would mediate spin-parallel Cooper pairing. The QCP is reached when  $T_C$  is tuned to  $T_C = 0$ . That magnetic fluctuations play an important role, is indicated by the field-induced superconductivity found in URhGe for a magnetic field of 12 T along the  $b$ -axis [173]. At this field a spin reorientation takes place and magnetic fluctuations reappear. It is therefore of interest to establish how far URhGe is from the QCP and to study these fluctuations in the vicinity of the QCP. In the vicinity of this point the Fermi liquid theory breaks down and new physics is expected to manifest itself (non-Fermi liquid physics (NFL)). An enhanced Sommerfeld coefficient (linear term in the electronic specific heat) of  $\gamma = 160$  mJ/mol K<sup>2</sup> and a small ordered magnetic moment of  $\sim 0.4 \mu_B$ /U-atom indicate that URhGe is close to a quantum phase transition. In the group of UTGe compounds, with T a transition metal, URhGe is surrounded by paramagnetic compounds (UCoGe and URuGe) and magnetically ordered compounds (UIrGe and UPdGe) [161].

Unlike UGe<sub>2</sub> [1] and UIr [3], neither hydrostatic pressure (up to 13.0 GPa) nor uniaxial pressure is effective in tuning URhGe to a quantum critical point, as pressure enhances  $T_C$  [192, 176].  $T_C$  can be reduced by appropriate chemical substitutions, but it is clear that these substitutions reduce the mean free path of the electrons and thereby destroy the superconductivity. However, the magnetic fluctuation spectrum is generally less sensitive to the crystal quality. Chemical substi-

tution leads to a loss of translational symmetry, but this does not necessarily inhibit quantum critical behavior, as demonstrated in, *e.g.*, the substitutional system CeCu<sub>6-x</sub>Au<sub>x</sub> [53]. This opens up the possibility to study a ferromagnetic quantum critical point in chemically substituted URhGe. For other examples of materials that exhibit non-Fermi liquid behavior induced by chemical substitution, see Ref. [193].

In principle, one has the choice of substituting any of the three elements U, Rh, or Ge by another element. U is the only magnetic ion in the compound and substituting U by, *e.g.*, Th, would result in a decrease in the number of magnetic 5*f* ions in the system. One would rather like to alter  $T_C$  in a way which has the same underlying mechanism as external pressure, namely tuning the lattice parameters and the *f*-ligand hybridization (either the *f-d* or *f-p* hybridization). This is achieved by substituting Rh (*f-d*) or Ge (*f-p*).

The choice of elements to substitute on the Rh site with the aim to reduce  $T_C$  is limited [161, 172]. UPdGe is a ferromagnet with  $T_C = 30$  K and therefore the substitution of Rh by Pd is not expected to decrease  $T_C$ . UNiGe, UPtGe, and UIrGe are antiferromagnets. It has been shown by Chevalier *et al.* [171] that in the URh<sub>1-x</sub>Ir<sub>x</sub>Ge series a sudden transition occurs from a ferromagnetic to an antiferromagnetic ground state near  $x = 0.45 - 0.50$ . Introducing  $T = \text{Ni, Pt, or Ir}$  is therefore expected to introduce competing antiferromagnetic correlations in U(Rh,*T*)Ge. UFeGe is not isostructural to URhGe, unlike the aforementioned compounds. A structural transition is therefore expected at a certain Fe concentration. Since URuGe and UCoGe are both paramagnetic and isostructural to URhGe, it was decided to investigate the effect of substituting Rh by Ru and Co.

A similar screening can be made for substitution on the Ge site. URhSi and URhSn have  $T_C = 9.5$  K and  $T_C = 16.5$  K, respectively. Chemical substitution of Ge for Si or Sn is not expected to decrease  $T_C$ . A few samples were prepared to check this expectation for URhGe<sub>1-x</sub>Si<sub>x</sub>.

It should be noted that chemical substitution of Rh and Ge by Co or Si, respectively, is isoelectronic. Hence there will only be an effect because of the size difference. In the case of substitution of Rh by Ru, however, there is also a change in valence changes since Ru has one electron less than Rh. In this case both size and valence will influence the hybridization.

A comparison of the lattice parameters *a*, *b*, and *c* and the unit-cell volume *V* for the systems of interest is made in table 6.1. The UTSi and UTGe compounds were first reported to crystallize in the CeCu<sub>2</sub> crystal structure (space group *Imma*) in which U occupies the Ce position and T and Si or Ge are randomly distributed over the Cu sites. Later, a careful analysis of neutron and X-ray diffraction data however indicated the TiNiSi structure (space group *Pnma*) [161, 162]. The TiNiSi structure is the ordered variant of the CeCu<sub>2</sub> structure where *T* and Si or Ge occupy inequivalent positions. To enable a straightforward comparison of lattice constants measured by different authors the TiNiSi notation will be used in table 6.1, *i.e.*, *a* and *b* are interchanged with respect to the CeCu<sub>2</sub> notation.

URhGe has the largest unit-cell volume *V*, followed by URuGe and URhSi.

**Table 6.1:** Lattice parameters  $a$ ,  $b$ ,  $c$ , unit-cell volume  $V$ , and some magnetic properties of URhGe, URuGe, UCoGe, and URhSi. The lattice parameters are determined at room temperature, except in Ref. [194], where they were determined at 80 K. The TiNiSi structure notation is used, *i.e.*  $a$  and  $b$  are interchanged with respect to the notation in the CeCu<sub>2</sub> structure. See the main text for details.  $\gamma$  is the coefficient of the electronic specific heat,  $T_C$  the Curie temperature, and  $\mu_S$  the ordered magnetic uranium moment. WTDP stands for weakly temperature dependent paramagnet and PM for paramagnet.

	Ref.	a (Å)	b (Å)	c (Å)	V (Å <sup>3</sup> )	$\gamma$ (mJ/mol·K <sup>2</sup> )	$T_C$ (K)	$\mu_S$ ( $\mu_B$ )
URhGe	[2]						9.5	0.42
	[161]	6.898	4.340	7.536	225.61			
	[167]					164	9.6	
	[195]	6.876	4.333	7.513	223.84			
	[163]	6.875	4.331	7.508	223.56	155	9.6	0.35
URuGe	[172]	6.678	4.359	7.539	219.46		WTDP	-
	[170]					35	WTDP	-
	[196]	6.687	4.343	7.559	219.53		WTDP	-
UCoGe	[172]	6.843	4.205	7.227	207.96		PM	-
	[170]					65	PM	-
	[197]	6.852	4.208	7.226	208.34		46 ?	-
URhSi	[194]	6.986	4.113	7.427	213.40	180.9	9.5	
	[196]	7.023	4.121	7.458	215.85		9.5	0.11
	[162]	7.002	4.121	7.451	215.00			0.50

UCoGe has by far the smallest  $V$ . Chemical substitution of Rh by Ru mainly affects the  $a$ -axis, whereas substitution by Co affects the  $b$  and, primarily, the  $c$ -axis. With the introduction of Si the  $a$ -axis increases and the  $b$ - and  $c$ -axes decrease.

Some magnetic properties are listed in table 6.1 as well. URhGe and URhSi have the same Curie temperature of 9.5 K. URuGe is a weakly temperature dependent paramagnet. Measurements down to 1.2 K suggest that UCoGe is a paramagnet as well, although Canepa *et al.* [197] reported  $T_C = 46$  K, deduced from resistivity data. Magnetization measurements at low temperatures in fields up to 35 T, suggest that UCoGe is relatively close to ferromagnetic order, because data taken on a powder sample show, compared to other paramagnetic systems like URuGe, a relatively large field-induced magnetic moment ( $0.58 \mu_B/\text{f.u.}$  at 35 T) [170]. URhGe and URhSi have relatively high  $\gamma$  values, whereas UCoGe and URuGe have moderate ones.

In this paper, dc magnetization measurements performed on the three series URh<sub>1-x</sub>Ru<sub>x</sub>Ge, URh<sub>1-x</sub>Co<sub>x</sub>Ge, and URhGe<sub>1-x</sub>Si<sub>x</sub> are reported. It was found that substitution by Co leads to an increase of  $T_C$  up to  $T_C = 20$  K for  $x = 0.60$ , beyond which  $T_C$  drops to 0 for  $x$  close to 1. Samples in which Ge is chemically substituted

by Si did not show any change in  $T_C$  up to  $x = 0.20$ . The U(Rh,Ru)Ge system, however, does show a complete suppression of the ferromagnetism for low  $x$ . After an initial increase,  $T_C$  decreases linearly and vanishes at a critical Ru concentration of  $x_{cr} \approx 0.38$ , suggesting a quantum critical point. The U(Rh,Ru)Ge system is investigated further by electrical resistivity, X-ray powder diffraction, specific heat, and magnetization under hydrostatic pressure to study the role of the  $f$ -ligand hybridization in decreasing  $T_C$  and to look for possible non-Fermi liquid behavior as the quantum critical point is approached. A brief preliminary account of these results was reported in Ref. [198].

## 6.2 Experimental

Polycrystalline samples of U(Rh,Ru)Ge, U(Rh,Co)Ge, and URh(Ge,Si) with Ru, Co, and Si concentrations  $x$  of  $0.0 \leq x \leq 1.0$  were prepared by arc melting the constituents U, Rh, Ru, Co (all 3N purity) and Ge (5N) under a high-purity argon atmosphere. Each sample was melted several times and turned over after each melt to improve the homogeneity. The as-cast buttons were wrapped in Ta foil and put in quartz ampoules together with a uranium getter. After evacuating and sealing the quartz ampoules, the samples were annealed for ten days at 875 °C. The single-phase nature of the samples was checked by electron probe micro-analysis (EPMA) and by X-ray powder diffraction. The X-ray diffraction patterns and the EPMA measurements showed no signs of impurity phases within the resolution of less than 5 vol.% and 2 vol.%, respectively.

The dc magnetization at ambient pressure was measured in a MPMS XL-5 Quantum Design SQUID magnetometer. Temperature scans were performed between 1.8 and 20 K in a field of 0.01 T and between 2 and 300 K in a field of 1 T. In both cases the samples were zero-field cooled. Field scans of the magnetization were made in fields up to 5.5 T at several temperatures.

Magnetization measurements at a pressure of 0.43 GPa were performed using an Oxford Instruments MagLab vibrating sample magnetometer (VSM). The pressure clamp cell was made of Cu alloyed with Be. Temperature scans were made in fields of 0.01 T and 1 T. Magnetic field scans were performed in fields up to 12 T at several temperatures. The pressure was determined by measuring the superconducting transition temperature  $T_s$  of a piece of lead inside the pressure cell ( $T_s = 7.2$  K at ambient pressure). The pressure transmitting medium was a mixture of methanol and ethanol (1 : 4).

Electrical resistivity,  $\rho(T)$ , measurements were performed using a standard four probe ac technique in zero field from 2 to 300 K in a MagLab system of Oxford Instruments.

X-ray diffraction measurements at room temperature were performed using a Bruker D3 Advance X-ray diffractometer with Cu-K $\alpha$  radiation. Powders made from the polycrystalline samples were covered by Kapton foil to prevent contamination. Rietveld analysis of the diffraction data was performed using the GSAS program [38].

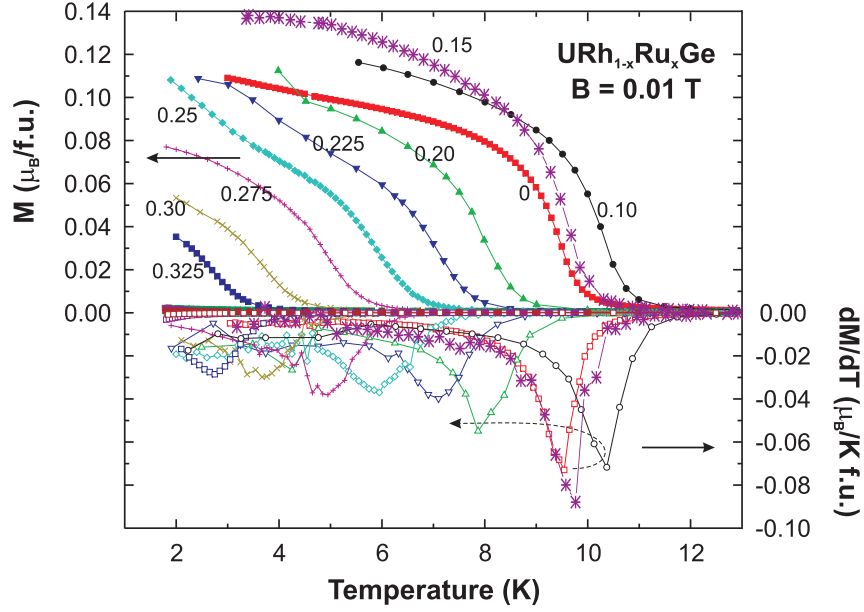


**Figure 6.1:** Temperature dependence of the dc magnetization of  $\text{URh}_{1-x}\text{Ru}_x\text{Ge}$  for various values of  $x$ . The samples were zero-field cooled and measured in a field of 0.01 T. The lower part of the figure shows the derivative of the magnetization. Note that the  $x = 0.10$  sample has a higher  $T_C$  than the pure  $\text{URhGe}$  sample.

The specific heat  $C_p(T)$  was measured using the semi-adiabatic method in combination with a mechanical heat switch in a  $^3\text{He}$  cryostat. The mass of the samples amounted to 3 - 4 grams.

## 6.3 Results

### 6.3.1 Magnetization at ambient pressure

The influence of the chemical substitution of Rh by Ru on the Curie temperature  $T_C$  was studied by dc magnetization  $M(T)$  at ambient pressure. The results are shown in Fig. 6.1. Also shown, in the lower part of the figure, is the derivative  $dM(T)/dT$ .  $T_C$  is defined as the temperature at which  $dM(T)/dT$  has a minimum. The magnetization was measured after zero-field cooling in a small field of 0.01 T, because a larger field will move the inflection point  $(dM(T)/dT)_{\min}$  to higher temperatures [163] and bias the determination of  $T_C$ . On the other hand, a small field of 0.01 T will most probably not significantly expel the magnetic domains when the sample is zero-field cooled.

In addition to  $M(T)$ , the magnetization as a function of magnetic field  $M(B)$  has been measured up to 5.5 T at several fixed temperatures. From these measurements Arrott plots are derived. In Fig. 6.2 the results for  $x = 0.25$  are shown as an example. The Curie temperatures deduced from the Arrott plots agree very well

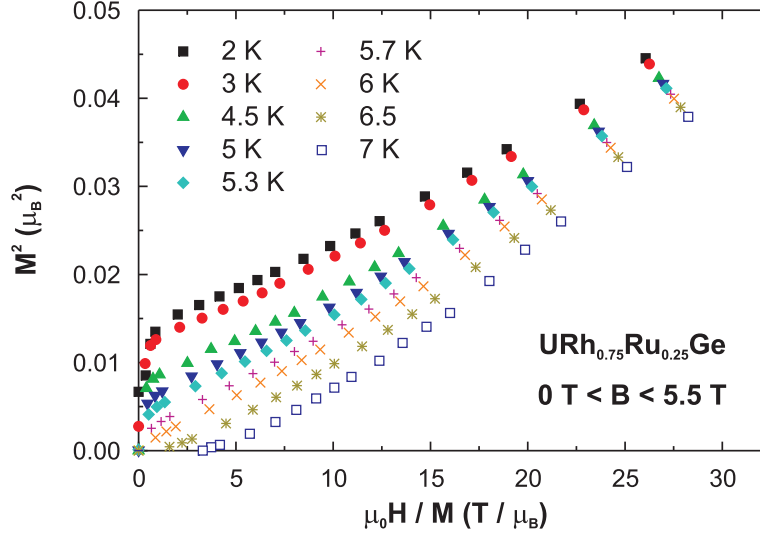


**Figure 6.2:** Arrott plots ( $M^2$  versus  $\mu_0 H/M$ ) of the magnetization of URh<sub>1-x</sub>Ru<sub>x</sub>Ge with  $x = 0.25$  measured between  $T = 2$  and 14 K. The isotherm through the origin determines  $T_C = 6$  K.

with the temperature at which  $(dM(T)/dT)_{0.01T}$  is minimum.

It is clearly seen in Fig. 6.1 that the pure URhGe compound has a  $T_C$  of about 9.6 K, in accordance with the literature value [2]. When Rh is chemically substituted with a small amount of Ru,  $T_C$  of URh<sub>1-x</sub>Ru<sub>x</sub>Ge shifts upwards to 10.4 K for  $x = 0.10$ . Subsequently, there is a monotonic decrease of the Curie temperature for increasing  $x$ . At  $x = 0.15$ ,  $T_C$  has reached roughly the same value as for  $x = 0$ . For the samples with  $x = 0.35, 0.375, 0.40$ , and  $0.60$  no transition was observed in the measured temperature range ( $T > 1.8$  K). However, the Arrott plots (not shown) clearly indicate a paramagnetic ground state for  $x = 0.40$  and  $0.60$ , whereas they do suggest ferromagnetism for  $x = 0.35$  below  $T_C \approx 1.3$  K. This is estimated by extrapolating the points of intersection of the Arrott isotherms for temperatures above  $T = 1.8$  K with the horizontal  $\mu_0 H/M$  axis.

Figure 6.1 indicates that for increasing Ru concentrations the transition broadens. The peak in  $(dM(T)/dT)$  loses height but gains in width, indicating an increase in disorder caused by chemical substitution. X-ray measurements (Sec. 6.3.3) clearly indicate a single-phase structure. A variation in the local Ru concentration  $x$  can therefore only exist on an atomic scale. A higher annealing temperature could possibly sharpen the transition.

In Fig. 6.3 the temperature dependence of the reciprocal susceptibilities is shown for the URh<sub>1-x</sub>Ru<sub>x</sub>Ge series. The susceptibility is measured in a field of 1 T. The temperature dependence of the reciprocal susceptibility of metallic compounds normally exhibits deviations from the linear Curie-Weiss behavior, which can be accounted for by fitting the data to the modified Curie-Weiss (MCW) law  $\chi(T) = C/(T - \theta) + \chi_0$ , where  $\chi_0$  represents a temperature-independent contribution. How-



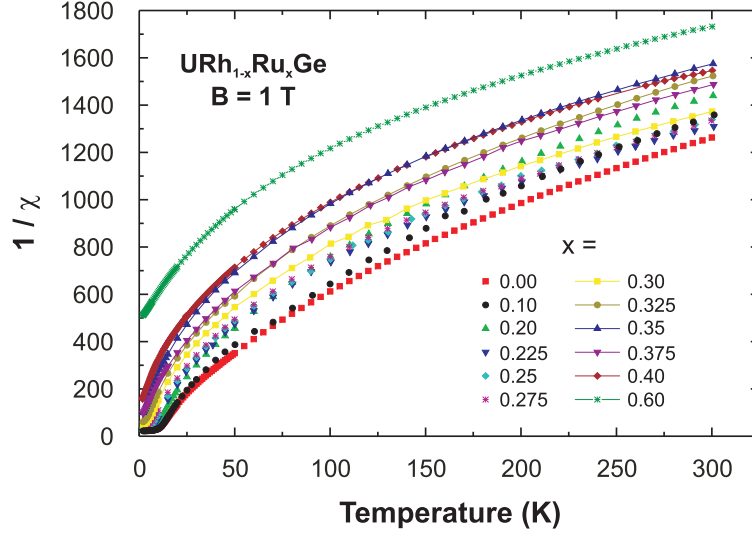


**Figure 6.3:** Inverse susceptibility  $1/\chi$  of  $\text{URh}_{1-x}\text{Ru}_x\text{Ge}$  as a function of temperature in a field of 1 T for different values of  $x$ .

ever, in polycrystalline samples of materials with strongly anisotropic magnetic properties pronounced deviations from the MCW behavior are often observed. Therefore, no attempt was made to model the susceptibility with the MCW law. Note that for single crystals of  $\text{URhGe}$  the susceptibility does follow a MCW behavior with  $\theta \approx T_C$ , as demonstrated in Ref. [2] for the easy-axis susceptibility.

In Fig. 6.4 the magnetization measured in 0.01 T as a function of temperature is shown for the  $\text{URh}_{1-x}\text{Co}_x\text{Ge}$  series. The Curie temperatures as deduced from  $(dM(T)/dT)_{\min}$  agree with those deduced from Arrott plots. Figure 6.5 shows the results for  $x = 0.60$  as an example.  $T_C$  increases monotonically up to 20 K for  $x = 0.60$ . For higher values of  $x$ ,  $T_C$  decreases and vanishes somewhere between  $x = 0.90$  and  $x = 1.0$ .

As in the case of Ru-substitution the transition broadens, probably due to the variation on the atomic scale of the Rh and Co concentrations. If this is the case, one expects an equal width of the  $dM/dT$  peak at  $T_C$  for two compounds symmetric with respect to  $x = 0.50$ , since compounds with this substitution concentration have the highest degree of disorder. In fact, after vertical scaling and horizontal translation the peaks for  $x = 0.40$  and  $x = 0.60$  are indeed identical. The decrease of the measured magnetization is probably caused by a smaller ordered magnetic moment. Susceptibility measurements in 1 T (see Fig. 6.6) indicate a smaller ordered magnetic moment for  $x = 0.60$  than for  $x = 0.40$ .

In Fig. 6.7 the magnetization measured in 0.01 T as a function of temperature is shown for the  $\text{URhGe}_{1-x}\text{Si}_x$  series. The Curie temperatures as deduced from  $(dM(T)/dT)_{\min}$  agree with those deduced from the Arrott plots. Figure 6.8 shows the Arrott plots for  $x = 0.20$ .  $T_C$  remains constant up to  $x = 0.20$ . The transition seems to be slightly broadened for  $x = 0.20$ , compared to  $x = 0$ , as in the case of

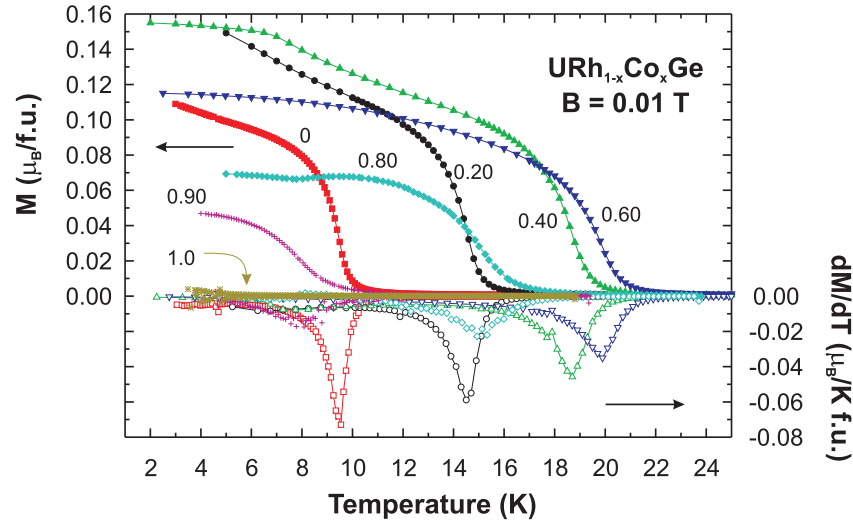


**Figure 6.4:** Temperature dependence of the dc magnetization of URh<sub>1-x</sub>Co<sub>x</sub>Ge for various values of  $x$ . The samples were zero-field cooled and measured in a field of 0.01 T. The lower part of the figure shows the derivative of the magnetization.

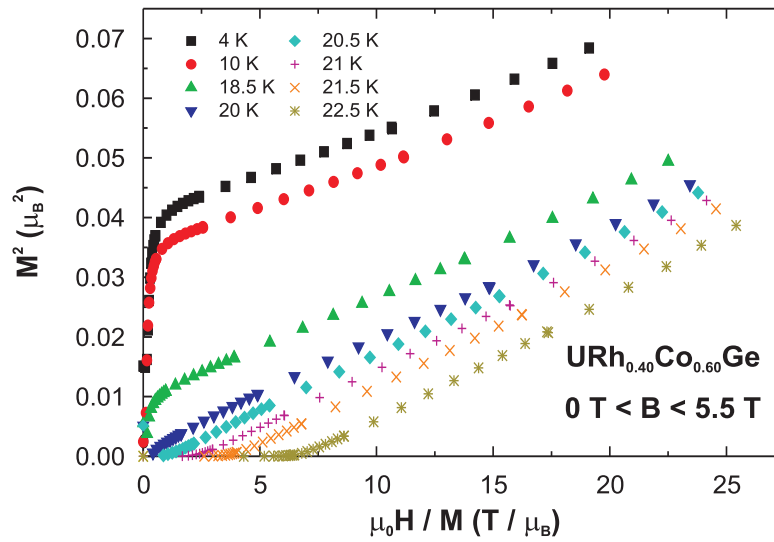


**Figure 6.5:** Arrott plots ( $M^2$  versus  $\mu_0 H / M$ ) of the magnetization of URh<sub>1-x</sub>Co<sub>x</sub>Ge with  $x = 0.60$  measured between  $T = 4$  and 22.5 K. The isotherm through the origin determines  $T_C = 20$  K.

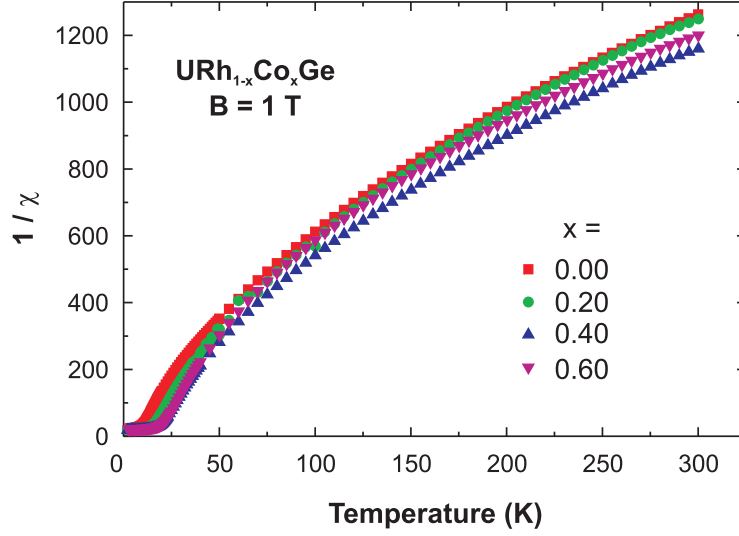


**Figure 6.6:** Inverse susceptibility  $1/\chi$  of  $\text{URh}_{1-x}\text{Co}_x\text{Ge}$  as a function of temperature in a field of 1 T for different values of  $x$ .

substitution of Rh by Ru. However, the peak in  $dM/dT$  for  $x = 0.20$  is also higher than for  $x = 0$ . Vertical scaling shows that the peaks are in fact equally sharp. Here the same is true as for substitution by Co. The ordered magnetic moment at 2 K in 1 T (Fig. 6.9) for  $x = 0.20$  is larger than for  $x = 0$ . In summary, chemical substitution of Ge by Si up to  $x = 0.20$  tends to enhance the ordered magnetic moment, but does not significantly change  $T_C$ . Note that this seems to indicate that in table 6.1 the value of  $\mu_s$  taken from Ref. [162] is more reliable than the value reported in Ref. [196].

### 6.3.2 Electrical resistivity

The  $\text{URh}_{1-x}\text{Ru}_x\text{Ge}$  series is further investigated by measuring the temperature dependence of the electrical resistivity  $\rho(T)$ . In Fig. 6.10 the low-temperature  $\rho(T)$  is shown for  $\text{URhGe}$ . Also shown is the derivative  $d\rho/dT$ . The Curie temperature  $T_C$  is defined as the intercept of the linear fits above and below  $T_C$ . For  $\text{URhGe}$   $T_C = 9.4$  K is obtained, in agreement with the magnetization results. Some authors define  $T_C$  differently, i.e. as the inflection point of the sharp increase in  $d\rho/dT$  around  $T_C$ , yielding a slightly higher value for  $T_C$ . The absolute values of  $\rho(T)$  reported here are somewhat smaller than the ones found by Tran and Troć [168] for polycrystals, but somewhat larger than reported by Prokeš *et al.* for a single crystal [163]. The residual resistance ratio (RRR) for the  $\text{URhGe}$  sample is 6, whereas for all the measured chemically substituted samples  $\text{RRR} \approx 2$  is obtained.

In Fig. 6.11 the temperature dependence of the electrical resistivity  $\rho(T)$  for  $\text{U(Rh,Ru)Ge}$  is shown. In the high-temperature region  $\rho(T)$  increases with decreasing temperature. At lower temperatures, the increase gradually changes to

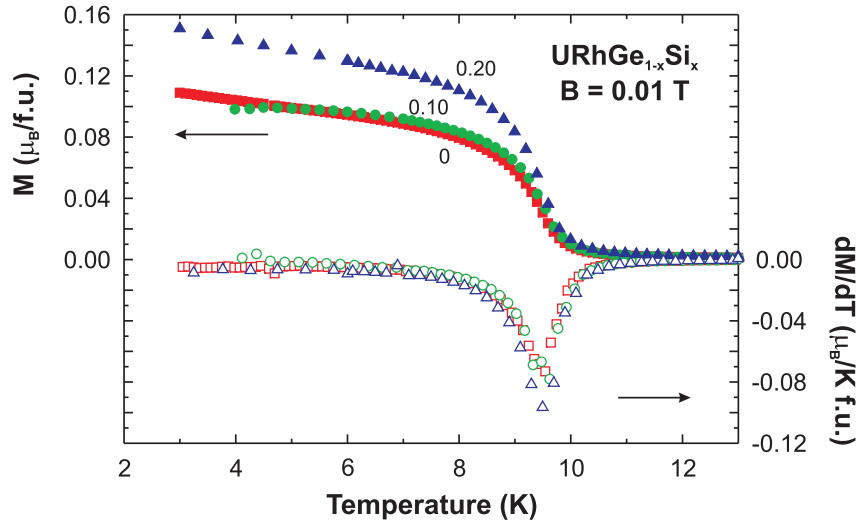


**Figure 6.7:** Temperature dependence of the dc magnetization of URhGe<sub>1-x</sub>Si<sub>x</sub> for various values of  $x$ . The samples were zero-field cooled and measured in a field of 0.01 T. The lower part of the figure shows the derivative of the magnetization.

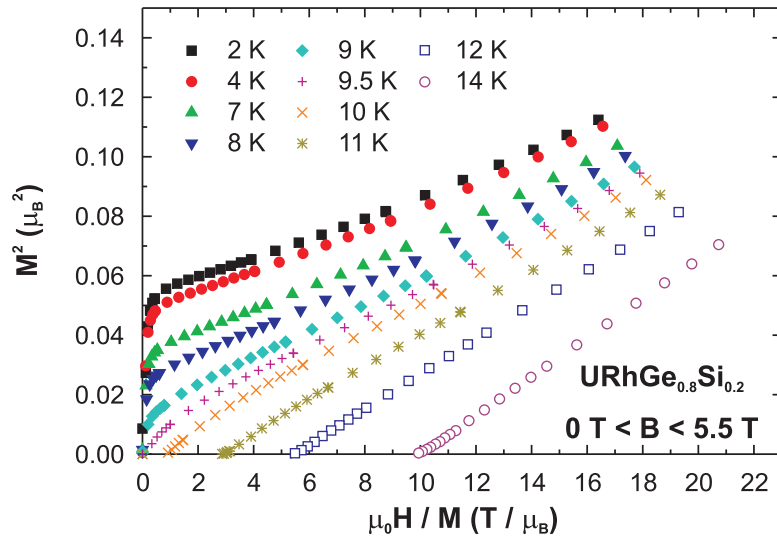


**Figure 6.8:** Arrott plots ( $M^2$  versus  $\mu_0 H / M$ ) of the magnetization of URhGe<sub>1-x</sub>Si<sub>x</sub> with  $x = 0.20$  measured between  $T = 2$  and 14 K. The isotherm through the origin determines  $T_C = 9.5$  K.

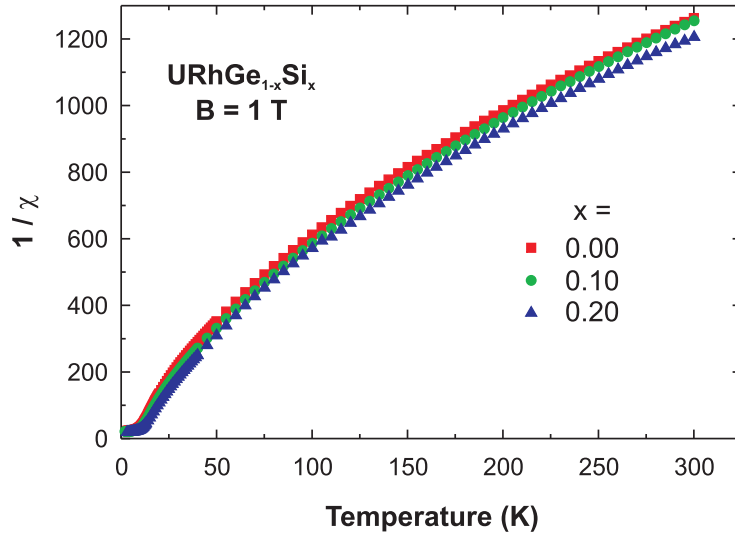


**Figure 6.9:** Inverse susceptibility  $1/\chi$  of  $\text{URhGe}_{1-x}\text{Si}_x$  as a function of temperature in a field of 1 T for different values of  $x$ .

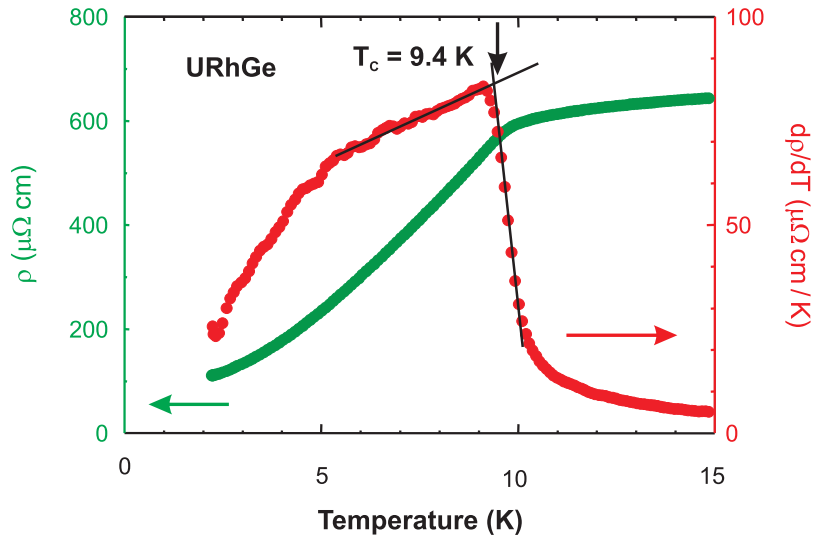


**Figure 6.10:** Low temperature part of the electrical resistivity  $\rho(T)$  of URhGe and the derivative  $d\rho/dT$ . The construction to determine  $T_C$  is shown.

a decrease, for different concentrations  $x$  at different temperatures, leading to a broad maximum. For URhGe it is seen that at  $T_C$  there is a sharp drop, caused by a decrease in spin-disorder scattering. For  $x > 0$ , the transition becomes less pronounced, in agreement with the magnetization data. Arrows indicate the Curie temperatures determined as mentioned above. For  $x \geq 0.35$  no transition was found in the measured temperature range.

Below  $T_C$ ,  $\rho(T)$  follows the behavior  $\rho_0 + AT^n$ . In table 6.2, values found for  $\rho_0$ ,  $A$ , and  $n$  are listed for a few samples. The fitting region is  $2\text{ K} < T < 6.5\text{ K}$ .

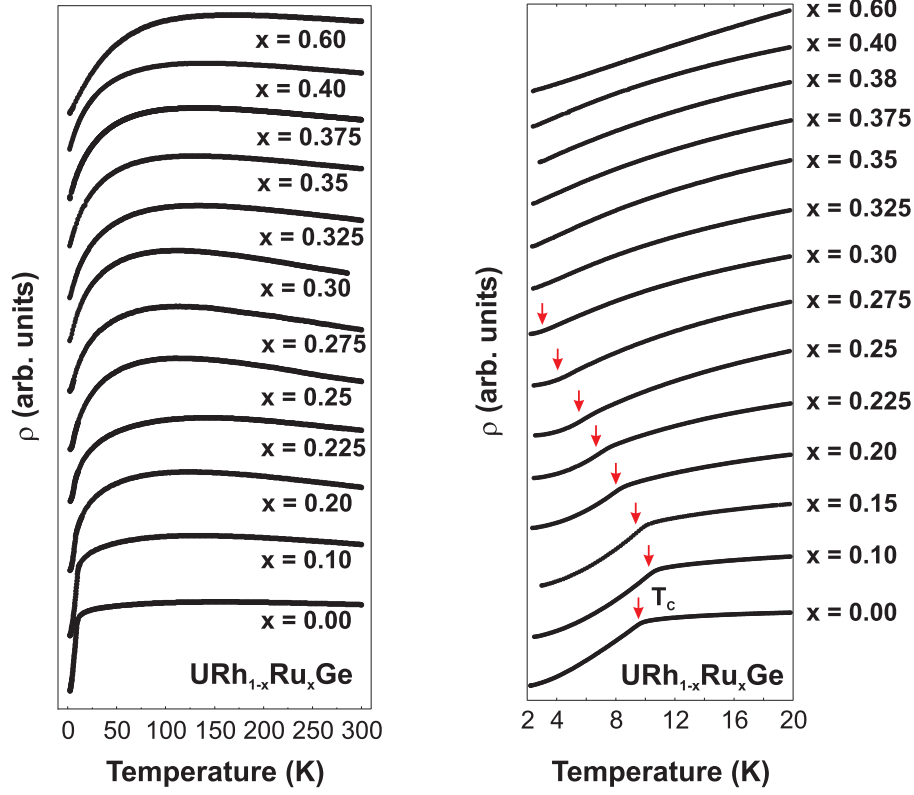


**Figure 6.11:** Temperature dependence of the electrical resistivity  $\rho$  measured on URh<sub>1-x</sub>Ru<sub>x</sub>Ge for various values of  $x$ . The Curie temperatures determined from the magnetization data are indicated by an arrow.

Since the parameters have been determined over a rather small  $T$  interval, the values are not very precise. However, it is possible to look for trends. The residual resistivity  $\rho_0$  increases with increasing  $x$  reflecting the atomic disorder caused by the Ru substitution. The exponent  $n$  also increases with increasing  $x$ , and attains values close to the Fermi-liquid value  $n = 2$ . Above the critical concentration an almost linear temperature dependence of  $\rho(T)$  is found with  $n = 1.19$ . A similar behavior is reported for UIr [199]. In order to investigate the full  $x$ -dependence of

**Table 6.2:** Obtained fitting values of the low-temperature electrical resistivity to the expression  $\rho = \rho_0 + AT^n$  for a few samples. The fitted temperature range is  $2 \text{ K} < T < 6.5 \text{ K}$ . Since the parameters have been determined over a rather small  $T$  interval, the values are not very precise.

	$x = 0$	$x = 0.10$	$x = 0.15$	$x = 0.20$	$x = 0.60$
$\rho_0$ ( $\mu\Omega \text{ cm}$ )	76.5	368.1	299.8	416.5	472.5
$A$ ( $\mu\Omega \text{ cm/K}^n$ )	6.9	1.85	0.90	0.51	3.36
$n$	1.94	2.10	2.18	2.41	1.19

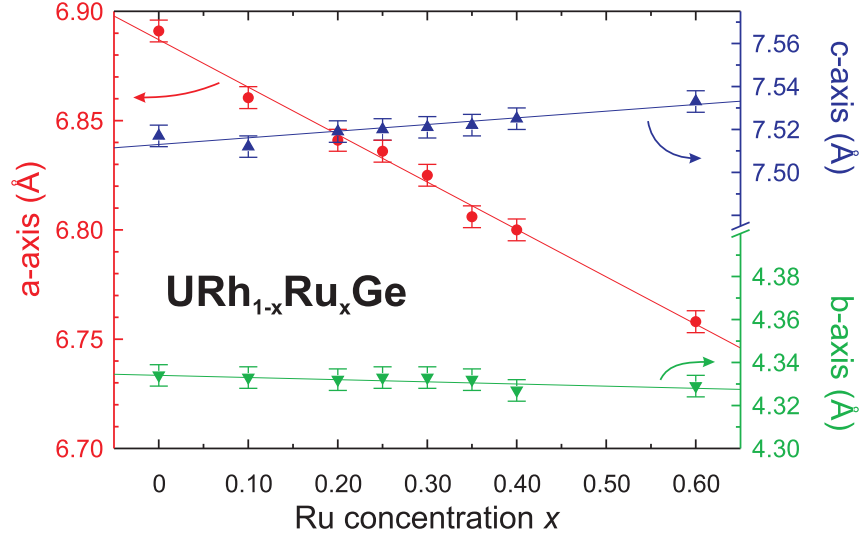


**Figure 6.12:** Lattice parameters  $a$  ( $\bullet$ ),  $b$  ( $\blacktriangledown$ ), and  $c$  ( $\blacktriangle$ ) of  $\text{URh}_{1-x}\text{Ru}_x\text{Ge}$  as a function of the Ru concentration  $x$  determined by X-ray powder diffraction at room temperature. The lines are fits to the data. It is clearly seen that substitution of Rh by Ru mainly affects the  $a$ -axis, whereas the  $b$ -axis can be considered to be constant.

$n$ , experiments at lower temperatures ( $T < 2$  K) are obviously required.

### 6.3.3 X-ray powder diffraction

Since  $\text{URhGe}$  and  $\text{URuGe}$  are isostructural but do not have the same unit-cell dimensions (the unit-cell volume of  $\text{URuGe}$  is slightly smaller), it is interesting to compare the volume effect of Rh substitution by Ru and of external pressure. Especially the  $x = 0.10$  sample could give valuable information about the nature of the mechanism leading to the observed increase of  $T_C$ . For this purpose X-ray powder diffraction measurements have been performed at room temperature on some of the samples.

The X-ray data confirm the orthorhombic  $Pnma$  structure of  $\text{URhGe}$  and show the same structure for  $\text{URh}_{1-x}\text{Ru}_x\text{Ge}$  for all  $x > 0$  measured. The deduced lattice parameters are shown in Fig. 6.12. No secondary phase was observed within experimental uncertainty. Note that the relative scales on the left-hand side as well as on the right-hand side in Fig. 6.12 are equal. It is clear that the  $a$ -axis is by far most affected by the substitution of Rh by Ru. The  $c$ -axis shows a slight increase with increasing  $x$ , whereas the  $b$ -axis remains practically constant. A linear fit describes the data well and shows that the lattice parameters of the  $\text{URh}_{1-x}\text{Ru}_x\text{Ge}$  series follow Vegard's law [200]. The  $a$ -axis can be described by  $a = (6.887(3) - 0.217(8) \cdot x) \text{ \AA}$ , the  $b$ -axis by  $b = (4.334(1) - 0.010(3) \cdot x) \text{ \AA}$ , and the  $c$ -axis by  $c = (7.513(2) + 0.031(5) \cdot x) \text{ \AA}$ . This leads to a unit-cell volume which is linear in  $x$  well within experimental uncertainty:  $V = (224.25(13) - 6.66(34) \cdot x) \text{ \AA}^3$ .

The value for URhGe ( $x = 0$ ) agrees with literature (table 6.1). The extrapolated value for URuGe,  $V = 217.59 \text{ \AA}^3$  for  $x = 1$ , is slightly smaller than found in table 6.1, but compares well with literature values as well.

Although substituting Rh by Ru mainly affects the  $a$ -axis, the reduction of the number of  $d$ -electrons and the substitution by a slightly smaller atom also affects the hybridization and thereby the magnetic properties. This will be further elaborated on in the discussion (Sec. 6.4).

Concerning the  $T_C$  maximum around  $x = 0.10$ . As can be seen in Fig. 6.12, the lattice parameters of URh<sub>1-x</sub>Ru<sub>x</sub>Ge show no special feature around  $x = 0.10$  within the experimental error. Likewise, the X-ray data do not show any anomaly in the lattice parameters in the region around  $x = x_{cr} = 0.38$ .

### 6.3.4 Specific heat

In the investigation of enhanced magnetic correlations as a quantum critical point is approached, knowledge of the linear electronic specific heat coefficient at low temperatures,  $\gamma$ , is essential. In Fig. 6.13 the temperature dependence of the specific heat divided by temperature ( $C_p/T$ ) in zero field is shown for a few characteristic samples of the URh<sub>1-x</sub>Ru<sub>x</sub>Ge series. Note the logarithmic temperature axis.

For temperatures above  $\sim 20$  K, the curves coincide. In this region, the specific heat is dominated by the phonon contribution. Fits to the equation  $C/T = \gamma + \beta T^2$  for temperatures between  $T = 15$  and  $22$  K lead to  $\beta = 0.60(1) \text{ mJ/mol K}^4$  for all values of  $x$ . From this value of  $\beta$  a Debye temperature  $\theta_D$  of about  $210$  K is obtained, in accordance with the value obtained by Prokeš *et al.* [163]. Values for  $\gamma$  range from  $115(3) \text{ mJ/mol K}^2$  for  $x = 0$  to  $91(3) \text{ mJ/mol K}^2$  for  $x = 0.50$ . The fit has been restricted to temperatures below  $22$  K because above this temperature the  $C/T$  curves start to deviate from the  $T^2$  dependence. For temperatures up to  $40$  K (the highest temperature measured) no indication of crystal field effects was observed.

Below  $\sim 15$  K short-range magnetic correlations start to play a role. At lower temperatures, a pronounced peak is observed, indicating the ferromagnetic transition. For  $x = 0$ , a Curie temperature of  $9.5$  K is obtained. The compound with  $x = 0.10$  has a slightly higher  $T_C$ . For  $x > 0.10$ ,  $T_C$  drops. For  $x = 0.38$  and  $0.50$ , no peak is observed down to the lowest temperature. The deduced Curie temperatures are consistent with the magnetization and electrical resistivity data. Also, the transition broadens, as it has been shown before for magnetization and resistivity data.

Note that the temperature dependence of the magnetic specific heat for  $0 < T < T_C$  changes from character in the case of chemical substitution. For URhGe it is found that  $C_p = \gamma T + AT^{3/2}$ , where the second term (a power law) corresponds to the contribution of ferromagnetic spin waves [65]. For finite  $x$  the spin-wave term becomes exponential, indicating the opening of a gap in the spin-wave excitation spectrum [65]. A detailed analysis will be published elsewhere [201].



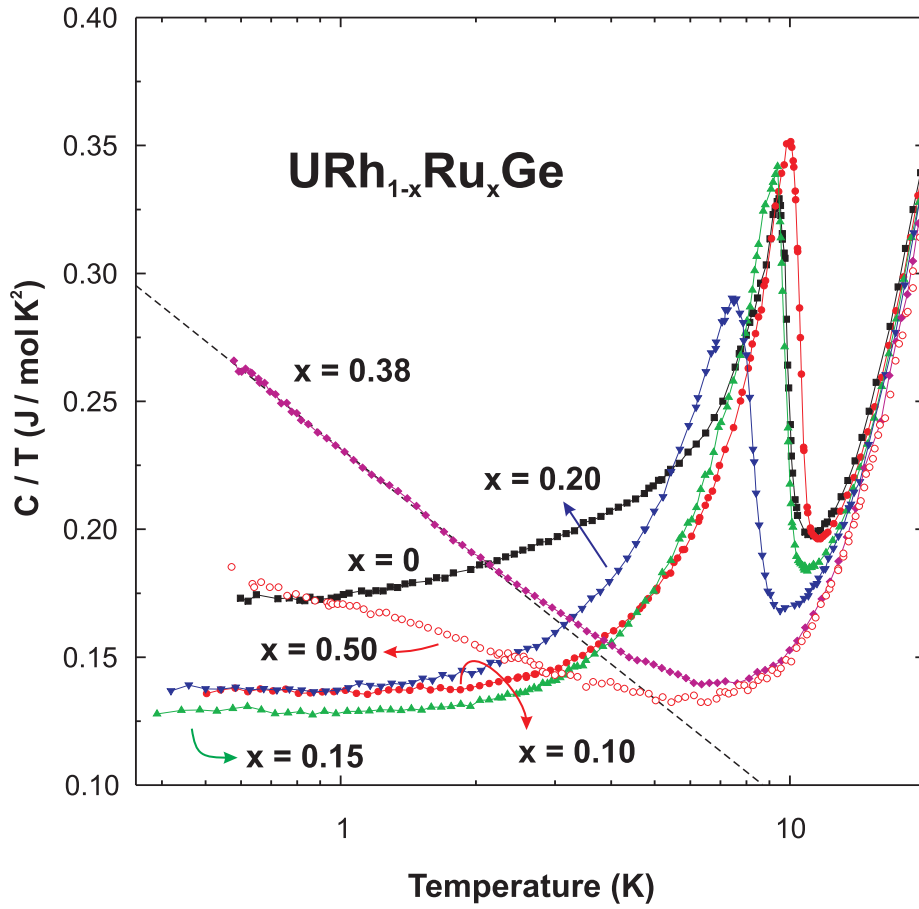


**Figure 6.13:** Specific heat divided by temperature ( $C/T$ ) of  $\text{URh}_{1-x}\text{Ru}_x\text{Ge}$  as a function of temperature for various values of  $x$ . Note the logarithmic horizontal scale. The solid line is a fit to  $C/T = -b \ln(T/T_0)$ .

The most interesting information is found at the lowest temperatures. For pure  $\text{URhGe}$ , a linear electronic coefficient of  $\gamma = 167 \text{ mJ/mol K}^2$  is found, consistent with literature (see table 6.1). As  $x$  is increased,  $\gamma$  decreases. For  $x = 0.10$ ,  $\gamma = 136 \text{ mJ/mol K}^2$ ; for  $x = 0.15$ ,  $\gamma = 127 \text{ mJ/mol K}^2$ ; for  $x = 0.20$ ,  $\gamma = 136 \text{ mJ/mol K}^2$ ; for  $x = 0.50$ ,  $\gamma = 181 \text{ mJ/mol K}^2$ . The compound with the concentration  $x = 0.38$  shows non-Fermi-liquid behavior. This confirms that  $x_{\text{cr}} = 0.38$  is the critical concentration as deduced previously from the magnetization measurements. A linear dependence of  $C/T$  on  $\ln T$  is found in the temperature region between 0.57 K and 2 K:  $C/T = -b \ln(T/T_0)$  with  $b = 0.061 \text{ J/mol K}^2$  and  $T_0 = 46 \text{ K}$ .

### 6.3.5 Magnetization under pressure

The purpose of measuring magnetization under pressure on compounds with one element substituted for another, is twofold. First of all, one may obtain the pressure dependence of  $T_C$  for the chemically substituted compound. This value can

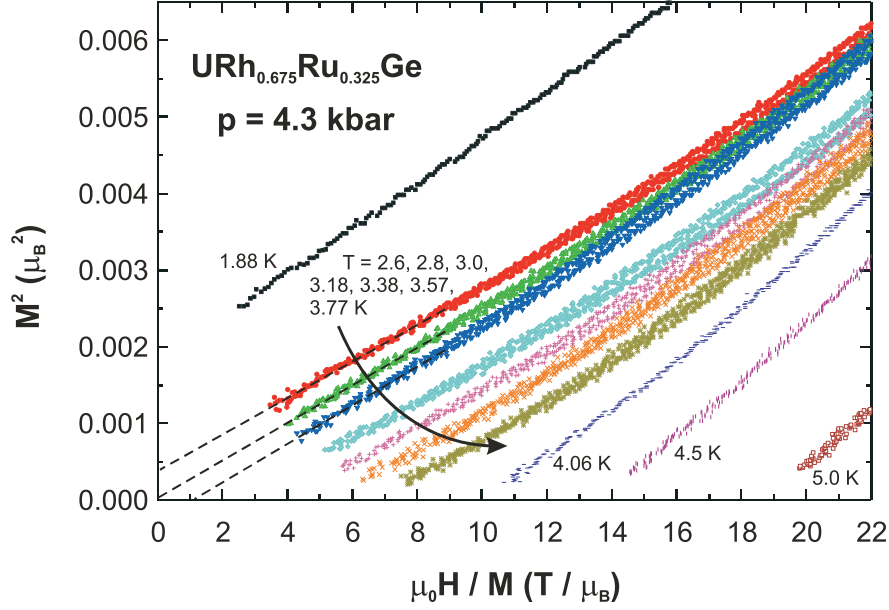


**Figure 6.14:** Arrott plots ( $M^2$  versus  $\mu_0 H/M$ ) of the magnetization of URh<sub>1-x</sub>Ru<sub>x</sub>Ge with  $x = 0.325$  measured between  $T = 1.88$  and  $5.0$  K at a pressure of  $p = 0.43$  GPa. The extrapolated isotherm through the origin determines  $T_C = 2.8$  K.

be compared to the (hydrostatic) pressure dependence of the pure compound. Secondly, the data might separate the two contributions leading to the change in  $T_C$ : the hybridization dependence on volume and on the number of electrons in the  $d$ -band. Combined concentration/pressure experiments have been carried out on, *e.g.*, CeCu<sub>6-x</sub>Au<sub>x</sub> [53].

A pressure of 0.43 GPa was applied to URh<sub>0.675</sub>Ru<sub>0.325</sub>Ge which is close to the quantum critical point, with  $T_C = 2.8$  K at ambient pressure (see figure below). In Fig. 6.14 the Arrott plot is shown, constructed from the magnetization measurements  $M(T)$ . Although field sweeps were performed up to 12 T, here only the (most interesting) low-field part is shown. The data have been corrected for the contribution of the Cu-Be pressure cell. Unfortunately the curves do not continue down to  $\mu_0 H/M = 0$ , because for low fields the measurements were disturbed by the signal of the piece of lead used for the pressure determination.

Linear extrapolation of the curves to lower values of  $\mu_0 H/M$  unmistakably shows that the  $T = 2.6$  K curve intersects the  $M^2$  axis, the  $T = 3.0$  K curve the  $\mu_0 H/M$  axis, and the  $T = 2.8$  K curve passes through the origin (within uncertainty), indicating that  $T_C = 2.8$  K. This value is the same as for ambient pressure. It is remarkable that a pressure of 0.43 GPa does not alter the Curie temperature, especially since the compound is close to a quantum phase transition. In Ref. [176] it is shown that  $dT_C/dp \approx 0.065$  K/kbar for URhGe, when fitting  $T_C(p)$  with a linear function over the whole pressure range up to 14.0 GPa, whereas  $dT_C/dp = 0.119(6)$  K/kbar is found by dilatometry as the pressure dependence for  $p \rightarrow 0$  [192].

A pressure of 0.43 GPa would thus lead to an enhancement  $\Delta T_C$  in the range 0.28 – 0.51 K in URhGe. However,  $\Delta T_C$  is essentially negligible for URh<sub>0.675</sub>Ru<sub>0.325</sub>Ge. The apparent strong  $dT_C/dp$  dependence on Ru substitution should be checked for other values of  $x$ .

In addition it should be mentioned that in a field of 1 T and at 2.5 K (the lowest temperature measured in 1 T) a moment of  $M = 0.065 \mu_B/\text{f.u.}$  is found at  $p = 0.43$  GPa. This can be compared to the larger value of  $M = 0.078 \mu_B/\text{f.u.}$  observed in the same field at ambient pressure.

## 6.4 Analysis and Discussion

### Ru substitution

The main results for the Ru-substitution are reported in Fig. 6.15a, where the Curie temperature  $T_C$  of the URh<sub>1-x</sub>Ru<sub>x</sub>Ge series is shown as a function of Ru concentration  $x$ , deduced from the magnetization and electrical-resistivity measurements. The values of  $T_C$  obtained by both techniques are equal within the experimental error and coincide with specific-heat results.

For the pure URhGe sample  $T_C = 9.5$  K is found, in agreement with the literature value [2]. Remarkably, when substituting small amounts of Rh by Ru, the Curie temperature shows an initial increase up to 10.5 K for  $x = 0.10$ . At higher Ru concentrations  $T_C$  is reduced and a linear decrease with a slope of  $-0.43$  K/at.% Ru is observed from  $x = 0.20$  onwards. For samples with  $x = 0.35, 0.375, 0.40$ , and  $0.60$  no ferromagnetism was detected in the measured temperature interval ( $T > 1.8$  K). The Arrott plots clearly indicate a paramagnetic ground state for  $x = 0.40$  and  $0.60$ . Extrapolation of the Arrott plots for the  $x = 0.35$  sample suggest that  $T_C \approx 1.3$  K (indicated in the figure by a filled square). This is consistent with the linear decrease of  $T_C$ . A linear extrapolation of  $T_C(x)$  leads to a critical concentration for the suppression of ferromagnetic order  $x_{cr} \approx 0.38$ . This is confirmed by the non-Fermi-liquid behavior observed in the specific heat for  $x = 0.38$  (Fig. 6.13).

In Fig. 6.15b the Ru concentration dependence  $x$  of the specific heat divided by temperature,  $C/T$ , at 0.6 K is shown as well as the literature value of the Sommerfeld coefficient  $\gamma$  for URuGe (see table 6.1). Clearly there is a minimum at  $x = 0.15$ . This is consistent with the initial increase of  $T_C$ . At  $x = 0.38$ ,  $C/T(0.6 \text{ K})$  is twice as high as for  $x = 0.15$ , followed by a decrease up to  $x = 0.50$ . This indicates that as the critical concentration is approached, magnetic correlations tend to become stronger. (Note that while the data do suggest a maximum of  $C/T$  near the quantum critical point, the exact form is speculative at this point.) In fact, the low-temperature part for  $x = 0.38$  can be fitted to the non-Fermi-liquid function  $C/T = -b \ln(T/T_0)$  with  $T_0 = 46$  K. This is exactly the function predicted by Millis [82] for a three dimensional ferromagnet at the quantum critical point. Here  $T_0$  is the spin-fluctuation temperature, *i.e.* a measure of the strength of the magnetic interactions. Specific-heat measurements on U(Rh,Ru)Ge compounds with  $x$  close

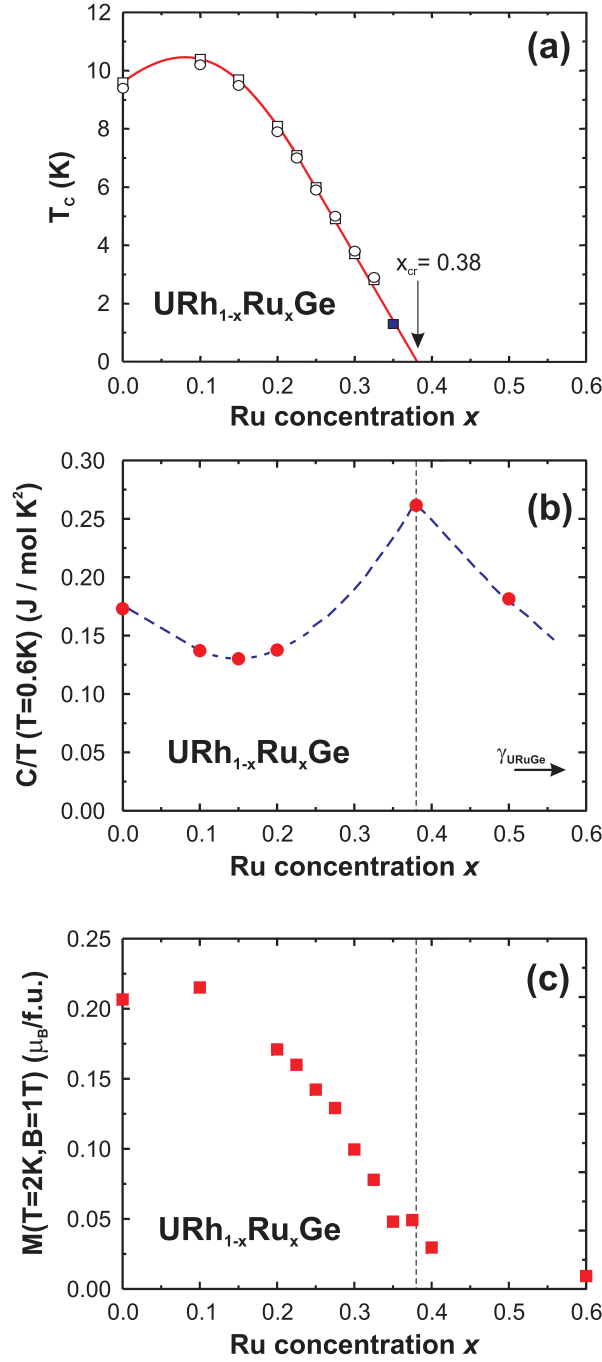


**Figure 6.15:** (a) Curie temperature  $T_C$  as a function of the Ru concentration  $x$  in URh<sub>1-x</sub>Ru<sub>x</sub>Ge as determined by magnetization (squares) and electrical resistivity (circles). The solid square is determined by extrapolation of Arrott plots (see main text). The solid line serves a guide to the eye. The critical Ru concentration for the suppression of ferromagnetic order is  $x_{cr} \approx 0.38$ . (b) Specific heat divided by temperature,  $C/T$ , at 0.6 K, as a function of Ru concentration  $x$ . The literature value of  $\gamma$  for URuGe is also indicated. (c) Magnetic moment  $M$  at 2 K in a field of 1 T as a function of Ru concentration  $x$ .

to the critical value should yield important information about the evolution from Fermi-liquid to non-Fermi-liquid behavior.

In Fig. 6.15c the magnetization at 2 K in a field of 1 T is shown as a function of Ru concentration  $x$ . Clearly it has a similar dependence on  $x$  as  $T_C$ , as expected. First an increase of  $M$  is observed, followed by a decrease for  $x > 0.10$ . Around  $x_{cr}$  a little hump is present in  $M(2\text{ K}, 1\text{ T}, x)$ . It might be possible that this hump is the signature of the critical point in fact being first order. For  $\text{ZrZn}_2$  a first order transition is signalled at the critical pressure by a jump in the Curie temperature  $T_C$  as well as in the magnetization  $M$  with increasing pressure  $p$  [61]. A similar anomaly in the magnetization  $M$  is observed for  $\text{UGe}_2$  [114]. Unfortunately, the number of data points in the vicinity of  $x_{cr}$  is too limited to draw definite conclusions on the nature of the transition at the critical point for  $\text{URh}_{1-x}\text{Ru}_x\text{Ge}$  at this stage.

The suppression of magnetism in  $4f$ -electron metals close to an electronic instability is often discussed in terms of a simple Doniach picture [48], *i.e.*, the competition between the on-site Kondo interaction and inter-site RKKY interaction. The control parameter - the exchange interaction  $J$  - increases with increasing hybridization. For weak hybridization, *i.e.* low Kondo temperature, the RKKY interaction is favored, while a large  $J$  favors the nonmagnetic Kondo-singlet ground state. Hence the generic  $T_C(p)$  passes over a maximum as observed, *e.g.*, for the pressure dependence of  $T_C$  in ferromagnetic  $\text{CeAg}$  [202]. This might be the case for  $\text{URhGe}$  as pressure enhances  $T_C$  [192, 176]. On the other hand, more sophisticated models, like the one proposed by Sheng and Cooper [203] obtain an increase of the magnetic ordering temperature with pressure for compounds like  $\text{UTe}$  by incorporating the change in the  $f$ -density spectral distribution under pressure in LMTD band-structure calculations. Such a model could in principle also explain the increase of  $T_C$  in  $\text{URhGe}$  under pressure and the initial increase of  $T_C$  in  $\text{U(Rh,Ru)Ge}$ . However, similar band-structure calculations for  $\text{URhGe}$  have not been performed yet, but would be highly desirable.

The decrease of  $T_C$  beyond  $x = 0.10$  is likely to be attributed to the effect of emptying the  $d$ -band, since Ru has one electron less than Rh. In a simple model, extracting electrons from the  $d$ -band of the “electron sea” gives the opportunity to the U  $f$ -electrons to fill the holes thus created in the  $d$ -band. This results in a strengthening of the  $f$ - $d$  hybridization, which in turn leads to a larger exchange parameter  $J$ , favoring the Kondo interaction. Apparently, this effect dominates the volume effect for  $x > 0.10$ . Disorder is expected to play a secondary role because  $T_C$  of  $\text{URh}_{1-x}\text{Co}_x\text{Ge}$  samples with similar disorder gradually increases up to 20 K for  $x = 0.60$ .

For  $x > 0.20$  the Curie temperature  $T_C$  shows a linear dependence on the control parameter, the Ru concentration  $x$ :  $T_C \sim |x - x_c|$ . In the magnetic phase diagram proposed by Millis [82] the magnetic ordering temperature for itinerant fermion systems varies as  $T_M \sim |\delta - \delta_c|^{z/(d+z-2)}$ , with  $\delta$  some control parameter driving the magnetic-to-nonmagnetic transition (*e.g.*, pressure, magnetic field, chemical substitution concentration),  $\delta_c$  the critical value of the control parameter,  $d$  the dimension

of the system, and  $z$  the dynamic critical exponent ( $z = 2$  for antiferromagnets and  $z = 3$  for ferromagnets). In the present case ( $d = 3$ )  $T_C \sim |x - x_c|^{3/4}$  would thus be expected, in contrast with the observed  $T_C \sim |x - x_c|$ . A possible explanation could be that the critical region does not extend all the way to  $x = 0.20$ . In this study  $T_C$  might not have been determined accurately and close enough to  $x_{cr}$ . An alternative explanation might be that the effective dimension for the magnetic correlations is reduced from  $d = 3$  to  $d = 2$ . This idea is supported by the strong magnetic anisotropy that essentially confines the magnetic moment to the  $b - c$  plane. However, the theoretical model then does not predict a logarithmic difference of  $C/T$ , as observed (Fig. 6.13), but a power law ( $C/T \sim T^{-1/3}$ ).

It is interesting to compare the volume effect due to substitution by Ru and due to pressure in URhGe. URhGe and URuGe are isostructural, the unit-cell volume of URuGe being slightly smaller. X-ray powder diffraction data on some of the samples show that the lattice parameters of the URh<sub>1-x</sub>Ru<sub>x</sub>Ge series follow Vegard's law (see Sec. 6.3.3). With an estimated isothermal compressibility  $\kappa = -V^{-1}(dV/dp)$  of 0.8 Mbar<sup>-1</sup> [192], 10 at.% substitution of Rh by Ru ( $x = 0.10$ ) corresponds to a pressure of 0.37 GPa. With  $dT_C/dp = 0.065$  K/kbar [176] this pressure results in a small increase of  $T_C$  to 9.8 K, while  $T_C \sim 10.5$  K for 10 at.% Ru substitution would suggest a much larger  $dT_C/dp \approx 0.24$  K/kbar, if attributed solely to a volume effect. The divergence may arise because the unit-cell reduction upon Ru substitution is strongly anisotropic and dominated by the decrease of the lattice parameter  $a$ , whereas hydrostatic pressure is expected to give a much more isotropic unit-cell reduction. Since uniaxial pressure along any direction enhances  $T_C$  [192], hydrostatic pressure will enhance  $T_C$  even more. This can be seen from the fact that, in first approximation,  $dT_C/dp_i \approx (1/3)dT_C/dp$ .

Furthermore, the effect of external pressure with the shrinkage of the  $a$ -axis due to Ru-substitution, a change of volume, affects the overlap of  $f$ - and  $d$ -orbitals, and therefore, leads to a change in energy of the  $f$ -band. The number of electrons in the system is however constant, and therefore – in a rigid-band picture – also the Fermi level. The change in Curie temperature is determined by the change in proximity of the  $f$ -band to the Fermi level. In the case of Ru substitution, on the other hand, the cause is the removal of electrons from the  $d$ -band.  $U$   $f$ -electrons are able to fill the space of the so created holes. This enhances the  $f$ - $d$  hybridization and  $T_C$  is affected. The Fermi level is lowered and approaches the  $f$ -band. As a side effect, a reduction in unit-cell volume is observed.

Hydrostatic pressure of 0.43 GPa on URh<sub>0.675</sub>Ru<sub>0.325</sub>Ge does not affect  $T_C$  as shown in Sec. 6.3.5, but does lower the magnetization in 1 T at low temperatures. This reduction could be explained by an increased delocalization of the electrons. This would however normally decrease  $T_C$ . For URhGe pressure along any of the three crystallographic axes enhances  $T_C$  [192]. In URh<sub>0.675</sub>Ru<sub>0.325</sub>Ge the  $a$ -axis is much smaller than for URhGe, whereas the  $b$ - and  $c$ -axes are comparable. Possibly the uniaxial pressure dependence along the  $a$ -axis changes sign with increasing Ru concentration  $x$ . The  $x = 0.325$  compound would be at the crossover between a



positive and a negative uniaxial pressure dependence of  $T_C$ . It would be interesting to measure other concentrations and at higher pressures.

The  $\text{URh}_{1-x}\text{Ru}_x\text{Ge}$  series deserves further investigation by measurements at lower temperatures and other Ru concentrations  $x$  in order to prove that the observed non-Fermi-liquid (NFL) behavior at  $x_{\text{cr}} = 0.38$  is an effect of the proximity to a zero-temperature phase transition, and not due to disorder, like proposed in the Kondo disorder model [80] and the Griffiths phase model [85]. In the Kondo disorder model a distribution of Kondo temperatures  $T_K$  can arise if a Kondo-lattice material has significant disorder. Around each magnetic impurity, antiferromagnetically coupled to the conduction electrons, the Kondo effect will occur at different values of  $T_K$ . Averaging over such a distribution can produce thermodynamic and transport properties with NFL-like dependencies. In the Griffiths phase model the presence of disorder is considered to lead to the coexistence of a metallic paramagnetic phase and a granular magnetic phase. In the paramagnetic phase the moments are quenched by the Kondo interaction, giving rise to FL behavior, while the magnetic phase is dominated by the RKKY interaction giving rise to ordered regions.

## Co and Si substitution

The main results from the Co and Si substitution study are reported in Fig. 6.16a, where the Curie temperature  $T_C$  of the  $\text{URh}_{1-x}\text{Co}_x\text{Ge}$  and  $\text{URhGe}_{1-x}\text{Si}_x$  series are shown as a function of Co and Si concentration  $x$ , deduced from the magnetization measurements. In Fig. 6.15b the magnetization at 2 K in a field of 1 T is shown.

Substituting Rh by Co in  $\text{URhGe}$  increases  $T_C$  considerably to a maximum of 20 K at  $x = 0.60$ . The Co concentration  $x_{\text{cr}}$  for which  $T_C = 0$  is close to 1. Hence  $\text{UCoGe}$  is close to a magnetic instability, easily reachable by substituting a few at.% Co by Rh. Although Canepa *et al.* [197] found a magnetic transition around 46 K for  $\text{UCoGe}$ , the results presented here are in accordance with other studies [172, 170] for temperatures down to 1.2 K and indicate no ferromagnetic order.

The number of  $d$ -electrons remains constant when substituting Rh by Co. Hence, any change in  $T_C$  should be an effect of a volume change. Assuming the lattice parameters of  $\text{URh}_{1-x}\text{Co}_x\text{Ge}$  to follow Vegard's law,  $x = 0.60$  corresponds to a pressure of 5.4 GPa (with  $\kappa = 0.8 \text{ Mbar}^{-1}$ ). With  $dT_C/dp = 0.065 \text{ K/kbar}$  [176] this pressure results in a small increase of  $\Delta T_C = 3.5 \text{ K}$ . Chemical substitution mainly affects the  $c$ -axis and the  $b$ -axis to a lesser extent, whereas the  $a$ -axis is hardly influenced. This is very different from hydrostatic pressure.

For the  $\text{URhGe}_{1-x}\text{Si}_x$  series  $T_C$  does not vary up to  $x = 0.20$  although there are significant changes in length for the  $a$ -,  $b$ -, and  $c$ -axes. It is however interesting that the magnetic moment at 2 K in 1 T is enhanced by 25 % for  $x = 0.20$ . This is an indication of the localization of magnetic moments, due to changes in hybridization.

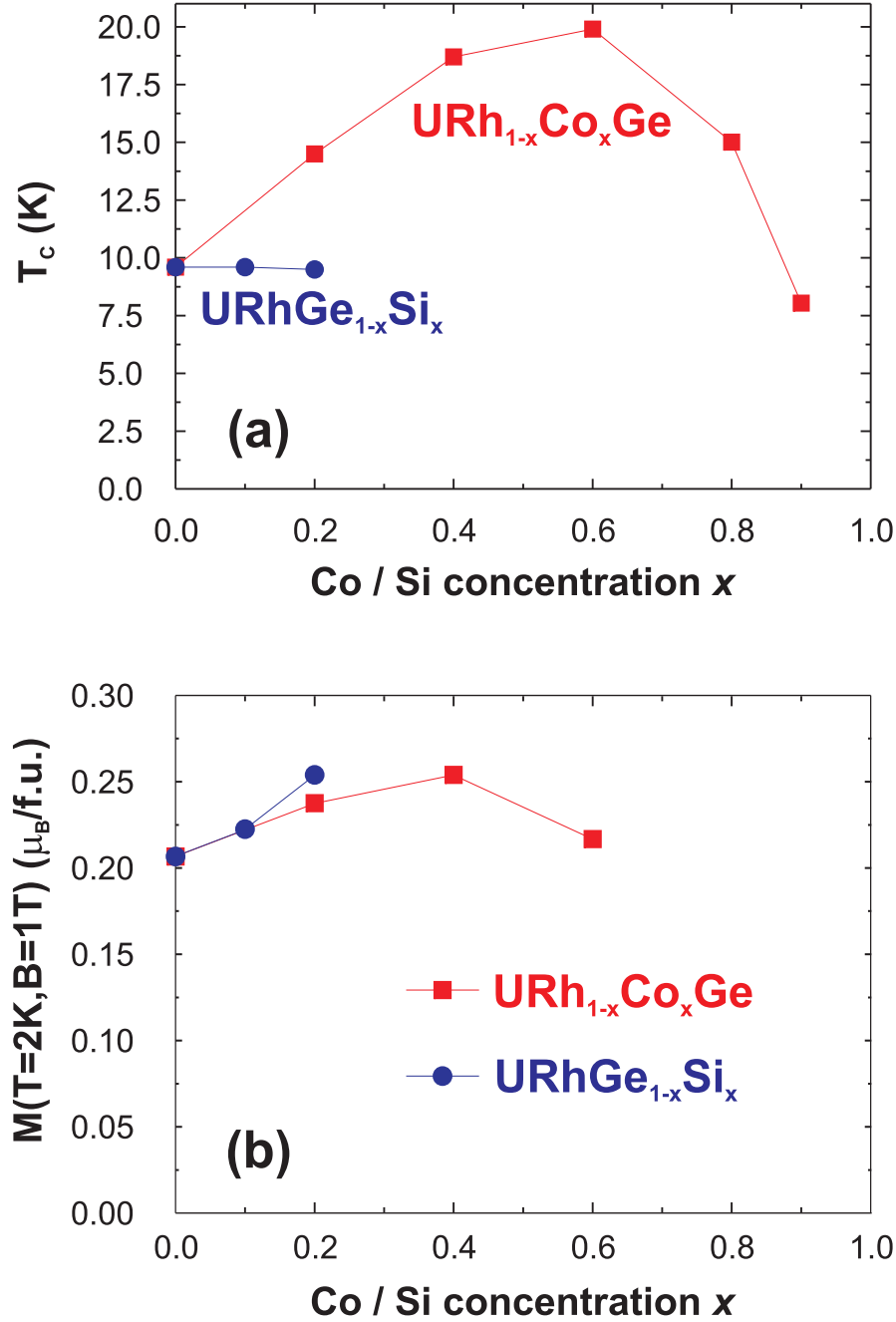


**Figure 6.16:** (Above) Curie temperature  $T_C$  as a function of the Co and Si concentration  $x$  in URh<sub>1-x</sub>Co<sub>x</sub>Ge and URhGe<sub>1-x</sub>Si<sub>x</sub> as determined by magnetization measurements. The solid lines serve a guide to the eye. The critical Co concentration  $x_{cr}$  for the suppression of ferromagnetic order is close to 1. Si doping on the Ge site does not affect  $T_C$ . (Below) Magnetic moment  $M$  at 2 K in a field of 1 T as a function of Co and Si concentration  $x$ .



## 6.5 Conclusions

In summary, the evolution of ferromagnetism in URhGe, in which atoms were substituted by Ru, Co, and Si, have been investigated. For substitution by Ru,  $T_C$  initially increases, which is attributed to a volume effect. For  $x > 0.10$ ,  $T_C$  decreases, which suggests that emptying the  $d$ -band governs the hybridization phenomena. Ferromagnetism is completely suppressed for  $x_{\text{cr}} \approx 0.38$ . At this critical concentration non-Fermi-liquid (NFL) behavior is observed in the specific heat. At low temperatures it is found that the specific heat can be described by  $C/T \sim -\ln T$ . For substitution by Co,  $T_C$  increases up to 20 K for  $x = 0.60$  and ferromagnetism is suppressed for  $x$  close to 1. This means that UCoGe is close to a quantum critical phase transition and provides a good candidate to study a ferromagnetic quantum critical point. Finally, substituting Ge by Si is found not to affect  $T_C$  up to  $x = 0.20$ .



---

---

# CHAPTER 7

---

## UIr

### 7.1 Introduction

THE FIRST REPORT OF THE EXISTENCE OF UIr was made in 1968 when it was found that UIr melts congruently at 1743 K [204]. It took nearly another twenty years to appear in literature again. Whereas UPt was studied rather well, little attention was paid to UIr. In 1987 Dommann *et al.* even wrote [205]: “Our motivation for preparing UIr was the hope to find a non-trivial superconductor and we were rather disappointed by the discovery of its ferromagnetism.” Besides the determination of its crystal structure and magnetic structure [205, 206, 207] only electrical resistivity at ambient pressure was reported by Brändle *et al.* [208], while Ōnuki *et al.* [209] mentioned that the electrical resistivity, thermoelectric power, Hall coefficient, magnetic susceptibility, and magnetization resemble the data for URh. Here the story of UIr ends for about ten years.

After the study of UIr by electrical resistivity under pressure and specific heat at ambient pressure [210], the non-trivial superconductivity Dommann *et al.* had been looking for in UIr was finally found in the year 2004. After UGe<sub>2</sub> [1] and URhGe [2], UIr is the third uranium based compound to show coexistence of ferromagnetism and superconductivity [3]. Just like in UGe<sub>2</sub>, the coexistence in UIr occurs within a limited pressure range (2.6-2.7 GPa), which is the critical pressure region in which the Curie temperature  $T_C$  is tuned to zero. With the coexistence of ferromagnetism and superconductivity UIr belongs to a class of materials, which exhibit unconventional ground state properties close to a quantum critical point. In this class of materials UIr even holds a special place because it is a system in which the crystal structure lacks inversion symmetry.

UIr crystallizes in the monoclinic PbBi-type structure (space group  $P2_1$ ) without inversion symmetry. The unit cell, with dimensions  $a = 5.62$  Å,  $b = 10.59$  Å, and

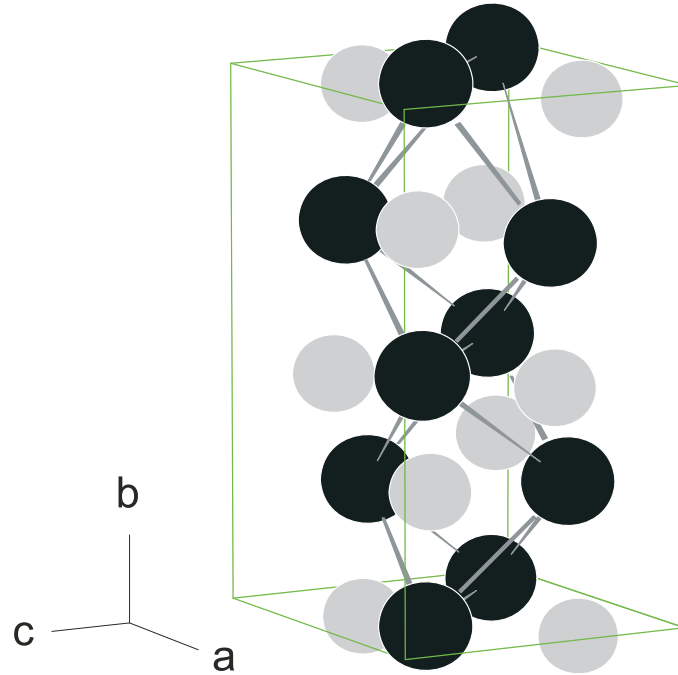


**Figure 7.1:** The monoclinic crystallographic structure of UIr. The uranium atoms are indicated in black and iridium atoms in gray. The figure shows the unit cell of UIr containing eight formula units.

$c = 5.60 \text{ \AA}$  ( $\alpha = 90^\circ$ ,  $\beta = 98.9^\circ$ ,  $\gamma = 90^\circ$ ), contains eight formula units with four inequivalent U and Ir sites [205]. The unit cell is shown in Fig. 7.1. UIr is a ferromagnet with a Curie temperature of  $T_C = 46 \text{ K}$  at ambient pressure. Magnetization measurements on a single crystal [211] revealed that the easy axis is parallel to  $[10\bar{1}]$  and that the anisotropy with the hard axes  $[101]$  and  $[010]$  is large. Along the easy direction, the average saturated moment is equal to  $0.5 \mu_B/\text{U-atom}$ . The coefficient of the linear electronic specific heat  $c/T = 50 \text{ mJ/mol K}^2$  indicates a moderate enhancement of the electron correlations at ambient pressure.

The pressure dependence of the ferromagnetic transition temperature was measured by magnetization and electrical resistivity [3]. As shown in Fig. 7.2,  $T_C$  is continuously suppressed for increasing pressures until the magnetic structure collapses at a pressure of about 1.7 GPa and again around 2.1 GPa into a new ferromagnetic structure with a higher  $T_C$ . For even higher pressures the ferromagnetic order is finally completely suppressed at a critical pressure of about 2.6-2.7 GPa. The saturated moment deduced from the magnetization measurements shows a strong reduction in the ordered moment at the transition from the low-pressure ordered structure to the high-pressure ordered moment. Close to the critical pressure superconductivity can be found below  $T_{sc} = 0.14 \text{ K}$  with an upper critical field of  $\mu_0 H_{c2}(0) = 26 \text{ mT}$ .

The first compound found to have a coexistence of magnetic order, superconductivity, and a lack of crystallographic inversion symmetry is CePt<sub>3</sub>Si [213]. An-

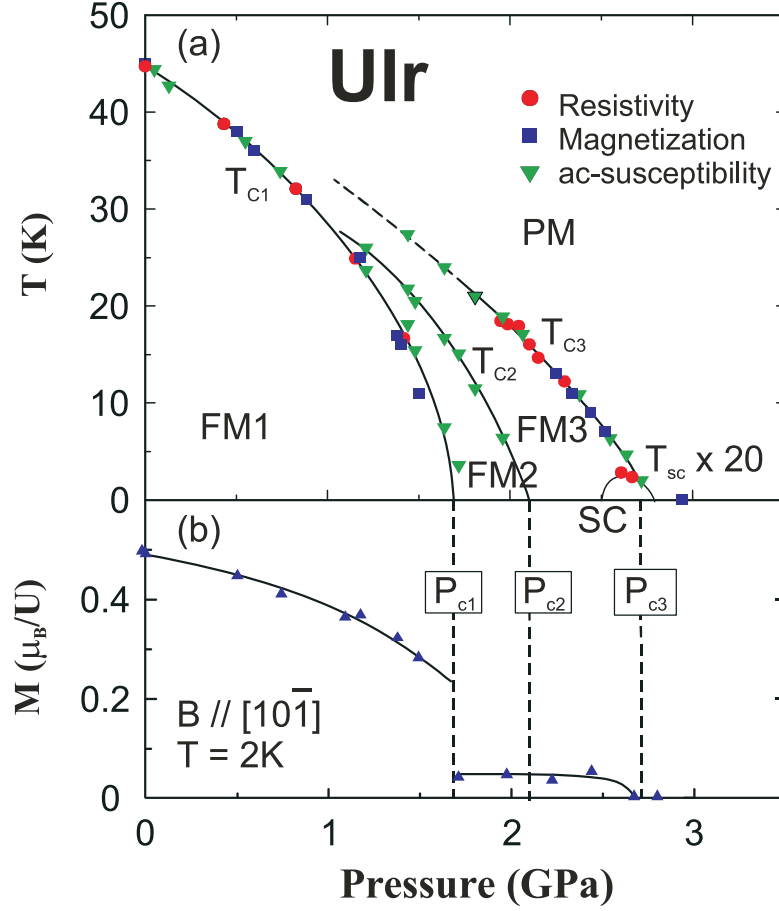


**Figure 7.2:** Magnetic phase diagram of UIr. (a) Pressure dependence of the Curie temperatures  $T_{C1}$ ,  $T_{C2}$ , and  $T_{C3}$  and superconducting transition temperature  $T_{sc}$ . The phase boundaries are determined by resistivity, magnetization, and ac-susceptibility. (b) Pressure dependence of the ordered moment  $M$  along the  $[10\bar{1}]$  direction. In the FM2 and FM3 phases the ordered moment is less than  $0.05 \mu_B/U$ . The figure is taken from Ref. [212].

tiferromagnetism sets in at  $T_N = 2.2$  K and superconductivity at  $T_c = 0.75$  K. The lack of inversion symmetry in the crystal is believed to exclude spin-triplet pairing, since in the absence of inversion symmetry the necessary set of degenerate electron states cannot be provided for this type of pairing [214]. However, a high value for the upper critical field  $\mu_0 H_{c2}(0)$  seems to exclude spin-singlet pairing [213]. It was proposed that a triplet-pairing state is still possible because the absence of the mirror  $z \rightarrow -z$  would yield a Rashba-type spin-orbit coupling [215]. Later it was shown that the antisymmetric spin-orbit coupling, which is present due to the lack of inversion symmetry in CePt<sub>3</sub>Si, leads to a lifting of the degeneracy in a special form which influences the Cooper pairing in such a way that the classification in even and odd parity or spin singlet and triplet state is obsolete [216]. The superconducting state may be viewed as a superposition of an  $s$ -wave and  $p$ -wave state which yields a particular gap form with accidental line nodes.

UIr, on the other hand, is a ferromagnet and it is thought that superconductivity therefore cannot be of a spin-singlet type due to the absence of a degeneracy between  $|\mathbf{k}, \uparrow\rangle$  and  $|\mathbf{k}, \downarrow\rangle$  states. An inversion symmetry guarantees [214] the degeneracy of  $|\mathbf{k}, \uparrow\rangle$  and  $|\mathbf{k}, \downarrow\rangle$  states, which is essential for spin-triplet pairing. UIr is very interesting, since the lack of inversion symmetry prohibits this degeneracy and as a result spin-triplet pairing, while the ferromagnetism is thought to prohibit spin-singlet pairing.

As shown in Fig. 7.2 there are three ferromagnetic phases separated by transitions in the pressure range from 1.7 to 2.1 GPa. The superconductivity can be associated with the quantum critical point of the third phase. Akazawa *et al.* [199] discusses the possibility of a structural transition from the monoclinic  $P2_1$  structure to a structure with inversion symmetry in addition to the magnetic transition. Since the temperature dependence of the electrical resistivity  $\rho(T)$  is continuous and since a structural change to the space group which is closest already requires huge displacements of atom positions, it is likely that UIr keeps lacking inversion symmetry up to 3.1 GPa. The transitions at high pressure are expected to be magnetic rather than structural transitions.

In this Chapter several ambient pressure measurements on single-crystalline samples of UIr are reported. The first experiment consisted of measuring the magnetization in magnetic fields up to 52 T, to search for a field-induced metamagnetic transition in UIr. Secondly, specific heat measurements down to 3 K in fields up to 14 T are discussed. Finally, thermal expansion and magnetostriction data are presented.

## 7.2 Magnetization in High Magnetic Fields\*

### 7.2.1 Introduction

Since UIr is close to a quantum critical point it is interesting to investigate the magnetic interactions at play. A metamagnetic transition is a transition from one magnetic state to another by the application of a magnetic field  $\mu_0 H$ . In compounds with a strong competition between the Kondo effect and the RKKY interaction (see Chapter 3), so-called strongly correlated systems characterized by an enhanced linear electronic specific heat coefficient, the ordered magnetic moment is small and is accompanied by large magnetic fluctuations. These fluctuations can be suppressed by a magnetic field leading to a metamagnetic transition. Such a transition characterizes the electronic interactions. Two examples of compounds with a metamagnetic transition are  $\text{UPt}_3$  [217, 218] with a transition at a field of 21 T and  $\text{URu}_2\text{Si}_2$  [219, 220, 221, 222] with several transitions around 35 T.

Magnetization measurements [211] show a small ordered magnetic moment of  $0.5 \mu_B/\text{U-atom}$  in 0 T and about  $0.58 \mu_B/\text{U-atom}$  in 7 T along the easy axis. These

---

\*Parts of this Section have been submitted to Journal of Magnetism and Magnetic Materials.

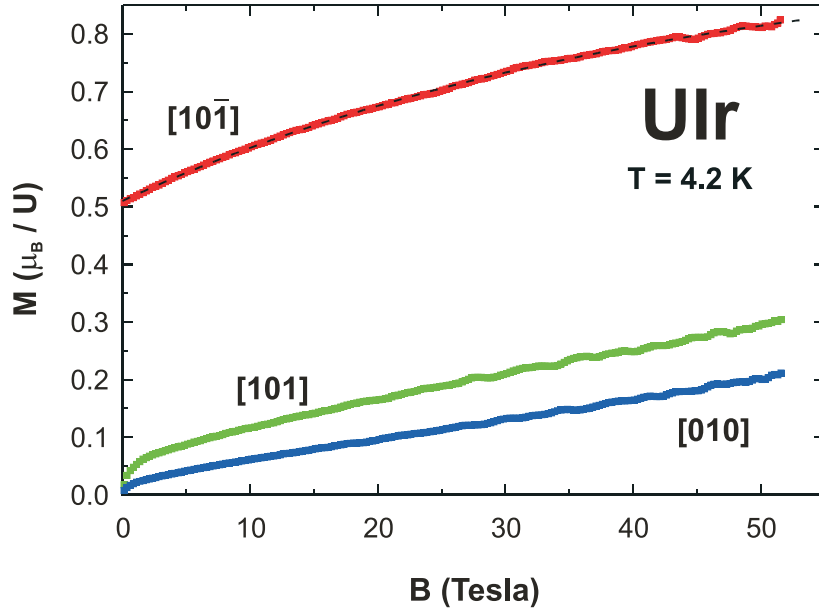


**Figure 7.3:** High-field magnetization  $M$  of single-crystalline UIr in a pulsed magnetic field  $\mu_0 H$  up to 52 T along the  $[10\bar{1}]$ ,  $[101]$ , and  $[010]$  directions at 4.2 K.

values are much smaller than the  $3.6 \mu_B/\text{U-atom}$  for free U-atoms. Up to 7 T no metamagnetism was observed. De Haas-van Alphen measurements up to 17 T  $[223]$  have shown no special features either. High magnetic fields are therefore required in the search for a metamagnetic transition.

### 7.2.2 Experimental

A single-crystalline sample of UIr was grown by the Czochralski technique in a tri-arc furnace. No subsequent heat treatment was applied to the crystal. From this crystal a cube with dimensions  $1 \times 1 \times 1 \text{ mm}^3$  and a mass of 13.2 mg was cut along the  $[10\bar{1}]$ ,  $[101]$ , and  $[010]$  axes of the monoclinic crystal structure. It was possible to cut a cube since the  $[10\bar{1}]$  and  $[101]$  directions are almost perpendicular (see Sec. 7.4.4). High field magnetization measurements up to a field of 52 T were performed at 4.2 K at the pulsed field facility LNCMP in Toulouse. After each magnetic pulse, the background was measured under the same experimental conditions by removing the sample out of the pick-up coil. Initial tests were performed in continuous magnetic fields up to 30 T at the magnet facility HFML in Nijmegen.

### 7.2.3 Results

In Fig. 7.3 the high field magnetization at a temperature of  $T = 4.2 \text{ K}$  in UIr is shown for pulsed magnetic fields along the  $[10\bar{1}]$ ,  $[101]$ , and  $[010]$  directions. In agreement with the low field magnetization measurements in fields up to 7 T  $[211]$ ,

a linear increase in the magnetization is observed for the  $[010]$  direction and a weak spin rotation followed by a linear increase in the magnetization for the  $[101]$  direction. Along the  $[10\bar{1}]$  direction, which is the easy axis for the magnetization, a sharp increase in magnetization is observed in low applied magnetic fields. This jump in magnetization of  $0.5 \mu_B/\text{U-atom}$  is caused by a domain repopulation of the ferromagnetic domains. For increasing magnetic fields the magnetization slowly increases. Up to the maximum applied field of 52 T no field-induced metamagnetic transition, related to a quenching of the magnetic interactions, is observed. The field dependence of the magnetization  $M(H)$  is accurately described by an empirical exponential function of the form

$$M(H) = M(0) + \Delta M (1 - e^{-\mu_0 H/B_0}) \quad (7.1)$$

with values of  $M(0) = 0.5101(2) \mu_B/\text{U-atom}$ ,  $\Delta M = 0.440(1) \mu_B/\text{U-atom}$ , and  $B_0 = 42.6(2)$  T. The fit is indistinguishable from the data points.

## 7.2.4 Discussion

The estimated high magnetic field moment  $M(H = \infty) = M(0) + \Delta M \approx 1 \mu_B/\text{U-atom}$  is significantly smaller than the free uranium  $5f^2$  ( $3.58 \mu_B$ ) or  $5f^3$  ( $3.62 \mu_B$ ) moments. High temperature susceptibility measurements on polycrystalline samples [205] showed Curie-Weiss behavior for temperatures between room temperature and 1200 K with an effective moment of  $3.61 \mu_B/\text{U-atom}$  and an unusually large antiferromagnetic Curie-Weiss temperature of  $\theta_{CW} = -430$  K. High temperature magnetization measurements on a single crystal [211] indicated an effective moment of  $3.57 \mu_B/\text{U-atom}$  and antiferromagnetic Curie-Weiss temperatures ranging from  $-300$  to  $-1000$  K depending on the orientation. The deviations from the Curie-Weiss behavior observed below a temperature of about 500 K signals a level splitting caused by crystalline electric field (CEF) effects, which is responsible for the strong magnetocrystalline anisotropy. At low temperatures only the lowest CEF level is occupied. This could explain the strongly reduced magnetic moment of  $\approx 1 \mu_B/\text{U-atom}$ .

The interaction field  $B_0 = 42.6(2)$  T, characteristic for the increase in magnetization along the easy axis, probes a magnetic interaction of the order of  $MB_0/k_B \approx 29$  K, which is somewhat smaller than the ferromagnetic ordering temperature of  $T_C = 46$  K.

## 7.2.5 Conclusions

No sign of a field-induced metamagnetic transition was found in UIr for fields up to 52 T. For high magnetic fields the magnetic moment saturates at a value of  $\approx 1 \mu_B/\text{U-atom}$ . This is strongly reduced compared to  $\approx 3.6 \mu_B/\text{U-atom}$  for free U atoms. The field dependence of the magnetization is characterized by an interaction field of  $B_0 = 42.6(2)$  T. The probed magnetic interactions are of the order of 29 K.



## 7.3 Specific Heat

### 7.3.1 Introduction

In the investigation of enhanced magnetic correlations in the neighborhood of a quantum critical point, knowledge of the specific heat is essential. In particular the linear specific heat coefficient  $\gamma$  at low temperatures gives direct information about the effective mass enhancement of the correlated electrons. A (moderate) heavy-fermion compound can often be tuned to a quantum critical point by applying pressure. In some cases this can also be achieved by applying high magnetic fields. The study of correlated systems in magnetic fields opens up a new dimension in the (magnetic) phase diagram. A suppression of the magnetic order, *i.e.* a lowering of the magnetic ordering temperature, or a suppression of *e.g.* the non-Fermi-liquid state into a Fermi-liquid state of a compound belong to the possibilities. In this Section a study of the specific heat of UIr in magnetic fields up to 14 T parallel to the easy axis for magnetization and in the temperature range from 3 to 300 K is reported.

### 7.3.2 Experimental

For the specific heat measurements the same single-crystalline batch of UIr was used as for the high-magnetic field measurements discussed in the previous Section. The batch was grown by the Czochralski technique in a tri-arc furnace. No subsequent heat treatment was applied to the crystal. From this crystal a plate with dimensions roughly  $2.5 \times 2.5 \times 0.5 \text{ mm}^3$  and a mass of 66.4 mg was cut with the  $[10\bar{1}]$  axes perpendicular to the plane. Specific heat measurements in fields up to 14 T were performed in the temperature range 3 – 300 K on a commercially available Physical Property Measurement Systems (PPMS) of Quantum Design at the Institut für Festkörperphysik (IFP) of the Forschungszentrum Karlsruhe (FZK). The measurements were performed by the heat relaxation method. Heat capacity was obtained by fitting a heat relaxation curve recorded after a heat pulse caused a temperature increase of approximately 2 %. The heat capacity of the addenda (Apiezon N grease) had been measured in a separate run without the sample, and was subtracted from the data. For further details, see Ref. [37].

### 7.3.3 Results and Discussion

In Fig. 7.4 the temperature dependence of the specific heat divided by temperature ( $c/T$ ) is shown in magnetic fields of 0, 2, 5, and 14 T. The insert shows a zoom of the data near the maximum in  $c/T$ . The zero-field data are in good quantitative agreements with previous measurements on polycrystalline UIr [210]. In zero field, a jump in the specific heat is observed at the ferromagnetic transition temperature  $T_C = 45.0(2) \text{ K}$ . This jump has a height of  $34.3(2) \text{ mJ/mol K}^2$  and is obtained by the equal-entropy method. Unfortunately, the specific heat in this temperature region

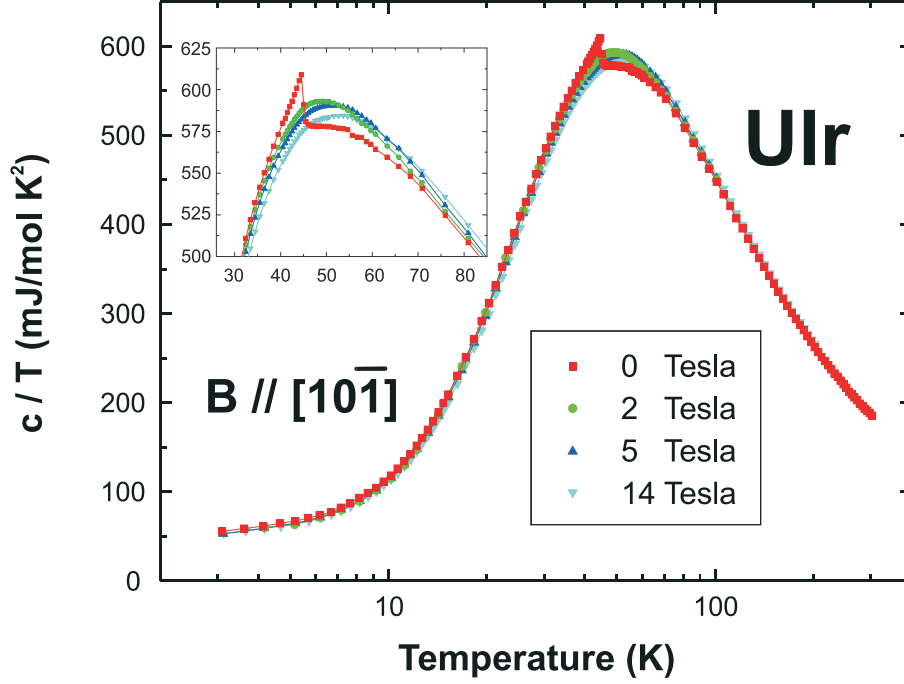


**Figure 7.4:** Specific heat  $c$  of UIr divided by temperature  $T$  ( $c/T$ ) as a function of temperature for fields up to 14 T in the temperature range of from 3 to 300 K. The inset shows a zoom of  $c/T$  near the maximum.

is dominated by the phonon contribution. However, from the insert the effect of a magnetic field is clear. The sharp peak in zero field is considerably broadened and shifted to higher temperature. Measurements in fields smaller than 1 T (not shown) indicate that the peak is already broadened for relatively small fields of 0.1 T.

The data at temperatures below 12 K can be fitted to  $c/T = \gamma + \beta T^2$ , where  $\gamma$  is the electronic specific heat coefficient and  $\beta = 12\pi^4 r R / (5\theta_D^3)$  the coefficient for the phonon contribution, with  $r = 2$  the number of atoms per formula unit,  $R$  the universal gas constant, and  $\theta_D$  is the Debye temperature. The data can be fitted satisfactorily for all magnetic fields with  $\gamma = 46(1)$  mJ/mol K<sup>2</sup> and  $\theta_D = 181$  K. These values compare well with the values  $\gamma = 40$  mJ/mol K<sup>2</sup> and  $\theta_D = 173$  K found in Ref. [210] for a polycrystal. Figure 7.4 clearly shows that a magnetic field of 14 T only causes a broadening of the peak at  $T_C$ .

Bauer *et al.* [210] have measured besides UIr also a polycrystal of ThIr to approximate the phonon contribution to  $c/T$  for UIr. In contrast to *e.g.* CePd<sub>2</sub>Si<sub>2</sub>, for which compound the  $c/T$  curve coincides with the  $c/T$  curve for LaPd<sub>2</sub>Si<sub>2</sub> at temperatures above  $\approx 25$  K [224], the  $c/T$  values for UIr and ThIr keep differing about 38.5 mJ/mol K<sup>2</sup> up to at least 75 K. Since the specific heat data for UIr in magnetic fields up to 14 T remain the same as for 0 T, the same conclusions can be drawn with respect to ThIr. If  $\gamma$  remains constant up to 70 K in zero field, the Kondo temperature  $T_K$  can be estimated to be at least 70 K. A rough estimation

through  $k_B T_K = \mu_B B^*$ , where  $k_B$  is the Boltzmann constant and  $B^*$  as magnetic field characterizing the magnetic interactions, shows that  $B^* \approx 100$  T. This is consistent with the result that  $\gamma$  is constant in fields up to 14 T. It also explains the absence of a field-induced metamagnetic transition in the magnetization measured in fields up to 52 T (see Sec. 7.2).

## 7.4 Thermal Expansion and Magnetostriction

### 7.4.1 Introduction

Thermal expansion is a fundamental thermodynamic property and is closely tied to the specific heat. It probes how the entropy of the system responds to volume changes and thus yields pressure dependencies of several thermodynamic properties. A big advantage of thermal expansion is that it probes the anisotropy in a system, since it can be measured along different directions. Remarkable uniaxial pressure dependencies of the Néel temperature  $T_N$  have been found for *e.g.* CeCu<sub>6-x</sub>Au<sub>x</sub> [225] and CePd<sub>2</sub>Si<sub>2</sub> [175]. In addition, comparison of the thermal expansion data with specific heat measurements gives the so-called Grüneisen parameter. It is a measure for the volume dependence of the dominant energy scale at a certain temperature.

In this Section thermal expansion and magnetostriction measurements on single-crystalline UIr are reported. The uniaxial pressure dependencies of the Curie temperature  $T_C$  at zero pressure have been determined.

The considerations in the Appendix of this Chapter show that with very high accuracy the  $[10\bar{1}]$ ,  $[101]$ , and  $[010]$  directions can be used as an orthogonal basis of the unit cell of UIr. Therefore the linear volume thermal expansion coefficient  $\alpha_V$  is simply a sum of the three coefficients  $\alpha_i$ , with  $i$  equal to one of the three directions  $[10\bar{1}]$ ,  $[101]$ , or  $[010]$ .

### 7.4.2 Experimental

High-precision measurements of the variation in the sample length  $L$  as a function of temperature  $T$  or as a function of magnetic field  $B$  have been performed on single-crystalline samples. The samples were prepared from the same batch as the samples for magnetization in high magnetic fields (Sec. 7.2) and for specific heat (Sec. 7.3). The batch was grown by the Czochralski technique in a tri-arc furnace. No subsequent heat treatment was applied to the crystal. From this crystal samples were cut with lengths of 1.287 mm for  $[10\bar{1}]$ , 2.10 mm for  $[101]$ , and 3.68 mm for  $[010]$ . Thermal expansion measurements in 0 and 5 T, applied along the easy axis for magnetization, have been performed in the temperature range from 5 to 250 K. The thermal expansion along  $[10\bar{1}]$ ,  $[101]$ , and  $[010]$  was measured as a function of temperature  $T$ . In addition, magnetostriction measurements were performed at 4, 45, and 150 K for magnetic fields between -10 and 10 T. Again the dilatation

was measured along  $[10\bar{1}]$ ,  $[101]$ , and  $[010]$  with the magnetic applied parallel to  $[10\bar{1}]$ .

The data have been collected using a home-built measuring cell at the Institut für Festkörperphysik (IFP) of the Forschungszentrum Karlsruhe (FZK). The measurements are based on the parallel-plate capacitance method. For the thermal expansion experiments the temperature was slowly raised at a reproducible rate of 20 mK/s over the whole temperature range. Averages are made every 0.1 K. The coefficient of thermal expansion  $\alpha$  is calculated by  $\alpha = (1/L)(dL/dT)$ . For further details, see Sec. 2.4.2.

### 7.4.3 Results

#### Thermal expansion

In Fig. 7.5 the coefficient of linear thermal expansion  $\alpha$  along the  $[10\bar{1}]$ ,  $[101]$ , and  $[010]$  directions of single-crystalline UIr is shown as a function of temperature  $T$  in the range from 5 to 250 K. The temperature dependence of the volume expansion  $\alpha_v = \alpha_{[10\bar{1}]} + \alpha_{[101]} + \alpha_{[010]}$  is shown for comparison (notice the figure shows  $\alpha_v/3$ ). See Sec. 7.4.4 for a justification of this formula. At high temperatures the thermal expansion is governed by the phonon contribution for all three orientations. For zero field the ferromagnetic order sets in at  $T_C = 45.0$  K and a sharp negative peak in the coefficient of linear thermal expansion is observed for all three directions. For 5 T the transition is considerably broadened. However, far below and far above  $T_C$  the curves for 0 and for 5 T coincide for a given direction. For all directions and both magnetic fields, the thermal expansion extrapolates to  $0 \text{ K}^{-1}$  as temperature goes to 0 K, as expected.

In the zero field case the data show some remarkable results below  $T_C$ . Firstly, the easy axis for the magnetization  $[10\bar{1}]$  behaves qualitatively different than the  $[101]$  and  $[010]$  directions. Whereas the latter two are positive for temperatures lower than a certain temperature below  $T_C$ , the former remains negative below  $T_C$ . Secondly, all three directions pass below  $T_C$  through a maximum (or minimum). This is different than for URhGe (see Fig. 5.3), where  $\alpha_i$  decreases monotonously towards  $0 \text{ K}^{-1}$  with decreasing temperature. In 5 T a large shoulder is present in the data, indicating that this feature is not suppressed in a magnetic field up to 5 T.

The observed steps in the coefficients of linear thermal expansion have the same sign but different sizes for the three directions. The values of the steps are listed in Table 7.1.

#### Magnetostriction

In Figs. 7.6, 7.7, and 7.8 the coefficient of magnetostriction  $\lambda = (1/L)dL/dB$  is shown for fields between -10 and 10 T applied along the  $[10\bar{1}]$  direction. The expansion is measured along the  $[10\bar{1}]$ ,  $[101]$ , and  $[010]$  directions, respectively, for 4, 45, and 150 K. Basically all the figures show qualitatively the same features.

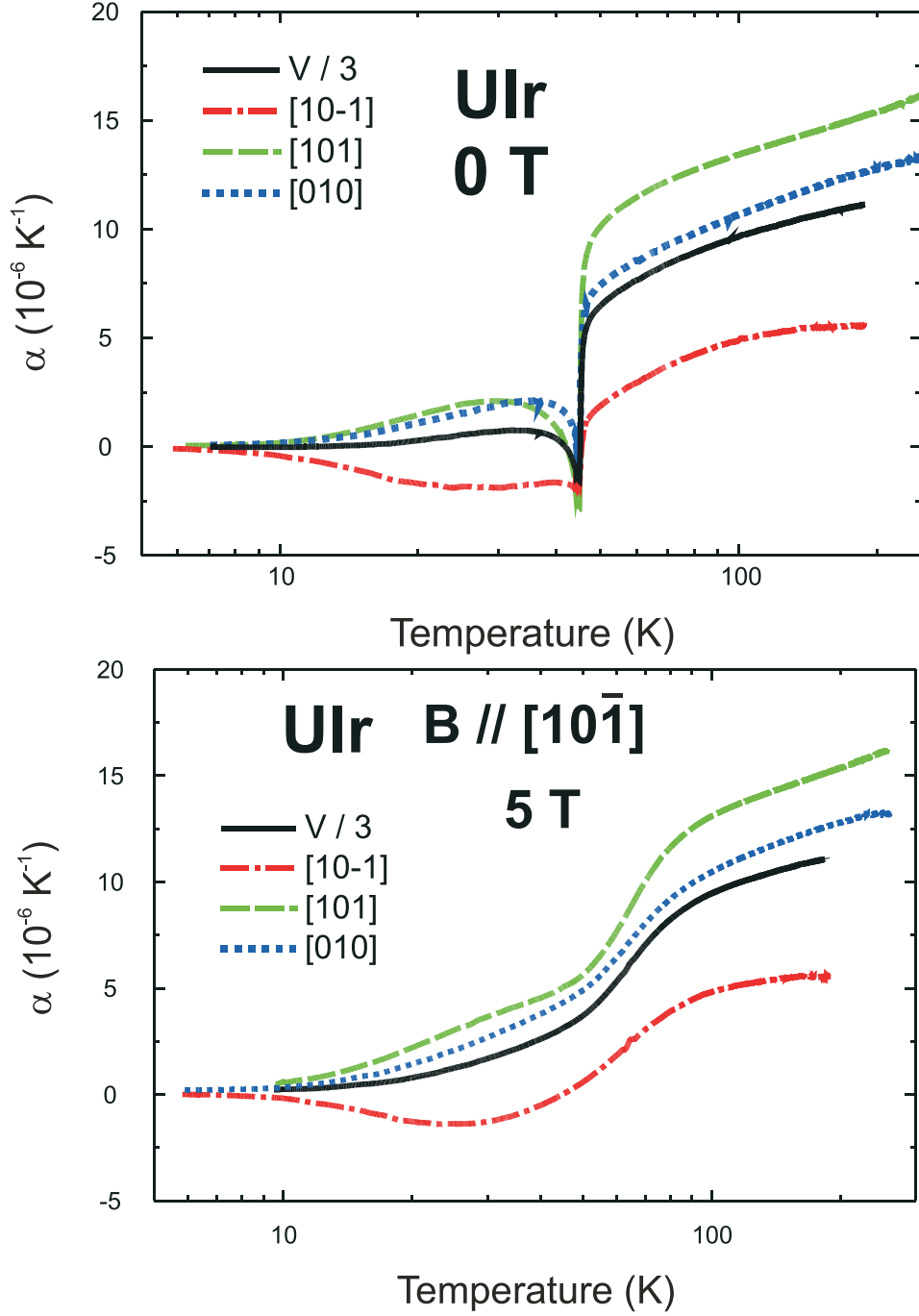


**Figure 7.5:** The coefficients of linear thermal expansion  $\alpha$  of UIr as a function of temperature  $T$  along the  $[10\bar{1}]$ ,  $[101]$ , and  $[010]$  directions in zero magnetic field (upper frame) and in an applied field of 5 T (lower frame). For comparison the volume expansion divided by a factor 3 ( $\alpha_v/3$ ) is also shown.

**Table 7.1:** Step anomalies in the coefficients of linear thermal expansion of single-crystalline UIr along the  $[10\bar{1}]$ ,  $[101]$ , and  $[010]$  directions. The corresponding pressure dependence of the Curie temperature,  $dT_C/dp$ , was deduced from the Ehrenfest relation (see text).

	$\Delta\alpha$ ( $10^{-6} \text{ K}^{-1}$ )	$dT_C/dp$ (K/kbar)
$[10\bar{1}]$	-3.0(3)	-0.22(2)
$[101]$	-14(1)	-1.10(8)
$[010]$	-7.6(5)	-0.55(4)
volume	-24.6(1.2)	-1.87(9)

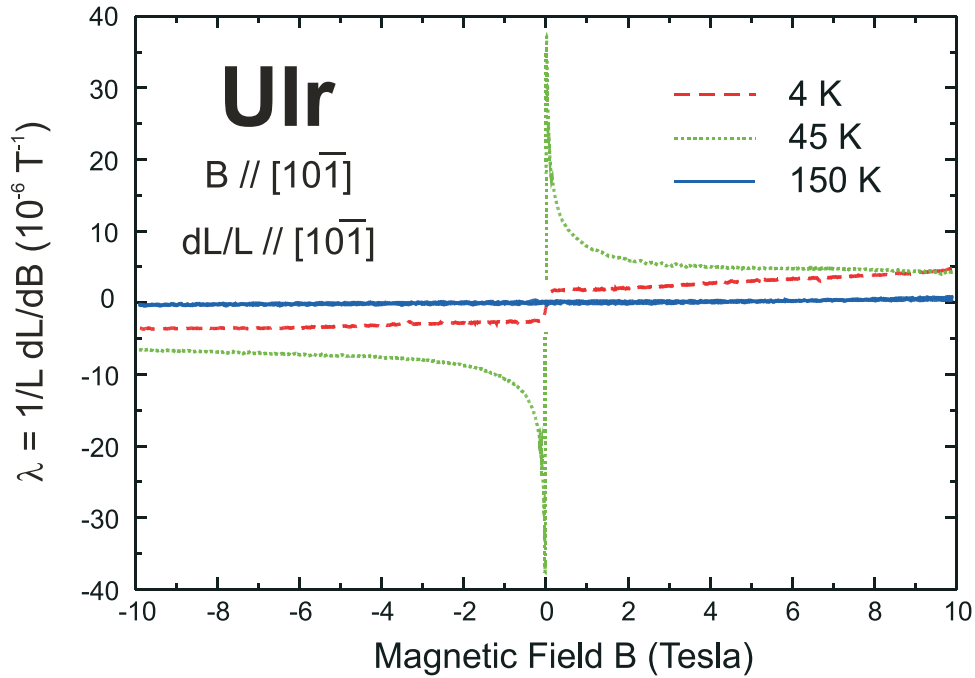


**Figure 7.6:** The magnetostriction coefficient  $\lambda = (1/L)dL/dB$  of UIr for applied magnetic fields  $B$  between -10 and 10 T at various temperatures. The magnetic field was applied parallel to  $[10\bar{1}]$  direction and the dilatation was measured along the  $[10\bar{1}]$ .

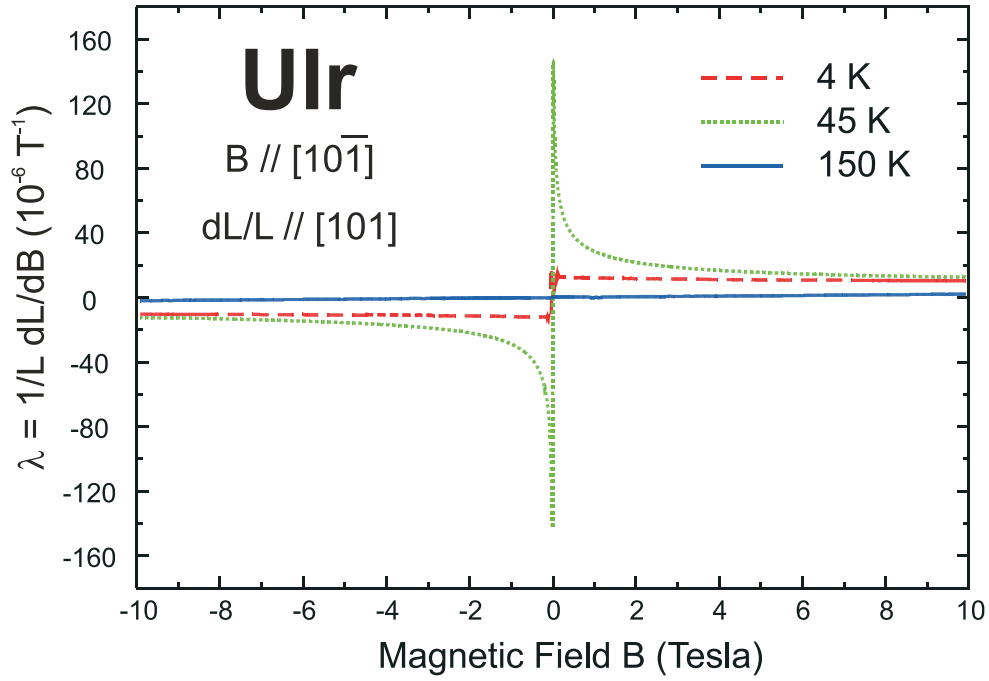


**Figure 7.7:** The magnetostriction coefficient  $\lambda = (1/L)dL/dB$  of UIr for applied magnetic fields  $B$  between -10 and 10 T at various temperatures. The magnetic field was applied parallel to  $[10\bar{1}]$  direction and the dilatation was measured along the  $[101]$ .

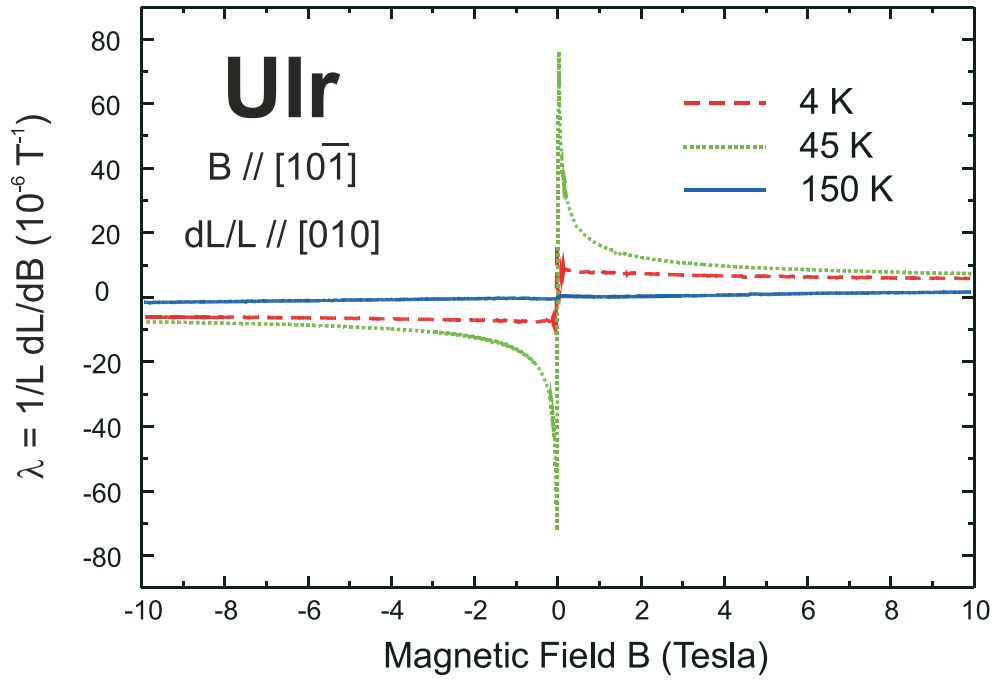


**Figure 7.8:** The magnetostriction coefficient  $\lambda = (1/L)dL/dB$  of UIr for applied magnetic fields  $B$  between -10 and 10 T at various temperatures. The magnetic field was applied parallel to  $[10\bar{1}]$  direction and the dilatation was measured along the  $[010]$ .

At 150 K the magnetostriction effect is small, as expected since UIr is far in the paramagnetic regime. At 45 K  $\lambda$  decreases quite rapidly because of the broadening of the ferromagnetic transition at this temperature. At 4 K the magnetostriction coefficient has a step around 0 T and increases slowly afterwards. The big difference between the figures is the scale. By applying a magnetic field along the  $[10\bar{1}]$  direction, the largest magnetostriction occurs in the  $[101]$  direction, followed by  $[010]$ . It should be noted that all values for  $\lambda$  are positive for positive fields and negative for negative fields. This means that the crystal always expands when applying a magnetic field.

#### 7.4.4 Discussion and Conclusions

In order to determine the uniaxial pressure dependence of the ferromagnetic transition temperature, the Ehrenfest relation can be applied. For a second-order phase transition, the uniaxial pressure dependence of the transition temperature is directly related to the step anomalies in the coefficient of linear thermal expansion and the specific heat by the Ehrenfest relation

$$\frac{dT_C}{dp_i} = \frac{V_m \Delta \alpha_i}{\Delta(c/T)}, \quad (7.2)$$

where the index  $i$  refers to the  $[10\bar{1}]$ ,  $[101]$ , or  $[010]$  directions,  $V_m = 2.48 \times 10^{-5} \text{ m}^3/\text{mol}$  is the molar volume, and  $\Delta(c/T) = 0.0343(2) \text{ J/mol K}^2$  is the anomaly in the specific heat divided by temperature (Sec. 7.3). By applying this relation to the experimental step anomalies in the coefficients of linear thermal expansion, the uniaxial pressure dependence of  $T_C$  along the  $[10\bar{1}]$ ,  $[101]$ , and  $[010]$  directions is obtained. The calculated values are listed in Table 7.1. The hydrostatic pressure dependence of  $T_C$  can be obtained by inserting the volume expansion for the coefficient of linear expansion in Eq. 7.2, or by summing the three contributions of the uniaxial pressure dependence. The different pressure dependencies of  $T_C$  as listed in Table 7.1 are all negative. This means that uniaxial pressure along any of the three measured directions will lower  $T_C$ . It is clear from the Table that for hydrostatic pressure, the component along  $[101]$  accounts for more than half of the reduction of  $T_C$ .

The calculated hydrostatic pressure dependence of  $dT_C/dp = -1.87(9) \text{ K/kbar}$  can be compared to the directly measured values. From Ref. [210]  $dT_C/dp = -1.1 \text{ K/kbar}$  is estimated and from Ref. [199]  $dT_C/dp = -1.5 \text{ K/kbar}$ . The thermal expansion data yield a comparably high value. The difference can only partly be explained by the uncertainty in the determination of the step in  $\alpha$ .

The shoulder in the data below  $T_C$  is remarkable. For URhGe (Sec. 5.2)  $\alpha_i$  below  $T_C$  goes to  $0 \text{ K}^{-1}$  monotonously. However, for UGe<sub>2</sub> an unusual temperature dependence of  $\alpha_i$  was found as well [226]. For UGe<sub>2</sub> an anomaly below  $T_C$  at ambient pressure was only seen in the thermal expansion. At high pressures, a transition was seen as well in magnetization and resistivity (see Refs. in Chapter 4). Because of its



very high sensitivity, thermal expansion was able to show this additional transition at ambient pressure. The shoulder in the data for UIr can indicate the existence of a - so far unknown - energy scale which competes with the magnetic order appearing at  $T_C = 45$  K. This competition leads to a hump in  $\alpha$  around 30 K. The data therefore suggest the existence of an additional energy scale with  $T^* \approx 30$  K, competing with the energy scale for magnetic order  $T_C = 45$  K. Possibly it is the signature of  $T_{C2}$  in Fig. 7.2 that may extrapolate to 30 K at  $p = 0$  GPa. In any case it is interesting to note that the magnetization in fields up to 52 T (Sec. 7.2) showed a magnetic interaction of  $\approx 29$  K.

Through the thermodynamic Maxwell relation

$$\lambda_i = \frac{1}{L_i} \frac{dL_i}{dB} = - \frac{dM}{dp_i} \quad (7.3)$$

with  $i$  equal to  $[101]$ ,  $[10\bar{1}]$  and  $[010]$ , the magnetostriction data show that the application of pressure along any direction decreases the magnetization. This is consistent with Fig. 7.2 for hydrostatic pressure.

## Appendix: Geometrical Considerations of Monoclinic Unit Cells

Crystals belonging to a monoclinic space group consist of unit cells having three axes ( $a$ ,  $b$ , and  $c$ ) of unequal lengths of which  $b$  is perpendicular to  $a$  and  $c$ , but  $a$  and  $c$  are not perpendicular to each other. The angle between  $a$  and  $c$  is denoted  $\beta$ . According to the monoclinic symmetry, all the parameters  $a$ ,  $b$ ,  $c$ , and  $\beta$  vary with temperature. In first instance it is therefore necessary to perform at least four different measurements in order to find the temperature dependence of all four parameters. Here the influence of  $\beta(T)$  on the coefficients of linear thermal expansion  $\alpha$  along the  $[101]$  and  $[10\bar{1}]$  directions is investigated.

In Fig. 7.9 the basal plane of a unit cell of UIr is shown. The  $b$  axis is perpendicular to the plane. The angle  $\delta$  between the two diagonals  $[101]$  and  $[10\bar{1}]$  is given

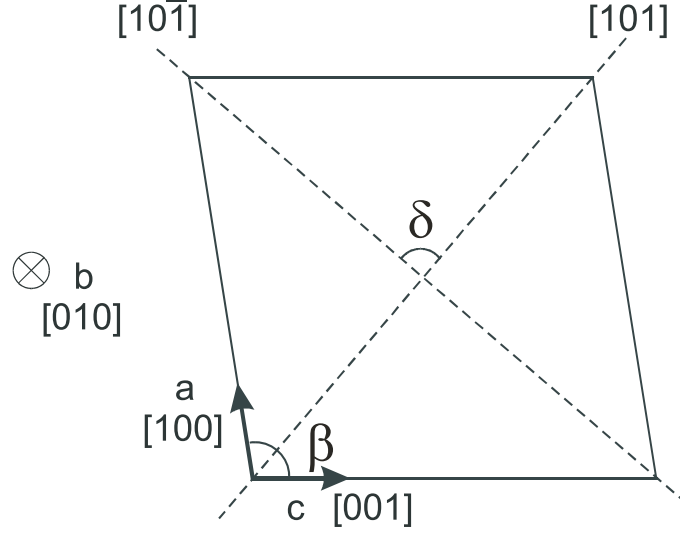


**Figure 7.9:** Basal plane of the monoclinic unit cell of UIr.

by

$$\cos \delta = \frac{a^2 - c^2}{\{(a^2 + c^2)^2 - (2ac \cos \beta)^2\}^{\frac{1}{2}}}. \quad (7.4)$$

The two diagonals are perpendicular if and only if  $a = c$ . Furthermore,  $\delta$  is temperature dependent, since  $a$ ,  $c$ , and  $\beta$  are temperature dependent.

Let  $X$  be the unit cell volume, the basal plane area, or any axis length in the monoclinic crystal, depending on a set of parameters  $p_1, p_2, \dots, p_N$ . The general formula

$$\alpha_X(p_1, p_2, \dots, p_n) = \frac{1}{|X|} \sum_i p_i \frac{\partial |X|}{\partial p_i} \alpha_{p_i} \quad (7.5)$$

is useful in determining the linear thermal expansion coefficient  $\alpha_X$ .

The exact volume of the unit cell is  $V_{\text{ex}} = abc \sin \beta$ . If  $\delta$  (Fig. 7.9) is close to  $90^\circ$ , then  $V$  can be approximated by

$$V_{\text{approx}} = \frac{1}{2} b \left| [101] \right| \cdot \left| [10\bar{1}] \right| = \frac{1}{2} b \left\{ (a^2 + c^2)^2 - (2ac \cos \beta)^2 \right\}^{\frac{1}{2}}. \quad (7.6)$$

Shortly it will be shown that for the particular case of UIr this approximation will yield an  $\alpha_V$  which is accurate within 0.6%. With Eq. 7.5 the following expressions are obtained:

$$\alpha_{V_{\text{ex}}} = \alpha_a + \alpha_b + \alpha_c - \alpha_\beta \frac{\pi}{180} \beta \tan(\beta - 90^\circ), \quad (7.7a)$$

$$\begin{aligned} \alpha_{V_{\text{approx}}} = & \alpha_a \frac{2a^2(a^2 - c^2 \cos 2\beta)}{(a^2 + c^2)^2 - (2ac \cos \beta)^2} + \alpha_b + \alpha_c \frac{2c^2(c^2 - a^2 \cos 2\beta)}{(a^2 + c^2)^2 - (2ac \cos \beta)^2} \\ & + \alpha_\beta \frac{\pi}{180} \frac{2\beta a^2 c^2 \sin 2\beta}{(a^2 + c^2)^2 - (2ac \cos \beta)^2}. \end{aligned} \quad (7.7b)$$

**Table 7.2:** Lattice parameters and angle  $\beta$  as determined by neutron scattering. Data taken from A. Dommann *et al.* [205].

$T$ (K)	$a$ (Å)	$b$ (Å)	$c$ (Å)	$\beta$ (deg)	$V$ (Å <sup>3</sup> )
16	5.605 (3)	10.552 (3)	5.576 (3)	99.12 (2)°	325.6 (4)
55	5.604 (4)	10.550 (4)	5.573 (4)	99.12 (3)°	325.3 (5)
293	5.620 (3)	10.590 (3)	5.598 (3)	98.93 (3)°	329.1 (5)

Here  $\alpha_\beta$  is defined as  $\alpha_\beta = (1/\beta) d\beta/dT$ .

The coefficients of linear thermal expansion for the two diagonals, with lengths  $|[10 \pm 1]| = \{a^2 + c^2 \pm 2ac \cos \beta\}^{\frac{1}{2}}$  are calculated to be

$$\begin{aligned} \alpha_{(10\pm 1)} = & a \frac{a \pm c \cos \beta}{a^2 + c^2 \pm 2ac \cos \beta} \alpha_a + c \frac{c \pm a \cos \beta}{a^2 + c^2 \pm 2ac \cos \beta} \alpha_c \\ & \mp \frac{\pi}{180} \beta \frac{ac \sin \beta}{a^2 + c^2 \pm 2ac \cos \beta} \alpha_\beta. \end{aligned} \quad (7.8)$$

It is easily checked that

$$\alpha_{(101)} + \alpha_{(10\bar{1})} = \alpha_{V_{\text{approx}}} - \alpha_b. \quad (7.9)$$

The lattice parameters as well as the angle  $\beta$  for UIr were determined by neutron scattering [205] and are shown in Table 7.2 at several temperatures. These values enable an estimation of how well  $\alpha_{V_{\text{ex}}}$  is approximated by  $\alpha_{V_{\text{approx}}}$ . Filling in the numbers yields

$$\left. \begin{aligned} \alpha_{V_{\text{ex}}} &= \alpha_a + \alpha_b + \alpha_c - 0.2713 \cdot \alpha_\beta \\ \alpha_{V_{\text{approx}}} &= \alpha_a + \alpha_b + \alpha_c - 0.2713 \cdot \alpha_\beta + 0.00402 \cdot (\alpha_a - \alpha_c) \end{aligned} \right\} \text{ at } T = 293 \text{ K}, \quad (7.10a)$$

$$\left. \begin{aligned} \alpha_{V_{\text{ex}}} &= \alpha_a + \alpha_b + \alpha_c - 0.2777 \cdot \alpha_\beta \\ \alpha_{V_{\text{approx}}} &= \alpha_a + \alpha_b + \alpha_c - 0.2777 \cdot \alpha_\beta + 0.00569 \cdot (\alpha_a - \alpha_c) \end{aligned} \right\} \text{ at } T = 55 \text{ K}. \quad (7.10b)$$

This shows that Eq. 7.9 is indeed a very good approximation to  $V_{\text{ex}}$  for the particular case of UIr.



---

# Summary

**U**NCONVENTIONAL ground state properties are found in the strongly correlated systems of  $\text{UGe}_2$ ,  $\text{URhGe}$ , and  $\text{UIr}$ . These compounds belong to a class of materials in which two phenomena - long thought to be mutually exclusive - appear simultaneously.  $\text{UGe}_2$  was the first of these three compounds to attract considerable attention because of the emergence of superconductivity well within the ferromagnetic state, followed by  $\text{URhGe}$ .  $\text{UIr}$  is special since its crystallographic structure lacks inversion symmetry.

The coexistence of ferromagnetism and superconductivity in the vicinity of a ferromagnetic quantum critical point, is the main motivation that the related compounds are investigated thoroughly. The fact that magnetic fluctuations are enhanced near a quantum critical point, just where superconductivity is found, strongly suggests that the attractive force between the electrons forming the Cooper pair, originates from the magnetic fluctuations. This thesis has the intention to contribute to the understanding of the role of ferromagnetism and ferromagnetic spin fluctuations in their coexistence with superconductivity, by employing several techniques.

## Chapter 4: $\text{UGe}_2$

The ferromagnetic domain sizes of  $\text{UGe}_2$  were studied by means of three-dimensional neutron depolarization at ambient pressure. It is concluded that the existence of field-tuned resonant tunneling between spin quantum states [117, 118] is highly unlikely. The requirement of this model is a ferromagnetic domain size of  $40 \text{ \AA}$ , whereas the neutron depolarization measurements indicate a size a factor of 1000 larger. The superconductivity, therefore, exists within a single ferromagnetic domain. The domain walls are not expected to strongly affect the bulk Cooper pair wave function, as suggested by Nishioka *et al.* [117, 118], since the domain-wall size is less than a few percent of the average domain size.

The  $\mu\text{SR}$  data taken in the critical regime of  $\text{UGe}_2$  suggest a coexistence of two subsystems with localized  $5f$  states responsible for the magnetic ordering and

delocalized states responsible for the superconducting properties. It is likely that electrons do not participate in both phenomena simultaneously, but are separated either in real space and/or in reciprocal space, *i.e.* different parts of the Fermi surface. This seems to contradict theoretical models [89, 90, 91, 92] in which the superconductivity and the ferromagnetism are assumed to be carried by the same electrons.

The depolarization of the spontaneous frequencies exhibit a peak at temperature  $T_X$ . It is shown that the peak could possibly develop because of the slowing down of magnetic fluctuations. This could play a role in the formation of Cooper pairs.

### Chapter 5: URhGe

Thermal expansion measurements on a single-crystalline sample of the itinerant ferromagnet URhGe show that below the ferromagnetic ordering temperature of  $T_C = 9.7$  K the coefficient of linear thermal expansion increases along all three orthorhombic axes. The uniaxial pressure dependence of the ferromagnetic transition temperature was determined by the Ehrenfest relation from the anomalies in the coefficients of linear thermal expansion and the specific heat. Positive values of  $dT_C/dp$  are found for all principal axes. Consequently, the hydrostatic pressure dependence is also positive and amounts to  $dT_C/dp = 0.119$  K/kbar. This positive pressure dependence contrasts the behavior reported for UGe<sub>2</sub> and UIr. In addition, the effective Grüneisen parameter was determined. The resulting low-temperature behavior points to an enhanced volume dependence of the ferromagnetic spin fluctuations at low temperatures and an equal volume scaling of the energy scales for the ferromagnetic order and the ferromagnetic spin fluctuations.

$\mu$ SR measurements on URhGe have been performed by recording the spin-lattice relaxation  $\lambda_Z$  as a function of externally applied magnetic field  $B_{\text{ext}}$  for two directions of the initial muon spin  $\mathbf{S}_\mu(0)$ . Since both  $\mathbf{S}_\mu(0) \parallel \mathbf{c}$  and  $\mathbf{S}_\mu(0) \perp \mathbf{c}$ , with  $\mathbf{c}$  the easy axis for the magnetization, the anisotropy of the spin dynamics could be measured. The magnetic field scans in the paramagnetic state, close to  $T_C$ , clearly show two different magnetic contributions, which can be identified as localized and itinerant magnetism. This fact strongly suggests that the  $5f$  electrons responsible for both magnetic order and superconductivity do not participate in both phenomena simultaneously but are separated either in real space and/or in reciprocal space, *i.e.* different parts of the Fermi surface.

### Chapter 6: URh<sub>1-x</sub>Ru<sub>x</sub>Ge

Since ferromagnetism in URhGe cannot be suppressed by applying external pressure (Ref. [176] and Sec. 5.2) the evolution of ferromagnetism in URhGe has been investigated by chemical substitution. In this study Rh atoms were substituted by Ru and Co whereas Ge made place for Si. For substitution by Ru,  $T_C$  was found to initially increase for increasing values of  $x$  in URh<sub>1-x</sub>Ru<sub>x</sub>Ge. This was attributed to a volume effect. For  $x > 0.10$ ,  $T_C$  decreases, which suggests that emptying the  $d$ -band governs the hybridization phenomena. Ferromagnetism is completely suppressed for

$x_{\text{cr}} \approx 0.38$ . At this critical concentration non-Fermi-liquid (NFL) behavior was observed in the specific heat. At low temperatures it was found that the specific heat can be described by  $C/T \sim -\ln T$ . For substitution by Co,  $T_C$  increases up to 20 K for  $x = 0.60$  and ferromagnetism is suppressed for  $x$  close to 1. This means that UCoGe is close to a quantum critical phase transition and provides a good candidate to study a ferromagnetic quantum critical point. Finally, substituting Ge by Si was found not to affect  $T_C$  up to  $x = 0.20$ .

### Chapter 7: UIr

No sign of a metamagnetic transition was found in UIr for pulsed fields up to 52 T. For high magnetic fields the magnetic moment saturates at a value of  $\approx 1 \mu_B/\text{U-atom}$ . This is strongly reduced compared to  $\approx 3.6 \mu_B/\text{U-atom}$  for free U atoms, possibly by crystalline electric fields. The field dependence of the magnetization is characterized by an interaction field of  $B_0 = 42.6(2)$  T. The probed magnetic interactions are therefore of the order of 29 K.

Fits of the low-temperature specific heat data in fields up to 14 T show that the parameters at play remain constant. The data can be fitted satisfactorily for all magnetic fields with  $\gamma = 46(1)$  mJ/mol K<sup>2</sup> and  $\theta_D = 181$  K. Therefore it was clearly shown that application of a magnetic field of 14 T has little influence on the specific heat (and thus the magnetic correlations) except for a broadening of the peak at  $T_C$ .

Thermal expansion data showed that uniaxial pressure along any direction in UIr will lower  $T_C$ . For hydrostatic pressure, the component along  $[101]$  accounts for more than half of the reduction of  $T_C$ . A remarkable shoulder is present in the curves of the linear thermal expansion coefficient  $\alpha$  around  $T^* \approx 30$  K. It can be explained by the existence of an energy scale which competes with the magnetic order appearing at  $T_C = 45$  K. This competition leads to a hump in  $\alpha$  around 30 K. It is at this moment unclear whether there is a connection with the magnetic interactions which were probed in the high-magnetic field measurements.





---

# Samenvatting

NCONVENTIONELE EIGENSCHAPPEN van de grondtoestand worden aangetroffen in de sterk gecorreleerde systemen  $\text{UGe}_2$ ,  $\text{URhGe}$  en  $\text{UIr}$ . Deze verbindingen behoren tot een klasse materialen waarin twee verschijnselen - die lang gedacht werden elkaar uit te sluiten - tegelijkertijd optreden.  $\text{UGe}_2$  was de eerste van deze drie verbindingen die aanzienlijke aandacht genoot vanwege het optreden van supergeleiding, diep in de ferromagnetische toestand, gevolgd door  $\text{URhGe}$ .  $\text{UIr}$  is speciaal omdat de kristallografische structuur inversie symmetrie ontbeert.

Het tegelijkertijd bestaan van ferromagnetisme en supergeleiding in de buurt van een ferromagnetisch quantum kritisch punt, is de belangrijkste motivatie waarom de betreffende verbindingen zo intensief worden bestudeerd. Het feit dat magnetische fluctuaties versterkt zijn in de buurt van een quantum kritisch punt, precies waar supergeleiding wordt gevonden, suggereert sterk dat de aantrekkende kracht tussen de elektronen die het Cooper paar vormen, zijn oorsprong heeft in de magnetische fluctuaties. Dit proefschrift heeft de intentie door middel van enkele meettechnieken een bijdrage te leveren aan het begrijpen van de rol van ferromagnetisme en ferromagnetische spin fluctuaties in hun coëxistentie met supergeleiding.

## Hoofdstuk 4: $\text{UGe}_2$

De ferromagnetische domein groottes van  $\text{UGe}_2$  werd bestudeerd door middel van drie-dimensionale neutronen depolarisatie bij kamerdruk. De conclusie is dat het bestaan van resonante tunneling, door een magnetisch veld geïnduceerd, tussen spin quantum toestanden [117, 118] hoogst onwaarschijnlijk is. De voorwaarde voor dit model is een ferromagnetische domein grootte van  $40 \text{ \AA}$ , terwijl de neutronen depolarisatiemetingen wijzen op een grootte die duizend keer groter is. De supergeleiding bestaat daarom binnen één enkel ferromagnetisch domein.

De domeinwanden worden niet verwacht een groot effect te hebben op de bulk Cooper paar golf functies, zoals gesuggereerd door Nishioka *et al.* [117, 118], terwijl de breedte van de domeinwand minder is dan enkele procenten van de gemiddelde

domeingrootte.

De  $\mu$ SR data die in het kritische temperatuurgebied van  $\text{UGe}_2$  zijn gemeten, suggereren een coëxistentie van twee subsystemen met gelocaliseerde  $5f$  toestanden, verantwoordelijk voor de magnetische ordening, en gedelocaliseerde toestanden, verantwoordelijk voor de supergeleidende eigenschappen. Het is waarschijnlijk dat electronen niet deelnemen in beide fenomenen tegelijkertijd, maar gesepareerd zijn in reële ruimte en/of in reciproke ruimte, dat wil zeggen verschillende delen van het Fermi oppervlak. Dit lijkt in strijd met theoretische model [89, 90, 91, 92] waarin de supergeleiding en het ferromagnetisme verondersteld worden te worden gedragen door dezelfde electronen.

De depolarisatie van de spontane frequenties vertonen een piek bij temperatuur  $T_X$ . Er wordt uiteengezet dat de piek zou kunnen ontstaan door het langzamer worden van magnetische fluctuaties. Dit zou een rol kunnen spelen in de formatie van Cooper paren.

## Hoofdstuk 5: URhGe

Metingen van de thermische uitzettingen aan een éénkristal van de itinerante ferromagneet URhGe laten zien dat onder de ferromagnetische ordeningstemperatuur van  $T_C = 9.7$  K de coëfficiënt van de lineaire thermische uitzetting toeneemt langs alle drie de orthorhombische assen. De uniaxiale drukafhankelijk van de ferromagnetische overgangstemperatuur werd bepaald door de Ehrenfest relatie van de anomalieën in de coëfficiënt van de lineaire thermische uitzetting en de soortelijke warmte. Positieve waarden van  $dT_C/dp$  werden gevonden langs alle principale assen. Daarom is de hydrostatische drukafhankelijk ook positief en bedraagt  $dT_C/dp = 0.119$  K/kbar. Deze positieve drukafhankelijk is anders dan het gedrag voor  $\text{UGe}_2$  en  $\text{UIr}$ . Ook is de effective Grüneisen parameter bepaald. Het resulterende lage temperatuur gedrag duidt op een versterkte volume afhankelijk van de ferromagnetische spin fluctuaties bij lage temperaturen en een even grote volume schaling van de energieschalen voor de ferromagnetische ordening en de ferromagnetische spin fluctuaties.

$\mu$ SR metingen aan URhGe zijn uitgevoerd door het bepalen van de spin-kristal relaxatie  $\lambda_Z$  als functie van het externe aangelegde magnetische veld  $B_{\text{ext}}$  voor twee richtingen van de initiële muon spin  $\mathbf{S}_\mu(0)$ . Aangezien zowel  $\mathbf{S}_\mu(0) \parallel \mathbf{c}$  als  $\mathbf{S}_\mu(0) \perp \mathbf{c}$ , met  $\mathbf{c}$  de makkelijke as voor de magnetisatie, kon de anisotropie van de spindynamica worden gemeten. De magnetische veld scans in de paramagnetische toestand, dicht bij  $T_C$ , laten duidelijk twee verschillende magnetische contributies zien, die geïdentificeerd kunnen worden als gelocaliseerd en itinerant magnetisme. Dit feit suggereert sterk dat de  $5f$  niet deelnemen aan beide fenomenen tegelijkertijd, maar gesepareerd zijn in reële ruimte en/of in reciproke ruimte, dat wil zeggen verschillende delen van het Fermi oppervlak. Dit lijkt in strijd met theoretische model [89, 90, 91, 92] waarin de supergeleiding en het ferromagnetisme verondersteld worden te worden gedragen door dezelfde electronen.

### Hoofdstuk 6: URh<sub>1-x</sub>Ru<sub>x</sub>Ge

Aangezien het ferromagnetisme in URhGe niet onderdrukt kan worden door externe druk aan te leggen (Ref. [176] en Sec. 5.2), is de evolutie van ferromagnetisme in URhGe onderzocht door chemische substitutie. In dit onderzoek zijn Rh atomen gesubstitueerd door Ru en Co terwijl Ge plaats maakte voor Si. Bij de substitutie van Ru is gevonden dat  $T_C$  in het begin hoger werd met toenemende waarden van  $x$  in URh<sub>1-x</sub>Ru<sub>x</sub>Ge. Dit werd toebedeeld aan een volume effect. Voor  $x > 0.10$ , neemt  $T_C$  af, wat suggereert dat het leegmaken van de  $d$ -band de hybridisatie fenomenen domineert. Ferromagnetisme wordt volledig onderdrukt voor  $x_{cr} \approx 0.38$ . Bij deze kritische concentratie wordt non-Fermi-liquid (NFL) gedrag geobserveerd in de soortelijke warmte. Bij lage temperaturen werd gevonden dat de soortelijke warmte beschreven kan worden door  $C/T \sim -\ln T$ . Voor substitutie door Co neemt  $T_C$  toe tot aan 20 K voor  $x = 0.60$  en ferromagnetisme wordt onderdrukt voor waarden van  $x$  dicht bij 1. Dit betekent dat UCoGe dicht bij een quantum kritische fase overgang is en verschaft een goede kandidaat om een ferromagnetisch quantum kritisch punt te bestuderen. Tot slot, substitutie van Ge door Si had geen effect op  $T_C$  tot aan  $x = 0.20$ .

### Hoofdstuk 7: UIr

Geen teken van een metamagnetische overgang is gevonden in UIr voor gepulste velden tot aan 52 T. Voor hoge magnetische velden satureert het magnetische moment bij een waarden van  $\approx 1 \mu_B/\text{U-atoom}$ . Dit is sterk gereduceerd vergeleken met  $\approx 3.6 \mu_B/\text{U-atoom}$  voor vrije U atomen, waarschijnlijk vanwege kristallijne elektrische velden. De veld afhankelijkheid van de magnetisatie wordt gekarakteriseerd door een interactie veld van  $B_0 = 42.6(2)$  T. The waargenomen magnetische velden zijn daarom van de orde van 29 K.

Een fit van soortelijke warmte data bij lage temperaturen in magnetische velden tot aan 14 T laat zien dat de parameters die een rol spelen, constant blijven. De data kunnen naar tevredenheid worden gefit voor alle magnetische velden met  $\gamma = 46(1)$  mJ/mol K<sup>2</sup> en  $\theta_D = 181$  K. Daarom is het duidelijk dat het aanleggen van een magnetisch veld van 14 T weinig effect heeft op de soortelijk warmte (en dus de magnetische correlaties) afgezien van een verbreding van de piek bij  $T_C$ .

Thermische uitzetting data laten zien dat uniaxiale druk langs welke richting dan ook de temperatuur  $T_C$  in UIr verlaagt. Voor hydrostatische druk neemt de component langs [101] meer dan de helft van de reductie van  $T_C$  voor zijn rekening. Een opmerkelijke schouder is aanwezig in de curves van de lineaire thermische uitzettingscoëfficiënt  $\alpha$  rondom  $T^* \approx 30$  K. Dit kan verklaard worden door het bestaan van een energieschaal die in competitie is met de magnetische ordening die bij  $T_C = 45$  K te voorschijn komt. Deze competitie leidt tot een schouder in  $\alpha$  rondom 30 K. Het is op dit moment niet duidelijk of er een verband is met de magnetische interacties die waargenomen zijn in de hoge magnetische veld metingen.



---

# BIBLIOGRAPHY

- [1] S. S. Saxena, P. Agarwal, K. Ahilan, F. M. Grosche, R. K. W. Haselwimmer, M. J. Steiner, E. Pugh, I. R. Walker, S. R. Julian, P. Monthoux, G. G. Lonzarich, A. Huxley, I. Sheikin, D. Braithwaite, and J. Flouquet, *Nature (London)* **406** (2000) 587
- [2] D. Aoki, A. Huxley, E. Ressouche, D. Braithwaite, J. Flouquet, J.-P. Brison, E. Lhotel, and C. Paulsen, *Nature (London)* **413** (2001) 613
- [3] T. Akazawa, H. Hidaka, T. Fujiwara, T. C. Kobayashi, E. Yamamoto, Y. Haga, R. Settai, and Y. Ōnuki, *J. Phys.: Condens. Matter* **16** (2004) L29
- [4] J. Bardeen, L. N. Cooper, and J. R. Schrieffer, *Phys. Rev.* **108** (1957) 1175
- [5] W. A. Fertig, D. C. Johnston, L. E. DeLong, R. W. McCallum, M. B. Maple, and B. T. Matthias, *Phys. Rev. Lett.* **38** (1977) 987
- [6] D. E. Moncton, D. B. McWhan, P. H. Schmidt, G. Shirane, W. Thomlinson, M. B. Maple, H. B. MacKay, L. D. Woolf, Z. Fisk, and D. C. Johnston, *Phys. Rev. Lett.* **45** (1980) 2060
- [7] M. Ishikawa and Ø. Fischer, *Solid State Comm.* **23** (1977) 37
- [8] F. Steglich, J. Aarts, C. D. Bredl, W. Lieke, D. Meschede, W. Franz, and H. Schäfer, *Phys. Rev. Lett.* **43** (1979) 1892
- [9] J. G. Bednorz and K. A. Muller, *Z. Phys. B* **64** (1986) 189
- [10] K. Miyake, S. Schmitt Rink, and C. M. Varma, *Phys. Rev. B* **34** (1986) 6554
- [11] M. T. Béal-Monod, C. Bourbonnais, and V. Emery, *Phys. Rev. B* **34** (1986) 7716
- [12] A. A. Menovsky and J. J. M. Franse, *J. Crystal Growth* **65** (1983) 286
- [13] C. Marín and E. Diéguez, *Orientation Of Single-Crystals By Back-Reflection Laue Pattern Simulation*, World Scientific (1999)
- [14] <http://www.ccp14.ac.uk/tutorial/lmgp/orientexpress.htm>
- [15] A. Schenck, *Muon Spin Rotation Spectroscopy: Principles and Applications in Solid State Physics*, Adam Hilger Ltd, Bristol and Boston (1985)
- [16] S. L. Lee, S. H. Kilcoyne, and R. Cywinski (eds.), *Muons Science*, Institut of Physics Publishing Bristol (1999)
- [17] S. Sakarya, Master's thesis, Delft University of Technology, (2002)

- 
- [18] P. Dalmas de Réotier and A. Yaouanc, *J. Phys.: Condens. Matter* **9** (1997) 9113
  - [19] A. Schenck and F. N. Gygax, *Handbook of Magnetic Materials*, volume 9, p. 60, Ed. K. H. J. Buschow, North-Holland, Amsterdam (1995)
  - [20] A. Amato, *Rev. Mod. Phys.* **69** (1997) 1119
  - [21] J. Chappert, *Muons and Pions in Materials Research*, Chap. 3, Ed. J. Chappert and R. I. Grynszpan, Elsevier, Amsterdam (1984)
  - [22] R. Kubo and T. Toyabe, *Magnetic Resonance and Relaxation*, p. 810, North-Holland, Amsterdam (1967)
  - [23] R. S. Hayano, Y.J. Uemura, J. Imazato, N. Nishida, T. Yamazaki, and R. Kubo, *Phys. Rev. B* **20** (1979) 850
  - [24] P. Dalmas de Réotier and A. Yaouanc, *J. Phys.: Condens. Matter* **4** (1992) 4533
  - [25] C. P. Slichter, *Principles of Magnetic Resonance*, Springer-Verlag, Berlin (1996)
  - [26] A. Abragam, *The Principles of Nuclear Magnetism*, Oxford University Press, London (1961)
  - [27] A. Yaouanc, P. Dalmas de Réotier, and E. Frey, *Phys. Rev. B* **47** (1993) 796
  - [28] R. Feyerherm, A. Amato, A. Grayevsky, F. N. Gygax, N. Kaplan, and A. Schenck, *Z. Phys. B* **99** (1995) 3
  - [29] M. Th. Rekveldt, *Z. Phys.* **259** (1973) 391
  - [30] R. Rosman and M. Th. Rekveldt, *Z. Phys. B* **79** (1990) 61
  - [31] R. Rosman and M. Th. Rekveldt, *Phys. Rev. B* **43** (1991) 8437
  - [32] M. McElfresh, *Fundamentals of Magnetism and Magnetic Measurements*, Quantum Design, Inc. (1994)
  - [33] N. H. van Dijk, PhD thesis, University of Amsterdam, (1994)
  - [34] A. de Visser, PhD thesis, University of Amsterdam, (1986)
  - [35] C. Meingast, B. Blank, H. Bürkle, B. Obst, T. Wolf, H. Wühl, V. Selvamanickam, and K. Salama, *Phys. Rev. B* **41** (1990) 11299
  - [36] R. Pott and R. Schefzyk, *J. Phys. E* **16** (1983) 444
  - [37] J. C. Lashley, M. F. Hundley, A. Migliori, J. L. Sarrao, P. G. Pagliuso, T. W. Darling, M. Jaime, J. C. Cooley, W. L. Hults, L. Morales, D. J. Thoma, J. L. Smith, J. Boerio-Goates, B. F. Woodfield, G. R. Stewart, R. A. Fisher, and N. E. Phillips, *Cryogenics* **43** (2003) 369
  - [38] A. C. Larson and R. B. V. Dreele, *GSAS, Technical Report NM87545*, Los Alamos National Laboratory (1994)
  - [39] J. Kondo, *Prog. Theor. Phys. Jpn.* **32** (1964) 37
  - [40] P. W. Anderson, *Phys. Rev.* **124** (1961) 41
  - [41] J. R. Schrieffer and P. A. Wolff, *Phys. Rev.* **149** (1966) 491
  - [42] M. A. Continentino, G. M. Japiassu, and A. Troper, *Phys. Rev. B* **39** (1989) 9734
  - [43] T. Koyama and M. Tachiki, *Phys. Rev. B* **34** (1986) 3272–3287
  - [44] T. Penney, F. P. Milliken, S. von Molnar, F. Holtzberg, and Z. Fisk, *Phys. Rev. B* **34** (1986) 5959

- [45] M. A. Ruderman and C. Kittel, *Phys. Rev.* **96** (1954) 99
- [46] T. Kasuya, *Prog. Theor. Phys.* **16** (1956) 45
- [47] K. Yosida, *Phys. Rev.* **106** (1957) 893
- [48] S. Doniach, *Physica B* **91** (1977) 213
- [49] H. H. Hill, *Plutonium 1970 and Other Actinides*, p. 1, AIME, New York (1970)
- [50] D. D. Koelling, B. D. Dunlap, and G. W. Crabtree, *Phys. Rev. B* **31** (1985) 4966
- [51] J. Hertz, *Phys. Rev. B* **14** (1976) 1165
- [52] P. Coleman, *Physica B* **259-261** (1999) 53
- [53] H. von Löhneysen, *J. Phys.: Condens. Matter* **8** (1996) 9689
- [54] C. M. Varma, Z. Nussinov, and W. van Saarloos, *Phys. Rep.* **361** (2002) 267
- [55] M. Vojta, *Rep. Prog. Phys.* **66** (2003) 2069
- [56] S. K. Ma, *Modern Theory of Critical Phenomena*, Benjamin, Reading (1976)
- [57] B. Widom, *J. Chem. Phys.* **43** (1965) 3892
- [58] K. G. Wilson, *Phys. Rev. B* **4** (1971) 3174
- [59] N. D. Mathur, F. M. Grosche, S. R. Julian, I. R. Walker, D. M. Freye1, R. K. W. Haselwimmer, and G. G. Lonzarich, *Nature* **394** (1998) 39
- [60] C. Pfleiderer, G. J. McMullan, S. R. Julian, and G. G. Lonzarich, *Phys. Rev. B* **55** (1997) 8330
- [61] M. Uhlarz, C. Pfleiderer, and S. M. Hayden, *Phys. Rev. Lett.* **93** (2004) 256404
- [62] D. Belitz, T. R. Kirkpatrick, and T. Vojta, *Phys. Rev. Lett.* **82** (1999) 4707
- [63] D. Belitz and T. R. Kirkpatrick, *Phys. Rev. Lett.* **89** (2002) 247202
- [64] C. Pfleiderer, *J. Phys.: Condens. Matter* **17** (2005) S987
- [65] A. Tari, *The Specific Heat of Matter at Low Temperatures*, Imperial College Press, London (2003)
- [66] N. H. van Dijk, F. Bourdarot, J. C. P. Klaasse, I. H. Hagmusa, E. Brück, and A. A. Menovsky, *Phys. Rev. B* **56** (1997) 14493
- [67] N. W. Ashcroft and N. D. Mermin, *Solid State Physics*, Harcourt College Publishers (1976)
- [68] L. D. Landau, *Sov. Phys. JETP* **3** (1957) 920
- [69] L. D. Landau, *Sov. Phys. JETP* **5** (1957) 101
- [70] L. D. Landau, *Sov. Phys. JETP* **8** (1957) 70
- [71] D. Pines and P. Nozières, *The Theory of Quantum Liquids*, Addison-Wesley, New York (1989)
- [72] G. Baym and C. J. Pethick, *Landau Fermi Liquid Theory*, John Wiley, New York (1991)
- [73] K. Kadowaki and S. B. Woods, *Solid State Comm.* **58** (1986) 507
- [74] P. Nozières P and A. Blandin, *J. Physique* **41** (1980) 193
- [75] D. L. Cox, *Phys. Rev. Lett.* **59** (1987) 1240
- [76] D. L. Cox and M. Jarrel, *J. Phys.: Condens. Matter* **8** (1996) 9825

- 
- [77] C. L. Seaman, M. B. Maple, B. W. Lee, S. Ghamaty, M. Torikachvili, J.-S. Kang, L. Z. Liu, J. W. Allen, and D. L. Cox, *Phys. Rev. Lett.* **67** (1991) 2882
- [78] H. Amitsuka, T. Hidano, T. Honma, H. Mitamura, and T. Sakakibara, *Physica B* **186-188** (1993) 337
- [79] B. Andraka, *Phys. Rev. B* **49** (1994) 3589
- [80] E. Miranda, V. Dobrosavljević, and G. Kotliar, *J. Phys.: Condens. Matter* **8** (1996) 9871
- [81] B. Andraka and G. R. Stewart, *Phys. Rev. B* **47** (1993) 3208
- [82] A. J. Millis, *Phys. Rev. B* **48** (1993) 7183
- [83] T. Moriya and T. Takimoto, *J. Phys. Soc. Jpn.* **64** (1995) 960
- [84] H. von Löhneysen, *J. Magn. Magn. Mat.* **200** (1999) 532
- [85] A. H. Castro Neto, G. Castilla, and B. A. Jones, *Phys. Rev. Lett.* **81** (1998) 3531
- [86] A. de Visser, J. J. M. Franse, and J. Flouquet, *Physica B* **161** (1989) 324
- [87] P. E. Brommer, *Physica B* **112B** (1982) 343
- [88] A. B. Pippard, *The Elements of Classical Thermodynamics*, Cambridge University Press, Cambridge (1964)
- [89] K. Machida and T. Ohmi, *Phys. Rev. Lett.* **86** (2001) 850
- [90] R. Roussev and A. J. Millis, *Phys. Rev. B* **63** (2001) 140504
- [91] A. B. Shick and W. E. Pickett, *Phys. Rev. Lett.* **86** (2001) 300
- [92] K. G. Sandeman, G. G. Lonzarich, and A. J. Schofield, *Phys. Rev. Lett.* **90** (2003) 167005
- [93] N. I. Karchev, K. B. Blagoev, K. S. Bedell, and P. B. Littlewood, *Phys. Rev. Lett.* **86** (2001) 846
- [94] T. R. Kirkpatrick, D. Belitz, T. Vojta, and R. Narayanan, *Phys. Rev. Lett.* **87** (2001) 127003
- [95] T. R. Kirkpatrick and D. Belitz, *Phys. Rev. B* **67** (2003) 024515
- [96] V. P. Mineev, *Phys. Rev. B* **66** (2002) 134504
- [97] V. P. Mineev and T. Champel, *Phys. Rev. B* **69** (2004) 144521
- [98] D. V. Shopova and D. I. Uzunov, *Phys. Rev. B* **72** (2005) 024531
- [99] A. Nevidomskyy, *Phys. Rev. Lett.* **94** (2005) 097003
- [100] H. Suhl, *Phys. Rev. Lett.* **87** (2001) 167007
- [101] A. A. Abrikosov, *J. Phys.: Condens. Matter* **13** (2001) L943
- [102] Y. Kitaoka, H. Kotegawa, A. Harada, S. Kawasaki, Y. Kawasaki, Y. Haga, E. Yamamoto, Y. Ōnuki, K. M. Itoh, E. E. Haller, and H. Harima, *J. Phys.: Condens. Matter* **17** (2005) S975
- [103] H. Kotegawa, A. Harada, S. Kawasaki, Y. Kawasaki, Y. Kitaoka, Y. Haga, E. Yamamoto, Y. Ōnuki, K. M. Itoh, E. E. Haller, and H. Harima, *J. Phys. Soc. Jpn.* **74** (2005) 705
- [104] P. Boulet, A. Daoudi, M. Potel, H. Noël, G. M. Gross, G. André, and F. Bourée, *J. Alloys Comp.* **247** (1997) 104
- [105] K. Oikawa, T. Kamiyama, H. Asano, Y. Ōnuki, and M. Kohgi, *J. Phys. Soc. Jpn.* **65** (1996) 3229



- [106] D. Aoki, A. Huxley, E. Ressouche, I. Sheikin, J. Flouquet, J.-P. Brison, and C. Paulsen, *J. Phys. Chem. Solids* **63** (2002) 1179
- [107] N. Kernavanois, B. Grenier, A. Huxley, E. Ressouche, J. P. Sanchez, and J. Flouquet, *Phys. Rev. B* **64** (2001) 174509
- [108] Y. Ōnuki, I. Ukon, S. W. Yun, I. Umehara, K. Satoh, T. Fukuhara, H. Sato, S. Takayanagi, M. Shikama, and A. Ochiai, *J. Phys. Soc. Jpn.* **61** (1992) 293
- [109] A. Huxley, I. Sheikin, and D. Braithwaite, *Physica B* **284-288** (2000) 1277
- [110] A. Huxley, I. Sheikin, E. Ressouche, N. Kernavanois, D. Braithwaite, R. Calemczuk, and J. Flouquet, *Phys. Rev. B* **63** (2001) 144519
- [111] T. C. Kobayashi, K. Hanazono, N. Tateiwa, K. Amaya, Y. Haga, R. Settai, and Y. Ōnuki, *J. Phys.: Condens. Matter* **14** (2002) 10779
- [112] Y. Haga, M. Nakashima, R. Settai, S. Ikeda, T. Okubo, S. Araki, T. C. Kobayashi, N. Tateiwa, and Y. Ōnuki, *J. Phys.: Condens. Matter* **14** (2002) L125
- [113] N. Tateiwa, K. Hanazono, T. C. Kobayashi, K. Amaya, T. Inoue, , K. Kindo, Y. Koike, N. Metoki, Y. Haga, R. Settai, and Y. Ōnuki, *J. Phys. Soc. Jpn* **70** (2001) 2876
- [114] C. Pfleiderer and A. D. Huxley, *Phys. Rev. Lett.* **89** (2002) 147005
- [115] N. Tateiwa, T. C. Kobayashi, K. Amaya, Y. Haga, R. Settai, and Y. Ōnuki, *Phys. Rev. B* **69** (2004) 180513(R)
- [116] A. Huxley A, E. Ressouche, B. Grenier, D. Aoki, J. Flouquet, and C. Pfleiderer, *J. Phys.: Condens. Matter* **15** (2003) S1945
- [117] T. Nishioka, G. Motoyama, S. Nakamura, H. Kadoya, and N. K. Sato, *Phys. Rev. Lett.* **88** (2002) 237203
- [118] T. Nishioka, G. Motoyama, S. Nakamura, H. Kadoya, and N. K. Sato, *Phys. Rev. Lett.* **91** (2003) 209702
- [119] D. E. Moncton, G. Shirane, W. Thomlinson, M. Ishikawa, and Ø. Fischer, *Phys. Rev. Lett.* **41** (1978) 1133
- [120] C. F. Majkrzak, G. Shirane, W. Thomlinson, M. Ishikawa, Ø. Fischer, and D. E. Moncton, *Solid State Comm.* **31** (1979) 773
- [121] W. Thomlinson, G. Shirane, D. E. Moncton, M. Ishikawa, and Ø. Fischer, *Phys. Rev. B* **23** (1981) 4455
- [122] I. R. Walker, F. M. Grosche, D. M. Freye, and G. G. Lonzarich, *Physica C* **282** (1997) 303
- [123] F. M. Grosche, S. J. S. Lister, F. V. Carter, S. S. Saxena, R. K. W. Haselwimmer, N. D. Mathur, S. R. Julian, and G. G. Lonzarich, *Physica B* **239** (1997) 62
- [124] N. K. Sato, N. Aso, K. Miyake, R. Shiina, P. Thalmeier, G. Varelogiannis, C. Geibel, F. Steglich, P. Fulde, and T. Komatsubara, *Nature (London)* **410** (2001) 340
- [125] N. Tateiwa, T. C. Kobayashi, K. Hanazono, K. Amaya, Y. Haga, R. Settai, and Y. Ōnuki, *J. Phys.: Condens. Matter* **13** (2001) L17
- [126] E. M. Chudnovsky and L. Gunther, *Phys. Rev. Lett.* **60** (1988) 661
- [127] E. B. Sonin, *Phys. Rev. B* **66** (2002) 100504(R)
- [128] M. Fauré and A. I. Buzdin, *Phys. Rev. Lett.* **94** (2005) 187202
- [129] E. B. Sonin, *Phys. Rev. Lett.* **95** (2005) 269701

- [130] M. Fauré and A. I. Buzdin, *Phys. Rev. Lett.* **95** (2005) 269702
- [131] S. Chikazumi, *Physics of Ferromagnetism*, Oxford University Press (1997)
- [132] E. Lhotel, C. Paulsen, and A. D. Huxley, *Phys. Rev. Lett.* **91** (2003) 209701
- [133] E. Lhotel, C. Paulsen, and A. D. Huxley, *J. Magn. Magn. Mat.* **272-276** (2004) 179
- [134] A. Yaouanc, P. Dalmas de Réotier, P. C. M. Gubbens, C. T. Kaiser, A. A. Menovsky, M. Mihalik, and S. P. Cottrel, *Phys. Rev. Lett.* **89** (2002) 147001
- [135] D. Andreica, PhD thesis, ETH-Zurich, (2001), Chapter 5
- [136] B. Bireckhoven and J. Wittig, *J. Phys. E* **21** (1988) 841
- [137] L. R. Walker and R. E. Walstedt, *Phys. Rev. B* **22** (1980) 3816
- [138] A. M. Mulders, C. T. Kaiser, S. J. Harker, P. C. M. Gubbens, A. Amato, F. N. Gygax, A. Schenck, P. Dalmas de Réotier, A. Yaouanc, K. H. J. Buschow, and A. A. Menovsky, *Phys. Rev. B* **67** (2003) 014303
- [139] A. Schenck and G. Solt, *J. Phys.: Condens. Matter* **16** (2004) S4639
- [140] A. Schenck A, M. Pinkpank, F. N. Gygax, K.-U. Neumann, K. R. A. Ziebeck, and A. Amato, *J. Phys.: Condens. Matter* **10** (1998) 8059
- [141] E. Frey and F. Schwabl, *Adv. Phys.* **43** (1994) 577
- [142] P. Dalmas de Réotier, A. Yaouanc, and E. Frey, *Phys. Rev. B* **50** (1994) 3033
- [143] P. Dalmas de Réotier, P. C. M. Gubbens, and A. Yaouanc, *J. Phys.: Condens. Matter* **16** (2004) S4687
- [144] P. C. M. Gubbens, P. Dalmas De Réotier, A. Yaouanc, A. A. Menovsky, and C. E. Snel, *Hyperfine Interactions* **85** (1994) 245
- [145] S. Watanabe and K. Miyake, *J. Phys. Soc. Jpn.* **71** (2002) 2489
- [146] S. Watanabe and K. Miyake, *Physica B* **312-313** (2002) 115
- [147] J. Flouquet, A. Huxley, I. Sheikin, N. Kernavanois, D. Braithwaite, E. Ressouche, S. Watanabe, and K. Miyake, *J. Phys. Soc. Jpn. Suppl. A* **70** (2001) 14
- [148] S. Raymond and A. Huxley, *Phys. Rev. B* **73** (2006) 094420
- [149] A. D. Huxley, S. Raymond, and E. Ressouche, *Phys. Rev. Lett.* **91** (2003) 207201
- [150] P. Monthoux and G. G. Lonzarich, *Phys. Rev. B* **59** (1999) 14598
- [151] L. Paolasini L, J. A. Paixão, G. H. Lander, A. Delapalme, N. Sato, and T. Komatsubara, *J. Phys.: Condens. Matter* **5** (1993) 8905
- [152] J. A. Paixão, L. C. J. Pereira, P. Estrela, M. Godinho, M. Almeida, L. Paolasini, M. Bonnet, J. Rebizant, and J. C. Spirlet, *J. Phys.: Condens. Matter* **11** (1999) 2115
- [153] J. Rossat-Mignod, *Handbook of the physics and chemistry of Actinides*, volume 1, p. 60, North-Holland, Amsterdam (1984)
- [154] K. Kuwahara, H. Sagayama, K. Iwasa, M. Kohgi, Y. Haga, Y. Ōnuki, K. Kakurai, M. Nishi, K. Nakajima, N. Aso, and Y. Uwatoko, *Physica B* **312-313** (2002) 106
- [155] R. Caspary, P. Hellmann, M. Keller, G. Sparn, C. Wassilew, R. Köhler, C. Geibel, C. Schank, F. Steglich, and N. E. Phillips, *Phys. Rev. Lett.* **71** (1993) 2146
- [156] R. Feyerherm, A. Amato, F. N. Gygax, A. Schenck, C. Geibel, F. Steglich, N. Sato, and T. Komatsubara, *Phys. Rev. Lett.* **73** (1994) 1849

- 
- [157] N. Metoki, Y. Haga, Y. Koike, and Y. Ōnuki, *Phys. Rev. Lett.* **80** (1998) 5417
- [158] N. Bernhoeft, N. Sato, B. Roessli, N. Aso, A. Hiess, G. H. Lander, Y. Endoh, and T. Komatsubara, *Phys. Rev. Lett.* **81** (1998) 4244
- [159] A. Schenck A, P. Birrer, F. N. Gygax, B. Hitti, E. Lippelt, M. Weber, P. Böni P, P. Fischer, H. R. Ott, and Z. Fisk, *Phys. Rev. Lett.* **65** (1990) 2454
- [160] H. Kumigashira, T. Ito, A. Ashihara, H. D. Kim, H. Aoki, T. Suzuki, H. Yamagami, and T. Takahashi, *Phys. Rev. B* **61** (2000) 15707
- [161] V. Sechovský and L. Havela, *Handbook of Magnetic Materials*, volume 11, p. 1, Ed. K. H. J. Buschow, North-Holland, Amsterdam (1998)
- [162] V. H. Tran, R. Troć, and G. André, *J. Magn. Magn. Mater.* **186** (1998) 81
- [163] K. Prokeš, T. Tahara, Y. Echizen, T. Takabatake, T. Fujita, I. H. Hagmusa, J. C. P. Klaasse, E. Brück, F. R. de Boer, M. Diviš, and V. Sechovský, *Physica B* **311** (2002) 220
- [164] A. B. Shick, *Phys. Rev. B* **65** (2002) 180509R
- [165] M. Diviš, L. M. Sandratskii, M. Richter, P. Mohn, and P. Novák, *J. Alloys Comp.* **337** (2002) 48
- [166] K. Prokeš, T. Tahara, Y. Echizen, T. Takabatake, T. Fujita, I. H. Hagmusa, J. C. P. Klaasse, E. Brück, F. R. de Boer, M. Diviš, and V. Sechovský, *Physica B* **334** (2003) 272
- [167] I. H. Hagmusa, K. Prokeš, Y. Echizen, T. Takabatake, T. Fujita, J. C. P. Klaasse, E. Brück, V. Sechovský, and F. R. de Boer, *Physica B* **281–282** (2000) 223
- [168] V. H. Tran and R. Troć, *Phys. Rev. B* **57** (1998) 11592
- [169] F. R. de Boer, E. Brück, V. Sechovský, L. Havela, and K. H. J. Buschow, *Physica B* **163** (1990) 175
- [170] K. H. J. Buschow, E. Brück, R. G. van Wierst, F. R. de Boer, L. Havela, V. Sechovský, P. Nozar, E. Sugiura, M. Ono, M. Date, and A. Yamagishi, *J. Appl. Phys.* **67** (1990) 5215
- [171] B. Chevalier, E. Hickey, and J. Etourneau, *J. Magn. Magn. Mater.* **90–91** (1990) 499
- [172] R. Troć and V. H. Tran, *J. Magn. Magn. Mater.* **73** (1988) 389
- [173] F. Lévy, I. Sheikin, B. Grenier, and A. D. Huxley, *Science* **309** (2005) 1343
- [174] L. Havela, M. Diviš, V. Sechovský, A.V. Andreev, F. Honda, G. Oomi, Y. Méresse, and S. Heathman, *J. Alloys Comp.* **322** (2001) 7
- [175] N. H. van Dijk, B. Fåk, T. Charvolin, P. Lejay, and J. M. Mignot, *Phys. Rev. B* **61** (2000) 8922
- [176] F. Hardy, A. Huxley, J. Flouquet, B. Salce, G. Knebel, D. Braithwaite, D. Aoki, M. Uhlarz, and C. Pfleiderer, *Physica B* **359–361** (2005) 1111
- [177] F. Hardy and A. D. Huxley, *Phys. Rev. Lett.* **94** (2005) 247006
- [178] F. Hardy, PhD thesis, CEA, Grenoble, (2004)
- [179] M. C. Lynch, S. P Cottrell, P. J. C King, and G. H. Eaton, *Physica B* **326** (2003) 270
- [180] N. Bloembergen, E. M. Purcell, and R. V. Pound, *Phys. Rev.* **73** (1948) 679
- [181] C. P. Slichter, *Principles of Magnetic Resonance*, Springer Verlag (1992)
- [182] G. G. Lonzarich and L. Taillefer, *J. Phys. C: Solid State Phys.* **18** (1985) 4339
- [183] G. Zwicknagl A. N. Yaresko and P. Fulde, *Phys. Rev. B* **65** (2002) 081103(R)

- 
- [184] G. Zwicknagl and P. Fulde, *J. Phys.: Condens. Matter* **15** (2003) S1911
- [185] T. Takahashi, N. Sato, T. Yokoya, A. Chainani, T. Morimoto, and T. Komatsubara, *J. Phys. Soc. Jpn* **65** (1995) 156
- [186] K. Prokeš, A. Gukasov, T. Takabatake, T. Fujita, and V. Sechovský, *Acta Phys. Pol. B* **34** (2003) 1473
- [187] S. W. Lovesey, *Theory of neutron scattering from condensed matter*, volume 2, Oxford University Press, Oxford (1984)
- [188] A. Yaouanc, P. Dalmas de Réotier, P. C. M. Gubbens, S. Sakarya, G. Lapertot, A. D. Hillier, and P. J. C. King, *J. Phys.: Condens. Matter* **17** (2005) L129
- [189] P. Dalmas de Réotier, A. Yaouanc, and P. Bonville, *J. Phys.: Condens. Matter* **8** (1996) 5113
- [190] P. Dalmas de Réotier, A. Yaouanc, P. C. M. Gubbens, S. Sakarya, E. Jiménez, P. Bonville, and J. A. Hodges, *Hyperfine Interactions* **158** (2004) 131
- [191] P. Dalmas de Réotier and A. Yaouanc, *Phys. Rev. B* **52** (1995) 9155
- [192] S. Sakarya, N. H. van Dijk, A. de Visser, and E. Brück, *Phys. Rev. B* **67** (2003) 144407
- [193] G. R. Stewart, *Rev. Mod. Phys.* **73** (2001) 797
- [194] K. Prokeš, E. Brück, K. H. J. Buschow, F. R. de Boer, V. Sechovský, P. Svoboda, X. Hu, H. Maletta, and T. J. Gortenmulder, *J. Appl. Phys.* **79** (1996) 5221
- [195] B. Chevalier, B. Lloret, P. Gravereau, B. Buffat, and J. Etourneau, *J. Magn. Magn. Mat.* **75** (1988) 13
- [196] V. Sechovský and L. Havela, *Ferromagnetic Materials*, volume 4, p. 309, Ed. E. P. Wohlfarth and K. H. J. Buschow, North-Holland, Amsterdam (1988)
- [197] F. Canepa, P. Manfrinetti, M. Pani, and A. Palenzona, *J. Alloys Comp.* **234** (1996) 225
- [198] S. Sakarya, N. H. van Dijk, N. T. Huy, and A. de Visser, *Physica B* **378-380** (2006) 970
- [199] T. Akazawa, H. Hidaka, H. Kotegawa, T. Kobayashi, T. Fujiwara, E. Yamamoto, Y. Haga, R. Settai, and Y. Ōnuki, *J. Phys. Soc. Jpn.* **73** (2004) 3129
- [200] L. Vegard, *Z. Phys.* **5** (1921) 17
- [201] N. T. Huy *et al.*, in preparation
- [202] A. Eiling and J. S. Schilling, *Phys. Rev. Lett.* **46** (1981) 364
- [203] Q. G. Sheng and B. R. Cooper, *J. Appl. Phys.* **75** (1985) 7035
- [204] J. J. Park and L. R. Mullen, *J. Res. NBS* **72A** (1968) 19
- [205] A. Dommann, F. Hulliger, and T. Siegrist, *J. Magn. Magn. Mat.* **67** (1987) 323
- [206] T. Siegrist, Y. Le Page, V. Gramlich, W. Petter, A. Dommann, and F. Hulliger, *J. Less-Common Metals* **125** (1987) 167
- [207] P. H. Frings, C. Vettier, A. Dommann, F. Hulliger, and A. Menovsky, *Physica B* **156-157** (1989) 832
- [208] H. Brändle, J. Schoenes, and F. Hulliger, *Helvetica Physica Acta* **61** (1988) 833
- [209] Y. Ōnuki, S. W. Yun, I. Ukon, A. Kobori, I. Umehara, K. Satoh, T. Fukuhara, H. Sato, and S. Takayanagi, *J. Phys. Soc. Jpn.* **61** (1992) 1751

- 
- [210] E. D. Bauer, E. J. Freeman, C. Sirvent, and M. B. Maple, *J. Phys.: Condens. Matter* **13** (2001) 5675
  - [211] A. Galatanu, Y. Haga, E. Yamamoto, T. D. Matsuda, S. Ikeda, and Y. Ōnuki, *J. Phys. Soc. Jpn.* **73** (2004) 766
  - [212] T. C. Kobayashi, S. Fukushima, H. Hidaka, H. Kotegawa, T. Akazawa, E. Yamamoto, Y. Haga, R. Settai, and Y. Ōnuki, *Physica B* **375-380** (2006) 355
  - [213] E. Bauer, G. Hilscher, H. Michor, Ch. Paul, E. W. Scheidt, A. Griбанov, Yu. Seropegin, H. Noel, M. Sigrist, and P. Rogl, *Phys. Rev. Lett.* **92** (2004) 27003
  - [214] P. W. Anderson, *Phys. Rev. B* **30** (1984) 4000
  - [215] L. P. Gorkov and E. I. Rashba, *Phys. Rev. Lett.* **87** (2001) 037004
  - [216] R. P. Kaur, D. F. Agterberg, and M. Sigrist, *Phys. Rev. Lett.* **94** (2005) 137002
  - [217] P. H. Frings, J. J. M. Franse, F. R. de Boer, and A. Menovsky, *J. Magn. Magn. Mater.* **31-34** (1983) 240
  - [218] K. Bakker, A. de Visser, A. A. Menovsky, and J. J. M. Franse, *Phys. Rev. B* **46** (1992) 544
  - [219] J.-G. Park, K. A. McEwen, S. de Brion, G. Chouteau, H. Amitsuka, and T. Sakakibara, *J. Phys.: Condens. Matter* **9** (1997) 3065
  - [220] K. Sugiyama, M. Nakashima, H. Ohkuni, K. Kindo, Y. Haga, T. Honma, E. Yamamoto, and Y. Ōnuki, *J. Phys. Soc. Jpn.* **68** (1999) 3394
  - [221] F. R. de Boer, J. J. M. Franse, E. Louis, A. A. Menovsky, J. A. Mydosh, T. T. M. Palstra, U. Rauchschwalbe, W. Schlabit, F. Steglich, and A. de Visser, *Physica B* **138** (1986) 1
  - [222] A. de Visser, F. R. de Boer, A. A. Menovsky, and J. J. M. Franse, *Sol. State Comm.* **64** (1987) 527
  - [223] E. Yamamoto, Y. Haga, H. Shishido, H. Nakawaki, Y. Inada, R. Settai, and Y. Ōnuki, *Physica B* **312** (2002) 302
  - [224] I. Sheikin, Y. Wang, F. Bouquet, P. Lejay, and A. Junod, *J. Phys.: Condens. Matter* **14** (2002) L543
  - [225] P. Estrela, A. de Visser, O. Stockert, K. Grube, and H. v. Löhneysen, *J. Magn. Magn. Mat.* **272-276** (2004) 23
  - [226] G. Oomi, K. Nishimura, Y. Ōnuki, and S. W. Yun, *Physica B* **186-188** (1993) 758



---

# Acknowledgements



IRST OF ALL I would like to thank all the members of my committee for the approval of my thesis and for giving me the opportunity to bring four years of scientific research to a successful end.

De meeste dank ben ik verschuldigd aan Niels van Dijk. Niet alleen vanwege het vertrouwen dat hij in mij heeft gesteld om vanaf mei 2002 aan een promotietraject te beginnen, maar ook vanwege de begeleiding die hij in de vier daaropvolgende jaren gaf op zowel theoretisch als experimenteel gebied. Ignatz de Schepper wil ik bedanken voor het feit dat hij mijn promotor wilde zijn en dit proefschrift heeft goedgekeurd. Ik ben hem zeer erkentelijk voor de belangstelling die hij op diverse gebieden in mij heeft getoond. Paul Gubbens bedank ik voor alles wat hij voor mij heeft gedaan. Marianne van Baaren ben ik dankbaar voor het voortreffelijk organiseren van al mijn buitenlandse trips, maar vooral ook voor de gezelligheid in de groep.

Het Van der Waals-Zeemaninstituut van de Universiteit van Amsterdam heeft een grote rol gespeeld tijdens de vier jaar van mijn promotie. De kritische blik van Anne de Visser heeft altijd voor verbetering gezorgd in al mijn werk. Chapter 6 originated in strong collaboration with Nguyen Than Huy. All the single crystals used in this thesis were made by Yingkai Huang and Ekkes Brück. I would like to thank all of them for their contribution to this thesis. Speciale dank gaat naar Ton Gortenmulder, voor de prettige ontvangst wanneer ik weer eens in Leiden langskwam om kristallen te oriënteren.

I am very grateful to my two French collaborators Pierre Dalmas de Réotier and Alain Yaouanc from Grenoble. Without you the many  $\mu$ SR experiments described in Chapters 4 and 5 would not have been as successful as they are now. Apart from this, I have learned tremendously much about science in general and  $\mu$ SR in particular. I am honored to have worked together with such good scientists as they are. I will never forget the most interesting scientific discussions during my PhD. These discussions with Pierre somehow always took place somewhere between two and three o'clock in the night in the GPS cabin at PSI or the EMU cabin at ISIS.



During the autumn of 2005 I spent three months in Karlsruhe for a part of my research. This visit was kindly enabled by Prof. von Löhneysen. The magnetization measurements under pressure were performed together with Marc Uhlarz. Although the specific heat measurements at the University didn't work out exactly as desired, Tobias Görlach should be mentioned for his enormous efforts. At the Forschungszentrum, Christoph Meingast and William Knafo were of great help for the thermal expansion measurements described in Chapter 7. I would like to thank all of them for the great time I had in Karlsruhe!

The technical support given by Adrian Hillier, when measurements on the EMU spectrometer at ISIS were running, was really marvelous. His interest and concern for the experiments have contributed to the  $\mu$ SR results of Chapter 5. Probably the biggest challenge of all was to get the uranium samples into the cryostat in the first place. I thank him for his great help!

The measurements on  $\text{UGe}_2$  at high pressure, described in Chapter 4, would not have been possible without the great support of Daniel Andreica. His pressure cell enabled me to perform the desired measurements. At this place Alex Amato should be thanked for the Knight shift measurements performed in his own beamtime.

The high-field measurements in Chapter 7 were performed at the LNCMP in Toulouse with the great support of Harisson Rakoto and Jean-Marc Broto. Thanks to them the experiments were a success! Preliminary measurements were performed in Nijmegen together with Jos Perenboom. I would like to thank all of them for their kind help.

During the four years of my PhD I had the pleasure to meet other PhD students from all over the world. First of all I will never forget the great times I had with Enrique. Whether in Villigen during muon measurements or high in the mountains in Zuoz in Switzerland, in Manzanares in Spain for his wedding, in Rome for a magnetism conference or just in Delft, it was always a pleasure to meet each other. Iulian and Jerome have been my two roommates at the IRI for a few years. The discussions about their home countries, Romania and the Philippines, and the philosophical conversations were always very interesting.

De muziek en het hele gebeuren daaromheen heeft een belangrijke rol in mijn leven gespeeld. Mijn dank gaat uit naar de leden van het Zuid-Hollands Symphonie Orkest met speciale dank aan Eunice en de andere kroegmaatjes. Verder bedank ik mijn muziekdocenten voor hun inspirerende lessen: Alfred Snel voor de pianolessen, Els Boerendonk voor de vioollessen en Aarnoud de Groen voor de orgellessen.


Zeer veel dank ben ik verschuldigd aan Peronik Amons. Zijn ondersteuning tijdens onze gesprekken was voor mij onontbeerlijk en maakte een wereld van verschil. Hierdoor ben ik in staat geweest de vele tegenslagen waarmee ik te kampen kreeg, te overwinnen.

Tot slot dank ik mijn broer Serhat voor zijn interesse, Madelon voor de kft van dit proefschrift en mijn moeder voor alles wat zij voor mij betekend heeft met haar kracht en haar steun door alle omstandigheden in de loop der tijd heen.



---

# Curriculum Vitae

ERDAR SAKARYA werd geboren op 10 maart 1979 in Den Haag. Na in 1997 het Gymnasium Haganum te Den Haag te hebben afgerond, ging hij Technische Natuurkunde studeren aan de Technische Universiteit Delft. Een jaar later behaalde hij zijn propedeuse cum laude. Tijdens zijn afstuderen maakte hij deel uit van de vakgroep Neutronenverstrooiing en Mössbauerspectroscopie aan het Interfacultair Reactor Instituut van de Technische Universiteit Delft. In april 2002 studeerde hij cum laude af. Bovendien was hij de beste afstudeerder van het studiejaar 2001 - 2002 en ontving hij de Natuurkundeprijs 2002 voor bijzondere afstudeerscriptie. Aansluitend volgde een vierjarig promotietraject aan hetzelfde Reactor Instituut, waarvan dit proefschrift het uiteindelijke resultaat is. Tijdens zijn promotie ging hij regelmatig naar het buitenland, zowel om onderzoek te doen aan diverse buitenlandse instituten, te weten ISIS (Oxford, Engeland), PSI (Villigen, Zwitserland), BENSC/HMI (Berlijn, Duitsland), en LNCMP (Toulouse, Frankrijk), als voor diverse cursussen zoals de HERCULES cursus (Higher Education Research Course for Users of Large Experimental Systems) in Grenoble (Frankrijk) en een zomerschool in Zuoz (Zwitserland). In het najaar van 2005 verbleef hij drie maanden aan de “Universität Karlsruhe (TH)” in Duitsland. In het kader van onderwijsverplichtingen was hij begeleider van practica voor de cursussen Stralingshygiëne niveau 4 en niveau 5.

Tijdens zijn studie was Serdar bijlesleraar wiskunde, natuurkunde en scheikunde voor leerlingen van het Gymnasium Haganum te Den Haag. Tevens bekleedde hij de functies van algemeen bestuurslid, secretaris en ten slotte voorzitter van het Zuid-Hollands Symfonie Orkest. Met dit orkest heeft hij op 24 april 2004 als solist het derde pianoconcert van Beethoven uitgevoerd.

Thans is Serdar werkzaam bij Hewitt Associates als actuariel medewerker. In het kader hiervan studeert hij naast zijn werk Actuariële Wetenschappen aan de Universiteit van Amsterdam.



---

## List of publications

A. Yaouanc, P. Dalmas de Réotier, P. Bonville, J. A. Hodges, P. C. M. Gubbens, C. T. Kaiser, and S. Sakarya, *Spin dynamics in geometrically frustrated compounds*, Physica B **326** (2003) 456-459

S. Sakarya, N. H. van Dijk, A. de Visser, and E. Brück, *Dilatometry study of the ferromagnetic order in single-crystalline URhGe*, Phys. Rev. B **67** (2003) 144407

S. Sakarya, N. H. van Dijk, A. de Visser, and E. Brück, *Thermal expansion measurements on a ferromagnetically ordered single-crystal URhGe*, J. Magn. Magn. Mater. **272-276** (2004) e15-e16

E. Jiménez, P. C. M. Gubbens, S. Sakarya, G. A. Stewart, P. Dalmas de Réotier, A. Yaouanc, J. Isasi, R. Sáez-Puche, and U. Zimmermann, *Interplay between  $Tm^{3+}$  and  $Cr^{5+}$  magnetic sublattices in  $TmCrO_4$* , J. Magn. Magn. Mater. **272-276** (2004) 568-570

O. Roubeau, P. C. M. Gubbens, D. Visser, M. Blaauw, P. Dalmas de Réotier, A. Yaouanc, J. G. Haasnoot, J. Reedijk, S. Sakarya, U. A. Jayasooriya, S. P. Cottrell, and P. J. C. King, *Observation of the spin-crossover in  $[Fe(btr)_2(NCS)_2 \cdot H_2O]$  ( $btr=4,4'$ -bis-1,2,4-triazole) with  $\mu SR$* , Chem. Phys. Letters **395** (2004) 177-181

P. Dalmas de Réotier, A. Yaouanc, P. C. M. Gubbens, S. Sakarya, E. Jiménez, P. Bonville, and J. A. Hodges, *Thermal Behaviour of the  $\mu SR$  Relaxation Rate at High Temperature in Insulators*, Hyperfine Interactions **158** (2004) 131

A. Yaouanc, P. Dalmas de Réotier, P. C. M. Gubbens, S. Sakarya, G. Lapertot, A. D. Hillier, and P. J. C. King *Testing the self-consistent renormalization theory for the description of the spin-fluctuation modes of MnSi at ambient pressure*, J. Phys.: Condens. Matter **17** (2005) L129

S. Sakarya, N. H. van Dijk, and E. Brück, *Determination of the ferromagnetic domain size in  $UGe_2$  by three-dimensional neutron depolarization*, Physica B **359-**

**361** (2005) 1120

S. Sakarya, N. H. van Dijk, and E. Brück, *Determination of the magnetic domain size in the ferromagnetic superconductor  $UGe_2$  by three-dimensional neutron depolarization*, Phys. Rev. B. **71** (2005) 174417

A. Yaouanc, P. Dalmas de Réotier, V. Glazkov, C. Marin, P. Bonville, J. A. Hodges, P. C. M. Gubbens, S. Sakarya, and C. Baines, *Magnetic Density of States at Low Energy in Geometrically Frustrated Systems*, Phys. Rev. Lett. **95** (2005) 047203

P. Dalmas de Réotier, G. Lapertot, A. Yaouanc, P. C. M. Gubbens, S. Sakarya, and A. Amato, *Evidence for an antiferromagnetic component in the magnetic structure of  $ZrZn_2$* , Phys. Lett. A **349** (2006) 513

P. C. M. Gubbens, M. Wagemaker, S. Sakarya, M. Blaauw, A. Yaouanc, P. Dalmas de Réotier, and S. P. Cottrell *Muon spin relaxation in  $Li_{0.6}TiO_2$  anode material*, Solid State Ionics **177** (2006) 145

P. Dalmas de Réotier, V. Glazkov, C. Marin, A. Yaouanc, P. C. M. Gubbens, S. Sakarya, P. Bonville, A. Amato, C. Baines, and P. J. C. King *Studies of  $R_2Ti_2O_7$  ( $R = Gd$  and  $Yb$ ); new results*, Physica B **374-375** (2006) 145

S. Sakarya, N. H. van Dijk, N. T. Huy, and A. de Visser, *Suppression of ferromagnetism in  $URhGe$  doped with  $Ru$* , Physica B **378-380** (2006) 970

E. Jiménez-Melero, P. C. M. Gubbens, M. P. Steenvoorden, S. Sakarya, A. Goosens, P. Dalmas de Réotier, A. Yaouanc, J. Rodríguez-Carvajal, B. Beuneu, J. Isasi, R. Sáez-Puche, U. Zimmerman and J. L. Martínez *A combined study of the magnetic properties of  $GdCrO_4$* , J. Phys.: Condens. Matter **18** (2006) 7893

S. Sakarya, N. H. van Dijk, A. de Visser, E. Brück, Y. Huang, J. A. A. J Perenboom, H. Rakoto, J.-M. Broto *High field magnetization measurements on  $UIr$  in the ferromagnetic state*, submitted to J. Magn. Magn. Mater.

S. Sakarya, N. T. Huy, N. H. van Dijk, A. de Visser, J. C. P. Klaasse, M. Wagemaker, T. J. Gortenmulder, M. Uhlarz and H. v. Löhneysen *Search for the ferromagnetic quantum critical points in  $URhGe$  by chemical substitution*, to be submitted